TURBULENCE MODELLING OF OSCILLATORY FLOWS OVER SMOOTH AND ROUGH SURFACES

A THESIS SUBMITTED TO THE UNIVERSITY OF MANCHESTER
FOR THE DEGREE OF DOCTOR OF PHILOSOPHY
IN THE FACULTY OF SCIENCE AND ENGINEERING

April 2000

By

Sophie Bella Letherman B.Sc. M.Sc.

Department of Engineering

Contents

List of Tables

List of Figures

Abstract

This study investigates turbulence models for application to boundary layer flows. Firstly, steady channel flow and transient pipe flows are considered. Calculations of a low-Reynolds-number k-ϵ model, a k-ϵ-S model (a strain parameter model which has not been applied to unsteady flows previously) and a Reynolds Stress Transport model are compared with experimental and DNS data. The eddy viscosity turbulence models (k-ϵ, k-ϵ-S) satisfactorily predict the mean flow parameters of steady channel flow. However the k-ϵ-S model proves superior in comparison with turbulence quantities. Near to the pipe wall, the k-ϵ-S model best captures the details of periodic pipe flow detail, whereas in the outer flow region the RSTM gives closest agreement with the experimental data.

The high-Reynolds-number k-ϵ and k-l eddy viscosity turbulence models are examined in a separate study of oscillatory flows over smooth and rough beds. The computations are considered over a wider range of experimental parameters than previously investigated. The turbulence models are assessed by comparison with field measurements and laboratory data sets including a new set of experimental measurements. Both models predict the bed shear stress and velocity adequately, but the k-ϵ model emerges as the superior scheme when considering turbulence quantities. An attempt is made to quantify the uncertainty in the Reynolds shear stress and eddy viscosity experimental data. The k-ϵ model calculations more frequently lie within the experimental uncertainty bands. However this uncertainty range is wide; any improvement would require a corresponding improvement in the experimental resolution of rough bed flows.

Declaration

No portion of the work referred to in this thesis has been submitted in support of an application for another degree or qualification of this or any other university or other institution of learning.

Copyright

The Author

The author graduated from the University of Warwick in 1995 gaining a second class honours degree in Mathematics. She also graduated from the University of Manchester in 1996 gaining an M.Sc. (taught course and dissertation) joint between the Mathematics and Aerospace Engineering departments. The following year the candidate joined the Department of Engineering at the University of Manchester to undertake the research reported in this thesis. The author is currently employed at U.M.I.S.T. as a research assistant.

Acknowledgements

First and foremost I would like to express my gratitude to my supervisors Prof. Peter K. Stansby and especially Dr. Mark A. Cotton for their advice and support throughout the course of my Ph.D. studies.

Many thanks to Dr. B. M. Sumer for kindly providing access to the data set for the experiments of Jensen, Sumer and Fredsøe (1989) and to Dr. P. M. Lloyd and Dr. C. Chen for providing the data for the UK Coastal Research Facility and the University of Manchester Tidal Flume experiments. I would also like to acknowledge the support of a UK Engineering and Physical Sciences Research Council (EPSRC) Research Studentship.

I wish to thank my family, my parents for their support, emotionally and financially, and their encouragement, and special thanks to my brother Simon for his invaluable advice, help and fantastic proofreading skills.

Great thanks to all my friends especially Des, Erez, Rachel, Tere, Clare and Jim, and all in the Edgar Morton Laboratory.

Above all very special thanks to Jon for his constant love and support.

Nomenclature

Roman symbols

a	particle amplitude of freestream velocity
a_R	relaxation factor
c_f	friction coefficient, $\tau_b/\frac{1}{2}\rho U_b^2$
c_U, c_k, c_S	convergence criterion for U, k and S
dm	constant for parabolic mesh spacing
D	channel or pipe internal diameter
D_k	height or diameter of roughness particle
f	frequency
f_w	wave friction factor
$f_{\frac{1}{2}}$	Nyquist frequency
g	acceleration due to gravity
h	total depth
k	turbulent kinetic energy
K	number of vertical computational cells
k_s	roughness parameter
l	length scale
p	pressure
P	turbulence production
r, θ, z	cylindrical polar co-ordinates
r_{ij}	residual of k equation
R	channel or pipe internal radius

Re	Reynolds number
Re_b	Reynolds number based on bulk velocity, $\rho U_b D/\mu$
S	strain parameter
S_j	source term in generic transport equation
S_M	maximum surface slope
t	time
t_{total}	total time
T	period of oscillation
T_L	large scale turbulent time scale
T_S	small scale turbulent time scale
u_i, u_j, u_k	Cartesian tensor velocity components (fluctuating)
U_i, U_j, U_k	Cartesian tensor velocity components (ensemble-averaged)
u, v, w	Cartesian velocity components (fluctuating)
U_i, U_j, U_k	Cartesian velocity components (ensemble-averaged)
u_r, u_θ, u_z	cylindrical polar velocity in r, θ, z directions (fluctuating)
U_r, U_θ, U_z	cylindrical polar velocity components r, θ, z directions (ensemble-averaged)
U_0	freestream velocity
U_b	bulk velocity
U_M	amplitude of velocity variation
U_τ	friction velocity, τ_b/ρ
x_i, x_j, x_k	Cartesian tensor co-ordinates
x, y, z	Cartesian co-ordinates
z	normal distance from wall, $R - r$

Greek symbols

δ	boundary layer thickness
δ_{ij}	Kronecker delta
ϵ	rate of dissipation of turbulent kinetic energy
$\hat{\epsilon}$	modified dissipation variable
γ	amplitude of bulk velocity oscillation as a fraction of time-averaged value

μ	dynamic viscosity
ω	angular frequency, $2\pi f$
θ	phase
ν	kinematic viscosity, μ/ρ
ν_t	eddy viscosity
κ	von Kármán's constant
ρ	density
σ	co-ordinate for computational mesh or standard deviation
σ'	uniformly spaced mesh coordinate
σ_t	turbulent Prandtl number
τ_b	bed or wall shear stress
ϕ_u	phase of ensemble-averaged velocity
ϕ_{uw}	phase of ensemble-averaged Reynolds shear stress
ϕ_τ	phase of wall shear stress

Subscripts

i, j, k	radial, temporal and axial node reference
b	bed or wall
c	centreline
t	turbulent
data	experimental data
fit	least-squares fit
min	minimum value
max	maximum value
poly	polynomial fit
1	first node in computational mesh
$1(t)$	first turbulent node in staggered computational mesh

Superscripts

$'$	fluctuating component

— time-average

$\bar{}$ instantaneous value

$^+$ normalised by wall variables, $(\tau_w/\rho; \nu)$

^{n} time step

Notation

<>	ensemble-averaged
||	amplitude
'capitals'	mean component
cyc	number of cycles of oscillation
int	sampling interval
iz	number of vertical computational nodes
ntper	number of numerical time steps

Additional terms in numerical models

A	flatness factor $(1 - \frac{9}{8}(A_2 - A_3))$ in RSTM
A_2, A_3	second and third invariants $(a_{ij}a_{ji}, a_{ij}a_{jk}a_{ki})$ in RSTM
AD_j, AM_j, AP_j, AU_j	coefficients in discretised transport equations
a_{ij}	anisotropic Reynolds stress tensor, $< u_i u_j > /k$
c_1, c_2	functions in pressure-strain term of RSTM
$c_\epsilon, c_{\epsilon 1}, c_{\epsilon 2}, c_{\epsilon 3}$	constants in dissipation equation
c_μ	constant in constitutive equation for eddy viscosity
c_s	constant in diffusion term of RSTM
D_ϵ	term relating ϵ to $\hat{\epsilon}$, $\epsilon = \hat{\epsilon} + D_\epsilon$
d_{ij}	diffusion term in Reynolds stress equation of RSTM
ϵ_{ij}	dissipation term in Reynolds stress equation of RSTM
f_1, f_2	functions in dissipation equation (in pressure-strain term of RSTM)
f_ϵ	function in dissipation term of RSTM
f_μ	function in constitutive equation for eddy viscosity

f_S	function in constitutive equation for k-ϵ-S model eddy viscosity
ν_t	turbulent kinematic viscosity
ϕ_{ij}	pressure-strain term in Reynolds stress equation
P_{ij}	production term in Reynolds stress equation
Re_t	turbulent Reynolds number, $k^2/\nu\hat{\epsilon}$
$\sigma_k, \sigma_\epsilon, \sigma_S$	turbulent Prandtl number for diffusion of k, ϵ, S
$< u_i u_j >$	Reynolds stress

Chapter 1

Introduction

The study of numerical modelling of turbulence in physical systems is of practical importance in many situations both in the natural world and in engineering systems. Turbulence models may be applied to calculate unsteady flows for which the mean and turbulence flow quantities alter with time. Unsteady turbulent systems may occur in many diverse situations, in tidal flows driving sediment transport, pollution dispersion, and around the legs of oil rigs, and also in engines of cars and aeroplanes and even in blood flow. Numerical modelling as an alternative to experimental studies is potentially less expensive in terms of equipment and also less time consuming. Turbulence modelling is also an alternative to direct numerical simulation (DNS), for which the complete Navier-Stokes equations (the equations that describe fluid flow) are solved numerically. At the present time DNS calculations are very expensive and take a long time, and have been carried out only for relatively simple flows.

The main purpose of this study is the comparison, evaluation, and to some extent development of turbulence models. The motivation initially was from the work of Ismael (1993a) and Guy (2000), who both examined numerical modelling of periodic pipe flow. A new turbulence model which had been not previously been applied to this type of flow was assessed in conjunction with two other numerical models, by comparison to DNS and experimental data. This led on to the work of Stansby (1997) studying oscillatory boundary layer flows (which are similar to unsteady pipe

flows) for both smooth and rough beds. Although much work has been carried out for smooth bed flow there is relatively little on rough bed flows. A variety of rough beds are likely to be encountered in the natural world, for example a sand bed in an estuary or a covering of stones or pebbles may produce a relatively high level of bed roughness. In this study a wide range of rough flow types are examined, comparing the numerical calculations with the results of small and large-scale laboratory and field experiments.

A review of internal and external turbulent boundary layer flows is given below with particular reference to reciprocating flows, including previous experimental and computational work. All internal flows specified below (channel and pipe flow) are smooth wall cases. The external boundary layer flows include both smooth and rough bottom surfaces.

Review of Previous Experimental Work

A great deal of experimental work has been carried out for oscillatory pipe and boundary layer flows over smooth beds. Early detailed measurements of pulsating pipe flow were carried out by Mizushina *et al* (1973, 1975). Velocity and pressure gradient measurements were recorded and Reynolds shear stresses were deduced from a momentum balance for an average Reynolds number (Re) of 10000 and a range of periods of oscillation from 0.76 s to 7.9 s. The researchers identified a critical frequency below which the velocity and Reynolds stresses were found to behave in a quasi-steady manner.

Ramaprian and Tu (1983) and Tu and Ramaprian (1983) reported a detailed Laser Doppler Anemometer (LDA) experimental study of turbulent periodic pipe flow using a mean Re of 50000 and two frequencies of oscillation, namely 0.5 Hz and 3.6 Hz. The study found that for the low frequency case the Reynolds stress response was akin to the phase-averaged velocity variation, whereas for the high frequency case the phase-averaged velocity variation was 'frozen'. This breakdown in the structural

equilibrium of the flow at high frequency was attributed to the effect of oscillation at the frequency of turbulence bursting.

Mao and Hanratty (1986) reported experimental records of the time variation of the wall shear stress in a turbulent pulsating pipe flow, presenting the results with respect to the dimensionless frequency parameter, $\omega^+ = \omega\nu/U_\tau^2$. Finnicum and Hanratty (1987) continued this research, recording measurements of wall shear stress in fully developed periodic pipe flow of frequencies ranging widely from 0.2 Hz to 0.0912 Hz giving a range of values for the dimensionless frequency parameter ω^+ from 0.0012 to 0.0912. The results demonstrate quasi-steady behaviour for values of ω^+ up to 0.004. The transitional band was found to be $0.004 \leq \omega^+ \leq 0.0375$, above which the turbulence no longer responds to the prescribed oscillation.

Lodahl *et al* (1998) recorded LDA measurements of velocity and hot wire bed shear stress measurements in a smooth circular pipe. The experimental set-up used was the same as that for Jensen *et al*, with additional circular pipes of varying diameters inserted into the test section of the originally rectangular oscillating water tunnel. The main focus of the experimental work was combined current and oscillatory flow, although some preliminary examinations of solely oscillatory flow and solely current flow were carried out separately. In their investigation of the transition to turbulence, Lodahl *et al* found that the oscillatory flow was governed by two non-dimensional quantities, the Reynolds number Re based upon the maximum freestream velocity and $R/(2\nu/\omega)^{1/2}$, the radius to Stokes layer thickness ratio. They also confirmed the findings of turbulence 'bursting' by Jensen *et al* (1989) that is the emergence of turbulence immediately preceding the reversal of flow in the wall shear stress.

Hino *et al* (1983) used hot-wire techniques and laser Doppler anemometry to measure smooth bed oscillatory boundary layer flow parameters using air as the working fluid.

Brereton *et al* (1990) report LDA measurements of oscillatory boundary layer flow over a range of frequencies up to 2 Hz. The time-averaged profiles of velocity and Reynolds stress were found to be independent of the driving frequency.

There now follows a review of previous experiments for rough bed boundary layers. Jonsson and Carlsen (1976) examined two rough bed cases in an oscillating water tunnel (taking a/k_s to be 124 and 28.4). A miniature propeller was used to measure the velocities of the flow. A variety of rough bed flows were studied by Sleath (1987) using LDAs to measure two components of the velocity within the range $0.74 \leq k_s \leq 1112$.

LDA techniques were also used by Sumer *et al* (1987) and Jensen *et al* (1989) to measure velocities and turbulence in high Reynolds number oscillatory boundary layer flows over both smooth and rough beds. Hot film probe measurements of the friction velocity in the smooth bed cases were also reported by Jensen *et al*

Lloyd *et al* (1997) conducted large-scale experiments at the UK Coastal Research Facility. The published study concentrates on flow around conical islands, but unpublished LDA measurements were also obtained for rough bed oscillatory flow with no island included. New experimental data acquired in the large-scale University of Manchester tidal flume investigates oscillatory flow over smooth and rough beds. LDAs were used to measure three components of velocity for relatively low-Reynolds-number flows.

Relatively few oscillatory flow field measurements have been reported. McLean (1983) used mechanical current meters to measure 30 tidal cycles of the velocity in the Jade estuary in Germany. Schröder (1987) used acoustic Doppler techniques to measure velocity for three tidal cycles of the Elbe estuary, also in Germany. The turbulence quantities were derived from a momentum balance.

Review of Previous Computational Work

DNS data sets are invaluable as alternative to experimental validatation of the numerical turbulence models. The DNS of Kim *et al* (1987) further supplemented by Kim (1990) provides data for Re of 180 and 395 where the Reynolds number is based on the centreline velocity and the channel half width.

Spalart and Baldwin (1989) provide direct numerical simulations of oscillatory flow over a smooth bed in the Reynolds number range 1.8×10^5 to 7.2×10^5. Justesen and Spalart (1990) supplemented this DNS data set with non-sinusoidal periodic flow calculations. Many numerical modellers have used this DNS data set for validation purposes.

Many turbulence model studies have been undertaken for smooth periodic pipe and boundary layer flows. Blondeaux and Columbini (1985) compared the periodic pipe flow data of of Tu and Ramaprian (1983) with the calculations of Saffman's (1970) k-ω scheme. They found satisfactory agreement with the data.

Ismael (1993a) applied the two-equation Launder and Sharma (1974) k-ϵ model to a range of experimental test cases of periodic pipe flow including Mizushina *et al* (1973, 1975), Tu and Ramaprian (1983) and Finnicum and Hanratty (1987). Ismael stated that the data did not cover an area close enough to the pipe wall to allow an assessment of the model in the near wall region. However the model was able to predict the velocity and Reynolds stresses satisfactorily, provided that flow reversal did not occur as it did in the high-frequency case of Mizushina *et al.*

Patel *et al* (1985) give a review of two-equation turbulence model formulations applied to smooth wall boundary layer flows. The eight turbulence models assessed include the Launder and Sharma (1974), Chien (1982) k-ϵ models and the Wilcox and Rubesin (1980) k-ω model. The 'pseudo-vorticity' ω is proportional to ϵ/k. Not all models yielded satisfactory results and the best agreement was given by the Launder-Sharma and the Wilcox-Rubesin schemes. Even so, Patel *et al* conclude

that further refinement is necessary for these models to be applied to near wall flows with confidence.

Justesen and Spalart (1990) compared the DNS data set of Spalart and Baldwin (1989) and their own non-sinusoidal DNS data with the low-Reynolds-number models of Jones and Launder (1972) and Chien (1982). They found that the Jones and Launder model was in good agreement with the data and the Chien model was less accurate. Thais *et al* (1999) also applied the two-equation Chien model and found reasonable agreement against smooth bed data of Jensen *et al* (1989). Cotton *et al* (2000) employed the Launder and Sharma (1974) k-ϵ model in comparison with the DNS data of Spalart and Baldwin (1989) and Justesen and Spalart (1990), and found agreement to be satisfactory although not exact.

A number of Reynolds Stress Transport models (RSTMs), more advanced than the two-equation formulations, have also been used to model periodic flows. Both k-ϵ and Reynolds Stress Transport models were applied by Kebede *et al* (1985) to the reciprocating pipe flow data of Tu and Ramaprian (1983). Due to the greater complexity of the second moment closure model and closer representation of the physical attributes of the flow, it might be expected that the RSTM would be the more successful model. However, Kebede *et al* found the reverse. The researchers concluded that there was need for improvement in the ϵ-equation, which among other things will improve calculation of the turbulence time and length scales, k/ϵ and $k^{1.5}/\epsilon$.

Cotton *et al* (2000) compared Shima's (1989) variation of the Launder and Shima closure with the Spalart and Baldwin and the Justesen and Spalart DNS data cases. The RSTM gives improvement in the computation of the bed shear stress compared to the two-equation k-ϵ model.

Rough bed oscillatory boundary layers are considered next. The one-equation k-l model was examined by Justesen (1991) against the experimental data of Sumer *et al* (1987) for $a/k_s = 720$ and 3700. Reasonable agreement was found for the bed

shear stress at both values of a/k_s, and also for the phase-averaged velocity profiles (although the details were not captured). In general the values of turbulent kinetic energy predicted by the k-l model were too high at $a/k_s = 720$ and too low at $a/k_s = 3700$. The k-l model did not predict the Reynolds shear stress accurately.

Justesen (1991) also compared the two-equation k-ϵ model with the experimental data of Sumer *et al* (1987) and Jensen *et al* (1989). In direct comparison with the k-l model, the k-ϵ formulation showed great improvement against the experimental data. The bed shear stress was again accurately predicted by the k-ϵ model, and improvement was found in comparison with the k-l model in capturing the velocity profiles at $a/k_s = 3700$. Again, prediction of the Reynolds shear stress is not wholly accurate. Although improvement is found compared to the k-l model at most phase positions, this is not true at all points in the cycle. Baumert and Radach (1992) also applied the k-ϵ model in comparison with the field data of McLean (1983) and Schröder (1987). Although reasonable agreement was found against the velocity and Reynolds shear stress data, McLean's data included a great deal of scatter. The k-ϵ model performed well against Schröder's velocity and turbulent kinetic energy data in the Elbe estuary. Stansby (1997) confirmed the findings of Baumert and Radach comparing the k-ϵ model calculations with the field data of McLean and Schröder. Thais *et al* (1999) also compared Chien's (1982) model and a high-Reynolds-number k-ϵ model to the measurements of Sleath (1987) and Jensen *et al* (1989) over rough beds. Both models resolved the velocity data well, but they were not so precise in their prediction of the turbulent kinetic energy data. In the transitional rough-to-smooth regimes of Sleath's experimental cases, the Chien model displayed significant superiority over the high-Reynolds-number model. However this was not so pronounced when compared with the high-Reynolds-number experimental tests of Sleath and Jensen *et al.*

Hanjalic *et al* (1995) computed transitional and fully rough high-Reynolds-number flows using a modified form of the Launder and Sharma (1989) RSTM. Satisfactory

agreement was found with the data of Jensen *et al* (1989) and the DNS of Spalart and Baldwin (1989), although discrepancies were found in comparison with the data of Hino *et al* (1983).

Harris (1997) compared both standard k-l and k-ϵ models with Lamb's analytical solution for laminar flow and with laboratory data (Jonsson and Carlsen, 1976 and Jensen *et al* 1989) and for transitional rough turbulent flow at laboratory scale (Savell 1986). A two-layer k-ϵ model was found to give best agreement with the turbulent case. Results were also presented for random wave boundary layers. Lam and Bremhorst (1981) used a modified ϵ equation in a low Reynolds number model while Tamaka and Sana (1994) also reviewed low Reynolds number models for oscillatory boundary layers and compared results with Jensen *et al* (1989) data for a smooth bed. Tanaka and Sana found that the Jones and Launder (1972) model gave the best results.

Vager and Karga (1969) examined k-l, k-ϵ closures in tidal flows and found that by a suitable choice of l, it was possible to get almost as good results as k-ϵ apparatus.

Sajjadi and Waywell (1998) also compared numerical results to the field data of McLean (1983) and Schröder (1987). The k-l and k-ϵ models were applied in conjunction with two variants on the RSTM formulation. Good agreement against the field data was found for all models.

Brereton and Mankbadi (1995) give an extensive review of experimental and computational studies of these near-wall flows. Thais *et al* (1999) provide a comprehensive review of literature on rough bed oscillatory flows in the introduction to their paper.

Summary of the Present Study

In this study the types of flow are split into two categories:

- Steady channel flow and unsteady pipe flow with smooth walls.

- Shallow water oscillatory boundary layer flow over rough beds (this includes one smooth bed case).

The 'steady' flows refer to conditions for a flow variable that is constant in time, for example the imposed mass flow rate or the pressure gradient, as opposed to the 'unsteady' regime in which the parameter varies in a prescribed manner. In regard to the channel and pipe flow three numerical formulations are assessed in comparison with DNS and experimental data. The first is the low-Reynolds-number two-equation k-ϵ model of Launder and Sharma (1974). The second is a three-equation model, termed the k-ϵ-S model, developed by Cotton and Ismael (1998) based on the Launder and Sharma k-ϵ formulation with a third transport equation dependent upon the 'strain parameter'. The third numerical model applied to the channel and pipe flow cases is a second moment closure model based upon Launder and Shima's (1989) Reynolds Stress Transport model and includes a modification developed by Shima (1989). For the shallow water oscillatory boundary layer flow over smooth and rough beds high-Reynolds-number formulations are necessary to overcome the difficulty of an uneven bottom surface. The one-equation high-Reynolds-number k-l model is assessed for this flow type in conjunction with a high-Reynolds-number k-ϵ model. An introduction to turbulence model types and the details of the mathematical formulation of all these numerical models are given in Chapter 2.

Relatively little code development was necessary in the course of this study, as the previous solution procedures were available. I modified both the channel and pipe flow code to include the numerical formulation of the *k-epsilon-S* model and the oscillatory flow code to include the k-l model, and also to incorporate the procedures given in chapter 3. Also the oscillatory flow code was converted by the author from Salford Fortran 77 to Salford Fortran 90. Chapter 3 outlines the solution procedures applied to each flow type separately and the reader is also referred to the work of Ismael (1993a) and Guy (2000) in the first instance and Stansby (1997) in the second for more detail. For the channel and pipe flow various methods of convergence

are also compared and an investigation into the formulation of the turbulent kinetic energy near to the wall is examined. In the oscillatory flow case the input to the numerical code is also described and the refined computational grid is given in more detail. Sensitivity tests have also been included for validation purposes in both cases. These topics are also included in Chapter 3.

Chapter 4 contains the results of the initial study of steady channel and periodic pipe flow. The Launder and Sharma k-ϵ model, Cotton and Ismael's k-ϵ-S model are first compared to the DNS channel flow data of Kim *et al* (1987) and Kim (1990). The periodic nature of the flow is then examined and this pipe flow study also includes the calculations of Shima's RSTM. Comparisons with the experimental data of Finnicum and Hanratty (1988) focus on the variation of the wall shear stress. For comparison with Tu and Ramaprian's (1983) measurements the variation of wall shear stress, velocity, Reynolds shear stress, turbulence time scales, strain parameter and damping functions are examined. All models give satisfactory agreement with the data. The principal findings indicate that the k-ϵ-S model is superior close to the wall, whilst the RSTM tends to be in best agreement with the data towards the centre of the channel and pipe.

The main results are included in Chapter 5, which covers the smooth and rough bed oscillatory boundary layer flows. In this chapter the high-Reynolds-number k-l and k-ϵ models are applied to a wide range of experimental flow cases. The model results are initially compared to the field data of McLean (1983) in the Jade estuary and Schröder's (1987) Elbe estuary measurements. Three cases of the Jensen *et al*'s (1989) data-set are studied, one smooth bed case and two rough bed cases. The models are also compared to data from the large scale experiments of Lloyd *et al* (1997) in the UK Coastal Research Facility and previously unpublished measurements from the University of Manchester Tidal Flume by Dr C. Chen and Dr. D. Chen, Dept. of Engineering. At high Reynolds numbers these rough bed boundary layer flows may be characterised by the dimensionless parameter a/k_s and the experimental

cases examined here give a wide range of this parameter from 86 to 3.6×10^6. Other relevant parameter for flows with large roughness particles are k_s/h, which ranges from 0.0001 to 0.1 for these cases, and also the range of the boundary layer thickness relative to the total depth, $0.22 \leq \delta/h \leq 13.5$. ($\delta$ is the boundary layer thickness calculated as a function of particle amplitude upon roughness factor (equation 5.2) that would occur with infinite depth.) Where possible the variation of bed friction velocity is examined. The cyclic variation and profiles of the phase averaged velocity, the derived Reynolds shear stress and turbulent kinetic energy are also compared. The eddy viscosity is an important variable in the k-l and k-ϵ models, and an attempt has been made to quantify the uncertainty in the derived experimental values for ν_t in order to evaluate the accuracy of the model calculation of this parameter. Overall the k-ϵ model emerges as the superior scheme. Neither model accurately reproduces the data values of the turbulence quantities in the outer boundary layer flow. The question is posed as to whether, without the provision of more accurate experimental data for rough bed oscillatory flows, it is possible to reliably assess a more complex turbulence model.

The conclusions drawn from all the results are discussed in Chapter 6.

A publication by the present author is also included on page 268. This sole-authored paper entitled:

k-l and k-ϵ Modelling in Oscillatory Flow over Rough Beds

was one of 14 accepted in the John F. Kennedy student paper competition for the XXVIIIth biennial congress *Hydraulic Engineering for Sustainable Water Management at the Turn of the Millennium* of the International Association of Hydraulic Research (IAHR). The author presented the paper at the conference that took place on 22nd - 27th August 1999 in Graz, Austria.

It should be noted that the following manuscript:

An Assessment of k-ϵ and k-l Turbulence Models for a Wide Range of

Oscillatory Rough Bed Flows

by S. B. Letherman, M. A. Cotton, P. K. Stansby, C. Chen and D. Chen

was submitted for publication in March 2000 to the Journal of Hydroinformatics.

Chapter 2

Mathematical Formulation

2.1 Governing Equations

The Navier-Stokes equations that describe fluid motion are derived from the principles of continuity and Newton's second law of motion. The details of this derivation are described in many textbooks, for example Schlichting (1979), and are therefore not presented here. A simplified form of the instantaneous Navier-Stokes equations can be used since the only fluids examined here are incompressible, isothermal, Newtonian fluids, for which the stress is linearly related to strain rate. For turbulent flows with no body forces the instantaneous continuity and momentum equations are

$$\frac{\partial \tilde{U}_i}{\partial x_i} = 0, \tag{2.1}$$

$$\frac{\partial \tilde{U}_i}{\partial t} + \tilde{U}_j \frac{\partial \tilde{U}_i}{\partial x_j} = -\frac{1}{\rho}\frac{\partial \tilde{p}}{\partial x_i} + \frac{\partial}{\partial x_j}\left(\nu \frac{\partial \tilde{U}_i}{\partial x_j}\right) \tag{2.2}$$

The instantaneous quantities can be separated into mean and fluctuating components given by

$$\tilde{U}_i = U_i + u_i, \quad \tilde{p} = p + p' \tag{2.3}$$

and thus statistical averages may be taken to form equations to represent the turbulence motion.

For steady flow a time average of the flow quantity is taken over a large time. The

time average is denoted by an overbar and is defined for an instantaneous quantity $\tilde{\Phi}$ such that

$$\overline{\Phi} = \lim_{T\to\infty} \int_0^T \tilde{\Phi} dt \tag{2.4}$$

For an unsteady flow, where the mean quantities change with time, the ensemble average, denoted by carat brackets, is applied. For a large or theoretically infinite number N of flow realisations, the ensemble average of a quantity $\tilde{\Phi} = \Phi + \phi$, where Φ and ϕ are the averaged and fluctuating components respectively, is given by

$$< \tilde{\Phi}(t) >= \lim_{N\to\infty} \frac{1}{N} \sum_{n=1}^{N} \tilde{\Phi}_n(t) = \Phi \tag{2.5}$$

where for the fluctuating component ϕ,

$$< \phi >= 0, \quad < \phi\Phi >= 0 \tag{2.6}$$

Thus the mean flow equations are derived by ensemble-averaging the instantaneous continuity and momentum equations, (2.1) and (2.2),

$$\frac{\partial U_i}{\partial x_i} = 0, \tag{2.7}$$

$$\frac{\partial U_i}{\partial t} + U_j \frac{\partial U_i}{\partial x_j} = -\frac{1}{\rho}\frac{\partial p}{\partial x_i} + \frac{\partial}{\partial x_j}\left(\nu \frac{\partial U_i}{\partial x_j} - < u_i u_j >\right) \tag{2.8}$$

These mean flow equations are in the same form as the instantaneous equations except for the additional turbulent diffusion term on the right hand side of the equation. The turbulence correlation $< u_i u_j >$, known as the Reynolds stress, is unknown. Thus the problem of closure arises since there are now more unknowns than equations. This problem is tackled by the use of turbulence models.

Three types of fluid flow are studied here:

- steady channel flow over smooth surfaces,
- unsteady periodic pipe flow over smooth surfaces, and
- oscillatory flow over smooth and rough beds.

All these types of flows are of the boundary layer or thin shear type, and thus the mean flow equations further simplify to the boundary layer equations given in the following section.

2.2 Boundary Layer Equations

Thin shear or boundary layer flows have a predominant flow direction with no recirculation, for example flows in channels, pipes and over planes. The Navier-Stokes equations can be simplified for these flows. The following assumptions can be applied in boundary layer flow (Ferziger and Perić 1996):

- In the main flow direction the diffusive transport term in the momentum equation is much smaller than the convective term and can be neglected;
- The velocity component in the principal flow direction is much larger than the components in the other directions and so the other velocity components may be neglected;
- The gradients in the direction perpendicular to the principal and cross stream flow directions are dominant and all other gradients can be neglected, with the sole exception of the pressure gradient. The pressure gradient in the principal flow direction is dominant and pressure gradients across the flow can be neglected.

The mean flow equations are reduced to the streamwise momentum equation only. The momentum equation for boundary layer flow is

$$\frac{\partial U}{\partial t} = -\frac{1}{\rho}\frac{\partial p}{\partial x} + \frac{\partial}{\partial z}\left(\nu\frac{\partial U}{\partial z} - < uw >\right) \tag{2.9}$$

The only non-zero Reynolds stress is the Reynolds shear stress $< uw >$.

2.2.1 Channel and Pipe Flow Boundary Conditions

Only smooth walled channels and pipes are examined here. The no-slip condition is applied at the wall and a symmetry condition at the centreline. Thus the streamwise mean velocity is zero at the wall and the first velocity gradient is set to zero at the centreline

$$U = 0 \quad \text{at} \quad z = R \tag{2.10}$$

$$\frac{\partial U}{\partial z} = 0 \quad \text{at} \quad z = 0 \tag{2.11}$$

where R is the radius of the pipe or channel. The no-slip and impermeability conditions apply to the Reynolds shear stress at the wall, and symmetry at the centreline also applies:

$$< uw >= 0 \quad \text{at} \quad z = 0 \quad \text{and} \quad z = R \tag{2.12}$$

2.2.2 Oscillatory Flow Boundary Conditions

Boundary layer oscillatory flow is described by the momentum equation (2.9) above. Boundary conditions are required for areas outside the boundary layer at the upper boundary and at the bed.

Upper Boundary

The freestream velocity outside the boundary layer is independent of the distance from the bed and varies sinusoidally, such that

$$U_0(t) = U_M \sin(\omega t) \tag{2.13}$$

where U_M is the amplitude of the velocity variation U_0, and $\omega = 2\pi/T$ where T is the period of oscillation of the flow. In this region outside the boundary layer where $U = U_0$ and the viscous term reduces to zero, the momentum equation (2.9) reduces to the Euler equation

$$\frac{\partial U_0}{\partial t} = -\frac{1}{\rho}\frac{\partial p}{\partial x} \tag{2.14}$$

Bed Boundary

The bed boundary conditions on U depend upon whether the bed is rough or smooth. The bed region is taken to be

$$30 < z^+_{\max} < 100 \tag{2.15}$$

where

$$z^+ = \frac{zU_\tau}{\nu} \tag{2.16}$$

and the friction velocity, U_τ is defined by the bed shear stress, τ_b such that

$$U_\tau = \sqrt{\frac{\tau_b}{\rho}} \tag{2.17}$$

In the present study both smooth and rough bed oscillatory flows are examined. For a smooth bed the universal velocity-distribution law (Schlichting 1979) is applied in the following form,

$$U^+ = 2.5 \ln z^+ + 5.5 \tag{2.18}$$

For a rough bed standard wall functions are applied. The law-of-the-wall for fully rough turbulent boundary layers (Schlichting 1979) is used

$$U^+ = \frac{U}{U_\tau} = \frac{1}{\kappa} \ln \left(\frac{z}{k_s} \right) + 8.5 \tag{2.19}$$

where k_s is the roughness parameter.

2.3 Closure: Turbulence models

2.3.1 Introduction to Eddy Viscosity and Reynolds Stress Transport Models

The boundary layer equations are not a closed set of equations and thus cannot be solved exactly. The fluctuating velocity components are unknown and determination of these Reynolds stresses is the main concern of numerical modelling: 'turbulence models' are employed to compute the Reynolds stresses. Two general methods of closure are discussed in the following section, namely eddy viscosity models and Reynolds stress transport models.

In 1877 Boussinesq introduced the eddy viscosity concept to model the Reynolds stresses (Rodi 1993). It assumes that the turbulent stresses are proportional to the mean velocity gradients. For general flows the eddy viscosity relation is given by

$$- < u_i u_j > = \nu_t \left(\frac{\partial U_i}{\partial x_j} + \frac{\partial U_j}{\partial x_i} \right) - \frac{2}{3} k \delta_{ij} \tag{2.20}$$

ν_t is called the kinematic turbulent viscosity, or kinematic eddy viscosity. For boundary layer flows equation (2.20) reduces to

$$- < uw >= \nu_t \frac{\partial U}{\partial z} \tag{2.21}$$

Turbulence models which use this concept are generally known as Eddy Viscosity Models (EVMs).

An alternative method of calculating the turbulent stresses is provided by Reynolds Stress Transport Models (RSTMs). These models do not use the Boussinesq eddy viscosity concept, but instead solve differential equations for the individual Reynolds stresses and the dissipation rate, ϵ. Two-equation eddy viscosity models are poor at resolving regions of stagnation, separation and recirculation (Ferziger and Perić 1996), and buoyancy effects are also treated approximately. RSTMs are more complex and represent a higher level of closure than EVMs and are often referred to as 'second-moment closures'. In contrast to EVMs, the differential equations of an RSTM give a delayed response to any change in the mean velocity gradient. This feature is of particular importance in the present study of unsteady pipe flows. The RSTM turbulent transport equations are derived from the instantaneous Navier-Stokes equations given by equation (2.2). The derivation is described in detail in Launder (1983). The exact Reynolds Stress Transport equations are stated below in equation (2.22) in which P_{ij} represents the term for production of the Reynolds stress due to the mean flow strain, ϕ_{ij} is the correlation between fluctuating pressure and fluctuating strain rate, d_{ij} represents the diffusion of the Reynolds stress, and ϵ_{ij} is the rate of destruction or dissipation.

$$\begin{aligned}
&\frac{\partial < u_i u_j >}{\partial t} + U_k \frac{\partial < u_i u_j >}{\partial x_k} = \\
P_{ij} \ldots \quad &- \left(< u_j u_k > \frac{\partial U_i}{\partial x_k} + < u_i u_k > \frac{\partial U_j}{\partial x_k} \right) \\
\phi_{ij} \ldots \quad &+ \left\langle \frac{p'}{\rho} \left(\frac{\partial u_j}{\partial x_i} + \frac{\partial u_i}{\partial x_j} \right) \right\rangle \\
d_{ij} \ldots \quad &+ \frac{\partial}{\partial x_k} \left(\nu \frac{\partial < u_i u_j >}{\partial x_k} - < u_i u_j u_k > - \frac{1}{\rho} \left\langle p' \left(u_j \delta_{ik} + u_i \delta_{jk} \right) \right\rangle \right)
\end{aligned} \tag{2.22}$$

$$-\epsilon_{ij} \ldots \qquad -2\nu\left\langle \frac{\partial u_i}{\partial x_k}\frac{\partial u_j}{\partial x_k}\right\rangle$$

The RSTM of Launder and Shima (1989) was developed from the Gibson and Launder (1987) model in order to extend the range of applicability of the model to include near-wall flow regions, by applying local equilibrium conditions at the wall for turbulent stresses and energy dissipation rate. The new model was compared to data for flat plate boundary flows with zero, adverse, and strong pressure gradients and tuned so that the Reynolds stress profiles in the near wall sublayer were adequate. In 1989 Shima further optimised the model after comparing the model solutions with steady fully developed channel flow data. The 1989 Shima version is employed in this study.

The following sections detail the equations of five turbulence models studied here to calculate the flows stated below:

- High-Reynolds-Number k-l Model, (k-l), applied to oscillatory flow.
- High-Reynolds-Number k-ϵ Model, (k-ϵ), applied to oscillatory flow.
- Launder and Sharma k-ϵ Model, (k-ϵ), applied to steady channel flow and unsteady periodic pipe flow.
- Cotton and Ismael k-ϵ-S Strain Parameter Model, (k-ϵ-S), applied to steady channel flow and unsteady periodic pipe flow.
- Shima Reynolds Stress Transport Model, (RSTM), applied to unsteady periodic pipe flow.

The high-Reynolds-number k-l and k-ϵ models are applied to oscillatory flows over smooth and rough beds (i.e. rectangular geometries). The other three models are applied principally to pipe flows and their equations are given in cylindrical polar co-ordinates (although this includes a switch to reduce to equations for channel flow). The only RSTM is the Shima model; all the other models are based upon the Boussinesq eddy viscosity concept.

2.3.2 High-Reynolds-Number k-l Model

High-Reynolds-number eddy viscosity models are only applicable to flow regions distant from boundaries, and thus these models employ algebraic functions near to walls, commonly known as 'wall functions'. Low-Reynolds-number EVMs, for example the Launder and Sharma k-ϵ model, are applicable over the entire flow domain, the model equations being integrated up to solid boundaries. The k-l model includes a differential equation to solve for the turbulent kinetic energy k, and ϵ is supplied via an algebraic relation (using a prescribed length scale, l). The high-Reynolds-number k-l model is the simplest model employed in this study. The same k-l model has been previously applied by Justesen (1991) to oscillatory boundary layer flows over rough beds. The full equations of the k-l model for flow in the x-z plane are given below:

$$- < uw >= \nu_t \frac{\partial U}{\partial z} \tag{2.23}$$

$$\nu_t = c_\mu \frac{k^2}{\epsilon} \tag{2.24}$$

$$\frac{\partial k}{\partial t} = \nu_t \left(\frac{\partial U}{\partial z}\right)^2 + \frac{\partial}{\partial z}\left[\left(\nu + \frac{\nu_t}{\sigma_k}\right)\frac{\partial k}{\partial z}\right] - \epsilon \tag{2.25}$$

$$\epsilon = c_\mu^{3/4} \frac{k^{3/2}}{\kappa z} \tag{2.26}$$

Standard values for the model constants are used are given in Table 1. The standard boundary conditions on velocity for smooth and rough beds are given in Section 2.2.2. The first term in the k-equation (2.25) is defined as production, P,

$$P = \nu_t \left(\frac{\partial U}{\partial z}\right)^2 \tag{2.27}$$

If the 'local equilibrium' assumption is applied to the k-transport equation (2.25), (that is, turbulence production and dissipation are taken to be equal) and the unsteady and diffusive terms are omitted from the equation, then it reduces to the following:

$$\epsilon = - < uw > \frac{\partial U}{\partial z} \tag{2.28}$$

Combining the Boussinesq viscosity concept (2.23) with the constitutive equation (2.24) gives the following expression for the Reynolds stress,

$$- < uw > = c_\mu \frac{k^2}{\epsilon} \frac{\partial U}{\partial z} \tag{2.29}$$

Eliminating the Reynolds stress from equations (2.28) and (2.29) gives

$$c_\mu = \left(\frac{- < uw >}{k} \right)^2 \tag{2.30}$$

In a fully developed flow near to a wall, uniform stress is assumed and molecular viscosity can be neglected, thus

$$U_\tau^2 = - < uw > = \nu_t \frac{\partial U}{\partial z} \tag{2.31}$$

Prandtl's mixing length approximation (estimating length scale l by κz) is given by

$$\nu_t = \kappa^2 z^2 \frac{\partial U}{\partial z} \tag{2.32}$$

Combining equations (2.31) and (2.32) gives

$$\frac{\partial U}{\partial z} = \frac{U_\tau}{\kappa z} \tag{2.33}$$

and thus

$$\nu_t = U_\tau \kappa z \tag{2.34}$$

Applying the uniform stress assumption (2.31) in equation (2.30) gives the bed boundary condition for k,

$$k = \frac{U_\tau^2}{\sqrt{c_\mu}} \tag{2.35}$$

At the surface the zero gradient condition applies

$$\frac{\partial k}{\partial z} = 0 \tag{2.36}$$

2.3.3 High-Reynolds-Number k-ϵ Model

The high-Reynolds-number k-ϵ model retains the k-transport equation (2.25) of the k-l model. However instead of resorting to an algebraic relation, ϵ is determined by

solution of a transport equation. The k-ϵ model is a two-equation eddy viscosity model. The high-Reynolds-number k-ϵ model is described by equations (2.23), (2.24) and (2.25), in addition to the following ϵ-transport equation:

$$\frac{\partial \epsilon}{\partial t} = c_{\epsilon 1}\frac{\epsilon}{k}\nu_t\left(\frac{\partial U}{\partial z}\right)^2 + \frac{\partial}{\partial z}\left[\left(\nu + \frac{\nu_t}{\sigma_\epsilon}\right)\frac{\partial \epsilon}{\partial z}\right] - c_{\epsilon 2}\frac{\epsilon^2}{k} \tag{2.37}$$

The boundary conditions given by equations (2.35) and (2.36) also apply here. The bed boundary condition on ϵ is formed by rearrangement of the constitutive equation and substitution of above expressions for ν_t and k

$$\epsilon = \frac{U_\tau^3}{\kappa z} \tag{2.38}$$

The zero gradient condition also applies at the surface, thus

$$\frac{\partial \epsilon}{\partial z} = 0 \tag{2.39}$$

2.3.4 Launder and Sharma k-ϵ Model

The Launder and Sharma (1974) k-ϵ model is a 'low-Reynolds-number' eddy viscosity model, and is thus applicable over the entire flow domain. EVMs of this type include additional functions and constants that are effective only near to a wall. The Launder and Sharma model is based upon the first low-Reynolds-number k-ϵ model, the Jones and Launder model (1972). This model is widely used, often being applied as a benchmark against which to assess new models. For a full discussion and the complete Launder and Sharma model equations see Ismael (1993a) and Guy (2000). For brevity the equations are given here for spatially fully developed, axisymmetric, swirl-free pipe flows as follows:

$$-\langle u_r u_z \rangle = \nu_t \frac{\partial U_z}{\partial r} \tag{2.40}$$

$$\nu_t = c_\mu f_\mu(Re_t)\frac{k^2}{\hat{\epsilon}} \tag{2.41}$$

$$f_\mu(Re_t) = \exp\left[\frac{-3.4}{(1+0.02Re_t)^2}\right]; \qquad Re_t = \frac{k^2}{\nu\hat{\epsilon}} \tag{2.42}$$

$$\frac{\partial k}{\partial t} = \nu_t\left(\frac{\partial U_z}{\partial r}\right)^2 + \frac{1}{r^j}\frac{\partial}{\partial r}\left(r^j\left(\nu + \frac{\nu_t}{\sigma_k}\right)\frac{\partial k}{\partial r}\right) - (\hat{\epsilon} + D_\epsilon) \tag{2.43}$$

$$\epsilon = \hat{\epsilon} + D_\epsilon \quad \text{where} \quad D_\epsilon = 2\nu \left(\frac{\partial k^{\frac{1}{2}}}{\partial r} \right)^2 \tag{2.44}$$

$$\begin{aligned} \frac{\partial \hat{\epsilon}}{\partial t} &= c_{\epsilon 1} \frac{\hat{\epsilon}}{k} \nu_t \left(\frac{\partial U_z}{\partial r} \right)^2 + \frac{1}{r^j} \frac{\partial}{\partial r} \left(r^j \left(\nu + \frac{\nu_t}{\sigma_\epsilon} \right) \frac{\partial \hat{\epsilon}}{\partial r} \right) \\ &\quad - c_{\epsilon 2} f_2 \frac{\hat{\epsilon}^2}{k} + c_{\epsilon 3} \nu \nu_t \left(\frac{\partial^2 U_z}{\partial r^2} \right)^2 \end{aligned} \tag{2.45}$$

$$f_2 = 1.0 - 0.3 \exp\left[-Re_t^2 \right] \tag{2.46}$$

For channel flow $j = 0$, taking r to be equivalent to the vertical direction (normally z in Cartesian co-ordinates) and $j = 1$ for pipe flow. z is the distance measured from the pipe wall to the centreline, so $z = R - r$ for a pipe radius R.

The boundary conditions for the turbulent kinetic energy, k and modified dissipation rate, $\hat{\epsilon}$ are given by,

$$\begin{aligned} k = \hat{\epsilon} &= 0 \quad \text{at} \quad r = R; \\ \frac{\partial k}{\partial r} = \frac{\partial \hat{\epsilon}}{\partial r} &= 0 \quad \text{at} \quad r = 0 \end{aligned} \tag{2.47}$$

The no-slip condition is applied to k at the wall. $\hat{\epsilon}$ is zero at the wall since Taylor series expansions of k and ϵ show that $\hat{\epsilon}$ has no zero order component near the wall. Axial symmetry at the centreline implies that the first derivatives of k and $\hat{\epsilon}$ are zero.

2.3.5 k-ϵ-S Strain Parameter Model

The k-ϵ-S model is a three-equation eddy viscosity model. This model was developed by Cotton and Ismael in the mid-to-late 1990s and for a more detailed discussion and development of the model the reader is referred to Cotton and Ismael (1998). This model retains the k- and $\hat{\epsilon}$-transport equations of the low-Reynolds-number k-ϵ model with only slight changes to some of the coefficients. The main difference is the introduction of $f_S(S)$ in the stress-strain relation, and the determination of the 'strain parameter' S via an S-transport equation. It should be noted that the

differential equation for S cannot be derived from the Navier-Stokes equations, but is based upon physical arguments related to Rapid Distortion Theory. The equations of the k-ϵ-S model for spatially fully developed, axisymmetric, swirl-free pipe flows are given by:

$$- < u_r u_z >= \nu_t \frac{\partial U_z}{\partial r} \tag{2.48}$$

$$\nu_t = c_\mu f_S(S) f_\mu(Re_t) \frac{k^2}{\hat{\epsilon}} \tag{2.49}$$

$$f_S(S) = \frac{2.88}{1 + 0.165S} \left(1 - 0.55\text{exp}[-(0.135S + 0.0015S^3)]\right) \tag{2.50}$$

$$f_\mu(Re_t) = 1 - 0.3\text{exp}[-0.02Re_t]; \qquad Re_t = \frac{k^2}{\nu\hat{\epsilon}} \tag{2.51}$$

$$\frac{\partial k}{\partial t} = \nu_t \left(\frac{\partial U_z}{\partial r}\right)^2 + \frac{1}{r^j}\frac{\partial}{\partial r}\left(r^j \left(\nu + \frac{\nu_t}{\sigma_k}\right)\frac{\partial k}{\partial r}\right) - (\hat{\epsilon} + D_\epsilon) \tag{2.52}$$

$$\epsilon = \hat{\epsilon} + D_\epsilon \quad \text{where} \quad D_\epsilon = 2\nu \left(\frac{\partial k^{\frac{1}{2}}}{\partial r}\right)^2 \tag{2.53}$$

$$\begin{aligned} \frac{\partial \hat{\epsilon}}{\partial t} &= c_{\epsilon 1}\frac{\hat{\epsilon}}{k}\nu_t \left(\frac{\partial U_z}{\partial r}\right)^2 + \frac{1}{r^j}\frac{\partial}{\partial r}\left(r^j \left(\nu + \frac{\nu_t}{\sigma_\epsilon}\right)\frac{\partial \hat{\epsilon}}{\partial r}\right) \\ &\quad -c_{\epsilon 2}\frac{\hat{\epsilon}^2}{k} + c_{\epsilon 3}\nu\nu_t \left(\frac{\partial^2 U_z}{\partial r^2}\right)^2 \end{aligned} \tag{2.54}$$

$$\frac{DS}{Dt} = \frac{k}{\hat{\epsilon}}\left(\frac{\partial U_z}{\partial r}\right)^2 + \frac{1}{r^j}\frac{\partial}{\partial r}\left(r^j \frac{\nu_t}{\sigma_S}\frac{\partial S}{\partial r}\right) - \frac{S}{(k/\hat{\epsilon})} \tag{2.55}$$

As with the Launder and Sharma model, $j = 0$ for channel flow and $j = 1$ for pipe flow. The values of the model constants and the von Kármán constant, κ are given in Table 1. The k-equation (2.52) is same as that of the Launder and Sharma model, equation (2.43). However the $\hat{\epsilon}$-equation (2.54) is altered from the k-ϵ version. σ_ϵ is set to 1.21 instead of 1.3 in the k-ϵ model, the function $f_2 = 1 - 0.3\text{exp}(-Re_t^2)$ is omitted and the coefficient $c_{\epsilon 3}$ is taken as 0.9, not 2.0. These model constants were optimised by comparison with DNS channel flow data and turbulent mixed convection data in vertical pipes (Cotton and Ismael 1998). The modified form of the dissipation rate, $\hat{\epsilon}$ is used throughout the model equations. The function f_S equals 1.0 when $S = c_\mu^{-1}$. Viscous damping, introduced by the function $f_\mu(Re_t)$, is far more limited than for the k-ϵ model, for example $f_\mu = 0.9$ at $\text{Re}_t = 50$, corresponding to

$z^+ \sim 7$ (Cotton and Ismael 1998). Under these equilibrium conditions ($S = c_\mu^{-1}$; $Re_t \to \infty$), the expression for ν_t, equation (2.49), resumes its high-Reynolds-number form:

$$\nu_t = c_\mu \frac{k^2}{\hat{\epsilon}} \tag{2.56}$$

The boundary conditions are given as

$$\begin{aligned} k = \hat{\epsilon} = S &= 0 \quad \text{at} \quad r = R \\ \frac{\partial k}{\partial r} = \frac{\partial \hat{\epsilon}}{\partial r} = \frac{\partial S}{\partial r} &= 0 \quad \text{at} \quad r = 0 \end{aligned} \tag{2.57}$$

The boundary conditions for k and $\hat{\epsilon}$ are the same as those for the k-ϵ model, for the same reasons. Analysis of equation (2.55) at the wall, with $k \sim z^2$ and $\hat{\epsilon} \sim z$, gives that $S \sim z^2$ and so the wall boundary condition $S = 0$ is applied. At the centreline the zero gradient condition is applied to all variables, due to axial symmetry.

2.3.6 Shima Reynolds Stress Transport Model

The Launder and Shima Reynolds stress transport model was based upon the Gibson and Launder model (Gibson and Launder 1987) and this model was extended so that it was also applicable to wall bounded flows. The model was optimised against data for flow over a flat plate and tuned so that the Reynolds stress profiles in the near wall sublayer were adequate. Shima introduced a slight variation in the model after comparing the results with steady fully developed channel flow data. It is the 1989 Shima version that is implemented in this study. For a full equation set and a more detailed discussion see Shima (1989) and Guy (2000). Following the work of Guy the equations for the Shima Reynolds Stress Transport Model (RSTM) in cylindrical polar co-ordinates (r, θ, z) for spatially fully developed, axisymmetric and swirl-free pipe flow are as follows:

$$\begin{aligned} \frac{\partial < u_r u_z >}{\partial t} &= P_{rz} + \phi_{rz} + \frac{1}{r}\frac{\partial}{\partial r}\left(r\left(\nu + c_s \frac{k}{\epsilon} < u_r^2 >\right)\frac{\partial < u_r u_z >}{\partial r}\right) \\ &\quad - \frac{1}{r^2}\left(\nu + c_s \frac{k}{\epsilon} < u_\theta^2 >\right) < u_r u_z > \end{aligned} \tag{2.58}$$

$$\frac{\partial < u_r^2 >}{\partial t} = \phi_{rr} + \frac{1}{r}\frac{\partial}{\partial r}\left(r\left(\nu + c_s\frac{k}{\epsilon} < u_r^2 >\right)\frac{\partial < u_r^2 >}{\partial r}\right) - \frac{2}{r^2}\left(\nu + c_s\frac{k}{\epsilon} < u_\theta^2 >\right)\left(< u_r^2 > - < u_\theta^2 >\right) - \frac{2}{3}\epsilon \quad (2.59)$$

$$\frac{\partial < u_\theta^2 >}{\partial t} = \phi_{\theta\theta} + \frac{1}{r}\frac{\partial}{\partial r}\left(r\left(\nu + c_s\frac{k}{\epsilon} < u_r^2 >\right)\frac{\partial < u_\theta^2 >}{\partial r}\right) + \frac{2}{r^2}\left(\nu + c_s\frac{k}{\epsilon} < u_\theta^2 >\right)\left(< u_r^2 > - < u_\theta^2 >\right) - \frac{2}{3}\epsilon \quad (2.60)$$

$$\frac{\partial < u_z^2 >}{\partial t} = P_{zz} + \phi_{zz} + \frac{1}{r}\frac{\partial}{\partial r}\left(r\left(\nu + c_s\frac{k}{\epsilon} < u_r^2 >\right)\frac{\partial < u_z^2 >}{\partial r}\right) - \frac{2}{3}\epsilon \quad (2.61)$$

$$\frac{\partial \epsilon}{\partial t} = (c_{\epsilon 1} + \psi_1 + \psi_2)\frac{\epsilon}{k}P + \frac{1}{r}\frac{\partial}{\partial r}\left(r\left(\nu + c_\epsilon\frac{k}{\epsilon} < u_r^2 >\right)\frac{\partial \epsilon}{\partial r}\right) - c_{\epsilon 2}\frac{\epsilon\hat{\epsilon}}{k} \quad (2.62)$$

The RSTM production, pressure-strain, and modified dissipation terms are given by the following equations:

$$P_{rz} = - < u_r^2 > \frac{\partial U_z}{\partial r}; \quad P_{zz} = -2 < u_r u_z > \frac{\partial U_z}{\partial r};$$

$$P = - < u_r u_z > \frac{\partial U_z}{\partial r} \quad (2.63)$$

$$\phi_{rz} = -c_1\epsilon a_{rz} - c_2 P_{rz} - \frac{3}{2}\left(c_{wl}\frac{\epsilon}{k} < u_r u_z > - c_{w2}c_2 P_{rz}\right) f_w \quad (2.64)$$

$$\phi_{rr} = -c_1\epsilon a_{rr} + \frac{2}{3}c_2 P - 2\left(c_{wl}\frac{\epsilon}{k} < u_r^2 > + \frac{2}{3}c_{w2}c_2 P\right) f_w \quad (2.65)$$

$$\phi_{\theta\theta} = -c_1\epsilon a_{\theta\theta} + \frac{2}{3}c_2 P + \left(c_{wl}\frac{\epsilon}{k} < u_r^2 > + \frac{2}{3}c_{w2}c_2 P\right) f_w \quad (2.66)$$

$$\phi_{zz} = -c_1\epsilon a_{zz} - c_2(P_{zz} - \frac{2}{3}P) + \left(c_{wl}\frac{\epsilon}{k} < u_r^2 > + \frac{2}{3}c_{w2}c_2 P\right) f_w \quad (2.67)$$

$$\hat{\epsilon} = \epsilon - D_\epsilon; \quad D_\epsilon = 2\nu\left(\frac{\partial k^{\frac{1}{2}}}{\partial z}\right)^2 \quad (2.68)$$

The RSTM parameters and functions are as follows,

$$c_s = 0.22; \quad c_\epsilon = 0.18; \quad c_{\epsilon 1} = 1.45; \quad c_{\epsilon 2} = 1.9$$

$$c_1 = 1 + 2.58AA_2^{0.25}\left(1 - \exp[-(0.0067Re_t)^2]\right); \quad c_2 = 0.75A^{0.5}$$

$$c_{w1} = -\frac{2}{3}c_1 + 1.67; \quad c_{w2} = \mathrm{MAX}\left(\left(\frac{\frac{2}{3}c_2 - \frac{1}{6}}{c_2}\right), 0\right); \quad f_w = \frac{k^{1.5}}{2.5\epsilon z} \quad (2.69)$$

$$\psi_1 = 1.5A\left(\frac{P}{\epsilon} - 1\right); \quad \psi_2 = 0.35(1 - 0.3A_2)\exp[-(0.002Re_t)^{0.5}] \quad (2.70)$$

$$A = 1 - \frac{9}{8}(A_2 - A_3); \quad A_2 = a_{rr}^2 + a_{\theta\theta}^2 + a_{zz}^2 + 2a_{rz}^2$$

$$A_3 = a_{rr}^3 + a_{\theta\theta}^3 + a_{zz}^3 + 3a_{rz}^2(a_{rr} + a_{zz}) \tag{2.71}$$

$$a_{rz} = \frac{< u_r u_z >}{k}; \quad a_{rr} = \frac{< u_r^2 >}{k} - \frac{2}{3}; \quad a_{\theta\theta} = \frac{< u_\theta^2 >}{k} - \frac{2}{3}$$

$$a_{zz} = \frac{< u_z^2 >}{k} - \frac{2}{3}; \quad Re_t = \frac{k^2}{\nu\epsilon} \tag{2.72}$$

z is the distance measured from the pipe wall to the centreline, such that $z = R - r$ for a pipe radius R . The boundary conditions on the normal stresses are given by:

$$< u_r^2 > = < u_\theta^2 > = < u_z^2 > \; = 0 \qquad \text{at} \quad r = R; \tag{2.73}$$

$$\frac{\partial < u_r^2 >}{\partial r} = \frac{\partial < u_\theta^2 >}{\partial r} = \frac{\partial < u_z^2 >}{\partial r} \; = 0 \qquad \text{at} \quad r = 0 \tag{2.74}$$

The no-slip and impermeability conditions apply to the normal stresses at the wall. The condition of axial symmetry applies at the centreline, hence the first radial derivatives are equal to zero. Note that the radial and tangential stresses are indistinguishable at the centreline. The boundary conditions on the dissipation rate, ϵ are

$$\begin{aligned} \epsilon &= 2\nu \left(\frac{\partial k^{\frac{1}{2}}}{\partial r} \right)^2 \qquad \text{at} \quad r = R; \\ \frac{\partial \epsilon}{\partial r} &= 0 \qquad\qquad\qquad\quad \text{at} \quad r = 0 \end{aligned} \tag{2.75}$$

ϵ is set to the zero order component of the Taylor series expansion near the wall for the wall boundary condition. Again, the axial symmetry condition is applied at the centreline.

2.3.7 Variant Model Constants in the k-l and k-ϵ Models

In this section the k-ϵ and k-l models referred to are the high-Reynolds-number form of the models, detailed in Sections 2.3.2 and 2.3.3. The 'standard' and 'variant' values of c_μ (appearing in the k-ϵ and k-l models) and σ_ϵ (applicable to the k-ϵ model only) are considered here. All other model constants are set to established standard values as shown in Table 1. Applying variant values of the model constants gives a 'like-with-like' comparison between the k-l and k-ϵ models. Thus any differences found in the model results will be directly attributable to modelling the transport effects of the rate of dissipation ϵ (k-ϵ model) in comparison to an algebraic relation (k-l model), and *not* to the values of the model constants. The value of $c_\mu = 0.09$ applied in the k-ϵ model approach is obtained from equation (2.30), since measurement of shear layer flows yields $- < uw > /k \approx 0.3$ (Rodi 1993). The value of $c_\mu = 0.08$ applied in the k-l model is the outcome of computer optimisation (Rodi 1993).

An expression may be obtained which relates all the values of the model constants. In a fully developed flow near to a wall uniform stress is assumed and molecular viscosity can be neglected. Assuming local equilibrium, and uniform stress near to a wall, and substituting the resulting expressions for $\partial U/\partial z$ (2.33), ν_t (2.34), k (2.35) and ϵ (2.38) into the steady form of equation (2.37) leads to the following relation between the model constants

$$\sigma_\epsilon = \frac{\kappa^2}{c_\mu^{1/2}(c_{\epsilon 2} - c_{\epsilon 1})} \tag{2.76}$$

Substituting the standard values of c_μ, $c_{\epsilon 1}$ and $c_{\epsilon 2}$ in equation (2.76) and further taking $\kappa = 0.4$ yields $\sigma_\epsilon = 1.11$, the k-ϵ model 'variant' value. In this case the standard value of 1.3 may be regarded as the outcome of an optimisation exercise (Jones and Launder 1972).

Tests comparing the standard and variant model constants have been performed on oscillatory flow cases, detailed in Chapter 5.7. The bed shear stress and velocity,

turbulent kinetic energy, the rate of dissipation of kinetic energy and eddy viscosity profiles were examined to ascertain the effect of altering the model constants. The percentage difference in bed shear stress computed using the 'standard' and 'variant' forms of the k-l models was less than 0.05% in all cases. The percentage change for the k-ϵ model was at most 2.1%. The sensitivity found in the case of the k-ϵ model, where only the turbulent Prandtl number for the diffusion of ϵ is altered, is perhaps in line with what might be expected. Tests on the k-l model, however, have revealed a surprising insensitivity to the value of c_μ, a constant that is central to the model formulation. The reason for this finding is believed to lie in the effective boundary condition on the turbulent viscosity at the bed-adjacent velocity control volume. Applying the boundary conditions (2.35) and (2.38) at the bed-adjacent control volume (see Chapter 3 for details of the numerics) results in the following expressions for k and ϵ,

$$k_{1(t)} = \frac{U_\tau^2}{c_\mu^{1/2}} \quad \text{and} \quad \epsilon_{1(t)} = \frac{U_\tau^3}{\kappa z_{1(t)}} \tag{2.77}$$

Substituting these expressions into equation (2.24) for ν_t gives the classical mixing length result

$$\begin{aligned} (\nu_t)_{1(t)} &= c_\mu \frac{k_{1(t)}^2}{\epsilon_{1(t)}} \\ &= c_\mu \left(\frac{U_\tau^2}{\sqrt{c_\mu}} \right)^2 \left(\frac{\kappa z_{1(t)}}{U_\tau^3} \right) \\ &= \kappa U_\tau z_{1(t)} \end{aligned} \tag{2.78}$$

and hence ν_t adjacent to the bed is independent of c_μ. It was decided on the basis of these tests to use the 'standard' turbulence model constants in all the calculations, as shown in Table 1.

2.4 Investigation into k-ϵ Model with Damping as $f(P/\epsilon)$

2.4.1 Development of Damping Function, $f(P/\epsilon)$

In 1976 Rodi developed an algebraic relation to calculate the Reynolds stresses (Rodi 1976). In this section an algebraic damping function is developed which is loosely based upon Rodi's work. Rodi approximated the $< u_i u_j >$ transport equation and assumed that the transport of $< u_i u_j >$ is proportional to the transport of k. After some working, the following algebraic stress relation is then obtained

$$\nu_t = -\frac{< u_1 u_2 >}{\frac{\partial U_1}{\partial x_2}} \qquad \text{where} \qquad \nu_t = c_\mu f(P/\epsilon)\frac{k^2}{\epsilon} \tag{2.79}$$

$$\text{thus} \qquad c_\mu f(P/\epsilon) = \frac{2}{3}\Big(1 - c_2\Big)\frac{c_1 - 1 + c_2\frac{P}{\epsilon}}{\Big(c_1 + \frac{P}{\epsilon} - 1\Big)^2} \tag{2.80}$$

$f(P/\epsilon)$ corresponds to Rodi's c_μ (Rodi 1976). It can be clearly seen that the relation (2.79) is of the same general form as that of the k-ϵ-S model from Section 2.3.5. The strain parameter S in the k-ϵ-S model becomes large near to the wall, before settling to lower values further away from the wall. In contrast P/ϵ does not become large near to the wall. A damping function $f(P/\epsilon)$ is outlined below, in addition to the Launder and Sharma k-ϵ model. The function was first developed as an algebraic relation and then if necessary the function could be further developed to incorporate a differential equation which includes a dependence upon P/ϵ.

Thus an eddy viscosity model of the following form was investigated,

$$- < u_1 u_2 > = c_\mu f(P/\epsilon)\frac{k^2}{\epsilon}\frac{\partial U_1}{\partial x_2} \tag{2.81}$$

As with the Launder and Sharma k-ϵ model and the k-ϵ-S model, $c_\mu = 0.09$ and k and ϵ are calculated from transport equations. Initially the form of P/ϵ produced by the k-ϵ and k-ϵ-S models was considered. The production of P is given by

$$P = < uw > \frac{\partial U}{\partial z} \tag{2.82}$$

$$\text{thus} \quad \frac{P}{\epsilon} = -\frac{< uw >}{k}\frac{k}{\epsilon}\frac{\partial U}{\partial z} \tag{2.83}$$

The Reynolds stress can be given by the following for the eddy viscosity models previously tested

$$- < uw >= c_\mu f \frac{k^2}{\epsilon} \frac{\partial U}{\partial z} \tag{2.84}$$

where $f = f_\mu(Re_t)$ for the k-ϵ model and $f = f_\mu(Re_t) f_S(S)$ for the k-ϵ-S model. Figure 1 plots f against P/ϵ where the main region is distinguished from the near wall region. The damping function $f(P/\epsilon)$ attempts to reproduce the shape of the curve in the main region only. Since the k-ϵ-S model at $Re = 5600$ for channel flow gives the smoothest curve (Figure 1(a)), the functions are fitted to this curve.

The plot of the region is a function of the form

$$f(P/\epsilon) = \frac{a}{1 + b(P/\epsilon)^c} \tag{2.85}$$

where a, b and c are constants, and a is the value of $f(P/\epsilon)$ when $P/\epsilon = 0$. A variety of curve fits were compared to the original data (Figure 2). The function considered closest to the original $f = 1.25/(1 + 0.7(P/\epsilon)^7)$ is shown in Figure 2(a). This function was used as the damping function $f(P/\epsilon)$ in the assessment of a new k-ϵ model.

The equations for the k-ϵ-(P/ϵ) model investigated in cylindrical polar co-ordinates are given below:

$$- < u_r u_z >= \nu_t \frac{\partial U_z}{\partial r} \tag{2.86}$$

$$\nu_t = c_\mu f_\mu(Re_t) f(P/\epsilon) \frac{k^2}{\hat{\epsilon}} \tag{2.87}$$

$$f(P/\epsilon) = \frac{1.25}{1 + 0.7(P/\epsilon)^7} \tag{2.88}$$

$$f_\mu(Re_t) = 1.0 - 0.3 \exp\left[-0.02 Re_t\right], \qquad Re_t = \frac{k^2}{\nu \hat{\epsilon}} \tag{2.89}$$

The k and ϵ transport equations are the same as those for the Launder and Sharma model, equations (2.43), (2.44) and $c_\mu = 0.09$. When this program was run the solution did not converge, nor indeed did it march in time to the first time step. Profiles of the damping function showed non-physical distributions, switching back and forth between two solutions. This behaviour is similar to that of the k-ϵ-S

model tested by Ismael (1991) where S was an algebraic function. Ismael explained this behaviour in an internal note, Jan. 1991, showing the behaviour of the model when a small perturbation is introduced to the velocity profile of the new model. Ismael concluded that, in general, the condition which gives exponential decay of the perturbation is too stringent, hence leading to instability. The explanation for the instability of the present model is believed to be very similar.

2.4.2 Expansion to k-ϵ-Π Model

The next step is to expand the model to include a third transport equation, Π equation, based upon the P/ϵ term. A possible method for this expansion is outlined in this section. The development of this model was not taken any further. Following the work of Cotton and Ismael (1994) and (1995), an ad hoc transport equation for the strain parameter was derived from arguments based upon Rapid Distortion Theory. This method of development (Cotton and Ismael 1995, appendix) can also be applied here.

Thus the equation may be re-cast as follows

$$\frac{\partial \Pi}{\partial t} = \frac{P}{k} + \text{Diffusion} - \frac{\Pi}{k/\epsilon} \tag{2.90}$$

Neglecting diffusion, the equation may be rearranged to give

$$\frac{\partial \Pi}{\partial t} + \frac{\Pi}{k/\epsilon} = \frac{P}{k} \tag{2.91}$$

This equation may be solved for Π, assuming the special case that P/k and k/ϵ are constants. Thus

$$\Pi = A \exp\left(-\frac{t}{k/\epsilon}\right) \tag{2.92}$$

For $t = 0$,

$$\Pi = \frac{P}{\epsilon}, \quad \text{thus} \quad A = \frac{P}{\epsilon} \tag{2.93}$$

Substituting (2.93) into (2.92) the Taylor series expansion of equation (2.92) for $\Pi = 0$ at $t = 0$ gives

$$\Pi = \frac{P}{\epsilon}\left[1 - \exp\left(-\frac{t}{k/\epsilon}\right)\right] \tag{2.94}$$

Summarising and rearranging

$$t \to \infty, \qquad \Pi \to \frac{P}{\epsilon} \tag{2.95}$$

$$t \ll \frac{k}{\epsilon}, \qquad \Pi \to \frac{P}{\epsilon}\left[1 - \left(1 - \frac{t}{k/\epsilon}\right)\right] = \frac{P}{k}t \tag{2.96}$$

Chapter 3

Numerical Procedures

Two numerical procedures were adopted to solve the equation sets detailed in the previous chapter. The first code named 'TRANSIT' calculates spatially fully developed one-dimensional, unsteady pipe flows using an iterative procedure to march the solution forward in time. TRANSIT includes the Launder and Sharma k-ϵ (Section 2.3.4) and k-ϵ-S (Section 2.3.5) models and the RSTM (Section 2.3.6) model and uses a finite volume / finite difference scheme.

The second code, 'SW1DV' solves for one-dimensional, shallow water flows using a semi-implicit finite volume scheme. High-Reynolds-number k-ϵ (Section 2.3.3) and k-l (Section 2.3.2) models are employed, with wall functions to accommodate both smooth and rough beds. In this study SW1DV is applied to purely reciprocating horizontal flows.

Relatively little work was carried out on numerical aspects of turbulence solution strategies in this study, and so the reader is referred to previous work for the full details of the numerical procedures, (Ismael 1993a, Cotton *et al* 1997, Guy 2000, Stansby 1997). Here an outline of the procedure is given and any changes or additions to the numerics by the author in this study are detailed in full. Two differing notations are used in the discretisation and solution procedures of 'TRANSIT' and 'SW1DV'. This is done in order to retain the same notation as previous authors.

The only exception is that z is used as the vertical co-ordinate in Section 3.1 instead y.

3.1 Channel and Pipe Flow

The numerical procedures for the equation sets in Chapter 2 applied to channel and pipe flows are detailed in Cotton (1987) and Guy (2000) and only a brief description is given here. The numerical code 'CONVERT' first developed by Cotton (1987) to calculate steady, spatially fully-developed pipe flows using the Launder and Sharma k-ϵ model. The finite difference / finite volume scheme of Leschziner (1982) was employed to solve for velocity, U, kinetic energy, k and its dissipation rate, ϵ. The program was subsequently developed by Ismael (1993a) and renamed 'TRANSIT' to calculate one-dimensional, spatially fully developed unsteady pipe flows and a k-residual convergence test was included. Guy (2000) updated TRANSIT to incorporate the RSTM of Launder and Shima (1989), including the minor re-optimisation of Shima (1989). Guy also modified the program to include calculations for ramp-transient flows.

In the present study TRANSIT has been further developed by the author to include the k-ϵ-S model of Cotton and Ismael (1998). Discretisation and solution procedures for the S-equation in the k-ϵ-S model are described in Section 3.1.1. The option for a 'three-field' test has also been added by the author to allow assessment of the convergence of U, k and S for the k-ϵ-S model (Section 3.1.2). Alternative treatments of k near the wall have also been included, given in Section 3.1.3. Sensitivity tests were carried out in the course of this study to ensure that the results are independent of the numerical parameters are given in Section 3.1.4. The TRANSIT code was written in FORTRAN 77, and run on Hewlett Packard Apollo 700 workstations under UNIX.

3.1.1 Solution Procedure

Discretised forms of the flow equations are obtained using Leschziner's finite difference / finite volume scheme. This involves formal integration over finite control volumes ensuring that the equations are conservative for each control volume. The integrals are then approximated as discretised forms on the corresponding computational grid. The equations for U, k, ϵ and S (or the RSTM equations) are then solved. These quantities are assumed to vary only in the radial direction and time.

Generic form of the EVM equations

The discretisation of all the model equations above are detailed in Guy (2000), apart from the S-equation due to the addition of the k-ϵ-S model in TRANSIT by the author. The S-equation involves a slight modification in the numerical treatment and thus the discretisation is outlined below. The S-equation takes the same generic form as the mean streamwise momentum equation and the k- and ϵ-transport equations:

$$\frac{\partial(\rho r\Phi)}{\partial t} = \frac{\partial}{\partial r}\left(r\Gamma\frac{\partial\Phi}{\partial r}\right) + rS_\Phi \tag{3.1}$$

where Φ is the dependent variable, Γ is the diffusion coefficient, and S_Φ is the source/sink term. For the S-transport equation Φ, Γ and S_Φ represent the following:

$$\Phi = S, \quad \Gamma = \frac{\mu_t}{\sigma_S}, \quad S_\Phi = \rho\frac{k}{\hat{\epsilon}}\left(\frac{\partial U_z}{\partial r}\right)^2 - \rho\left(\frac{S\hat{\epsilon}}{k}\right) \tag{3.2}$$

The boundary conditions on S and the other parameters (U_z, k and ϵ) are the same as before and may be expressed in terms of Φ,

$$\Phi = 0 \qquad \text{at} \qquad r = R \tag{3.3}$$

$$\frac{\partial\Phi}{\partial r} = 0 \qquad \text{at} \qquad r = 0 \tag{3.4}$$

Computational grid

The finite volume / finite difference discretisation method of Leschziner (1982) is applied. Before this can be done the computational grid and control volume notation must be defined. On the radial grid distance from the centreline at the i^{th}

grid line is denoted by r_i. Therefore the $(i-1)^{\text{th}}$ and the $(i+1)^{\text{th}}$ gridlines denote the adjacent lines in the direction of the centreline and wall respectively. The distance between the $(i-1)^{\text{th}}$ and i^{th} gridlines is given by $(\Delta r)_i$, and similarly the distance between the i^{th} and $(i+1)^{\text{th}}$ gridlines is given by $(\Delta r)_{i+1}$. Note that $(\Delta r)_i > (\Delta r)_{i+1}$ since the grid spacing increases towards the centreline.

The $(j-1)^{\text{th}}$ and j^{th} temporal grid nodes are represented by t_{j-1} and t_j which indicate the previous and present times. The difference between these times is denoted by $(\Delta t)_j$.

A staggered grid is used for the RSTM model, where by the turbulence quantities are stored at 'secondary' gridlines bisecting the previously described 'primary' gridlines at which the mean velocity variable is stored. This staggered grid and the discretisation is described by Guy (2000), and since we are merely dealing with the S-transport equation here, only the primary grid arrangement is discussed.

A brief description of the control volume arrangement follows. The i^{th} primary control volume associated with the $(r)_i^{\text{th}}$ primary radial grid line is bounded by the $(r_-)_i$ and $(r_+)_i$ gridlines on the lower and upper faces respectively and the t_{j-1} and t_j temporal faces. The wall and centreline control volume requires special treatment. For the S-equation this is the same treatment as for the other transport equations in an EVM and so the reader is referred to Guy (2000). For a primary control volume the radial cross sectional area (apart from a factor of 2π) is given by

$$\int_{(r_-)_i}^{(r_+)_i} r dr = \overline{r_i}(\Delta r\pm)_i \tag{3.5}$$

where $\overline{r_i}$ is the mean radius and $(\Delta r\pm)_i$ is the radial dimension of the primary control volume defined by

$$\overline{r_i} = \frac{1}{2}[(r_+)_i + (r_-)_i], \quad (\Delta r\pm)_i = (r_+)_i - (r_-)_i \tag{3.6}$$

Discretisation method

The terms of the generic equations are integrated over each control volume. Leschziner (1982) applies the following rules to the resulting integral equations:

1. Quantities are uniform over temporal faces of control volumes.
2. Quantities at radial faces are evaluated by linear interpolation.
3. Quantities are constant and take present time value over radial faces of control volumes.
4. Sources are constant over control volumes and evaluated at the present-time grid node.

An implicit scheme is derived from the above assumptions which relates quantities at nodes $(i-1,j)$, (i,j), $(i+1,j)$ and $(i,j-1)$. This scheme was chosen in preference to, for example, an explicit scheme because of the superior stability. For a general control volume each term of equation (3.1) is integrated over the control volume from r_- to r_+ and t_{j-1} to t_j. Discretised forms of the unsteady, diffusion and source terms in equation (3.1) are obtained by integration and application of the above assumptions (1)-(4) to the resulting integrals:

$$\begin{aligned} & \int_{r_-}^{r_+} \rho r(\Phi_j - \Phi_{j-1})dr \\ = \; & \rho\overline{r_i}(\Phi_{i,j} - \Phi_{i,j-1})(\Delta r\pm)_i \end{aligned} \tag{3.7}$$

$$\begin{aligned} & \int_{t_{j-1}}^{t_j} \left[r_+\Gamma_+ \left(\frac{\partial\Phi}{\partial r}\right)_+ - r_-\Gamma_- \left(\frac{\partial\Phi}{\partial r}\right)_- \right] dt \\ = \; & (r_+)_i(\Delta t)_j(\Gamma_+)_{i,j} \left(\frac{\Phi_{i+1,j} - \Phi_{i,j}}{(\Delta r)_{i+1}}\right) \\ & -(r_-)_i(\Delta t)_j(\Gamma_-)_{i,j} \left(\frac{\Phi_{i,j} - \Phi_{i-1,j}}{(\Delta r)_i}\right) \end{aligned} \tag{3.8}$$

$$\begin{aligned} & \int_{t_{j-1}}^{t_j} \int_{r_-}^{r_+} rSdrdt \\ = \; & \overline{r_i}(\Delta r\pm)_i(\Delta t)_j S_{i,j} \end{aligned} \tag{3.9}$$

The original equation (3.1) in discretised form now reads

$$\begin{aligned}\rho\overline{r_i}(\Phi_{i,j}-\Phi_{i,j-1}) &= (r_+)_i(\Delta t)_j(\Gamma_+)_{i,j}\left(\frac{\Phi_{i+1,j}-\Phi_{i,j}}{(\Delta r)_{i+1}}\right)\\ &\quad -(r_-)_i(\Delta t)_j(\Gamma_-)_{i,j}\left(\frac{\Phi_{i,j}-\Phi_{i-1,j}}{(\Delta r)_i}\right)\\ &\quad +\overline{r_i}(\Delta r\pm)_i(\Delta t)_j S_{i,j} \qquad (3.10)\end{aligned}$$

This equation may be rewritten as

$$AP_{i,j}\Phi_{i+1,j}+AD_{i,j}\Phi_{i,j}+AM_{i,j}\Phi_{i-1,j}=AU_{i,j}\Phi_{i,j-1}+V_{i,j}S_{i,j} \qquad (3.11)$$

where the coefficients are given by

$$\begin{aligned}AP_{i,j} &= -(r_+)_i(\Delta t)_j(\Gamma_+)_{i,j}/(\Delta r)_{i+1}\\ AM_{i,j} &= -(r_-)_i(\Delta t)_j(\Gamma_-)_{i,j}/(\Delta r)_i\\ AU_{i,j} &= \rho\overline{r_i}(\Delta r\pm)_i\\ AD_{i,j} &= AU_{i,j}-AP_{i,j}-AM_{i,j}\\ V_{i,j} &= \overline{r_i}(\Delta r\pm)_i(\Delta t)_j \qquad (3.12)\end{aligned}$$

The corresponding generic equations for the control volume cases adjacent to the wall and at the centreline control volumes respectively are given by

$$AD_{ny-1,j}\Phi_{ny-1,j}+AM_{ny-1,j}\Phi_{ny-2,j}=AU_{ny-1,j}\Phi_{ny-1,j-1}+V_{ny-1,j}S_{ny-1,j} \qquad (3.13)$$

$$AP_{2,j}\Phi_{3,j}+AD_{2,j}\Phi_{2,j}=AU_{2,j}\Phi_{2,j-1}+V_{2,j}S_{2,j} \qquad (3.14)$$

Equations (3.11), (3.13) and (3.14) may be written in the form of a tri-diagonal matrix as follows

$$\begin{pmatrix} AD_{ny-1,j} & AM_{ny-1,j} & & & & \\ AP_{ny-2,j} & AD_{ny-2,j} & AM_{ny-2,j} & & & \\ & \ddots & \ddots & \ddots & & \\ & & AP_{3j} & AD_{3j} & AM_{3j} & \\ & & & AP_{2j} & AD_{2j} & \end{pmatrix}\begin{pmatrix}\Phi_{ny-1,j}\\ \Phi_{ny-2,j}\\ \vdots\\ \Phi_{3,j}\\ \Phi_{2,j}\end{pmatrix}=\begin{pmatrix}C_{ny-1,j}\\ C_{ny-2,j}\\ \vdots\\ C_{3,j}\\ C_{2,j}\end{pmatrix} \qquad (3.15)$$

where the vector coefficients are given by

$$C_{i,j}=AU_{i,j}\Phi_{i,j-1}+V_{i,j}S_{i,j} \qquad (3.16)$$

Diagonal dominance in the S-equation

The k and ϵ transport equations in the k-ϵ-S model use the above discretisation, however the treatment for the S-equation differs, in that a technique to promote diagonal dominance is applied in order to increase the stability of the solution. For the S-equation the source term in equation (3.16) is given by

$$C_{i,j} = AU_{i,j}\Phi_{i,j-1} + \left[\rho\frac{k}{\hat{\epsilon}}\left(\frac{\partial U_z}{\partial r}\right)^2 - \rho\left(\frac{S\hat{\epsilon}}{k}\right)\right]\overline{r_i}(\Delta r\pm)_i(\Delta t)_j \tag{3.17}$$

A non-standard implicit source term treatment is implemented for the S-equation. This involves including the negative part of the source term into $AD_{i,j}$, thus

$$AD_{i,j} = AD_{i,j} + \rho\frac{\hat{\epsilon}}{k}\overline{r_i}(\Delta r\pm)_i(\Delta t)_j \tag{3.18}$$

Hence the source term is now given by

$$\begin{aligned} C_{i,j} &= AU_{i,j}\Phi_{i,j-1} + \left[\rho\frac{k}{\hat{\epsilon}}\left(\frac{\partial U_z}{\partial r}\right)^2 - \rho\left(\frac{S\hat{\epsilon}}{k}\right)\right]\overline{r_i}(\Delta r\pm)_i(\Delta t)_j \\ &\quad +\rho\left(\frac{S\hat{\epsilon}}{k}\right)\overline{r_i}(\Delta r\pm)_i(\Delta t)_j \\ &= AU_{i,j}\Phi_{i,j-1} + \rho\frac{k}{\hat{\epsilon}}\left(\frac{\partial U_z}{\partial r}\right)^2\overline{r_i}(\Delta r\pm)_i(\Delta t)_j \end{aligned} \tag{3.19}$$

The solution is then marched in time from known initial conditions. An iterative procedure is required to obtain a converged solution within specified criteria at each time step. An under relaxation technique, originally applied by Cotton (1987), is adopted to ensure stability. A field convergence or k-residual test assesses whether a solution is converged. The 2-D channel flow equations are also discretised in Guy (2000).

3.1.2 Convergence Tests

Three tests have been investigated to assess whether a converged solution has been obtained:

- Two-field convergence test: based on U and k fields

- Three-field convergence test: based on U, k and S fields
- k residuals

For all three tests, if convergence is not attained within a certain number of iterations, namely 100, then it is considered to be unattainable. The test is applied immediately after solving the discretised equations, for the second and subsequent iterations.

Field Convergence Test

Cotton (1987) originally formulated this test. For any field, ϕ, the solution is considered to have converged if the following inequality is satisfied,

$$\left| \frac{(\phi_i)_{k+1} - (\phi_i)_k}{(\phi_i)_k} \right|_{\forall i} \leq c_\phi \tag{3.20}$$

where the subscript i represents the field number ($i = 2 \text{ to } 100$), k the iteration number, and c_ϕ the convergence criterion.

For the k-ϵ model, the field convergence test was applied to the U and k fields, since they have large gradients. The test is considered to be stringent, as the solution might not be expected to converge on account of these steep gradients. Note that the stringency of the convergence test is eventually dependent on the tolerance of the convergence criterion (and also the value of the under-relaxation factor). Standard values for the convergence criterion, c_ϕ are given as:

$$c_U = 10^{-4} \tag{3.21}$$

$$c_k = 10^{-3} \tag{3.22}$$

The two-field convergence test on the U and k fields was also applied to the k-ϵ-S model and proved adequate. Even so, it was thought appropriate, due to the very large gradients near the wall, that the S-field should also be included in the convergence test. This test was added to TRANSIT by the present author. The

test follows the same form as in equation (3.20), and the convergence criterion used is as follows

$$c_S = 10^{-4} \tag{3.23}$$

The extra test on the S-field in fact proved unnecessary as it gave essentially the same results as the original test. Additionally, this test increased the computational effort. An indication of computational effort required is given by the number of times that the tri-diagonal set is solved for a given problem.

k Residuals

The k residual convergence test was applied by Ismael (1993a). The k-equation was chosen due to the large changes in the k-field, as mentioned in Section 3.1.2, thus providing a stringent test. The residual, r_{ij} of the k-equation is defined as:

$$r_{ij} = AP_j k_{ij+1} + AD_j k_{ij} + AM_j k_{ij-1} - AU_j k_{i-1j} - V_j S_{ij} \tag{3.24}$$

Thus the residual is the imbalance in a 're-constructed' discretised k-equation following solution for k at time level i. Equation (3.24) may be rewritten to show the contribution of the unsteady, production, diffusion and dissipation processes.

$$\begin{aligned} r_{ij} = \; & - \; AU_{ij}(k_{ij} - k_{ij-1}) && \text{unsteady} \\ & + \; V_{ij}(\mu)_{ij}\left(\partial U_z/\partial r\right)^2_{ij} && \text{production} \\ & - \; AP_{ij}(k_{i+1j} - k_{ij}) + AM_{ij}(k_{ij} - k_{i-1j}) && \text{diffusion} \\ & - \; V_{ij}\rho\epsilon_{ij} && \text{dissipation} \end{aligned} \tag{3.25}$$

The test requires that the ratio of the residual to the maximum of unsteady, production, diffusion, or dissipation processes is less then a specific value, denoted by c_k . Thus convergence is attained if the following inequality is satisfied:

$$\frac{|\,\text{residual}|}{\max(|\,\text{unsteady}|,|\,\text{production}|,|\,\text{diffusion}|,\,|\,\text{dissipation}|)} \leq c_k \tag{3.26}$$

where $c_k = 10^{-3}$.

This test will be used from this point onwards.

3.1.3 Treatment of the k Equation Near the Wall

Consider the following term in the dissipation equation (2.44)

$$c_{\epsilon 2}\frac{\epsilon^2}{k} \tag{3.27}$$

This term becomes infinite at a solid boundary, since ϵ is finite but k is zero. The problem can be resolved by the replacement of ϵ by a new dissipation variable $\hat{\epsilon}$, given by equation (2.44) with the boundary condition $\hat{\epsilon} = 0$ at the wall.

$\hat{\epsilon}$ is the subject of the second transport equation, see Section 2.3.4. In the k-equation, however, ϵ is to be recovered and is now written as $\hat{\epsilon} + D_\epsilon$. Previous experience (Cotton 1987) has shown that the use of D_ϵ as given by equation (2.44) may cause convergence difficulties in near-wall regions. This problem has been investigated by applying several different methods near to the wall. These are described below.

'Switch' Method

This method has been applied in turbulence modelling in recent years, and was used by Cotton (1987), Cotton and Jackson (1990) and Ismael (1993a). The following relation is used instead of equation (2.44), up to a specified distance from the wall,

$$\epsilon = \hat{\epsilon} + \frac{2\nu k}{z^2} \qquad \text{for} \qquad z^+ \leq z_b^+ \tag{3.28}$$

The accuracy of this relation can be justified by comparing the original (2.44) and modified (3.28) forms of D_ϵ. First expand k as follows:

$$k = Az^2 + Bz^3 + \ldots \tag{3.29}$$

where A and B are constants. This can be rearranged to give

$$k = Az^2\left(1 + \frac{B}{A}z + \ldots\right) \tag{3.30}$$

Substituting the first term into this expanded form

$$2\nu\frac{k}{z^2} = 2\nu A + 2\nu Bz + \ldots \tag{3.31}$$

and for the second term

$$\begin{aligned} k^{\frac{1}{2}} &= A^{\frac{1}{2}} z \left(1 + \frac{1}{2}\frac{B}{A} z + \ldots\right) \\ \frac{\partial k^{\frac{1}{2}}}{\partial z} &= A^{\frac{1}{2}} + \frac{B}{A^{\frac{1}{2}}} z + \ldots \\ 2\nu \left(\frac{\partial k^{\frac{1}{2}}}{\partial z}\right)^2 &= 2\nu(A + 2Bz + \ldots) \\ &= 2\nu A + 4\nu B z + \ldots \end{aligned} \tag{3.32}$$

Thus, these terms agree to first order accuracy. Two different values of z_b^+ were investigated, 1.5 and 2.0.

This method is not favoured as it incorporates a step change or 'switch' in the turbulence model formulation. The following methods retain the original form of the k-ϵ model and change the numerical discretisation near the wall.

Quadratic Approximation

This method was developed by Ismael (1993b and c). Instead of the normal linear approximation, it uses a quadratic approximation to the derivative in the discretisation of the k transport equation at the near-wall control volume. Following Ismael, consider a variable ϕ. The quadratic through the three points (ϕ_n, ψ_n), (ϕ_{n-1}, ψ_{n-1}), and (ϕ_{n-2}, ψ_{n-2}) is given by the Lagrange polynomial formula

$$\begin{aligned} \phi &= \frac{(\psi - \psi_{n-1})(\psi - \psi_{n-2})}{(\psi_n - \psi_{n-1})(\psi_n - \psi_{n-2})}\phi_n \\ &+ \frac{(\psi - \psi_n)(\psi - \psi_{n-2})}{(\psi_{n-1} - \psi_n)(\psi_{n-1} - \psi_{n-2})}\phi_{n-1} \\ &+ \frac{(\psi - \psi_n)(\psi - \psi_{n-1})}{(\psi_{n-2} - \psi_n)(\psi_{n-2} - \psi_{n-1})}\phi_{n-2} \end{aligned} \tag{3.33}$$

Differentiating w.r.t. ψ, evaluating at $\psi = \psi_n$, and using the following notation,

$$\begin{aligned} \psi_n &= 1 \\ \triangle\psi_n &= \psi_n - \psi_{n-1} = 1 - \psi_{n-1} \\ \triangle\psi_{n-1} &= \psi_{n-1} - \psi_{n-2} \end{aligned} \tag{3.34}$$

The required formula is then obtained,

$$\left(\frac{\partial\phi}{\partial\psi}\right)_{\psi=1} = \frac{\triangle\psi_n + (1-\psi_{n-2})}{\triangle\psi_n(1-\psi_{n-2})}\phi_n - \frac{(1-\psi_{n-2})}{\triangle\psi_n\triangle\psi_{n-1}}\phi_{n-1} + \frac{\triangle\psi_n}{(1-\psi_{n-2})\triangle\psi_{n-1}}\phi_{n-2} \quad (3.35)$$

This discretisation is applied to the $(\frac{\partial k^{\frac{1}{2}}}{\partial z})^2$ term in the k transport equation only.

As shown above, the two forms of D_ϵ are identical if k varies quadratically near the wall. Since this method works for the special form of D_ϵ near the wall, it should also be possible to obtain a converged solution using the original form of D_ϵ all the way to the wall. This was found to be true. However, some convergence difficulties were experienced dependent upon the method of convergence testing. The quadratic approximation method failed when using the k-residual convergence test. Convergence problems were found sometimes when using the three-field convergence test. This method worked consistently in conjunction with the two-field convergence test.

'Staggered' Interpolation

This method also uses the original form of D_ϵ all the way to the wall. It is a simple method to form k in the term $\nu\left(\frac{\partial k^{1/2}}{\partial z}\right)^2$. First k is interpolated to the control volume faces, as shown in Figure 3. $k^{\frac{1}{2}}$ is calculated, and linear interpolation then is used to form $\left(\frac{\partial k^{\frac{1}{2}}}{\partial\psi}\right)_j$.

Discussion

All results were produced using the unsteady flow code TRANSIT which incorporates several turbulence models applied to pipe and channel flow, written in FORTRAN 77, and run on the HP700 workstations in the School of Engineering, Manchester University.

Coding for the three-field convergence method, and for the quadratic approximation and staggered interpolation was added by the author to TRANSIT. Options for a particular convergence method and for a treatment of the k equation near the wall were also added to enable the user to choose a particular method.

Tables 2–5 give the values of the friction coefficient for each method for the k-ϵ and k-ϵ-S models for channel flow at Reynolds numbers 5600 and 13750. The percentage change in comparison with the results of Blundell and Cotton (1995) is recorded. (Blundell and Cotton used the two-field convergence test and the quadratic approximation.) The tables also give the number of calls to the matrix solution subroutine (described by the heading 'SOLVE') to give a measure of the computational effort required for each run.

Tables 6 and 7 give the same friction coefficient results as Table 3 for the k-ϵ-S model for channel flow with $Re = 5600$. However the results are compared with those produced by the program 'SMOD.F' written in FORTRAN by Cotton (1997b). In Table 6 the results are compared to those of Cotton when the switch at $z+ = 2.0$ was applied near the wall. Table 7 compares the results to those of Cotton when he applied the staggered discretisation. Cotton used the three field convergence test for both runs.

The percentage error is calculated using the friction coefficient as follows

$$\%\text{change} = \frac{c_{f\text{test}} - c_{f\text{standard}}}{c_{f\text{standard}}} \times 100 \tag{3.36}$$

to the nearest 0.1%. The percentage change indicates whether the solution is accurate, and the difference between the various methods. The results indicated by †‡ on Tables 2–7 represent a direct comparison with the results of Blundell and Cotton, that is the convergence test used and treatment of k near the wall are the same as those used for the TRANSIT solution. '—' indicates that the solution does not converge.

The program fails when the quadratic discretisation is used in conjunction with the

k residuals convergence test. If the convergence criterion is changed, so that it is 10 times the normal value, then the program does not fail, but clearly accuracy is sacrificed.

The program also fails for the k-ϵ-S model with $Re = 5600$ using the quadratic discretisation and the three-field convergence test. This could be due to the large gradients in the S field near the wall.

The results at the higher Reynolds number give a better indication of the accuracy of the various methods, since $Re = 5600$ is very low for engineering flows. The switch method does seem more efficient in terms of computational effort, but this involves a change in the turbulence model near the wall. The other methods that change only numerically are preferable. The staggered discretization method is more reliable than the quadratic interpolation and uses less computational effort.

Comparison with an alternative set of results produced by Cotton, (Table 6 and 7) confirmed the accuracy of the program, and in fact the percentage change was slightly smaller than that reported by Blundell and Cotton (Table 3).

Development of Standard Procedures

The methods which will be taken as standard for all further work are the 'staggered' discretisation, in conjunction with the k residual convergence test. The option to use the other methods has been retained in the code.

3.1.4 Sensitivity Tests

Sensitivity tests are carried out in order to show the extent to which the results from the k-ϵ and k-ϵ-S models are independent of the arbitrary numerical parameters used to obtain a solution. As in Section 3.1.3, the tests were applied to both models for channel flow at Reynolds numbers 5600 and 13750 (Kim *et al* 1987, Kim 1990). Similarly, the tests are assessed by considering the value of the friction coefficient,

c_f determined by the convergence criterion, c_k. Firstly, it is necessary to check that a converged solution is obtained. A solution is considered converged when the value of the c_f becomes constant. For periodic flow, similar cycles in a graph of c_f must be attained.

The solution must also be independent of the approximate initial conditions.

Then tests are applied to the numerical parameters, namely,

1. Number of radial grid nodes, iz
2. Position of the near-wall node, z^+_{iz-1}
3. Initial time step, $(\Delta t)_0$
4. Relaxation factor, a_R
5. Convergence criterion, c_k
6. Total duration, t_{total}

These tests are to investigate whether the standard values used for these numerical parameters are adequate. More stringent and lenient tests are applied to see whether the results obtained with the standard procedures are accurate, and to assess the computational effort in each case. The accuracy of each test is determined by the error of c_f which is given by the percentage change with respect to the standard value of c_f, see equation (3.36). If the error is within $\pm 1\%$ then the standard value is considered adequate, as the error is negligible compared to the errors produced by the simplifications in the turbulence models.

Tables 8–13 give the results of these tests. The values of the tested parameter, the friction coefficient, the percentage change compared to the standard, and the number of times the matrix equations are solved are given.

Discussion

For each of the numerical parameters tested, similar results were obtained for the low-Reynolds-number k-ϵ and k-ϵ-S turbulence models at a given Reynolds number. The values of c_f obtained from the sensitivity tests were in general within the required $\pm 1\%$ of the standard value. Altering the values of the initial time step, relaxation factor, convergence criterion and total duration had no significant effect on the c_f value. The position of the near wall node does have a slight effect on the solution but this was within the acceptable error limit. Halving the number of radial grid nodes gave unacceptable errors, particularly for the k-ϵ model which gave 1.71% error for $Re = 5600$ and 1.88% error for $Re = 13750$. The k-ϵ-S model produced slightly more acceptable discrepancies at 0.96% and 1.19% respectively. Doubling the number of radial grid nodes gives satisfactory results. Since increasing the stringency of the test reduces the discrepancy, it can be concluded that the standard values give adequate results.

The last column in each table, 'SOLVE' shows the number of times the matrix equations are solved in order to obtain a converged solution. This gives an indication of the computational effort required for each case. The general trend is that for a more stringent test the computational effort increases, and vice versa.

3.2 Shallow Water 1-D Oscillatory Flow

The 1-D numerical code applied to oscillatory flows over smooth and rough beds is a version of the 3-D numerical procedure described by Stansby (1997). k-ϵ and k-l turbulence models given in Sections 2.3.2 and 2.3.3, are employed with wall functions. An implicit time-stepping scheme is used. The mesh spacing varies parabolically in the vertical direction to give fine resolution near the bed in order to resolve the large gradients of velocity, kinetic energy and dissipation. The computational mesh is described by a σ-coordinate scheme. The equations are solved by a conservative

finite volume scheme in which the nodes for velocity and the turbulence quantities are staggered in the vertical direction. Two versions of the 1-D code are applied here, mainly due to differing input conditions. These are described in Section 3.2.1. The parabolic mesh generation is given in Section 3.2.2. The discretisation and solution procedure is described in Section 3.2.3 with particular attention paid to the differences between the two versions of SW1DV. The sensitivity to numerical parameters is detailed in Section 3.2.4. The SW1DV code was written in Salford FORTRAN 77 by Prof P. K. Stansby and converted to Salford FORTRAN 90 by the author in the present study to run on a PC with a Pentium II processor under Windows 95/98/NT.

3.2.1 Input Parameters

Two versions of the 1-D code are used in this study. The input parameter for the solution of the momentum equation is the main distinguishing factor between the versions. The first version uses the driving pressure gradient as the input quantity, and in the second version the volumetric flow rate, or bulk velocity, is the controlling parameter.

The choice of version is dependent upon the controlling variable in each experimental case to which the numerical results are compared. In those cases for which maximum surface slope, S_M is given, usually in field experiments, the driving horizontal pressure gradient, $\partial p/\partial x$ may be obtained as a function of time given by

$$-\frac{1}{\rho}\frac{\partial p}{\partial x} = gS_M \cos\left(\frac{2\pi t}{T}\right) \tag{3.37}$$

In those cases for which the freestream velocity, U_0 is the controlling variable, the driving pressure gradient is then derived from the inviscid Euler equation, given by

$$\frac{dU_0}{dt} = -\frac{1}{\rho}\frac{\partial p}{\partial x} \tag{3.38}$$

These two cases are referred to as the 'pressure gradient' version of SW1DV. However in large scale laboratory experiments the bulk velocity generally is the controlling

variable. In these cases the 'bulk velocity', U_b version of the code SW1DV is used, and an additional equation describing the volumetric flow rate as a function of time is used

$$U_b(t) = \frac{1}{h}\int_0^h U dz \tag{3.39}$$

3.2.2 Mesh Generation

Following Stansby (1997) the numerical grid varies parabolically to give a fine mesh near the bed and near the surface. This is to ensure that large gradients of velocity and the turbulence quantities occurring in these regions will be solved accurately. A σ co-ordinate is introduced to ensure that the mesh fits the bed and surface with surface elevation

$$\sigma = \frac{z-\eta}{h} \tag{3.40}$$

This is illustrated in Figure 4. Surface elevation is not used in this study and in fact $\eta = h$. The following parabolic transformation is applied to compress the σ mesh near to the bed and surface symmetrically about the mid-depth:

$$\frac{d\sigma_{\text{mesh}}}{d\sigma'_{\text{mesh}}} = b(\sigma_{\text{mesh}} + a)(1 - \sigma_{\text{mesh}} + a) \tag{3.41}$$

where $0 \leq \sigma_{\text{mesh}} \leq 1$ defines the σ mesh, $\sigma = \sigma_{\text{mesh}} - 1$ and $0 \leq \sigma'_{\text{mesh}} \leq 1$ is a uniformly spaced mesh. a and b are algebraically related constants ($a << 1$). The constants are defined by the following method. Inverting and rearranging equation (3.41) gives

$$\frac{d\sigma'_{\text{mesh}}}{d\sigma_{\text{mesh}}} = \frac{1}{b(1+2a)}\left[\frac{1}{(\sigma_{\text{mesh}} + a)} + \frac{1}{(1 - \sigma_{\text{mesh}} + a)}\right] \tag{3.42}$$

and then integrating by σ_{mesh}

$$\sigma'_{\text{mesh}} = \frac{1}{b(1+2a)} \ln\left(\frac{\sigma_{\text{mesh}} + a}{1 - \sigma_{\text{mesh}} + a}\right) + C \tag{3.43}$$

To evaluate b and C, substitute $\sigma'_{\text{mesh}} = 0$ when $\sigma_{\text{mesh}} = 0$ into equation (3.43), thus

$$C = -\frac{1}{b(1+2a)} \ln\left(\frac{a}{1+a}\right) \tag{3.44}$$

Substituting equation (3.44) into equation (3.43) gives

$$\sigma'_{\text{mesh}} = \frac{1}{b(1+2a)} \ln\left[\left(\frac{\sigma_{\text{mesh}}+a}{a}\right)\left(\frac{1+a}{1-\sigma_{\text{mesh}}+a}\right)\right] \tag{3.45}$$

Then taking $\sigma'_{\text{mesh}} = 1$ when $\sigma_{\text{mesh}} = 1$ gives

$$b = \frac{2}{1+2a} \ln\left(1+\frac{1}{a}\right) \tag{3.46}$$

These constants and the number of vertical grid nodes determine the degree of compression.

Applying $a << 1$ and at the bed $\sigma_{\text{mesh}} = \delta\sigma << 1$ to equation (3.45) gives,

$$\begin{aligned} \delta\sigma' &= \frac{1}{b(1+2a)} \ln\left(\frac{\delta\sigma+a}{a}\right) \\ &= \frac{1}{b(1+2a)} \frac{\delta\sigma}{a} \end{aligned} \tag{3.47}$$

Applying the above assumptions at the bed to equation (3.46) gives

$$b \simeq -\frac{2}{1+2a} \ln a \tag{3.48}$$

Substituting equation (3.48) into (3.47)

$$\delta\sigma' \simeq -\frac{\delta\sigma}{2a \ln a} \tag{3.49}$$

Since $\delta\sigma' = 1/K$, at the bed and surface:

$$\delta\sigma = \frac{\delta z}{h} \simeq \frac{-2a \ln a}{K} \tag{3.50}$$

where K is the number of vertical cells.

3.2.3 Discretisation and Solution Procedure

In this section the numerical discretisation on the conventional staggered mesh system is described. There are two solution procedures for velocity, dependent upon the input of either pressure gradient or bulk velocity. The discretisation and solution procedure for the U, k and ϵ parameters is described for the 'pressure gradient'

version. The differences in the solution procedure for U between the 'pressure gradient' version and the 'bulk velocity' version are also explained. For the k and ϵ parameters the solution procedures are exactly the same in both versions. The conventional staggered mesh system is used. The cells are numbered centrally k where $k = 1, \ldots, K$, with $k = 1$ for the bed cell and $k = K$ for the surface cell. This is illustrated in Figure 5.

For homogeneous flows the momentum equation (2.8) takes the discretised form with the following equation

$$\begin{aligned} U_k^{n+1} = \quad & U_k^n + \delta t\, g\, S_M cos(2\pi t/T) \\ + \quad & \delta t \frac{d\sigma'}{d\sigma}_k \left(\frac{\nu^n_{k+\frac{1}{2}} \frac{d\sigma'}{d\sigma}_{k+\frac{1}{2}} (u^{n+1}_{k+1} - u^{n+1}_k) - \nu^n_{k-\frac{1}{2}} \frac{d\sigma'}{d\sigma}_{k-\frac{1}{2}} (u^{n+1}_k - u^{n+1}_{k-1})}{(\delta\sigma' h)^2} \right) \end{aligned} \tag{3.51}$$

where n denotes time level, δt is time step, $\delta\sigma' = 1/K$, the subscript E has been omitted from ν_E to simplify the notation, and S_M is the maximum surface slope effectively defining the driving pressure gradient. Note $\sigma_{\frac{1}{2}}$ corresponds to the bed and $\sigma_{K+\frac{1}{2}}$ to the surface in this notation.

The tri-diagonal matrix with matrix elements $a_{m,m}$ and right hand side term b_m (with $m = 1, \ldots, K$) is defined by for $k = 1$,

$$a_{1,1} = 1 + \frac{\gamma^n \delta t \frac{d\sigma'}{d\sigma}_1}{h\,\delta\sigma'} + \delta t \frac{\nu^n_{1\frac{1}{2}} \frac{d\sigma'}{d\sigma}_{1\frac{1}{2}} \frac{d\sigma'}{d\sigma}_1}{(h\,\delta\sigma')^2}$$

$$a_{1,2} = -\delta t \frac{\nu^n_{1\frac{1}{2}} \frac{d\sigma'}{d\sigma}_{1\frac{1}{2}} \frac{d\sigma'}{d\sigma}_1}{(h\ \delta\sigma')^2} \tag{3.52}$$

$$b_1 = U_1^n + \delta t\, g S_M \cos(2\pi t/T) \tag{3.53}$$

for $k = 2, \ldots, K-1$,

$$a_{k,k-1} = -\delta t \frac{\nu^n_{k-\frac{1}{2}} \frac{d\sigma'}{d\sigma}_{k-\frac{1}{2}} \frac{d\sigma'}{d\sigma}_k}{(h\,\delta\sigma')^2}$$

$$a_{k,k} = 1 + \delta t \frac{\nu^n_{k+\frac{1}{2}} \frac{d\sigma'}{d\sigma}_{k+\frac{1}{2}} \frac{d\sigma'}{d\sigma}_{k}}{(h\,\delta\sigma')^2} + \delta t \frac{\nu^n_{k-\frac{1}{2}} \frac{d\sigma'}{d\sigma}_{k-\frac{1}{2}} \frac{d\sigma'}{d\sigma}_{k}}{(h\,\delta\sigma')^2}$$

$$a_{k,k+1} = -\delta t \frac{\nu^n_{k+\frac{1}{2}} \frac{d\sigma'}{d\sigma}_{k+\frac{1}{2}} \frac{d\sigma'}{d\sigma}_{k}}{(h\,\delta\sigma')^2} \tag{3.54}$$

$$b_k = U^n_k + \delta t\, g S_M \cos(2\pi t/T) \tag{3.55}$$

and for $k = K$,

$$a_{K,K-1} = -\delta t \frac{\nu^n_{K-\frac{1}{2}} \frac{d\sigma'}{d\sigma}_{K-\frac{1}{2}} \frac{d\sigma'}{d\sigma}_{K}}{(h\,\delta\sigma')^2}$$

$$a_{K,K} = 1 + \delta t \frac{\nu^n_{K-\frac{1}{2}} \frac{d\sigma'}{d\sigma}_{K-\frac{1}{2}} \frac{d\sigma'}{d\sigma}_{K}}{(h\,\delta\sigma')^2} \tag{3.56}$$

$$b_K = U^n_K + \delta t\, g S_M \cos(2\pi t/T) \tag{3.57}$$

Equations (3.52)-(3.57) may be written in the form of a tri-diagonal matrix as follows:

$$\begin{pmatrix} a_{1,1} & a_{1,2} & & & & \\ a_{2,1} & a_{2,2} & a_{2,3} & & & \\ & \ddots & \ddots & \ddots & & \\ & & a_{K-1,K-2} & a_{K-1,K-1} & a_{K-1,K} & \\ & & & a_{K,K-1} & a_{K,K} & \end{pmatrix} \begin{pmatrix} U^{n+1}_1 \\ U^{n+1}_2 \\ \vdots \\ U^{n+1}_{K-1} \\ U^{n+1}_K \end{pmatrix} = \begin{pmatrix} b_1 \\ b_2 \\ \vdots \\ b_{K-1} \\ b_K \end{pmatrix} \tag{3.58}$$

ν_E at time level n was used above to advance U to time level $n+1$ and k and ϵ are then advanced to time level $n+1$.

For the 'bulk velocity' version the pressure gradient is unknown. The bulk velocity is defined by equation (3.39). Here this is given by

$$U_b = \sum_{k=1}^{K} U_k \left(\frac{\partial \sigma}{\partial \sigma'}\right)_k \delta\sigma'_k \tag{3.59}$$

Since the bulk velocity is known, equation (3.59) is used so that now the number of unknowns and equations are equal and thus we can solve for U. A full

$(K+1) \times (K+1)$ matrix is applied to solve for U. $a_{1,1} \ldots a_{K,K}$ are given by equations (3.52), (3.54) and (3.56) as above. The right hand side term is now given by

$$b_k = U_k^n \quad \text{for} \quad k = 1, \ldots, K \tag{3.60}$$

The value for bulk velocity at time n is added to the end of the vector, thus

$$b_{K+1} = U_b^{n+\frac{1}{2}} \tag{3.61}$$

The driving pressure gradient, $\partial p/\partial x = \rho g S_M \cos(2\pi t/T)$ is added to the end of the U^{n+1} vector. The pressure gradient term in equation (3.51) and the bulk velocity term in equation (3.59) are added to the matrix via vectors d_m and e_m as follows:

$$d_k = -h\,\delta t\,\delta\sigma_k \tag{3.62}$$

$$\begin{aligned} e_1 &= \delta\sigma' \frac{\delta\sigma}{\delta\sigma'_1} \\ e_k &= \delta\sigma' \frac{\delta\sigma}{\delta\sigma'_k} \\ e_K &= \delta\sigma' \frac{\delta\sigma}{\delta\sigma'_K} \end{aligned} \tag{3.63}$$

Thus the matrix is now given by

$$\begin{pmatrix} a_{1,1} & a_{1,2} & & & & d_1 \\ a_{2,1} & a_{2,2} & a_{2,3} & & & d_2 \\ & \ddots & \ddots & \ddots & & \vdots \\ & & a_{K-1,K-2} & a_{K-1,K-1} & a_{K-1,K} & d_{K-1} \\ & & & a_{K,K-1} & a_{K,K} & d_K \\ e_1 & e_2 & \ldots & e_{K-1} & e_K & 0 \end{pmatrix} \begin{pmatrix} U_1^{n+1} \\ U_2^{n+1} \\ \vdots \\ U_{K-1}^{n+1} \\ U_K^{n+1} \\ -\frac{1}{\rho}\frac{\partial p}{\partial x} \end{pmatrix} = \begin{pmatrix} U_1^n \\ U_2^n \\ \vdots \\ U_{K-1}^n \\ U_K^n \\ U_b^{n+\frac{1}{2}} \end{pmatrix} \tag{3.64}$$

Gaussian elimination is then used by the bulk velocity code to solve for U.

For the turbulence quantities, vertical diffusion is again handled implicitly, source terms for k explicitly and source terms for ϵ semi-implicitly. k and ϵ are defined at vertical mesh points between those for U since this is most convenient for specifying

ν_E for vertical diffusion. The equation for k is thus discretised as

$$k^{n+1}_{k+\frac{1}{2}} = k^n_{k+\frac{1}{2}} + \delta t(P^n_{k+\frac{1}{2}} - \epsilon^n_{k+\frac{1}{2}}) + \delta t \frac{d\sigma'}{d\sigma}_{k+\frac{1}{2}} \frac{\frac{\nu^n_{k+1}}{\sigma_k}\frac{d\sigma'}{d\sigma}_{k+1}(k^{n+1}_{k+1\frac{1}{2}} - k^{n+1}_{k+\frac{1}{2}}) - \frac{\nu^n_k}{\sigma_k}\frac{d\sigma'}{d\sigma}_{k}(k^{n+1}_{k+\frac{1}{2}} - k^{n+1}_{k-\frac{1}{2}})}{(\delta\sigma' h)^2} \tag{3.65}$$

A tridiagonal matrix is formed for k with $m = 1, \ldots, K$ corresponding to $k = 1\frac{1}{2}, \ldots, K + \frac{1}{2}$, since values on the bed are not required and wall functions are used to specify magnitudes at $k = 1\frac{1}{2}$.

With $m = 1$ we require from equation (2.35)

$$a_{1,1} = 1$$

$$a_{1,2} = 0 \tag{3.66}$$

$$b_1 = \frac{U^2_\tau}{\sqrt{c_\mu}} \tag{3.67}$$

for $m = 2, \ldots, K-1$, corresponding to $k = 2\frac{1}{2}, \ldots, K - \frac{1}{2}$,

$$a_{m,m-1} = -\delta t \frac{\frac{\nu^n_k}{\sigma_k}\frac{d\sigma'}{d\sigma}_{k}\frac{d\sigma'}{d\sigma}_{k+\frac{1}{2}}}{(h\,\delta\sigma')^2}$$

$$a_{m,m} = 1 + \delta t \frac{\frac{\nu^n_k}{\sigma_k}\frac{d\sigma'}{d\sigma}_{k}\frac{d\sigma'}{d\sigma}_{k+\frac{1}{2}}}{(h\,\delta\sigma')^2} + \delta t \frac{\frac{\nu^n_{k+1}}{\sigma_k}\frac{d\sigma'}{d\sigma}_{k+1}\frac{d\sigma'}{d\sigma}_{k+\frac{1}{2}}}{(h\,\delta\sigma')^2}$$

$$a_{m,m+1} = -\delta t \frac{\frac{\nu^n_{k+1}}{\sigma_k}\frac{d\sigma'}{d\sigma}_{k+1}\frac{d\sigma'}{d\sigma}_{k+\frac{1}{2}}}{(h\,\delta\sigma')^2} \tag{3.68}$$

$$b_m = k^n_{k+\frac{1}{2}} + \delta t(P^n_{k+\frac{1}{2}} - \epsilon^n_{k+\frac{1}{2}}) \tag{3.69}$$

For $m = K$ without wind shear we require zero gradient which is given to close approximation

$$a_{K,K-1} = -1$$

$$a_{K,K} = 1 \tag{3.70}$$

$$b_K = 0 \tag{3.71}$$

The equation for ϵ is discretised as

$$\epsilon^{n+1}_{k+\frac{1}{2}} = \epsilon^{n}_{k+\frac{1}{2}} + \delta t \left(c_{1\epsilon} \frac{\epsilon^{n+1}_{k+\frac{1}{2}}}{k^n_{k+\frac{1}{2}}} P^n_{k+\frac{1}{2}} - c_{2\epsilon} \frac{\epsilon^{n+1}_{k+\frac{1}{2}} \epsilon^n_{k+\frac{1}{2}}}{k^n_{k+\frac{1}{2}}} \right) + \delta t \frac{d\sigma'}{d\sigma}_{k+\frac{1}{2}} \frac{\frac{\nu^n_{k+1}}{\sigma_\epsilon} \frac{d\sigma'}{d\sigma}_{k+1} (\epsilon^{n+1}_{k+1\frac{1}{2}} - \epsilon^{n+1}_{k+\frac{1}{2}}) - \frac{\nu^n_k}{\sigma_\epsilon} \frac{d\sigma'}{d\sigma}_{k} (\epsilon^{n+1}_{k+\frac{1}{2}} - \epsilon^{n+1}_{k-\frac{1}{2}})}{(\delta\sigma' h)^2} \tag{3.72}$$

For ϵ with $m = 1$ we require from equation (2.38)

$$a_{1,1} = 1$$

$$a_{1,2} = 0 \tag{3.73}$$

$$b_1 = \frac{U^3_\tau}{\kappa h \sigma_{1\frac{1}{2}}} \tag{3.74}$$

for $m = 2, \ldots, K-1$, corresponding to $k = 2\frac{1}{2}, \ldots, K - \frac{1}{2}$,

$$a_{m,m-1} = -\delta t \frac{\frac{\nu^n_k}{\sigma_\epsilon} \frac{d\sigma'}{d\sigma}_{k} \frac{d\sigma'}{d\sigma}_{k+\frac{1}{2}}}{(h\,\delta\sigma')^2}$$

$$a_{m,m} = 1 + \delta t \frac{\frac{\nu^n_k}{\sigma_\epsilon} \frac{d\sigma'}{d\sigma}_{k} \frac{d\sigma'}{d\sigma}_{k+\frac{1}{2}}}{(h\,\delta\sigma')^2} + \delta t \frac{\frac{\nu^n_{k+1}}{\sigma_\epsilon} \frac{d\sigma'}{d\sigma}_{k+1} \frac{d\sigma'}{d\sigma}_{k+\frac{1}{2}}}{(h\,\delta\sigma')^2} - \delta t \left(c_{1\epsilon} \frac{P^n_{k+\frac{1}{2}}}{k^n_{k+\frac{1}{2}}} - c_{2\epsilon} \frac{\epsilon^n_{k+\frac{1}{2}}}{k^n_{k+\frac{1}{2}}} \right)$$

$$a_{m,m+1} = -\delta t \frac{\frac{\nu^n_{k+1}}{\sigma_\epsilon} \frac{d\sigma'}{d\sigma}_{k+1} \frac{d\sigma'}{d\sigma}_{k+\frac{1}{2}}}{(h\,\delta\sigma')^2}$$

$$b_m = \epsilon^n_{k+\frac{1}{2}} \tag{3.75}$$

For $m = K$ the following equations are imposed

$$a_{K,K-1} = 0$$

$$a_{K,K} = 1 \tag{3.76}$$

$$b_K = \frac{(k_{K+\frac{1}{2}} \sqrt{c_\mu})^{\frac{3}{2}}}{0.07 \kappa h} \tag{3.77}$$

3.2.4 Sensitivity Tests

Sensitivity tests were also carried out by the author for the SW1DV code, as in Section 3.1.4 for the TRANSIT code, to determine whether the results are independent of the numerical parameters. The tests are applied to both models for two experimental cases, JSF13 and UMTF. These experimental cases are described in Chapter 5. The JSF13 case uses the driving pressure gradient code, and the UMTF case uses the bulk velocity version. The tests are applied to the following numerical parameters:

1. Number of vertical grid nodes, iz
2. Position of the near-bed node, $z^+_{1\max}$
3. Total depth, h
4. Number of time steps per cycle, $ntper$
5. Total number of cycles, cyc
6. Constant for parabolic mesh spacing, dm

Again the standard values are assessed by applying more stringent and lenient tests, and the error is determined by the percentage change in the value of wave friction factor, f_w. Tables 14-19 give the results of the tests for the SW1DV code.

Discussion

Table 14 shows the results of the sensitivity tests on the number of vertical grid nodes. Large percentage changes ($5\% - 9\%$) in f_w are found for the UMTF case. Only 10 vertical cells are used as the standard number. The total number of vertical nodes should be increased in this case, however this number is restricted by the values of $z^+_{\max}$ and z_1/k_s. In order to keep the values of $z^+_{\max}$ and z_1/k_s within the ranges given in equations (2.15) and (5.17) the standard values of iz must be retained. The effect of altering the position of the near-bed grid node, $z^+_{1\max}$ from approximately

30 to 100 is shown in Table 15. This could only be achieved by altering the number of grid nodes. There is negligible effect for the JSF13 case, however large percentage changes were again found for the UMTF case.

The percentage change is negligible or within $\pm 1\%$ for the number of time steps per cycle (Table 17), the total number of cycles (Table 18) and the constant for parabolic mesh spacing (Table 19). The only exception is in Table 18 for the JSF13 case applying the k-ϵ model, for which halving the number of cycles gives a 2.19% change in f_w. Since the more stringent test gives satisfactory results the standard value is taken to be acceptable. For the total depth (Table 16), only the JSF13 case was tested since the depth must be kept constant for the UMTF case. Here decreasing the depth had a greater effect but since the largest percentage change was 1.25% this was deemed to be reasonable.

Chapter 4

Results I: Smooth Channel and Pipe Flow

Steady channel flow and unsteady pipe flow over smooth walls is examined in this chapter. The results of the Launder and Sharma k-ϵ model (Section 2.3.4), the Cotton and Ismael k-ϵ-S model (Section 2.3.5), and the Launder and Shima RSTM model (Section 2.3.6) are compared with the DNS data of Kim *et al* (1987) and Kim (1990) for steady channel flow in Section 4.1. In Section 4.2 the results of the same turbulence models are compared with periodic pipe flow experimental data of Finnicum and Hanratty (1988) and Tu and Ramaprian (1983) and Ramaprian and Tu (1983). Throughout this chapter the 'k-ϵ' model refers to the Launder and Sharma k-ϵ model.

4.1 Steady Channel Flow

Steady, spatially fully-developed, turbulent channel or pipe flow is characterised by the Reynolds number, which is based upon the bulk velocity and channel width or pipe diameter in this case, and thus given by

$$Re_b = \frac{\rho U_b D}{\mu} \tag{4.1}$$

The fluid properties were set to the standard temperature and pressure values for air for all steady flow calculations, as given below

- density, $\rho = 1.225$ kg/m^3
- kinematic viscosity, $\nu = 1.461 \times 10^{-5}$ m/s
- dynamic viscosity, $\mu = 1.790 \times 10^{-5}$ kg/ms
- Also, full channel width, or pipe diameter = 0.1 m

The value of the bulk velocity, U_b therefore depends upon the corresponding Reynolds number, Re_b. The solutions are marched in time from approximate initial profiles until steady conditions are obtained. Details of the numerical calculations performed are described by Guy (2000).

4.1.1 Comparisons with DNS Channel Flow Data of Kim *et al*

The study of two-dimensional fully-developed channel flow by Kim *et al* (1987) and further study by Kim (1990) produced DNS data sets. Direct Numerical Simulation (DNS) applies the complete Navier Stokes equations to the flow problem. The present channel flow results are compared against the DNS data, and thus the performance of the k-ϵ and k-ϵ-S models in channel flow may be assessed.

The DNS data produced by Kim *et al* numerically modelled turbulent channel flow for the Reynolds number calculated at approximately 5600. The value of Re_t at the centre-line was defined to be 180 ($Re_t = U_\tau D/\nu$). Kim (1990) later used the same procedure to produce DNS results for channel flow with $Re_t = 395$ at the centre-line, giving a higher bulk Reynolds number, $Re_b = 13750$. The DNS data for the mean velocity, Reynolds stresses (thus giving the kinetic energy), and dissipation rates are available for both cases. Using the data given, other parameters such as turbulent time scales, and turbulent Reynolds number can then be calculated, giving further

opportunity for comparison and analysis of the turbulence models under consideration.

For both Reynolds numbers the k-ϵ-S model calculated Re_t to be in better agreement with the DNS value than the k-ϵ model. For the lower Reynolds number the DNS value of Re_t is defined to be 180, compared to 173 (-4%) for the k-ϵ-S model and 168 (-7%) for the k-ϵ model. In the higher Reynolds number case, for which 395 is the DNS data value of Re_t at the centre-line, the k-ϵ-S model gives 386 (-2%) and the k-ϵ model gives 370 (-6%). In a related measure of accuracy the k-ϵ-S model also gives a closer value than the k-ϵ model for the friction coefficient compared to the DNS data, which is defined for steady fully-developed turbulent flow as

$$c_f = \frac{\tau_b}{\frac{1}{2}\rho U_b^2} \tag{4.2}$$

c_f is calculated as 8.18×10^{-3} (DNS) compared to $7.66 \times 10^{-3}(-6\%)$ and $7.17 \times 10^{-3}(-12\%)$ for the k-ϵ-S and k-ϵ models, respectively. This is in good agreement with Dean's correlation of $c_f = 0.073 Re_m^{-0.25} = 8.44 \times 10^{-3}$ (Kim *et al* 1987), where Re_m is the Reynolds number base on the mean bulk velocity.

Mean Velocity Profiles

Figure 6 gives the mean velocity profiles U^+ against z^+ on semi-logarithmic axes (the velocity is normalised by wall co-ordinates $U^+ = U/U_\tau$) for the DATA (DNS results), KES (the k-ϵ-S model) and KE (the k-ϵ model) for (a) $Re_b = 5600$ and (b) $Re_b = 13750$. For the higher Reynolds number, the DNS data follows the logarithmic law (Kim 1990) for the region from $z^+ \approx 30$ to $z^+ \approx 200$, given by

$$U^+ = 2.39 \ln z^+ + 5.45 = 5.5 \log_{10} z^+ + 5.45 \tag{4.3}$$

However, DNS data for the lower Reynolds number case was quoted to follow an alternative logarithmic curve (Kim *et al* 1987) from $z^+ \approx 30$ to $z^+ \approx 150$, given by,

$$U^+ = 2.5 \ln z^+ + 5.5 = 5.8 \log_{10} z^+ + 5.5 \tag{4.4}$$

For both higher and lower Reynolds number cases the DNS data and the two models are in very close agreement in the viscous sublayer region ($z^+ < 5$). However, as z^+ increases, both the models over-predict the mean velocity, with the k-ϵ-S model in closer agreement with the data than the k-ϵ model, particularly for the higher Reynolds number case. Furthermore, the k-ϵ-S model then tends to be in reasonable agreement with the data towards the centre-line, for which the k-ϵ model is slightly high.

Reynolds Shear Stress Profiles

In the Reynolds shear stress profiles, Figure 7, the k-ϵ-S model is in good agreement with the data for low values of z^+, until the maxima at $z^+ \approx 30$. However, the k-ϵ model gives rather low values of the Reynolds stress compared to the data in the region for $z^+ \lesssim 10$. The k-ϵ model maxima are at lower values than the DNS data for both plots. The k-ϵ-S model continues to give good agreement with the data, although the values are slightly low towards the centre-line for the lower Reynolds number case. The k-ϵ model results are markedly lower than the data and the k-ϵ-S model for the main region of the channel.

Turbulent Kinetic Energy Profiles

Again the k-ϵ-S model gives good results for the turbulent kinetic energy compared with the data, Figure 8. The k-ϵ model calculates the near-wall peak significantly below the data, whereas the k-ϵ-S model is in good agreement for $Re_b = 13750$, and slightly high for $Re_b = 5600$ in the region $z^+ \gtrsim 30$. As k^+ decreases to zero at the wall, the k-ϵ-S model is in better agreement with the data than the k-ϵ model. As k^+ decreases towards the centre-line both models are in close agreement with each other and in fairly close agreement with the data, each slightly high for $Re = 5600$, and slightly low for $Re = 13750$. It should be noted that the k-ϵ-S model was tuned against the channel flow DNS data for k^+ (and other quantities).

Turbulent Dissipation Rate Profiles

The profiles of ϵ^+ against z^+ are shown in Figure 9 for both Reynolds numbers. In the region of the channel for $z^+ \gtrsim 20$ ϵ^+ varies inversely with z^+, and both models capture this well at $z^+ \gtrsim 50$. Both models give incorrectly high values of the dissipation rate in the region $7 \gtrsim z^+ \gtrsim 17$, the k-ϵ-S model doing better than the k-ϵ model. The k-ϵ-S model also captures the plateau in this region whilst the k-ϵ model merely predicts a maximum. However both models give vastly incorrect predictions of ϵ^+ in the viscous sublayer, ϵ^+ drops at $z^+ = 0$, whereas the data gives increasing values of ϵ^+ towards the wall, with $\epsilon^+ \approx 0.17$ and 0.22 at the wall for the respective lower and higher values of Reynolds number.

Damping Function Profiles

Figures 10 and 11 show the variation of the damping function for the two models. Figure 10 gives the composite damping functions for both models, whilst Figure 11 shows the constituent parts of the k-ϵ-S damping function. The damping for the k-ϵ-S model has a high value of approximately 0.9 at the wall, which then drops sharply to 0.05 at $z^+ \approx 5$. In contrast, the k-ϵ model has a very low value of damping (≈ 0.02) in the viscous sublayer region. The damping predicted by the k-ϵ model reaches a plateau in the region $z^+ \gtrsim 80$, at about 0.8 and 0.9 for the lower and higher Reynolds numbers respectively. The k-ϵ-S model gives far higher values of damping than the k-ϵ model for $z^+ \gtrsim 60$. At $z^+ \approx 180$ the values of the composite damping function for $Re_b = 5600$ and $Re_b = 13750$ are about 1.25 and 1.1, respectively. Thus, for the region $z^+ \gtrsim 60$, the general trend is that the composite damping function for the k-ϵ model *increases* with higher Reynolds number, whereas for the k-ϵ-S model, the damping function *decreases* with increasing Reynolds number. This trend is also observed by Cotton and Ismael (1998) who conclude that if $f = f_\mu(Re_t)$ is an increasing function, then the damping function at a given value of z^+ also increases with Re_b. Figure 11 shows the separate and composite damping functions of the k-ϵ-S model ($f_S(S)$ and $f_\mu(Re_t)$). The damping due to Re_t is unity throughout the

main region, and has only little effect for $z^+ \lesssim 15$ dropping to ≈ 0.7 at the wall. The damping due to the strain parameter, $f_S(S)$ is very similar to that of the composite damping function.

Strain Parameter Profiles

Profiles of the strain parameter, S are shown in Figure 12. The strain parameter is zero at the wall rising rapidly in the sublayer region to a value of 280 for $Re_b = 5600$ and 260 for $Re_b = 13750$ at $z^+ \approx 10$. S then drops again rapidly to a value of approximately 20 at $z^+ \approx 60$ and then decays towards zero at the centre-line due to the symmetry condition giving zero gradient at the centreline.

Turbulent Time Scale Profiles

It is of interest to consider other parameters, such as k^+/ϵ^+, a turbulent time scale:

$$\frac{k^+}{\epsilon^+} = \frac{k/U_\tau^2}{\epsilon\,\nu/U_\tau^4} = \frac{k/\epsilon}{(\nu/U_\tau^2)} \tag{4.5}$$

In Figure 13 the models and data show similar trends, an almost linear increase from zero up to $z^+ \approx 120$ for the lower Reynolds number and up to $z^+ \approx 250$ for the higher Reynolds number. The k-ϵ-S model follows the data trend in the viscous sublayer region, increasing more rapidly than the k-ϵ model. This is understandable since the k^+ profile of the k-ϵ-S model gives higher values in this region.

Turbulent Reynolds Number Profiles

The turbulent Reynolds number, $Re_t = k^2/\nu\epsilon = (k^+)^2/\epsilon^+$ is of interest since both models have damping functions dependent upon this parameter. In Figure 14 neither model follows the trend of the DNS data which differs greatly for each Reynolds number. However, the k-ϵ-S model is in general agreement with the data in the region $z^+ \lesssim 100$ for the higher Reynolds number.

Anisotropic Shear Stress Profiles

The anisotropic shear stress, $a_{uv} =< uw > /k$, Figure 15 of the models are in general agreement with the data. However, near the wall the k-ϵ-S model gives a peak of 0.2 instead of dropping to zero at the wall. This could be due to the variation of $f_S(S)$ near the wall seen earlier.

4.2 Unsteady Pipe Flow

Fully-developed pulsating pipe flow depends upon the mean bulk Reynolds number, $\overline{Re_b}$, which can be expressed as

$$\overline{Re_b} = \frac{\rho \overline{U_b} D}{\mu} \tag{4.6}$$

The harmonically pulsating bulk velocity characterises the periodic pipe flow for all the numerical calculations. The bulk velocity, U_b is given by

$$U_b = \overline{U_b} + |U_b| \cos\theta \tag{4.7}$$

where

$$\theta = \omega t \tag{4.8}$$

Thus the bulk velocity varies as a harmonic function with time, with frequency ω, about a mean level $\overline{U_b}$ and with amplitude $|U_b|$. The Strouhal number and relative amplitude, γ are also parameters of unsteady turbulent flow

$$\text{Strouhal number} = \frac{\omega D}{\overline{U_b}} \tag{4.9}$$

$$\gamma = \frac{|U_b|}{\overline{U_b}} \tag{4.10}$$

4.2.1 Wall Shear Stress in Unsteady Flows

In their study of imposed sinusoidal oscillations on turbulent flow in a pipe, Finnicum and Hanratty (1988) used a dimensionless frequency parameter, ω^+ against which

to compare the response of the amplitude and phase of the wall shear stress. This non-dimensional frequency parameter is defined as

$$\omega^+ = \frac{\omega\nu}{\overline{U_\tau^2}} \tag{4.11}$$

where

$$\overline{U_\tau^2} = \frac{\overline{\tau_b}}{\rho} \tag{4.12}$$

The non-dimensional relative amplitude, γ^+ is generally defined as

$$\gamma^+ = \frac{|U_b|}{\overline{U_\tau}} \tag{4.13}$$

However, in the case of Finnicum and Hanratty, it is defined in terms of the centre-line velocity, $|U_c|$ (presumably for simplicity in experimentation) as

$$\gamma^+ = \frac{|U_c|}{\overline{U_\tau}} \tag{4.14}$$

Following the work of Ismael (1993a), for high frequencies (originally in Mao and Hanratty 1986)

$$\frac{|\tau_b|}{\gamma^+\rho\overline{U_\tau^2}} = \sqrt{\omega^+} \tag{4.15}$$

where γ^+ is defined by equation (4.13), and a 'quasi-laminar' collapse of data is theoretically obtained when this term $|\tau_b|/(\gamma^+\rho U_\tau^2)$ is plotted against ω^+. For low frequencies, quasi-steady oscillation is given as (Ismael 1993a)

$$\frac{|\tau_b|}{\gamma^+\rho\overline{U_\tau^2}} = (2+m)\sqrt{\frac{A}{2}}\overline{Re_b}^{\frac{m}{2}} \tag{4.16}$$

where A and m are real numbers, for example in the Blasius equation $A = 0.079$ and $m = -0.25$.

4.2.2 Friction Coefficient in Unsteady Flow

Following the work of Ismael and Cotton (1996) and an internal note by Cotton (1997a) asymptotes of the amplitude and phase of the friction coefficient in unsteady flows can be derived for high and low frequencies. The mean Reynolds number, $\overline{Re_b}$, Strouhal number, and relative amplitude, γ are defined as in equations (4.6), (4.9)

and (4.10) respectively. In this approach it is assumed that the derivation of c_f from a steady value at $\overline{Re_b}$ responds linearly to oscillation of the bulk velocity about its mean value

$$c_f = c_f(\overline{Re_b}) + \Delta \tag{4.17}$$

where

$$\Delta = A_0 + A_1 U_b + A_2 \frac{\partial U_b}{\partial t} + \ldots \tag{4.18}$$

$$\overline{\Delta} = A_0 \tag{4.19}$$

Therefore

$$\overline{c_f} = c_f(\overline{Re_b}) + A_0 \tag{4.20}$$

As $\gamma \to 0, U_b \to \overline{U_b}$, thus $A_0 \to 0$

$$\overline{c_f} = c_f(\overline{Re_b}) \tag{4.21}$$

Δ is a pure harmonic

$$c_f = \overline{c_f} + |c_f|\cos(\omega t + \phi) \tag{4.22}$$

With $A_0 = 0$, the amplitude of the friction coefficient, $|c_f|$ varies linearly with γ, and the phase of the c_f, ϕ_{c_f} is independent of γ. It follows that

$$\overline{c_f} = f_1(\overline{Re_b}) \tag{4.23}$$

$$\frac{|c_f|}{\gamma} = f_2(\overline{Re_b}, \frac{\omega D}{\overline{U_b}}) \tag{4.24}$$

$$\phi_{c_f} = f_3(\overline{Re_b}, \frac{\omega D}{\overline{U_b}}) \tag{4.25}$$

Analysing the high frequency response, and making certain assumptions detailed by Cotton (1997a) there results the following expression for the amplitude of the friction coefficient,

$$|c_f| = 2\gamma\overline{c_f}\left(1 - 2\sqrt{\frac{\omega\nu}{2\overline{U_b}^2\overline{c_f}^2}} + \frac{\omega\nu}{\overline{U_b}^2\overline{c_f}^2}\right)^{\frac{1}{2}} \tag{4.26}$$

where $c_f(\theta) = \tau(\theta)/\frac{1}{2}\rho(U(\theta))^2$. $|c_f|$ is required in terms of $\overline{c_f}, \omega^+$ and γ. Since,

$$\omega^+ = \frac{\omega\nu}{\overline{U_\tau}^2} \tag{4.27}$$

$$\overline{U_\tau}^2 = \frac{\overline{\tau_b}}{\rho} = \frac{1}{2}\overline{U_b}^2\overline{c_f} \tag{4.28}$$

Therefore

$$\frac{\omega\nu}{\overline{U_b}^2\overline{c_f}^2} = \frac{\omega\nu}{2\overline{U_\tau}^2\overline{c_f}} = \frac{\omega^+}{2\overline{c_f}} \tag{4.29}$$

Substituting equation (4.29) into equation (4.26) gives

$$|c_f| = 2\gamma\overline{c_f}\left(1 - \sqrt{2}\left(\frac{\omega^+}{2\overline{c_f}}\right)^{\frac{1}{2}} + \frac{\omega^+}{2\overline{c_f}}\right)^{\frac{1}{2}} \tag{4.30}$$

Rearranging equation (4.30) gives

$$\frac{|c_f|}{\gamma\overline{c_f}} = 2\left(1 - \sqrt{2}\left(\frac{\omega^+}{2\overline{c_f}}\right)^{\frac{1}{2}} + \frac{\omega^+}{2\overline{c_f}}\right)^{\frac{1}{2}} \tag{4.31}$$

Thus the amplitude of the friction coefficient, normalised by the relative amplitude and the time mean of the friction coefficient, can be plotted against the frequency parameter, $\omega^+/2\overline{c_f}$.

Similarly the following expression for the phase of the friction coefficient was obtained

$$\phi_{c_f} = \tan^{-1}\frac{\sqrt{\frac{\omega\nu}{2\overline{U_b}^2\overline{c_f}^2}}}{-1 + \sqrt{\frac{\omega\nu}{2\overline{U_b}^2\overline{c_f}^2}}} \tag{4.32}$$

Substituting expression (4.29) into this equation gives

$$\phi_{c_f} = \tan^{-1}\frac{\sqrt{\frac{1}{2}\frac{\omega^+}{2\overline{c_f}}}}{-1 + \sqrt{\frac{1}{2}\frac{\omega^+}{2\overline{c_f}}}} \tag{4.33}$$

4.2.3 Comparisons with Experimental Data of Finnicum and Hanratty

Finnicum and Hanratty (1988) obtained experimental data for periodic pipe flow using water as the working fluid. In the present simulation the following property values are used (Finnicum and Hanratty 1988):

- density, $\rho = 988.45$ kg/m^3
- kinematic viscosity, $\nu = 8.66 \times 10^{-7}$ m^2/s

- dynamic viscosity, $\mu = 8.56 \times 10^{-4}$ kg/ms
- and pipe diameter, D = 0.0508 m

23 sets of data were obtained within the ranges $8650 \leq \overline{Re}_b \leq 44900$ and 0.2 Hz $\leq f \leq 1.5$ Hz corresponding to a possible Strouhal number range of $0.07 < \omega D/\overline{U}_b < 2.8$. The input data for each experimental run is shown in Table 20, that is the long-time-mean bulk Reynolds number, the frequency, and the long-time-mean bulk velocity. The values of the non-dimensional frequency parameter, $\omega^+ = (\omega\nu/\overline{U_\tau^2})$ are also given. It should be noted that the values of ω^+ for the experimental data will differ from those of the turbulence models, as shown in Table 20 which gives the values of ω^+ for all solutions. In the experiments a fixed relative amplitude of centre-line velocity oscillation of 10% was used, whereas in the numerical calculations a constant fractional amplitude of bulk velocity equal to 20% was used. This difference in conditions is not considered to have any significant effect since the normalisation of the data reduces the dependence upon amplitude (Ismael and Cotton 1996).

Amplitude of the Wall Shear Stress

Figure 16 shows a log-log plot of the dimensionless wall shear stress amplitude against the dimensionless frequency parameter, ω^+ for the experimental data of Finnicum and Hanratty given in Table 20, and for the corresponding numerical solutions of the k-ϵ-S, k-ϵ and RSTM turbulence models. The dotted line is the quasi-laminar solution, equation (4.15), for high frequencies. It can be seen that all the model solutions and the experimental data are in good agreement for $\omega^+ \gtrsim 0.05$. All the solutions collapse on the quasi-laminar asymptote. At lower frequencies ($0.008 \lesssim \omega^+ \lesssim 0.03$) all models, with the possible exception of the k-ϵ model, give higher values of wall shear stress than the data, with the k-ϵ-S model doing better than the RSTM. The range from $\omega^+ \approx 0.007$ to $\omega^+ \approx 0.02$ is of particular interest. This range of frequencies give the solutions to cases 9 – 12 in Table 20. The data indicate a dip in this region that is not wholly captured by any of the models. The

explanation for this is uncertain. At $\omega^+ \approx 0.007$ (case 9) the data give an amplitude of approximately 0.084, which the RSTM captures. The corresponding values of the k-ϵ-S and k-ϵ models are much lower (≈ 0.007). However, in the next two cases the data jumps to a lower value of amplitude (≈ 0.007), before increasing again to approximately 0.1 in case 12. None of the turbulence models follow this pattern. The k-ϵ model captures the low values in cases 10 and 11 best. The other two models, and particularly the RSTM, give much higher values compared to the data. In fact in this region the amplitude of the wall shear stress for both the k-ϵ-S and RSTM models increases roughly as a straight line on log-log axes with respect to the frequency parameter. At low frequencies, the distribution varies, with the data tending to higher values of amplitude (≈ 0.09) than the model solutions (≈ 0.07). All solutions settle to fairly constant but differing values of amplitude of the wall shear stress. It should be noted that the solutions in this range of low frequency ($\omega^+ \lesssim 0.006$) are weakly Reynolds number dependent, equation (4.16).

The data, k-ϵ-S and RSTM models do tend to give the same value of ω^+ for each case, whilst the k-ϵ value of the frequency parameter is slightly higher for each case. This is thought to be due to the normalisation of the frequency parameter, since the value of U_τ, for the k-ϵ model (and hence the wall shear stress τ_b) is approximately 10% lower than that of the data and the other models.

The numerical order (cf. Table 20) and the order corresponding to increasing ω^+ are the same for the wall shear stress amplitude and phase for all the solutions. The order for the experimental data and for each turbulence model was plotted, but for brevity the plots are not included in this study.

Phase of Wall Shear Stress

Figure 17 shows a plot of the wall shear stress phase with respect to negative pressure gradient, $(-dp/dx)$, against the dimensionless frequency parameter for the experimental data and each turbulence model. There is a general collapse of the

experimental and numerical results on the quasi-laminar asymptote (high frequency response) at $\phi_\tau - \phi_{-\frac{\partial p}{\partial x}} \approx -45^o$ (Ismael 1993a). The collapse is not as pronounced as for the amplitude. The phase angles calculated by the RSTM are in very good agreement with the data throughout the frequency range. The predicted phase angles of the k-ϵ-S and k-ϵ models overshoot at high frequencies and undershoot at low frequencies. At $\omega^+ \approx 0.02$ the overshoot of the k-ϵ model is larger, with a phase difference of approximately $+10^o$ compared to that of approximately $+5^o$ for the k-ϵ-S model. However at low frequencies ($\omega^+ \lesssim 0.003$), the reverse occurs. The k-ϵ-S model gives a larger difference in the phase angles ($\approx -10^o$), whereas the k-ϵ model gives only a slight undershoot in the quasi-steady region.

In the narrow region $0.008 \lesssim \omega^+ \lesssim 0.01$, there is a large difference in phase angle between the models and data, with the k-ϵ model giving rather good agreement, and the k-ϵ-S model the worst agreement with the data. This frequency band is discussed further, later in this section.

Further Frequency Dependent Variables

Figure 18 shows plots of the frequency dependent variables used above to normalise the wall shear stress amplitude for the numerical models. This is to investigate whether the observed trends in the amplitude are a result of non-dimensionalisation. Figure 18(a) shows that the amplitude of the centre-line velocity is quite similar for the two eddy-viscosity models and higher at low frequencies than the RSTM. This could in some part explain the variation of the turbulence models at low frequencies in Figure 16 (at least for RSTM compared to KES). The time-mean of the friction velocity given in (Figure 18b) shows good agreement between the RSTM and k-ϵ-S, which give higher values of $U_\tau/\overline{U_b}$ than the k-ϵ model. Figure 18(c) shows the amplitude of the wall shear stress normalised by the relative amplitude, the density, and the square of the bulk velocity. In this plot the turbulence models are in very good agreement in the quasi-steady region.

Similarly, Figure 19 gives the frequency dependent variables used above to present the wall shear stress phase. Figure 19(a) shows fairly good agreement between the numerical models for the phase of the pressure gradient relative to the phase of the bulk velocity. However, there is more variation between the models for the phase of the wall shear stress relative to the phase of the bulk velocity. The overshoots and undershoots are more clear, and the trends described between the models for Figure 17 are similar here. Thus these effects are not due to the normalisation.

Amplitude and Phase of the Friction Coefficient

The amplitude and phase of the friction coefficient in the form described in Section 4.2.2 are shown for the turbulence models in Figure 20. The analytical functions described in equations (4.31) and (4.33) for high frequencies and the aymptotes are also plotted. Due to the normalisation of the wall shear stress data, and lack of experimental data for the normalisation parameters, experimental data for the friction coefficient could not be calculated. In Figure 20(a) the amplitude of the friction coefficient for all the numerical models is in very good agreement with the analytical function at frequencies of $\omega^+/2\overline{c_f} \gtrsim 1$ (equivalent to $\omega^+ \approx 0.02$). The numerical models are also in fairly good agreement with the function for the phase of the friction coefficient (Figure 20(b)) at $\omega^+/2\overline{c_f} \gtrsim 2$, with the possible exception of the k-ϵ model. At lower frequencies the model solutions are in less good agreement with each other. In Figure 20(a) the k-ϵ model tends to give the lowest amplitude, and the k-ϵ-S model the highest. Most significantly, no dip is found in the amplitude of the friction coefficient in cases 9 – 12, for $0.6 \lesssim \omega^+/2\overline{c_f} \lesssim 1$. This is related to c_f using $U_b(\theta)$ in the denominator. For the phase of the friction coefficient in Figure 20(b) the RSTM lags the k-ϵ-S model by approximately 10^o and the k-ϵ model by approximately 20^o at low frequencies. This is the inverse of the trend found for the phase of the wall shear stress. For the phase of the friction coefficient mainly the RSTM, but also the other two turbulence models, follow the trend of the analytical function, with a constant difference in the phase angle.

Figure 21 shows the amplitude and phase of the friction coefficient, as in Figure 20, but here extra calculations for each turbulence model at low values of $\omega^+/2\overline{c_f}$ are shown. This is to ascertain whether the calculations at low frequencies tend towards a quasi-steady asymptote. The amplitude of the friction coefficient is in good agreement with the low frequency analysis, and the phase results are slightly high.

Cyclic Variation of the Wall Shear Stress and Friction Coefficient for Cases 9 – 12

Figures 22 – 25 give the cyclic variation of the wall shear stress and local friction coefficient for cases 9 – 12 of the Finnicum and Hanratty experiments (see Table 20). This is to investigate the behaviour of the dip found in the amplitude of the wall shear stress in these cases. For all solutions, the values of ω^+ for these cases can be seen in Table 20. The amplitude of the wall shear stress roughly corresponds to the difference between the maximum and minimum value of $|\tau_b|/(\rho\overline{U_b}^2)$ for each model. In Figure 22(a) (case 9, for experimental data $\omega^+ = 0.0075$), the wall shear stress amplitude of the RSTM ($\approx 2.0 \times 10^{-3}$ peak-to-peak) is significantly greater than that of the k-ϵ-S model ($\approx 1.6 \times 10^{-3}$). The k-ϵ model amplitude (1.5×10^{-3}) is similar to that of the k-ϵ-S model. It can be seen in Figures 23(a) to 25(a) that as the frequency increases ($0.009 \lesssim \omega^+ \lesssim 0.02$), the amplitude of the k-ϵ-S model and RSTM curves become closer. The k-ϵ model amplitude remains low but steadily increases with frequency. For Figure 25(a), ($\omega^+ \approx 0.0172$) the amplitudes of the k-ϵ-S and RSTM curves are nearly equal ($\approx 2.5 \times 10^{-3}$), with the k-ϵ model giving a similar but slightly lower amplitude of $\approx 2.25 \times 10^{-3}$. This trend confirms the pattern observed in Figure 16.

The cyclic variation of the friction coefficient for case 9 ($\omega^+ \approx 0.0075$) is given in Figure 22(b). The shape of the curve of the friction coefficient is similar to the inverse of that for the wall shear stress, but stretched due to the function $1/(1+\gamma\cos\omega t)^2$. Here, the amplitude of the k-ϵ-S model is clearly highest, whilst those of the other

two models are fairly similar. This is illustrated by Figure 20(a).

To summarise, for case 9 the order of the amplitude of the wall shear stress for the turbulence models from highest to lowest is
(1) RSTM, (2) k-ϵ-S, (3) k-ϵ,
whereas for the friction coefficient it is
(1) k-ϵ-S, (2) RSTM, (3) k-ϵ.
The k-ϵ-S and RSTM models have 'swapped over'. That is, the shape of the curves has been inverted, but the amplitudes of the results produced by turbulence models have not. This can be explained by the pattern of the multiplication factor necessary to convert from wall shear stress to friction coefficient. The shape is that of a cosine curve, arising from the (inverse) of the square of the bulk velocity variation.

The curves of the k-ϵ-S and RSTM models for the wall shear stress cross over. Thus, when multiplied by a cosine curve, the curves are inverted, but must still cross over, and the rank order of the solutions is maintained, resulting in the local friction coefficient curve. The k-ϵ model curve for the wall shear stress does not cross either of the other curves, and the value of the amplitude remains lower with respect to the other turbulence models.

Figure 22(a) shows that for the phase of the wall shear stress (for $\omega^+ \approx 0.075$) the order for each turbulence model from leading to lagging is
(1) k-ϵ-S, (2) RSTM, (3) k-ϵ.
The phase angles of the turbulence models become increasingly similar for run 10 and 11 (Figures 23(a) and 24(a)). However, for run 12, Figure 25(a), the RSTM clearly lags the k-ϵ-S model, which itself lags the k-ϵ model. The phase difference of the friction coefficient in Figures 22(b) to 25(b) confirms the plot of phase of the friction coefficient in Figure 20(b). This is reassuring, but it does not explain the presence of the dip in the wall shear stress amplitude for the frequency range $0.007 \lesssim \omega^+ \lesssim 0.02$.

4.2.4 Comparisons with Experimental Data of Tu and Ramaprian

Tu and Ramaprian (1983) experimented with harmonically pulsating pipe flow, similar to the experiments of Finnicum and Hanratty. Two oscillation frequencies were studied in detail by Tu and Ramaprian, 0.5 Hz and 3.6 Hz. In the present study, comparisons are made only with the lower frequency test case 0.5 Hz, for which the oscillation amplitude, $(|U_b|/\overline{U_b})$, was 0.64. The fluid used was water. The following data gives the parameters of the experiment:

- pipe diameter, $D = 0.0504$ m
- density, $\rho = 1000$ kg/m^3
- dynamic viscosity, $\mu = 9.4 \times 10^{-4}$ kg/ms
- frequency, $f = 0.5$ Hz
- time-mean bulk velocity, $\overline{U_b} = 0.911$ m/s
- amplitude of bulk velocity, $|U_b| = 0.58$ m/s

Tu and Ramaprian measured the wall shear stress and velocity, and the Reynolds shear stress data were then deduced. Figures 26 – 42 show comparisons of the experimental data of Tu and Ramaprian and the results of three computational models; the k-ϵ-S model, k-ϵ model, and RSTM. Radial profiles of the ensemble-averaged velocity and the Reynolds shear stress plotted against z/R are given for four different phase positions in a cycle of oscillation; $\theta = 6.9^o, 93.3^o$ in the decelerating period of a cycle, and $\theta = 179.9^o, 266.1^o$ in the accelerating period of a cycle. This illustrates changes in profile shape. The variation with phase position is also shown at two different radial locations, $z/R = 0.25$ and 0.9, near to the wall and the centre-line respectively. The phase shifts will be seen most clearly in these plots. The variation of the amplitude and phase of the first harmonic are also given. For details of the calculations and numerical procedures see Ismael (1993a) who compared the

data of Tu and Ramaprian with numerical results produced using the k-ϵ model. In this study the additional results of the k-ϵ-S model are presented.

Cyclic Variation of Wall Shear Stress and Friction Coefficient

Figure 26 shows the variation through a cycle of (a) wall shear stress and (b) local friction coefficient. Clearly the computational results for the wall shear stress are in quite good agreement with the data. The k-ϵ-S model has the smallest amplitude and does not predict the minimum at $\theta = 180^o$ as well as the other two models. However, it compares well with the data at phase positions $50^o \lesssim \theta \lesssim 130^o$ and $220^o \lesssim \theta \lesssim 270^o$. For the cyclic variation of the friction coefficient the differences between the results are more varied. The RSTM model compares well with the wall shear stress data across the whole cycle. The k-ϵ model predicts the maximum value much lower than the data and the k-ϵ-S model much higher. Both these models lead the data by approximately 20^o at the maximum, compared to the RSTM model which leads the data by about 5^o at this point.

Cyclic Variation of Velocity

Figure 27 shows the cyclic variation of the ensemble-averaged axial velocity ($U_z/\overline{U_b}$) for two radial positions (a) $z/R = 0.25$ and (b) $z/R = 0.9$. In both plots the models agree well with the data. Near to the wall, $z/R = 0.25$, the k-ϵ-S model is in closer agreement with the data than the RSTM. However, near to the centre-line, $z/R = 0.9$, the RSTM is, in general, in better agreement with the data than the k-ϵ-S model. The k-ϵ model closely follows the trend of the k-ϵ-S model in both plots.

Cyclic Variation of Reynolds Shear Stress

There are greater phase shifts between the data and the models results for the cyclic variation of the Reynolds shear stress, Figure 28 for (a) $z/R = 0.25$ and (b) $z/R = 0.9$. In Figure 28(a) the RTSM lags the data whilst the two eddy-viscosity

models lead the data. This trend is also apparent for (b) $z/R = 0.9$. For both radial positions the trend of the experimental data for phase positions $220^o \lesssim \theta \lesssim 300^o$ is not picked up by any of the models. Again the k-ϵ-S model follows the data trend more closely near the wall than the centreline. The RSTM is in closest agreement with the data for both radial positions.

Radial Profiles of Velocity

Figure 29 shows the radial profiles of the ensemble-averaged axial velocity for four different phase positions over a cycle, $\theta = 6.9^o, 93.3^o, 179.9^o$ and 266.1^o for (a) the k-ϵ model and (b) the k-ϵ-S model compared with the data. The variation over a cycle of the velocity data is fairly widespread. Both models are in very good agreement with the data.

Figure 30 gives another perspective of the results shown in Figure 29. Here the data and the two model solutions are shown (a) over the decelerating period of a cycle, $\theta = 6.9^o, 93.3^o$ and (b) over the accelerating period of a cycle, $\theta = 179.9^o, 266.1^o$. Again, the data and model solutions are in very close agreement.

Radial Profiles of Reynolds Shear Stress

Figure 31 shows the radial profiles of the Reynolds shear stress over a cycle for (a) the k-ϵ model and (b) the k-ϵ-S, model compared with the data. Both models follow the general trends of the experimental data for each phase position. Figure 32 shows this information more clearly. The models tend to over-predict the data in the decelerating period of a cycle, Figure 32(a), and under-predict the data in the accelerating period of a cycle, Figure 32(b). The k-ϵ model is in closer agreement with the data in the decelerating period of a cycle, whilst the k-ϵ-S model is in closer agreement with the data for the accelerating period of a cycle.

Amplitude and Phase Profiles of the Velocity

Figure 33 shows (a) the amplitude and (b) the phase profiles of the ensemble-averaged axial velocity. In Figure 33(a) the k-ϵ-S model agrees very closely with the data towards the wall, ($z/R \lesssim 0.5$), whereas towards the centre-line ($z/R \gtrsim 0.5$), the RSTM follows the data trend better than the other two models. The phase profiles also show a similar trend, with the k-ϵ-S model in best agreement with the data for $z/R \lesssim 0.5$. In this region towards the wall ($z/R \lesssim 0.5$), the RSTM predicts a leading phase, and the k-ϵ model a lagging phase with respect to the data. For $z/R \gtrsim 0.5$ the two eddy-viscosity models both lead the phase data, the RSTM lags the data.

Amplitude and Phase Profiles of the Reynolds Shear Stress

Figures 34(a) for the amplitude and 34(b) for the phase of the Reynolds shear stress show quite large differences between the data and the model solutions. All the turbulence models follow the general trends of the data across the pipe radius, but all predict higher amplitudes than the data. The RSTM is in better agreement with the data than the eddy-viscosity models. This is more evidently the case for the phase profiles. As with the phase of the ensemble-averaged axial velocity where the phase is negative, the two eddy-viscosity models tend to lead, and the RSTM lag with respect to the phase of the experimental data. This trend in phase is also observed in Figures 28(a) and (b) for the cyclic variation of Reynolds shear stress at both radial positions. (The phase differences are larger near to the centre-line, Figure 28(b).) The k-ϵ-S model in general for both the amplitude and phase plots is in slightly better agreement with the data than the k-ϵ model. However, very close to the wall the k-ϵ-S model phase profile predicts a drop of $\approx 2^o$ in phase, whilst the other two models give a small rise in phase.

Radial Profiles of Turbulent Time Scale

Figure 35 gives a normalised turbulent time scale ($\omega k/\epsilon$) over the (a) accelerating and (b) decelerating period of a cycle for the k-ϵ-S and k-ϵ models. There is a wide variation in this parameter between phase positions. Although both models follow similar trends for each phase position, there is also a difference between the models, with the k-ϵ model giving higher values of time scale than the k-ϵ-S model at each phase position for $z/R \gtrsim 0.05$.

Radial Profiles of Anisotropic Shear Stress

The anisotropic shear stress, $< u_r u_z > /k$ is shown in Figure 36 over the (a) decelerating and (b) accelerating period of a cycle. Again both models follow a similar trend for each phase position, but give a wide variation for the magnitude of the anisotropic shear stress. However, since the variation is less than that of $< u_r u_z >$ and k individually, the turbulence 'structure' is partially retained.

Strain Parameter Profiles

Figure 37 shows profiles of the strain parameter, S, over a cycle for the k-ϵ-S model. Figure 37(a) shows the parameter across the pipe radius, whilst Figure 37(b) shows the strain parameter near to the wall for $z/R \leq 0.06$. The profile of the strain parameter across the pipe radius for unsteady pipe flow is broadly similar to that for steady channel flow (Figure 12), giving a very high peak near to the wall. Closer examination near to the wall in Figure 37(b) shows great variation for each phase position across a cycle. The maximum is predicted at increasing values of z/R for increasing values of phase for $6.9^o \leq \theta \leq 266.1^o$. The value of the strain parameter is highest for $\theta = 266.1^o (S \approx 370)$ and lowest for $\theta = 179.7^o (S \approx 125)$.

Figure 38 shows the parameter $(\frac{k}{\epsilon}\frac{\partial U}{\partial z})^2$ which is comparable to the strain parameter (under 'equilibrium' conditions) for the k-ϵ-S and k-ϵ model over (a) the accelerating and (b) the decelerating period of a cycle, near to the wall ($z/R \leq 0.06$). There

is great variation between the models for this parameter. The maxima for the k-ϵ-S model tend to peak at far greater values of $(\frac{k}{\epsilon}\frac{\partial U}{\partial z})^2$ than for the k-ϵ model, ($60 \lesssim (\frac{k}{\epsilon}\frac{\partial U}{\partial z})^2 \lesssim 270$ for the k-ϵ-S model, and $30 \lesssim (\frac{k}{\epsilon}\frac{\partial U}{\partial z})^2 \lesssim 60$ for the k-ϵ model).

Damping Function Profiles

Figure 39 shows the damping function profiles near to the wall ($z/R \leq 0.06$) for the k-ϵ-S and k-ϵ models over (a) the accelerating and (b) the decelerating period of a cycle. The damping for the k-ϵ-S model at phase position 266.1^o is far greater than that at 6.9^o and 93.3^o, which in turn is greater than the damping at 179.9^o. In general the damping for the k-ϵ-S model is greater than that for the k-ϵ model, apart from at $\theta = 179.9^o$. Comparison with Figure 38 shows that for each phase position the larger the strain parameter, the greater the damping.

Amplitude and Phase of Strain Parameters

Figure 40 compares the amplitude of the strain parameter, S for the k-ϵ-S model, and $(\frac{k}{\epsilon}\frac{\partial U}{\partial z})^2$ for the k-ϵ-S and k-ϵ models, (a) across the pipe radius, and (b) near to the wall. Figure 40(b) reveals the wide variation in the region $z/R \leq 0.015$ between the two turbulence models. The highest values of amplitude for the k-ϵ-S model are $|S| \approx 150$ and $|(\frac{k}{\epsilon}\frac{\partial U}{\partial z})^2| \approx 120$, compared to $|(\frac{k}{\epsilon}\frac{\partial U}{\partial z})^2| \approx 20$ for the k-ϵ model.

Figure 41 shows the phase of the strain parameters calculated by the k-ϵ-S and k-ϵ models. The phase of S and $(\frac{k}{\epsilon}\frac{\partial U}{\partial z})^2$ for the k-ϵ-S model are in close agreement for $z/R \lesssim 0.1$, whereas the phase of $(\frac{k}{\epsilon}\frac{\partial U}{\partial z})^2$ for the k-ϵ model is quite different. However for $z/R \gtrsim 0.1$ the phase of $(\frac{k}{\epsilon}\frac{\partial U}{\partial z})^2$ for the two models are in fairly close agreement whilst the phase of S is much lower.

Numerical Accuracy

Figure 42 assesses the numerical accuracy of the k-ϵ-S and k-ϵ models, plotting the sensitivity of a) the k-ϵ-S and (b) the k-ϵ models to the numerical time steps $dt/2, dt$

and $2dt$, for the cyclic variation of the wall shear stress. Both models give excellent agreement at all time steps, infact the solutions are indistinguishable on the scale given by Figure 42. Thus the numerical accuracy is deemed to be adequate, and the effects observed are assumed to be unaffected by numerical errors.

Comparison of Model Solutions with the Steady Flow Case

Figures 43 – 46 compare the k-ϵ-S and k-ϵ models with the steady flow case. Figure 43 compares turbulence time scales of the two models. There is a wide variation across a cycle compared to the steady flow data. The anisotropic shear stress (Figure 44) also shows a very wide variation compared to the steady flow case. However, as mentioned above the 'structure' is retained. For both models the steady flow solution is very close to the solution for $\theta = 6.9^o$ for $z/R \lesssim 0.1$.

Again, in Figure 45 for the strain parameters of the k-ϵ-S model, the steady flow solution is close to the solution for $\theta = 6.9^o$ near to the wall. This trend is also observed in Figure 46 for $(\frac{k}{\epsilon}\frac{\partial U}{\partial z})^2$ for the k-ϵ model. However, this trend is not thought to be of particular significance.

Chapter 5

Results II: Smooth and Rough Bed Oscillatory Flow

5.1 Introduction

In this chapter, the data for seven individual experimental cases are compared against the calculations of the high-Reynolds-number k-l and k-ϵ models detailed in Sections 2.3.2 and 2.3.3, respectively. Two sets of field data are examined, the measurements of McLean (1983) in the Jade estuary and those of Schröder (1987) in the Elbe estuary are analysed in Sections 5.2 and 5.3. Three cases of the laboratory experiments of Jensen *et al* (1989) are examined in Section 5.4. Firstly 'JSF10' is the only smooth bed case studied in this chapter, 'JSF12' is a transitional case between rough and smooth turbulent regimes and 'JSF13' is a fully rough turbulent case. This group of the three experiments by Jensen *et al* is referred to as 'JSF'. The measurements of Lloyd *et al* (1997) at the UK Coastal Research Facility ('UKCRF') are discussed in Section 5.5. Lastly 'UMTF' denotes the data obtained by Dr. C. Chen and Dr. D. Chen at the University of Manchester tidal flume. Some results from this data set are given in Letherman *et al* (2000).

The physical parameters of all the data sets are given in Table 21. This table gives the period of oscillation T, the depth of water h, the freestream or surface velocity

U_0, the amplitude of the freestream velocity $a = U_0/(2\pi/T)$, and the roughness parameter k_s.

The Reynolds number $Re = aU_0/\nu$ for each case is also given. Experimental values of $U_{\tau,\max}$ are given for the JSF, UKCRF and UMTF cases. However for the Jade and Elbe cases the following formula is used to obtain $U_{\tau,\max}$ (Nielsen 1992, p. 25)

$$f_w = \frac{U_{\tau,\max}^2}{\frac{1}{2}U_0^2} = \exp\left[5.5\left(\frac{a}{k_s}\right)^{-0.2} - 6.3\right] \tag{5.1}$$

The following sections discuss the roughness parameter k_s, the location of the theoretical bed level and the boundary layer thickness δ, of the smooth and rough bed oscillatory flows. The experimental data sampling and the number of cycles of oscillation measured in each case are also examined. An approximation for the turbulent kinetic energy in those experimental cases which measure only two components of velocity is also considered.

In Sections 5.2 – 5.6 each experimental case is examined individually; a brief summary of the experiment is given and then the data and model results are compared. In each case, where possible, the bed shear stress, velocity, Reynolds shear stress, turbulent kinetic energy and eddy viscosity are examined. The turbulent time scale k/ϵ is also considered for the Jade and Elbe cases. An estimation of the turbulent kinetic energy is considered for the JSF and UMTF data sets. Additionally for both these cases an estimation of experimental uncertainty is made, in particular for comparison with the Reynolds shear stress and eddy viscosity. For all cases comparisons are presented for the variation through a cycle at given heights above the bed. Vertical profiles at given phase positions are also examined for the JSF, UKCRF and UMTF cases. For the Jade, Elbe and JSF cases the sensitivity of the numerical results to the 'standard' and 'variant' model constants outlined in Section 2.3.7 is discussed further in Section 5.7.

5.1.1 Roughness Parameter

A bed is considered smooth if the height or diameter of the roughness particles D_k is small compared to the thickness of the viscous sublayer (Cebeci and Smith 1974). This is the case for JSF10. For all the other experimental cases D_k is large compared to the viscous sublayer and for each case a value for k_s is given in Table 21 to indicate the roughness of the elements on the bed. The authors of the Jade, Elbe, JSF12 and JSF13 cases each calculated their own value of k_s. Following Sleath (1987) for the UKCRF and UMTF cases, k_s is taken to be $2D_k$. The parameters a/k_s, k_s/h and the dimensionless roughness parameter $k_s^+ = k_s U_{\tau,\max}/\nu$ (Table 21) give the relative roughness of each case. For surfaces covered with uniform roughness elements, the effective roughness k_s^+ is grouped into three categories:

$$\begin{aligned} \text{hydraulically smooth} \quad & k_s^+ \leq 5 \\ \text{transitional} \quad & 5 \leq k_s^+ \leq 70 \\ \text{fully rough} \quad & k_s^+ \geq 70 \end{aligned}$$

When roughness elements are so large that the viscous sublayer is small in comparison, the flow is considered to be fully rough turbulent. These cases are dependent upon the ratio a/k_s only. The transitional region has a reduced sublayer thickness and these cases may still have Reynolds number dependence, but a/k_s is also a defining parameter. The diagram in Fredsøe and Deigaard (1992, p.33) sheds some light on this matter, illustrating the dual dependence on Reynolds number and a/k_s with defined rough turbulent, smooth turbulent and transitional regions. This diagram has been reproduced in Figure 47 with some of the additional present cases also marked on. Thus the Elbe ($k_s^+ = 820$), JSF13, UKCRF and UMTF cases are fully rough turbulent, whereas JSF12 lies in the transitional rough to smooth regime.

5.1.2 Theoretical Bed Level

This leads to the question of where the theoretical bed level should be located. There is no standard method to be followed. Sleath (1987) quoted a suggestion

that the origin should be taken $0.35D_k$ below the top of the roughness element. Nezu and Nakagawa (1993) look at this problem in some detail. From a range of experimental results they conclude that the theoretical bed level should be within the range $0.15 \leq z/k_s \leq 0.3$ below the roughness height. In the two cases of Jonsson and Carlsen (1976) the theoretical bed level is taken to be $0.2D_k$ and $0.4D_k$ below the top of the roughness elements. In the present study, the theoretical bed level z is taken to be $0.2D_k$ below the top of the roughness elements, as illustrated in Figure 48.

5.1.3 Boundary Layer Thickness

For a rough bed the following formula by Fredsøe and Deigaard (1992, p.25) provides the boundary layer thickness δ:

$$\frac{\delta}{k_s} = 0.09 \left(\frac{a}{k_s}\right)^{0.82} \tag{5.2}$$

Fredsøe and Deigaard define δ as the height of the maximum velocity above the bed, illustrated in Figure 49. For the smooth bed case JSF10, the value of $\delta = 0.05$ m is given by the measurements of Jensen *et al* (1989). This is in excellent agreement with the formula $\delta/a = 0.086Re^{-0.11}$ for a smooth bed (Fredsøe and Deigaard 1992, p.29). An indication of the existence of a freestream is given by the value of δ/h or whether the boundary layer cannot physically extend beyond the surface (that is, where $\delta/h > 1$).

5.1.4 Data Sampling

The number of cycles of oscillation for which measurements were recorded, *cyc* and the sampling interval, *int* are also given in Table 21. The value of *int* for the Elbe estuary measurements is not known. Sleath (1987) stated that for $cyc > 50$ no significant improvement in the consistency of the statistics is obtained with the increase in the number of cycles sampled. Thus it can be concluded that only the JSF and UMTF cases have measurements for enough cycles of oscillation to gain

adequate mean (ensemble averaged) flow data. This is corroborated by the fact that the mean flow data for the Jade estuary ensemble averaged, over 30 half cycles, is somewhat scattered. For the Elbe estuary this problem is circumvented by using the original recorded measurements over 3 cycles and no averaging is attempted. For the UKCRF case the data is recorded over only 6 cycles. This problem is discussed in more detail in Section 5.5.

5.1.5 Formulating the Turbulent Kinetic Energy

The turbulent kinetic energy is defined as:

$$k = \frac{1}{2}\left(< u^2 > + < v^2 > + < w^2 >\right) \tag{5.3}$$

However in some cases, namely the JSF and UMTF, the spanwise component of velocity, V was not measured and thus only two components of velocity are available. A variety of approximations for turbulent kinetic energy are available in the literature. Mendoza and Shen (1990) assumed that $< v^2 >$ and $< w^2 >$ are equivalent, using the formula $k = \frac{1}{2}(< u^2 > +2 < w^2 >)$ to obtain the experimental kinetic energy. Svendsen (1987) used a modified version of this $k = \frac{1.3}{2}(< u^2 > + < w^2 >)$. Townsend (1976, p.429) suggested that the value of k was likely to be in the range $1.3k' < k < 1.5k'$ where $k' = \frac{1}{2}(< u^2 > + < w^2 >)$, and this approximation has been examined here in more detail. The relative turbulence intensities (Hinze 1975, p.641) in a boundary layer along a rough wall obtained by Corrisin and Kistler are shown in Figure 50. The turbulent kinetic energy (equation (5.3)) obtained from these values has also been plotted by the author. Figure 51 shows three approximations compared to the exact turbulent kinetic energy. The closest approximation was deemed to be that of Svendsen:

$$k = \frac{1.3}{2}\left(< u^2 > + < w^2 >\right) \tag{5.4}$$

and this formula was used to obtain the experimental kinetic energy for the JSF and UMTF cases.

5.2 Jade

McLean (1983) recorded field measurements in the Jade estuary in Germany at a site near Wilhelmshaven. McLean used orthogonally mounted mechanical current meters to obtain a record of three instantaneous velocity components. The velocity was recorded over thirty half tidal cycles of the Jade. The velocity and Reynolds shear stress (determined from the velocity measurements) is shown here in Figures 52 and 53 across half a cycle of oscillation at an elevation of 2.14 m above the bed. This corresponds to $z/h = 0.11$ and $z/\delta = 0.05$ as given in Table 21. These values indicate that the results are presented in the lower region of the boundary layer. There is considerable scatter in the data. Since no reference phase position is given only the magnitudes may be compared to the model results. For the k-l and k-ϵ model calculations, a maximum surface slope S_M of 2×10^5 was assumed (Baumert and Radach 1992).

Cyclic Variation of Flow Parameters

In Figures 52 and 53 the velocity and Reynolds shear stress model results are compared to the data. These results confirm the findings of Baumert and Radach (1992) and Sajjadi and Waywell (1998). Both models compute the velocity variation (Figure 52) accurately. The model prediction of the Reynolds shear stress is somewhat high in the accelerating quarter cycle, particularly when using the k-l model. The k-ϵ model lags the k-l model by about 5^o at the start of the cycle. This finding is repeated throughout the comparisons with other cases.

Figure 54 shows that both model variations of turbulent kinetic energy lag the velocity by about 10^o or 1240 s at the start of the cycle. At maximum flow rate the lag reduces to about 2^o (250 s). Figure 55 compares the turbulence time scales (k/ϵ) of both models. As might be expected the lags between the models are of the same order as the turbulence time scales. The time scale of the k-ϵ model peaks at 1000 s, and that for the k-l model peaks at 700 s near the start of the cycle. The time scale

reduces to about 100 s for both models at maximum flow rate.

5.3 Elbe

The second set of field data used in this study was obtained by Schröder (1987) in the Elbe estuary. Schröder used an acoustic Doppler technique to measure all three components of velocity at 1.9 m above the bed over three cycles of oscillation. This elevation corresponds to $z/h = 0.373$ and $z/\delta = 0.03$, which would indicate that the measurements were again made in the lower boundary layer near to the bed. In both the Elbe and Jade cases, the value of δ calculated using equation (5.2) is actually greater than the water depth ($h = 5.1$ m for the Elbe). The value of the maximum surface slope S_M was taken to be 5×10^{-5} (Baumert and Radach 1992).

Cyclic Variation of Flow Parameters

Figures 56 – 60 show the model results compared with Schröder's data for the velocity, turbulent kinetic energy, Reynolds shear stress, velocity gradient and turbulent eddy viscosity. Again, as observed by Baumert and Radach (1992) and Sajaddi and Waywell (1998), the agreement between the model results and data for the velocity and turbulent kinetic energy is good in general. However there is a large discrepancy between the calculations of Reynolds stress and the data. The model values are about three times the magnitude of the data at maximum flow. The models give an almost constant value of the ratio $- < uw > /k \simeq 0.3$. This constant value has also been found in other shear layer flow experiments (Rodi 1993, p.28). Thus it would appear that Schröder's values of Reynolds stress are unduly small. To the writer's knowledge there are no independent model results available to verify this, since neither Baumert and Radach nor Sajaddi and Waywell include calculations of the Reynolds stress.

The velocity gradient data in Figure 59 are scattered and, given the quality of the data, both models give reasonable agreement. However there is a large difference

between the k-ϵ and k-l model results, with maxima at 0.08 s^{-1} and 0.05 s^{-1} respectively. This leads to a similar discrepancy between the model results for the turbulent eddy viscosity ($\nu_t = - < uw > /(dU/dz)$). However the data bear little relation to the model values. Schröder calculated the data by dividing a least squares fit of the Reynolds shear stress by a least squares fit of the velocity gradient, and then taking a least squares fit of the resulting values, which could produce uncertainty in the eddy viscosity data. This is discussed further in Section 5.4. Even so, it can clearly be seen that the magnitude of the model values (the k-l model in particular) is much greater than that of the data.

A similar cyclic variation in the turbulent time scale (k/ϵ) to that Jade estuary is shown in Figure 61. Again the correspondence between the values of turbulent time scale and the phase lag between the turbulent kinetic energy and the velocity is notable. This lag can be observed more easily in Figure 62 which on one page compares the velocity, Reynolds stress, kinetic energy and turbulent time scale for half a cycle of oscillation from about 5 to 11 hours. For this case, the difference in magnitude and phase between the k-ϵ and k-l model results is much less than for the Jade.

5.4 JSF

Jensen *et al* (1989) took measurements for 11 smooth bed cases and 4 rough bed cases in a small oscillating water tunnel. Laser Doppler anemometers were used to obtain phase averaged mean flow and turbulence measurements both perpendicular to the bed and in the streamwise directions. Hot film probe measurements of the bed shear stress were also recorded. Table 21 gives the parameters of the three data sets compared here: JSF10 is the only smooth bed case, JSF12 is a transitional case from rough-to-smooth ($k_s^+ = 44$) and JSF13 is entirely rough turbulent ($k_s^+ = 84$). Apart from the difference in the bed, JSF10 has all the same physical parameters as JSF13. Comparisons between the k-ϵ and k-l model calculations and the JSF10

and JSF13 data are presented as cycle variation over half a cycle at 5 heights above the bed. The profiles against height at 12 phase positions across half a cycle from $0^o - 165^o$ at 15^o intervals are also presented for JSF10, JSF12 and JSF13.

Cyclic Variation of Friction Velocity

Figures 63 and 64 compare the bed friction velocity data and model results across one cycle of oscillation for cases JSF12 and JSF13. The k-ϵ model agreement is good in both cases. The k-l model predicts the phase well but is 15% – 20% in error in magnitude at the maximum and minimum values for both cases. In Figure 64 the k-ϵ model prediction of the minimum to be 9% lower in magnitude compared to the data. However in the first half of the cycle, for which the k-ϵ prediction is merely a translation of the results in the second half of the cycle, the agreement is good. This indicates incomplete reciprocation in the cyclic variation of the experimental data.

Profiles of Flow Parameters

Figures 65 – 67 present the velocity profiles for the JSF10, JSF12 and JSF13 cases at phase positions between 0^o and 165^o at 15^o intervals. The agreement between the data and model results is very good in all cases throughout the half cycle, and the k-ϵ model captures the data extremely well for the JSF12 case. In all cases the k-ϵ model is better than the k-l around maximum velocity for phase positions 60^o – 120^o and for $0.1 < z/h < 0.3$.

The kinetic energy profiles for all three JSF cases are presented in Figures 68 – 70. Figure 68 shows that both models under-predict the data at phase positions 0^o – 45^o and 105^o – 165^o for JSF10 for which the k-l model does better then the k-ϵ. At maximum velocity 60^o – 90^o the reverse is true, particularly for $z/h < 0.5$. Similar results are found for the JSF13 case (Figure 70) although both models (particularly the k-ϵ model) are closer to the data results than previously. However for JSF12 (Figure 69) the k-ϵ model results are very close to the data, and the k-l model tends

to over-predict these results. This, of course, is subject to the approximation for the experimental values of k from equation (5.4).

Similar trends apply to the Reynolds shear stress given in Figures 71 – 73, although in general the k-ϵ predictions are far closer to the data, especially for $z/h < 0.2$ at all phase positions.

Eddy Viscosity Data Formulation

In order to compare eddy viscosity profiles the eddy viscosity data must first be obtained. Eddy viscosity is formed by dividing the Reynolds shear stress by the velocity gradient (equation (2.21)). Thus the velocity gradient must also be obtained. Justesen (1991) used two methods to obtain eddy viscosity profiles:

1. ν_t derived from measured Reynolds stresses and smoothed velocity profiles from experimental data. Or,

2. ν_t derived from measured Reynolds stresses and velocity profiles computed using the k-ϵ model.

Here eddy viscosity profiles for all three JSF cases are derived using a form of the first method described below. The cyclic variation of eddy viscosity is also obtained at the given elevations for JSF10 and JSF13, and an uncertainty measure in the data is also calculated.

The velocity profiles are in the general shape of an exponential curve. Thus a least squares fit of the following form is applied to the velocity data profiles:

$$\left(\frac{dU}{dz}\right)_{\text{fit}} = c_1 \exp(-d_1 z) + c_2 \exp(-d_2 z) \tag{5.5}$$

where c_1, c_2, d_1 and d_2 are constants. The original measured velocity data and the least squares fit are compared in Figures 74 – 76 for JSF10, JSF12 and JSF13 at phase positions 0^o – 165^o. It can be seen that the fit is not adequate at those phase positions which have low magnitudes of velocity. The fit is poor at 0^o and 15^o. For

the JSF12 case the fit is also unreliable at 30°. The velocity gradient of the fits are shown in Figures 77 – 79 only for those phase positions at which the fit is good.

Applying equation (2.21), the negative Reynolds shear stress is divided by the velocity gradient fit to derive the eddy viscosity data profiles. Figures 80 – 82 compare the data to the k-ϵ and k-l model calculations. For $z/h > 0.2$ the eddy viscosity data is rather scattered. The eddy viscosity calculated by the k-l model continues to increase with height. This is because ν_t in the k-l model is directly dependent upon height, due to the length scale $l = \kappa z$ in the ϵ equation. The k-ϵ model predicts a much lower magnitude of ν_t for $z/h = 0.1$, but since the data are so scattered it is difficult to draw any conclusions. For the JSF13 case (Figure 82) the data are smoother around maximum velocity at ωt of 60° and 75°. This might be expected as the quality of the fit improves with increasing velocity, resulting in a satisfactory velocity gradient. Here the agreement between the k-ϵ model and the data is extremely good throughout the depth.

Cyclic Variation of Flow Parameters

The data for the cyclic variation of flow parameters is only provided for JSF10 and JSF13. No cyclic variation plots are given here for case JSF12. The five elevations at which comparisons are made for each case are given below:

- JSF10: $z/h = 0.022, 0.89, 0.27, 0.58, 0.84$
- JSF13: $z/h = 0.013, 0.04, 0.13, 0.38, 0.84$

This gives a range of heights throughout the boundary layer and an additional elevation ($z/h = 0.084$) above the boundary layer ($z/\delta = 2.4$ for JSF10 and 1.8 for JSF13).

The agreement between the data and model calculations for the velocity in Figures 83 and 84 is generally very good. A notable exception is for the smooth bed case

very close to the bed (Figure 83(a)) where there seems to be some incomplete reciprocation of the flow in the experimental data.

The data for k (equation (5.4)) in Figures 85 and 86 are rather scattered but a general trend can be easily seen. In Figure 85, when close to the bed, both models calculations lead the JSF10 data by 20°. The k-l model continues to lag the data throughout the elevations, whereas the k-ϵ model is in phase with the data in Figure 85(c). In contrast the k-l model captures the magnitude of the data much better at all elevations; the k-ϵ model under-predicts the data. For the rough bed case the k-ϵ model calculations are in much better agreement with the kinetic energy profile data in the lower boundary layer (Figure 86(a) – (c)). The k-l model over-predicts the data and k-ϵ model calculations in this region. Again in the outer boundary layer (Figures 86(d) and (e))-, the k-l model leads the data and the k-ϵ model results, but captures the magnitude of the data better than the k-ϵ model.

Uncertainty Measure for the Reynolds Shear Stress Data

The plots of Reynolds shear stress for cases JSF10 and JSF13 at 5 elevations are given in Figures 87 and 88. It is clear that there is considerable scatter in the data. To overcome this problem the following method described in Letherman (1999) and Letherman *et al* (2000) fits a continuous polynomial $\phi_{\text{poly}}(\omega t)$ to the Reynolds stress experimental data at each elevation. A root mean square uncertainty value $\pm\Delta\phi$ at each elevation is then calculated as

$$\Delta\phi = \left[\frac{1}{n}\sum_{i=1}^{n}\left(\phi_{\text{data},i} - \phi_{\text{poly},i}\right)^2\right]^{\frac{1}{2}} \tag{5.6}$$

where $i = 1, \ldots, n$ represents the discrete record of the Reynolds shear stress experimental data at a given elevation.

In Figures 87 and 88 the 'fit' is represented as a dot-dash line with vertical uncertainty bars superimposed at regular intervals. 71% of the original data points fall within the uncertainty range. In Figures 87(b) and (c) both models' results generally fall within the uncertainty range. The k-ϵ model captures the phase response of

the data fit better than the k-l model. In the outer boundary layer region (Figures 87(d) and (e)) the k-l model captures data better than the k-ϵ model, but neither come within the uncertainty range for most of the cycle of oscillation. For JSF13 in Figure 88 the k-ϵ model is definitely much closer to the data at all elevations. Close to the bed in Figure 88(a), both models overpredict the maximum and minimum points of the data. At higher elevations the k-ϵ model generally comes within the uncertainty range. The k-l model over-predicts the data and at higher elevations tends to lead the data and k-ϵ model.

The velocity gradient data is compared to model results in Figures 89 and 90. This compares the 'data', the velocity gradient obtained from the original velocity data, denoted by the solid dots, and the 'fit', that is the velocity gradient obtained from the least squares fit of equation (5.5) to the velocity data denoted by the circles. As explained above only those data points at which an adequate fit exists are shown on Figures 89 and 90, that is between 30^o and 165^o at 15^o intervals, at all 5 elevations.

For the JSF10 case in the lower boundary layer region (Figure 89(a) – (c)) both 'data' and 'fit' points are reasonably in phase with the model results. The 'fit' points under-predict both the model calculations and the 'data' points. The points are quite scattered in the upper boundary layer region (Figure 89(d) – (e)) where $z/h = 0.58$ and $z/h = 0.84$. This is also true for the JSF13 case (Figure 90). However the curves of the 'data' and 'fit' points are smoother, although they still show little agreement. Although the 'data' points are closer to the model calculations, it is the 'fit' points that are used to calculate the eddy viscosity. Applying equation (2.21) to obtain the eddy viscosity, the polynomial fit to the Reynolds shear stress data is divided by the velocity gradient fit. The uncertainty in the Reynolds shear stress fit at each elevation and each available phase position (from 30^o – 165^o at 15^o intervals) is also divided by the velocity gradient. Thus eddy viscosity data and the 'inherited' uncertainty ranges are obtained and compared to the model calculations in Figures 91 and 92 for JSF10 and JSF13 respectively. The data and uncertainty

measures in Figures 91 and 92 are rather uneven. However the k-ϵ model does seem to capture the data better in JSF10 at $z = 0.022$ m and 0.089 m (Figures 91(a) and (b)). The superiority of the k-ϵ model can be clearly seen in Figures 92(a), (b) and (c) for the JSF13 case. The phase response of the data in Figures 92(a) is definitely predicted by the k-ϵ model. As before, the k-l model tends to over-predict the magnitude of the data at higher elevations in the outer regions of the boundary layer.

5.5 UK Coastal Research Facility (UKCRF)

While only a brief description of this experiment was given in Letherman *et al* (2000); the experimental details are described more fully here. Experiments were conducted by Lloyd *et al* (1997) at the UK Coastal Research Facility in HR Wallingford, Oxfordshire. The UKCRF is a large-scale wave-current basin. A photograph of the facility is shown in Figure 93. Oscillating flows are generated in the 36 m $\times$ 19 m basin by four variable speed reversible pumps controlled by a PC. The sumps, pumps and flow straighteners provide control of the transverse velocity profile. Only the horizontal bed section of the facility is of concern here ($h = 0.48$ m). The bed was covered in 10 mm effective diameter granite chippings. The flow parameters of the experiment are detailed in Table 21. Measurements of three components of velocity were made using acoustic Doppler velocimeters and ultrasonic current meters. Figure 94 illustrates the experimental set-up.

The velocities were measured at 11 different heights from the bed between 0.004 m and 0.471 m. Samples were recorded over six complete cycles of oscillation ($T = 180$ s) at a frequency of 25 Hz (every 0.04 s). From the raw data, quantities such as mean velocities and (possibly) the turbulence quantities and Reynolds stresses may be extracted. Noise in the measurements may be due to the instruments or unwanted particles in the fluid and to errors, for example skewness in the oscillation.

Usually the mean flow quantities are extracted from the raw data by ensemble-averaging over a large number of oscillations. The six cycles of oscillation recorded here are not enough, however, to obtain a reasonable ensemble average. As mentioned above, 50 or more cycles would be recommended. Thus an alternative method is applied by the author to extract the mean velocity.

The raw velocity data ensemble-averaged over six cycles are presented at 11 depths in Figure 95. There is a great deal of noise in the data. The expected predominant frequency in the flow is the driving frequency $f = 1/180$ Hz. In order to extract the mean velocity, a Fourier transform of the raw data is taken and a cut-off filter is applied to remove the noise. This method is illustrated for the bulk velocity (integrated over the depth) which is calculated using equation (3.39). The bulk velocity derived from the measured streamwise velocity ensemble averaged over six cycles is shown in Figure 96.

Extraction of the Mean Velocity

The discrete Fourier transform of the bulk velocity is taken by applying the following equation

$$\mathrm{fft}(k) = \sum_{n=1}^{N} U(n) \exp\left[\frac{-i \times 2\pi(k-1)(n-1)}{N}\right] \quad \text{for} \quad 1 \leq k \leq N \tag{5.7}$$

where i is the complex number $\sqrt{-1}$. This equation describes a discrete Fourier transform converting the time-dependent data to frequency-dependent data. The amplitude of the velocity in the streamwise direction is calculated and plotted against frequency as illustrated in Figure 97. The predominant frequencies at $f = 0.0056$ Hz and 0.017 Hz represent the first and third harmonics. These harmonics were evident throughout the individual velocity records at different elevations. The following low-pass filter was applied to remove the noise and turbulence:

$$H(f) = \begin{cases} 1 & \text{for} \quad 0 \leq f \leq x \\ 0 & \text{for} \quad x \leq f \leq f_{\frac{1}{2}} \end{cases} \tag{5.8}$$

where x the cut-off frequency is taken to be 0.05, and $f_{\frac{1}{2}}$ is the Nyquist, or folding frequency. Thus all the amplitudes above 0.05 Hz were set to zero and the following inverse Fourier transform was calculated, given by

$$U_{\text{smooth}}(n) = \frac{1}{N}\sum_{k=1}^{N} \text{fft}(k) \exp\left[\frac{i \times 2\pi(k-1)(n-1)}{N}\right] \quad \text{for} \quad 1 \leq n \leq N \qquad (5.9)$$

The smoothed bulk velocity is shown in Figure 98 with the noise and turbulence extracted. This smoothed bulk velocity is used as input to the code to calculate the model results.

Extraction of the Turbulence Quantities

The question of distinguishing the turbulence data from noise now arises. It is hoped that the frequency spectrum of the turbulence quantities will lie inbetween that of the mean and noise. To find the frequency spectrum of the turbulence data, the turbulence time scales must be estimated. The large scale turbulence denoted T_L is obtained as k/ϵ. k can be estimated as $< u >^2$. The dissipation ϵ can be estimated from equation (2.38), $\epsilon =< u >^3 /\kappa z$, where $\kappa = 0.4$. Therefore

$$T_L = \frac{k}{\epsilon} \simeq \frac{\kappa z}{< u >} \qquad (5.10)$$

The small-scale (Kolmogorov) turbulence time scale is equivalent to

$$T_S = \left(\frac{\nu}{\epsilon}\right)^{\frac{1}{2}} \simeq \left(\frac{\nu\kappa z}{< u >^3}\right)^{\frac{1}{2}} \qquad (5.11)$$

The approximate frequency range of the turbulence can then be calculated.

The value of $< u >$ was estimated as 0.02 m/s by ensemble averaging. Taking a depth of 0.2 m for example the large-scale turbulence is given by $T_L = 0.2 \times 0.4/0.02 \simeq 4$s. This gives a frequency of roughly 0.25 Hz. For the small scale turbulence,

$$T_S = \left(\frac{10^{-6} \times 0.4 \times 0.2}{0.02^3}\right)^{\frac{1}{2}} \simeq 0.1\,\text{s} \qquad (5.12)$$

which gives a frequency of approximately 10 Hz. The Nyquist frequency 12.5 Hz is half of the sampling frequency. Thus the noise is the same order as the small-scale

turbulence. This problem could be overcome by using a larger sampling frequency. A sampling frequency ten times that of the small scale turbulence e.g. 100 Hz might be adequate.

The uncertainty of a sample can be estimated by calculating the standard deviation. Given $n = 1, \ldots, N$ discrete measurements of the velocity U, the mean of a sample at a particular phase position is given by

$$\overline{U} = \frac{1}{N} \sum_{n=1}^{N} U_n \tag{5.13}$$

The standard deviation of the sample is given by

$$\sigma = \left(\frac{1}{N} \sum_{n=1}^{N} (U_n - \overline{U})^2 \right)^{\frac{1}{2}} \tag{5.14}$$

This is equivalent to the usual method used for extracting the turbulence quantities, as used by Jensen *et al* (1989), Sleath (1987) and McLean (1983). The uncertainty of the mean of the sample is given (to a 95% confidence level) by

$$\Delta U = \pm 2 \frac{\sigma}{\sqrt{N-1}} \tag{5.15}$$

Say $\sigma = 0.02$ (estimated for the turbulence quantity $< u >$), then

$$\text{for} \quad N = 6, \qquad \Delta U \simeq \pm 0.02$$

$$\text{for} \quad N = 100, \quad \Delta U \simeq \pm 0.004$$

Thus if only six cycles are sampled then the uncertainty of the mean is of the same order as the turbulence quantities, and thus the actual turbulence values could be invalid. The more cycles of oscillation that are sampled, the less the uncertainty. If 100 cycles are sampled then the uncertainty is much less than the magnitude of the turbulence quantities and so the derived turbulence values should be more accurate.

To summarise, the UKCRF data is not adequate to extract the turbulence quantities. The reasons for this are:

- The number of cycles sampled was too low. The order of uncertainty of the mean velocity is the same as the order of magnitude of the turbulence quantities since only 6 cycles have been sampled. To obtain a statistically valid

phase average then approximately 50 cycles of oscillation should be measured.

- The sampling rate of 25 samples per second was not high enough. The small-scale turbulence is the same order as the noise. A sampling rate of 100 Hz is recommended for this experiment.

Thus only the mean velocity data is adequate. The smoothed velocity data is derived using the same method as above for the bulk velocity. The cyclic variation of the smoothed velocity data is compared to the model results at 11 heights above the bed in Figure 99. The agreement between the model calculations and the data is reasonably good at all heights. The velocity data is also presented in semi-logarithmic profile plots at phase positions 0^o – 160^o in 20^o intervals in Figure 100. Here it can be seen more clearly that the k-ϵ model captures the data better than the k-l model, particularly around the point of maximum velocity. The semi-logarithmic fits used to obtain the experimental values of the friction velocity are shown for the 100^o – 160^o phase positions.

The friction velocity through one cycle of oscillation is given in Figure 101. Both the k-ϵ and k-l model calculations lead the data by approximately 10^o. Again as for cases JSF12 and JSF13 the k-ϵ model computes the magnitude of U_τ better than the k-l model, which tends to over-predict the cycle maxima.

5.6 University of Manchester Tidal Flume (UMTF)

The UMTF is a large-scale tidal flume situated in the Simon Building of the University of Manchester. The dimensions of the flume are 11 m long × 3.3 m wide × 0.2 m deep. A schematic of the experimental set-up is shown in Figure 102. A unidirectional variable speed pump generates oscillatory current flows with a nearly sinusoidal velocity variation. The valves change the direction of the flow. Flow straighteners help to produce a uniform transverse velocity. The rough bed was

made from a uniform covering of gravel with a 5 mm diameter on a smooth bottom surface. 2-D Laser Doppler Velocimeters measure the streamwise and vertical velocity components. The experimental data was measured by Dr. C. Chen and Dr. D. Chen of the Engineering Dept., University of Manchester.

UMTF Input to the Bulk Velocity Code

The measured velocity was used as input to the bulk velocity code to give the k-ϵ and k-l model calculations of the flow. The bulk velocity derived by the author from the measured velocities using equation (3.39) is compared to the cyclic variation of U at the maximum measurement height in Figure 103. Before this can be used in the code the data must be smoothed. As with the UKCRF case, this is achieved by the author by applying a Fourier transform to the data. The amplitude of the velocity is plotted against frequency in Figure 104. A low-pass cutoff filter (equation 5.8) is applied at $f = 0.08$ Hz such that all amplitudes above 0.08 Hz are set to zero. An inverse Fourier transform is then applied and the smoothed data are compared to the original bulk velocity in Figure 105. A polynomial fit of order 11 is fitted to the smoothed data to obtain the bulk velocity at many phase positions across a cycle. This is illustrated in Figure 106.

As mentioned in Section 3.2.4 an attempt was made to use 100 vertical nodes in the model calculations. Additionally the position of the first velocity node was to satisfy the following criteria:

$$30 \leq \quad z^+_{1\max} \quad \leq 100 \tag{5.16}$$

$$0.03 \leq \quad z_1/k_s \quad \leq 0.1 \tag{5.17}$$

The first restriction was satisfied without exception. Unfortunately it was not possible to simultaneously use 100 nodes and satisfy equation (5.17). In comparison with the UMTF data only 10 velocity nodes could be used whilst maintaining z_1/k_s as low as possible.

Cyclic Variation of Friction Velocity

The cyclic variation of friction velocity is given in Figure 107. Again the experimental values are derived from a semi-logarithmic fit to the measured velocity profiles. Both models compute the magnitude of the data well, however they lead the data by approximately 20°. This is similar to the findings for the UKCRF which were processed in a similar manner, but not of Jensen *et al* (1989) for which the U_τ data and model results were in phase. For the JSF12 and JSF13 cases many more velocity points were measured in the logarithmic region, thus providing a more reliable fit. An alternative method of deriving the friction velocity is shown in Figure 108. This is same as Figure 107 with the additional estimation of square of the friction velocity, U_τ is equal to the Reynolds shear stress close to the wall where viscous stress is negligible:

$$U_\tau^2 = \frac{|\tau_b|}{\rho} = - < uw > \tag{5.18}$$

Here the shear stress is shown for the measurement point $z = 0.011$ m. The magnitude is roughly 0.66 times that of the data and model predictions, but the phase of both models lags the data by about 20°.

Profiles of Flow Parameters

The velocity profiles are shown in Figure 109 for 0° – 345° at 15° intervals. The model results are in reasonable agreement with the data but the peaks at 0.01 m $\leq z \leq$ 0.02 m are not captured for phase positions 90° – 150° and 270° – 330°. Figure 110 shows the semi-logarithmic fit to the UMTF velocity data in order to obtain the friction velocity. Figure 111 shows the turbulent kinetic energy profiles. The model predictions at about 0.01 m show an anomalous peak at 45° – 150° and 225° – 330°. This is likely to be the result of using too few vertical nodes in the model calculations. For $z > 0.01$ m the k-ϵ model predicts the data well and the k-l model tends to over-predict the data.

Again irregular peaks can be seen close to the bed in the model calculations of

Reynolds shear stress in Figure 112. Similarly the k-ϵ model predictions are closer to the data than the k-l in the upper region of the boundary layer.

In order to derive the eddy viscosity data, data processing must be carried out as described for the JSF cases in Section 5.4. Firstly the velocity gradient is derived. The velocity data profiles and least squares fits are given in Figure 113. Figure 114 then shows the gradient of the fits and the data at those phase positions for which the fit is good: namely 0^o, $75^o - 180^o$ and $240^o - 345^o$. Equation (2.21) is then applied to the Reynolds shear stress and velocity gradient fit to obtain the eddy viscosity. This is compared to the model calculations in Figure 115. Again the model calculations are unreliable close to the bed. The magnitude of ν_t predicted by the k-l model increases with height, this trend was also found with the JSF case. The k-ϵ model captures the data much better at $z > 0.02$.

Cyclic Variation of Flow Parameters

Figure 116 shows the variation of velocity over one cycle of oscillation. Eight elevations are examined from $z = 0.01$ m to 0.08 m representing $z/\delta = 0.3$ to 2.3. In all examinations of the data at $z = 0.01$ m there is some error in the data. At the other elevations the velocity data is predicted well by the model calculations in general. At higher elevations the model results under-predict the magnitude of the maximum forward and reverse velocity by about 10%. The cyclic variation of kinetic energy is shown in Figure 117, with the experimental data again represented by the approximation (5.4). In Figure 117(b) the k-l model captures the maxima but not the minima of the experimental data better than the k-ϵ model. This pattern is repeated for plots 117(c), (d) and (e). However in this lower boundary layer region the k-ϵ model predicts the data phase response better. In the outer boundary layer regions Figure 117 (f) – (h) the k-l model over-predicts and the k-ϵ model under-predicts the data.

The cyclic variation of Reynolds shear stress is given in Figure 118. A polynomial of

order 5 was fitted to the data and experimental uncertainty was estimated using the same method as before for JSF10 and JSF13 (Section 5.4). At the lower elevations $z = 0.02 - 0.05$ m the k-l model is somewhat more accurate than the k-ϵ model, which tends to calculate values of Reynolds shear stress that are too low. Again the k-l model tends to lead the data, the higher the elevation the greater the lead. The k-ϵ model is more accurate in resolving the phase response of the Reynolds shear stress. At higher elevations (Figure 118(f) – (h)) there seems to be some error in the resolution of the data. Possibly the values have become too small for the measuring instruments to record a difference between them.

Figure 119 gives the data and least squares fit of the velocity gradient compared to the model results. At higher elevations $z \geq 0.04$ the fit and data are in good agreement, and for Figure 119(c), (d) and (e) the model agreement is also reasonably good. Close to the bed (b) and near to the surface (f) – (h) the data values of the velocity gradient are much larger than the model results.

The eddy viscosity data is formed in the same manner as before (see Section 5.4) and the uncertainty from the Reynolds shear stress fit to the data is 'inherited' by ν_t. In Figure 120 the model results and the data show little agreement. Both models return greater values of the eddy viscosity than the derived data, the k-l model giving values of up to 10 times as much as the data. Towards the bed for (b) $z = 0.02$ m to (d) $z = 0.04$ m the k-ϵ model resolves the phase response of the data well. However, the accuracy of the data after much processing is uncertain.

5.7 Sensitivity to Standard and Variant Model Constants

The final section in this chapter is concerned with the sensitivity of the computations to the turbulence model constants. This has been previously discussed in Section 2.3.7. The value of c_μ in the k-l model is altered from the standard value of 0.08 for

this model, to the variant value of 0.09, usually used for the k-ϵ model. For the k-ϵ model it is σ_ϵ, the turbulent Prandtl number for diffusion that is examined. The standard value of $\sigma_\epsilon = 1.3$ is compared to the variant value $\sigma_\epsilon = 1.1$.

The flow parameter examined is the friction velocity U_τ for the Jade, Elbe, JSF12 and JSF13 cases shown in Figures 121 – 124. It can be easily seen that the difference between the results for the standard and variant model constants for the k-l model are negligible. The percentage difference between the calculations at the maximum is always less than 0.5%. This insensitivity to the value of c_μ is surprising and has been discussed in Section 2.3.7. As expected, altering the value of σ_ϵ in the k-ϵ model produces a slight difference in the results. The percentage change between the standard and variant results at $U_{\tau,\max}$ varied between 1% and 3%.

Chapter 6

Conclusions

Steady Channel and Unsteady Pipe Flow

The low-Reynolds number Launder and Sharma (1974) k-ϵ and the Cotton and Ismael (1998) k-ϵ-S turbulence models were applied to the steady channel flow cases of Kim *et al* (1987) and Kim (1990) for Re of 5600 and 13750. Both the k-ϵ and k-ϵ-S models capture the features of steady channel flow. The k-ϵ-S model tends to be in better agreement with the DNS data of Kim *et al* (1987, 1990). The most pronounced example of this agreement is at the near-wall peak of the turbulent kinetic energy, where the k-ϵ model is significantly below the data and k-ϵ-S model calculations. The turbulent dissipation rate profile of the Kim *et al* DNS data near to the wall (for $z^+ \lesssim 10$) is not captured by either model. The models do not agree with the data profiles of the turbulent Reynolds number and anisotropic shear stress towards the centreline ($z^+ \gtrsim 100$ for $Re = 5600$ and $z^+ \gtrsim 200$ for $Re = 13750$)

The EVM models above and the Launder and Shima (1989) RSTM (including Shima's (1989) modification) were applied to transient pipe flow and compared over a range of frequencies with the wall shear stress and friction coefficient data of Finnicum and Hanratty (1988). The dimensionless frequency parameter $\omega^+ = \omega\nu/\ \overline{U_\tau^2}$ characterises the pipe flow. The amplitude of the wall shear stress is well predicted by the Launder and Sharma k-ϵ model, Cotton and Ismael k-ϵ-S model

and RSTM at high frequencies for which $\omega^+ \geq 0.05$. All solutions collapse onto a quasi-laminar asymptote. A dip exists in the Finnicum and Hanratty (1988) experimental data for the amplitude of the wall shear stress within the frequency range $0.007 \lesssim \omega^+ \lesssim 0.02$. This is not wholly captured by any of three turbulence models applied (k-ϵ, k-ϵ-S and RSTM). Overall the Launder and Sharma k-ϵ model appears to be the most accurate of the three in the region of transition from quasi-steady to quasi-laminar states. The RSTM model captures the phase of the Finnicum and Hanratty data better than the two EVM models.

These three models were also compared to the periodic pipe flow experimental data of Tu and Ramaprian (1983). Cyclic variation of the wall shear stress and friction velocity were examined and flow velocity and Reynolds shear stress variation were considered across a cycle at two radial positions, near to the wall and near to the centreline. Profiles were also given at four phase positions across a cycle. The k-ϵ-S model tends to be in closer agreement with the Tu and Ramaprian data towards the wall, whereas the RSTM is better towards the centreline. The RSTM model tends to lag the data and the EVM models lead the data. This phase difference is more pronounced towards the centreline of the pipe.

Overall an RSTM which models the transport of the individual turbulent stresses is necessary to capture the finer details of transient flow. The k-ϵ-S model predicts the flow better than the k-ϵ model and tends to capture the flow as well as, if not better than, the RSTM model near to the wall. However, the superiority of the RSTM and indeed the k-ϵ-S model may not compensate for the greater complexity of the models and the inevitable increased computational effort.

Shallow Water Oscillatory Flow over Smooth and Rough Beds

High-Reynolds-number one-equation k-l and two-equation k-ϵ turbulence models have been applied to oscillatory flows over rough and smooth beds. These flows represent a wide range of defining parameters.

The models were compared to seven different experimental cases including the field data of McLean (1983) and Schröder (1987), the small-scale laboratory experiments of Jensen, Sumer and Fredsøe (1989) and the large-scale laboratory experimental data of Lloyd *et al* (1997) and data from the University of Manchester Tidal Flume of Dr. C. Chen and Dr. D. Chen, Dept. of Engineering, University of Manchester.

It is found that the agreement with the velocity data is satisfactory for both models, although the k-ϵ model is the superior scheme. Both models predict the cyclic variation and profiles of velocity adequately. The k-ϵ model resolves the Reynolds shear stress and turbulent kinetic energy in the lower boundary layer ($z/\delta \lesssim 0.2$) significantly better than the k-l model. However in the outer boundary layer ($z/\delta \gtrsim 0.5$) it is difficult to judge the relative accuracy of either model given the uncertainty in the experimental data. Although k-ϵ model does not accurately predict the magnitude of the turbulence quantities well in the outer flow region, the phase response in this region is predicted fairly well. The k-ϵ model performs better than the k-l scheme in comparison with the derived experimental eddy viscosity data. In particular, the k-l model produces values of ν_t far greater than the data in the outer region of the flow. This is due to the length scale $l = \kappa z$ increasing linearly with height. However the experimental uncertainty bands for the Reynolds shear stress and eddy viscosity data are large and the accuracy of the model assessment for these parameters is questionable.

It would be interesting compare these results with a variation of the k-l model, for which the length scale, l only increased linearly up to a certain height, which is illustrated in Figure 125.

Overall the k-ϵ model performance is better than the one-equation k-l scheme, as might be expected. This is attributed solely to the inclusion of a rate equation for ϵ in the k-ϵ model. Even so the agreement between the k-ϵ model results and the experimental data for the Reynolds stresses are poor in the outer flow region. This is possibly due to the breakdown of the eddy viscosity concept in this region, or

possibly due to the uncertainty in the experimental data. In the transient pipe flow an RSTM model was necessary to capture the flow details in this region. This might also prove to be the case for rough bed oscillatory flows. However, it may not be possible to assess such a turbulence model properly, without first obtaining more accurate data sets.

References

Baumert, H. and Radach, G. (1992) *Hysteresis of Turbulent Kinetic Energy in Nonrotational Tidal Flows: A Model Study*, J. Geophysical Research, **97**(C3), 3669-3677.

Blondeaux, P. and Columbini, M. (1985) *Pulsatile Turbulent Pipe Flow*, Proc. 5th Symp. on Turb. Shear Flows, Cornell University, 16.15-16.21.

Blundell, C. and Cotton, M. A. (1995) *Supplementary results to: Turbulence Model Development with Reference to Strain Rate, Vorticity and Turbulence Timescales*, Internal Report, University of Manchester.

Brereton, G. J. and Mankbadi, R. R. (1995) *Review of Recent Advances in the Study of Unsteady Turbulent Internal Flows*, Appl. Mech Rev., **48**, 189-212.

Brereton, G. J., Reynolds, W. C. and Jayaraman, R. (1990) *Response of a Turbulent Boundary Layer to Sinusoidal Free-Stream Unsteadiness*, J. Fluid Mech. **221**, 131-159.

Cebeci, T. and Smith, A. M. O. (1974) *Analysis of Turbulent Boundary Layers.* Academic Press, New York.

Chien, K. Y. (1982) *Predictions of Channel and Boundary-Layer Flows with a Low-Reynolds-Number Turbulence Model*, AIAA Journal, **20**, 33-38.

Cotton, M. A. (1987) *Theoretical Studies of Mixed Convection in Vertical Tubes*, Ph.D. Thesis, Faculty of Science, University of Manchester.

Cotton, M. A. (1997a) *Friction Coefficient in Unsteady Flows*, Internal Note, School of Engineering, University of Manchester.

Cotton, M. A. (1997b) *Private communication*

Cotton, M. A. and Jackson, J. D. (1990) *Vertical Tube Air Flows in the Turbulent Mixed Convection Regime Calculated using a low-Reynolds-number k-ϵ model*, Int. J. Heat Mass Transfer, **33**, 275-286.

Cotton, M. A. and Ismael, J. O. (1995) *Some Results for Homogeneous Shear Flows Computed using a Strain Parameter Model of Turbulence*, Proc. 10th Symposium on Turbulent Shear Flows, Pennsylvania State Univ.

Cotton, M. A. and Ismael, J. O. (1996) *Initial Formulation of a Strain Parameter Closure for Turbulent Shear Flows*, Internal Report, School of Engineering, University of Manchester.

Cotton, M. A., Guy, A. W. and Launder B. E. (1997) *Second-Moment Modelling of Periodic and Transient Pipe Flow*, Proc. 11th Symp. on Turbulent Shear Flows, Grenoble, France, 14-6 to 14-11.

Cotton, M. A. and Ismael, J. O. (1998) *A Strain Parameter Turbulence Model and its Application to Homogeneous and Thin Shear Flows*, Int. J. Heat Fluid Flow, **19**, 326-337.

Cotton, M. A., Craft, T. J., Guy, A. W. and Launder, B. E. (2000) *A Comparison of Eddy Viscosity and Second Moment Closures in Periodic Motion*, Flow, Turb and Combustion, in press.

Ferziger, J. H. and Perić, M. (1996) *Computational Methods for Fluid Dynamics*, Springer-Verlag, Berlin.

Finnicum, D. S. and Hanratty, T. J. (1988) *Influence of Imposed Flow Oscillations on Turbulence*, Physiochem. Hydrodynamics, **10**, 585-598.

Fredsøe, J. and Deigaard, R. (1992) *Mechanics of Coastal Sediment Transport.* Advanced Series on Ocean Engineering Vol. 3, World Scientific, Singapore.

Gibson, M. M. and Launder, B. E. (1987) *Ground Effects on Pressure Fluctuations in the Atmospheric Boundary Layer*, Proc. Sixth Symp. Turbulent Shear Flows, Toulouse, France.

Guy, A. W. (2000) *A Study of Periodic and Ramp-Transient Unsteady Turbulent Pipe Flow using Two-Equation and Reynolds Stress Transport Models*, Faculty of Science and Engineering, University of Manchester, Ph.D. thesis in preparation.

Hanjalić, K., Jakirlić, S. and Hadžić (1995) *Compuataion of Oscillating Turbulent Flows at Transitional Re-Numbers*, In Turbulent Shear Flows 9, (Eds: F. Durst *et al.*), 323-342, Springer-Verlag, Berlin.

Harris, J. M. (1997) *Modelling Random Wave Boundary Layers*, Ph. D. Thesis, Dept. of Civil Engineering, University of Liverpool.

Hino, M., Kashiwayanagi, M., Nakayama, A. and Hara, T. (1983) *Experiments on the Turbulence Statistics and the Structure of a Reciprocating Oscillatory Flow*, J. Fluid Mech., **131**, 363-400.

Hinze, J. O. (1975) *Turbulence*, 2nd Edition, McGraw-Hill, New York.

Ismael, J. O. (1991) *Progress Report on the Near Wall Damping of the Reynolds Stress in Low Reynolds Number k-ϵ Models*, Internal Report, Department of Mechanical Engineering, University of Manchester.

Ismael, J. O. (1993a) *Theoretical Studies of Unsteady Turbulent Pipe Flow*,

Ph.D. Thesis, Faculty of Science, University of Manchester.

Ismael, J. O. (1993b) *Examination of the Turbulent Kinetic Energy Equation at the Near-Wall Node*, Internal Report, Department of Mechanical Engineering, University of Manchester.

Ismael, J. O. (1993c) *Discretization of the Generic Transport Equation at the Near-Wall Control Volume Using a Quadratic Approximation to the Near-Wall Derivative*, Internal Report, Department of Mechanical Engineering, University of Manchester.

Ismael, J. O. and Cotton, M. A. (1996) *Calculations of Wall Shear Stress in Harmonically Oscillated Turbulent Pipe Flow Using a Low-Reynolds-number k-ϵ model*, J. Fluids Eng., **118**, 189-194.

Jensen, B. L., Sumer, B. M. and Fredsøe, J. (1989) *Turbulent Oscillatory Boundary Layers at High Reynolds Numbers*, J. Fluid Mech., **206**, 265-297.

Jonsson, I. G. and Carlsen, N. A. (1976) *Experimental and Theoretical Investigations in an Oscillatory Turbulent Boundary Layer*, J. Hydraulic Res., **29**, 704-711.

Jones, W. P. and Launder, B. E. (1972) *The Prediction of Laminarization with a Two-Equation Model of Turbulence*, Int. J. Heat Mass Transfer, **15**, 301-314.

Justesen, P. (1991) *A Note on Turbulence Calculations in the Wave Boundary Layer*, J. Hydr. Res., **29**, 704-711.

Justesen, P. and Spalart, P. R. (1990) *Two-equation Turbulence Modelling of Oscillatory Boundary Layers*, AIAA Paper, AIAA-90-0496 (28th Aeorspace Sciences Meeting).

Kebede, W., Launder B. E. and Younis, B. A. (1985) *Large-Amplitude Periodic*

Pipe Flow: A Second Moment Closure Study, Proc. 5th Symp. on Turb. Shear Flows, Cornell University, 16.23-16.29.

Kim, J., Moin, P. and Moser, R. (1987) *Turbulence Statistics in Fully Developed Channel Flow at Low Reynolds Number*, J. Fluid Mech., **177**, 133-166.

Kim, J., (1990) *Channel Flow – DNS by Kim et al.*, Internet address: http://vortex.mech.surrey.ac.uk

Lam, C. K. G. and Bremhorst, K. A. (1981) *Modified Form of the k-ϵ Model for Predicting Wall Turbulence*, Journal of Fluids Eng., **103**, 456-460.

Launder, B. E. (1983) *Turbulence Models and Their Applications : Volume 2 Second Moment Closure Methodology and Practice; Physical and Analytical*, Report TF4/82/4, Thermodynamics and Fluid Mechanics Division, Mechanical Engineering Dept., University of Manchester Institute of Science and Technology.

Launder, B. E. and Sharma, B. I. (1974) *Application of the Energy Dissipation Model of Turbulence to the Calculation of Flow near a Spinning Disc*, Lett. Heat and Mass Transfer, **1**, 131-138.

Launder, B. E. and Shima, N. (1989) *Second-Moment Closure for the Near-Wall Sublayer: Development and Application*, AIAA, **27**, 1319-1325.

Leschziner, M. A. (1982) *An Introduction and Guide to the Computer Code PASSABLE*, Preliminary Version, Mech. Eng. Dept., University of Manchester Institute of Science and Technology.

Letherman, S. B. (1999) *k-l and k-ϵ Modelling of Oscillatory Flows over Rough Beds*, Proc. of 28th Biennial IAHR Congress, Graz, Austria (Eds. M. N. Abbott *et al.*) p.463. (Papers are available on CD-ROM)

Letherman, S. B., Cotton, M. A., Stansby, P. K., Chen, C. and Chen, D. (2000) *An Assessment of k-ϵ and k-l Turbulence Models for a Wide Range of Oscillatory Rough Bed Flows*, submitted to the Journal of Hydroinformatics.

Lloyd. P. M., Stansby, P. K. and Chen, D. (1997) *Experiments in the UK Coastal Research Facility*, Internal Report, School of Engineering, University of Manchester.

Lodahl, C. R., Sumer, B. M. and Fredsœ, J. (1998) *Turbulent Combined Oscillatory Flow and Current in a Pipe*, J. Fluid Mech., **373**, 313-348.

Mao, Z-X and Hanratty, T. J. (1986) *Studies of the Wall Shear Stress in a Turbulent Pulsating Pipe Flow*, J. Fluid Mech., **170**, 545-564.

McLean, S. R. (1983) *Turbulence and Sediment Transport Measurements in a North Sea Tidal Inlet (the Jade)*. North Sea Dynamics (Eds. J. Sündermann and W. Lenz), 436-425, Springer-Verlag, Berlin.

Mendoza, C. and Shen,H. W. (1990) *Investigation of Turbulent Flow over Dunes*, J. Hydraulic Eng. ASCE, **114**, 459.

Mizushina, T., Maruyama T. and Shiozaki, Y. (1973) *Pulsating Turbulent Flow in a Tube*, J. Chem. Eng. Japan, **6**, 487-494.

Mizushina, T., Maruyama T. and Hirasowa, H. (1975) *Structure of Turbulence in Pulsating Pipe Flows*, J. Chem. Eng. Japan, **8**, 210-216.

Nezu, I. and Nakagawa, H. (1993) *Turbulence in Open-Channel Flows*, A. A. Balkema, Rotterdam.

Nielsen, P. (1992) *Coastal Bottom Boundary Layers and Sediment Transport*, Advanced Series on Ocean Engineering Vol. 4, World Scientific, Singapore.

Olivari, D., Lecture Series Director (1993) *Introduction to the Modelling of*

Turbulence, Lecture Series 1993-02, von Karman Institute for Fluid Dynamics, Chaussée de Waterloo, 72, B-1640 Rhode Saint Genèse, Belgium.

Patel, V., Rodi, W. and Scheurer, G. (1985) *Turbulence Models for Near Wall and Low-Reynolds Number Flows: A Review*, AIAA Journal, **23**, 1308-1319.

Ramaprian, B. R. and Tu, S. W. (1983) *Fully Developed Periodic Turbulent Pipe Flow. Part 2. The Detailed Structure of the Flow*, J. Fluid Mech., **137**, 59-81.

Rodi, W. (1976) *A New Algebraic Stress Relation for Calculating the Reynolds Stresses*, Mechanics of Fluids, ZAMM, **56**, T219-T221

Rodi, W. (1993) *Turbulence Models and their Applications in Hydraulics*, 3rd Edition, A. A. Balkema, Rotterdam.

Saffman, P. G. (1970) *A Model for Inhomogeneous Turbulent Flow*, Proc. Roy. Soc. London, **317**, 417-433.

Sajjadi, S. G. and Waywell, M. N. (1998) *A Stable Algorithm for Reynolds Stress Turbulence Modelling with Applications to Rectilinear and Circular Tidal Flows*, Int. J. Num. Meth. Fluids, **26**, 251-280.

Savell, I. A. (1986) *An Experimental Study of Near-Bed Hydrodynamics of Waves and Steady Current and the effect on Sediment Transport*, Ph. D. Thesis, Dept. of Engineering, University of Manchester.

Schlichting, H. (1979) *Boundary Layer Theory*, McGraw-Hill, New York.

Schröder, M. (1987) *Messung des turbulenten Impuls- und Saltztransports in der Mischungszone der Elbe*, Technical Report GKSS 87/E/16, GKSS-Forschungszentrum Geesthacht.

Shima, N. (1989) *Calculation of a Variety of Boundary Layers with a Second-Moment Closure Applicable up to a Wall*, Proc. Seventh Symp. Turbulent Shear Flows, Stanford Univ.

Sleath, J. F. A. (1987) *Turbulent Oscillatory Flow over Rough Beds*, J. Fluid Mech. **182**, 369-409.

Spalart, P. R. and Baldwin, B. S. (1989) *Direct Numerical Simulation of a Turbulent Oscillating Boundary Layer*, in Turbulent Shear Flows 6 (Eds. J. C. André *et al*), 417-440, Springer-Verlag, Berlin.

Stansby, P. K. (1997) *Semi-Implicit Finite Volume Shallow-Water Flow and Solute Transport Solver with k-ϵ Turbulence Model*, Int. J. Num. Meth. Fluids, **35**, 285-313.

Sumer, B. M., Jensen, B. L. and Fredsøe, J. (1987) *Turbulence in Oscillatory Boundary Layers*, in Advances in Turbulence, (Eds. G. Comte-Bellot and J. Mathieu), 556-567, Springer-Verlag, Berlin.

Svendsen, I. A. (1987) *Analysis of Surf Zone Turbulence*, J. Geophysical Research, **92**(C5), 5115-5124.

Tanaka, H. and Sana, A. (1994) *Numerical Study on Transition to Turbulence in a Wave Boundary Layer* Sediment Transport Mechanics in Coastal Environments and Rivers. (Eds. M. Belorgey, R. D. Rajaona and J. F. A. Sleath), 14-25, Euromech 310, 13th - 17th Sept. 1993, World Scientific, Singapore.

Tennekes, H. and Lumley J. L. (1972) *A First Course in Turbulence*, MIT Press, Cambridge, Mass.

Thais, L., Chaplain, G. and Smaoui, H. (1999) *Reynolds Number Variation in Oscillatory Boundary Layers. Part I. Purely Oscillatory Motion*, Coastal Engineering, **36**, 111-146.

Townsend, A. A. (1976) *The Structure of Turbulent Shear Flows*, Cambridge University Press.

Tu, S. W. and Ramaprian, B. R. (1983) *Fully Developed Periodic Turbulent Pipe Flow. Part 1. Main Experimental Results and Comparison with Predictions*, J. Fluid Mech., **137**, 31-58.

Vager, B. G. and Kagan, B. A. (1969) *The dynamics of the Turbulent Boundary Layer in a Tidal Current*, Atmos. and Ocean Physics, **5**(2), 168-179.

Wilcox, D. C. and Rubesin, W. M. (1980) *Progress in Turbulence Modelling for Complex Flow Fields Including Effects of Compressibility*, NASA Tech. Paper 1517.

Tables

EVM	κ	c_μ	$c_{\epsilon 1}$	$c_{\epsilon 2}$	$c_{\epsilon 3}$	σ_k	σ_ϵ	σ_S
High-Reynolds-number k-l	0.4	0.08	—	—	—	1.0	—	—
High-Reynolds-number k-ϵ	0.4	0.09	1.44	1.92	—	1.0	1.3	—
Launder and Sharma k-ϵ	0.4	0.09	1.44	1.92	2.0	1.0	1.3	—
Strain parameter k-ϵ-S	0.4	0.09	1.44	1.92	0.9	1.0	1.21	6.0

Table 1: Eddy viscosity model constants and von Kármán's constant

cf. Blundell 7.278 and Cotton		$C_f \times 10^{-3}$		SOLVE	
		Convergence test		Convergence test	
Near-wall		U and k	k residuals	U and k	k residuals
Switch	at $z^+ = 1.5$	7.3065 (+0.4%)	7.3065 (+0.4%)	7004	6880
	at $z^+ = 2.0$	7.3456 (+0.9%)	7.3456 (+0.9%)	6876	6828
Quadratic Approx.		† 7.1411 (-1.8%)	—	13956	—
Staggered Discret.		7.1852 (-1.3%)	7.1852 (-1.3%)	10504	9900

†Direct comparison with results of Blundell and Cotton (1995)
'—' indicates that the solution does not converge.

Table 2: Comparison of convergence tests and treatment of k near the wall: k-ϵ model for channel flow $Re = 5600$

cf. Blundell 7.729 and Cotton		$C_f \times 10^{-3}$			SOLVE		
		Convergence test			Convergence test		
Near-wall		U, and k	U, k and S	k residuals	U and k	U, k and S	k residuals
Switch	at $z^+ = 1.5$	7.6971 (-0.4%)	7.6970 (-0.4%)	7.6971 (-0.4%)	8115	18590	8610
	at $z^+ = 2.0$	7.6952 (-0.4%)	7.6952 (-0.4%)	7.6952 (-0.4%)	8130	18365	8560
Quadratic Approx.		† 7.6005 (-1.7%)	—	—	17115	—	—
Staggered Discret.		7.6634 (-0.7%)	7.6634 (-0.7%)	7.6634 (-0.7%)	11930	33970	13030

Table 3: Comparison of convergence tests and treatment of k near the wall: k-ϵ-S model for channel flow $Re = 5600$

cf. Blundell 5.811 and Cotton		$C_f \times 10^{-3}$		SOLVE	
		Convergence test		Convergence test	
Near-wall		U and k	k residuals	U and k	k residuals
Switch	at $z^+ = 1.5$	5.8866 (+1.3%)	5.8866 (+1.3%)	10832	11696
	at $z^+ = 2.0$	5.9183 (+1.9%)	5.9183 (+1.9%)	10816	11496
Quadratic Approx.		† 5.7543 (-1.0%)	—	22576	
Staggered Discret.		5.7900 (-0.4%)	5.7900 (-0.4%)	15712	17052

Table 4: Comparison of convergence tests and treatment of k near the wall: k-ϵ model for channel flow $Re = 13750$

cf. Blundell 6.333 and Cotton		$C_f \times 10^{-3}$			SOLVE		
		Convergence test			Convergence test		
Near-wall		U, and k	U, k and S	k residuals	U and k	U, k and S	k residuals
Switch	at $z^+ = 1.5$	6.3377 (+0.1%)	6.3377 (+0.1%)	6.3377 (+0.1%)	13165	23205	12230
	at $z^+ = 2.0$	6.3355 (+0.0%)	6.3355 (+0.0%)	6.3355 (+0.0%)	13165	22995	12205
Quadratic Approx.		† 6.2610 (-1.1%)	6.2610 (-1.1%)	—	24025	69385	—
Staggered Discret.		6.3116 (-0.3%)	6.3116 (-0.3%)	6.3116 (-0.3%)	16975	34290	12930

Table 5: Comparison of convergence tests and treatment of k near the wall: k-ϵ-S model for channel flow $Re = 13750$

c.f. Cotton 7.6993		$C_f \times 10^{-3}$		
		Convergence test		
Near-wall		U and k	U, k and S	k residuals
Switch	at $z^+ = 1.5$	7.6971 (-0.03%)	7.6970 (-0.03%)	7.6971 (-0.03%)
	at $z^+ = 2.0$	7.6952 (-0.05%)	‡ 7.6951 (-0.05%)	7.6952 (-0.05%)
Quadratic Approx.		7.6005 (-1.28%)	—	—
Staggered Discret.		7.6634 (-0.47%)	7.6634 (-0.47%)	7.6634 (-0.47%)

‡Direct comparison with results of Cotton

Table 6: Comparison of convergence tests and treatment of k near the wall with results of Cotton for which the switch near the wall at $z^+ = 2.0$ was used: k-ϵ-S model for channel flow $Re = 5600$

c.f. Cotton 7.6678		$C_f \times 10^{-3}$		
		Convergence test		
Near-wall		U and k	U, k and S	k residuals
Switch	at $z^+ = 1.5$	7.6971 (+0.38%)	7.6970 (+0.38%)	7.6971 (+0.38%)
	at $z^+ = 2.0$	7.6952 (+0.36%)	7.6951 (+0.36%)	7.6952 (+0.36%)
Quadratic Approx.		7.6005 (+0.88%)	—	—
Staggered Discret.		7.6634 (-0.06%)	‡ 7.6634 (-0.06%)	7.6634 (-0.06%)

‡Direct comparison with results of Cotton

Table 7: Comparison of convergence tests and treatment of k near the wall with results of Cotton for which staggered discretisation near the wall was used: k-ϵ-S model for channel flow $Re = 5600$

Turbulence Model	No. of Nodes	$C_f \times 10^3$	% change	SOLVE
k-ϵ Re = 5600	101	7.1852		9900
	201	7.1466	−0.54	10304
	51	7.3084	+1.71	9828
k-ϵ-S Re = 5600	101	7.6758		13460
	201	7.6758	−0.28	13700
	51	7.6758	+0.96	12950
k-ϵ Re = 13750	101	5.7900		17052
	201	5.7900	−0.55	16968
	51	5.7900	+1.88	16396
k-ϵ-S Re = 13750	101	6.3223		13320
	201	6.3223	−0.28	13275
	51	6.3223	+1.19	13125

Table 8: Sensitivity tests on TRANSIT based on number of radial grid nodes, iz.

Turbulence Model	z^+_{iz-1}	$C_f \times 10^3$	% change	SOLVE
k-ϵ	0.25	7.1852		9900
Re = 5600	0.125	7.2098	+0.34	27363
	0.5	7.1777	−0.10	7680
k-ϵ-S	0.25	7.6758		13460
Re = 5600	0.125	7.7122	+0.47	35777
	0.5	7.6252	−0.66	8735
k-ϵ	0.25	5.7900		17052
Re = 13750	0.125	—		—
	0.5	5.7872	−0.05	11584
k-ϵ-S	0.25	6.3223		13320
Re = 13750	0.125	6.3505	+0.45	37237
	0.5	6.2818	−0.64	12560

'—' indicates that the solution did not converge.

Table 9: Sensitivity tests on TRANSIT based on position of near wall node, z^+_{iz-1} .

Turbulence Model	$(\Delta t)_0$	$C_f \times 10^3$	% change	SOLVE
k-ϵ	$\nu/U_b U_\tau$	7.1852		9900
Re = 5600	$0.5\nu/U_b U_\tau$	7.1852	0.0	12472
	$2\nu/U_b U_\tau$	7.1854	0.0	8464
k-ϵ-S	$\nu/U_b U_\tau$	7.6758		13460
Re = 5600	$0.5\nu/U_b U_\tau$	7.6758	0.0	13180
	$2\nu/U_b U_\tau$	7.6758	0.0	13494
k-ϵ	$\nu/U_b U_\tau$	5.7900		17052
Re = 13750	$0.5\nu/U_b U_\tau$	5.7900	0.0	21804
	$2\nu/U_b U_\tau$	5.7900	0.0	14816
k-ϵ-S	$\nu/U_b U_\tau$	6.3223		13320
Re = 13750	$0.5\nu/U_b U_\tau$	6.3223	0.0	23210
	$2\nu/U_b U_\tau$	6.3223	0.0	13549

Table 10: Sensitivity tests on TRANSIT based on initial time step, $(\Delta t)_0$.

Turbulence Model	a_R	$C_f \times 10^3$	% change	SOLVE
k-ϵ	0.2	7.1852		9900
Re = 5600	0.1	7.1852	0.0	16656
	0.4	7.1852	0.0	10124
k-ϵ-S	0.2	7.6758		13460
Re = 5600	0.1	7.6758	0.0	18900
	0.4	7.6757	0.0	12530
k-ϵ	0.2	5.7900		17052
Re = 13750	0.1	5.7901	0.0	27040
	0.4	5.7900	0.0	14760
k-ϵ-S	0.2	6.3223		13320
Re = 13750	0.1	6.3223	0.0	15150
	0.4	6.3223	0.0	13640

Table 11: Sensitivity tests on TRANSIT based on relaxation factor, a_R .

Turbulence Model	c_k	$C_f \times 10^3$	% change	SOLVE
k-ϵ	0.01	7.1852		9900
Re = 5600	0.005	7.1852	0.0	20344
	0.02	7.1852	0.0	5812
k-ϵ-S	0.01	7.6758		13460
Re = 5600	0.005	7.6758	0.0	24445
	0.02	7.6758	0.0	6635
k-ϵ	0.01	5.7900		17052
Re = 13750	0.005	5.7900	0.0	25176
	0.02	5.7900	0.0	11876
k-ϵ-S	0.01	6.3223		13320
Re = 13750	0.005	6.3223	0.0	20015
	0.02	6.3223	0.0	11605

Table 12: Sensitivity tests on TRANSIT based on convergence criterion, c_k .

Turbulence Model	$t_{total}(s)$	$C_f \times 10^3$	% change	SOLVE
k-ϵ	15.0	7.1852		9900
Re = 5600	30.0	7.1852	0.0	13900
	7.5	7.1952	+0.1	7900
k-ϵ-S	15.0	7.6758		13460
Re = 5600	30.0	7.6752	0.0	18460
	7.5	7.6979	+0.3	10960
k-ϵ	6.0	5.7900		17052
Re = 13750	12.0	5.7900	0.0	25052
	3.0	5.7943	+0.1	13052
k-ϵ-S	6.0	6.3223		13320
Re = 13750	12.0	6.3223	0.0	23320
	3.0	6.3241	0.0	8320

Table 13: Sensitivity tests on TRANSIT based on total duration, t_{total} .

Case	Model	iz	$f_w \times 10^{-2}$	% change
JSF13	k-l	101	0.726	
		201	0.732	+0.88
		51	0.724	-0.23
JSF13	k-ϵ	101	0.640	
		201	0.648	1.25
		51	0.640	0.0
UMTF	k-l	11	2.40	
		21	2.40	0.0
		6	2.25	-6.25
UMTF	k-ϵ	11	2.55	
		21	2.33	-8.6
		6	2.42	-5.1

Table 14: Sensitivity tests on SW1DV based on number of grid nodes, iz

Case	Model	iz	$z^+_{1\,\max}$	$f_w \times 10^{-2}$	% change
JSF13	k-l	101	41.88	0.726	
		81	52.58	0.725	-0.14
		61	70.68	0.724	-0.28
		46	95.33	0.724	-0.28
JSF13	k-ϵ	101	39.39	0.640	
		81	49.45	0.639	-0.16
		61	66.50	0.639	-0.16
		46	89.83	0.641	+0.16
UMTF	k-l	11	35.45	2.40	
		9	44.20	2.38	-0.83
		7	58.37	2.32	-3.33
		5	85.20	2.16	-10.00
UMTF	k-ϵ	11	35.89	2.55	
		9	45.12	2.56	+0.39
		7	59.73	2.50	-1.96
		5	86.42	2.27	-10.98

Table 15: Sensitivity tests on SW1DV cases based on the position of the near-bed grid node, $z^+_{1\,\max}$

Case	Model	h (m)	$f_w \times 10^{-2}$	% change
JSF13	k-l	0.366	0.726	
		0.732	0.721	-0.68
		0.168	0.724	-0.28
JSF13	k-ϵ	0.637	0.640	
		1.274	0.639	-0.16
		0.319	0.648	+1.25

Table 16: Sensitivity tests on JSF cases based on total depth, h .

Case	Model	*ntper*	$f_w \times 10^{-2}$	% change
JSF13	k-l	580	0.726	
		1000	0.726	-0.13
		250	0.727	+0.14
JSF13	k-ϵ	580	0.640	
		1000	0.640	0.0
		250	0.641	+0.16
UMTF	k-l	10000	2.40	
		20000	2.40	0.0
		5000	2.40	0.0
UMTF	k-ϵ	10000	2.55	
		20000	2.55	0.0
		5000	2.55	0.0

Table 17: Sensitivity tests on SW1DV cases based on number of steps per cycle, *ntper*

Case	Model	*cyc*	$f_w \times 10^{-2}$	% change
JSF13	k-l	5	0.726	
		10	0.726	0.0
		2.5	0.726	0.0
JSF13	k-ϵ	5	0.640	
		10	0.640	-0.78
		2.5	0.640	+2.19
UMTF	k-l	10	2.40	
		20	2.40	0.0
		5	2.40	0.0
UMTF	k-ϵ	10	2.55	
		20	2.55	0.0
		5	2.55	0.0

Table 18: Sensitivity tests on SW1DV cases based on number of cycles, *cyc* .

Case	Model	dm	$f_w \times 10^{-2}$	% change
JSF13	k-l	0.022	0.726	
		0.044	0.724	-0.28
		0.011	0.730	+0.55
JSF13	k-ϵ	0.0096	0.640	
		0.0019	0.638	-0.31
		0.0048	0.645	+0.78
UMTF	k-l	0.05	2.40	
		0.1	2.39	-0.42
		0.025	2.42	+0.83
UMTF	k-ϵ	0.05	2.55	
		0.1	2.55	0.0
		0.025	2.53	-0.78

Table 19: Sensitivity tests on SW1DV cases based on constant for parabolic mesh spacing, dm .

Run no.	$\overline{Re}_b$	$f(\frac{\omega}{2\pi})(Hz)$	$\overline{U}_b(m/s)$	ω^+			
				DATA	k-ϵ	k-ϵ-S	RSTM
1	44900	0.35	0.76542	0.00120	0.0013	0.0012	0.0011
2	42000	0.35	0.71599	0.00135	0.0014	0.0013	0.0013
3	29400	0.25	0.50119	0.00180	0.0019	0.0018	0.0017
4	23700	0.20	0.40402	0.00210	0.0023	0.0021	0.0020
5	31800	0.60	0.54210	0.00375	0.0040	0.0037	0.0036
6	25200	0.40	0.42959	0.00375	0.0040	0.0037	0.0037
7	20100	0.30	0.34265	0.00420	0.0045	0.0042	0.0041
8	23000	0.45	0.39209	0.00495	0.0054	0.0050	0.0048
9	21400	0.60	0.36481	0.00750	0.0081	0.0075	0.0073
10	17100	0.50	0.29151	0.00930	0.0100	0.0092	0.0090
11	14500	0.50	0.24719	0.01230	0.0135	0.0123	0.0121
12	17900	1.00	0.30515	0.01720	0.0189	0.0171	0.0171
13	10600	0.45	0.18070	0.01950	0.0212	0.0192	0.0189
14	10700	0.50	0.18241	0.02100	0.0232	0.0210	0.0208
15	15300	1.00	0.26082	0.02250	0.0251	0.0224	0.0225
16	14600	1.00	0.24889	0.02440	0.0273	0.0243	0.0244
17	14200	1.00	0.24207	0.02580	0.0287	0.0255	0.0256
18	10300	0.60	0.17559	0.02700	0.0301	0.0270	0.0269
19	8750	0.60	0.14916	0.0360	0.0405	0.0357	0.0358
20	11400	1.00	0.19434	0.03750	0.0427	0.0370	0.0372
21	9200	1.00	0.15684	0.05500	0.0625	0.0522	0.0528
22	10300	1.50	0.17559	0.0675	0.0756	0.0614	0.0621
23	8650	1.50	0.14746	0.09150	0.1008	0.0793	0.0815

Table 20: Input data for periodic pipe flow experiments of Finnicum and Hanratty and ω^+ values for experimental data of Finnicum and Hanratty and turbulence models for the amplitude of the wall shear stress.

Case	Expt. Type	T (s)	h (m)	U_0 (m/s)	a (m)	D_k (m)	k_s (m)	a/k_s	k_s/h	δ (m)	δ/h	k_s^+	Re	f_w ×1e-3	$U_{\tau,\max}$ ×1e-2	cyc	int (ms)
Jade	field	44700	20.0	1.0	7114	0.002	0.002	3.6e6	0.0001	43	2.1	69	7.1e9	2.40	3.46	30	330
Elbe	field	44700	5.1	1.1	7826	0.02	0.02	3.9e5	0.0039	69	13.5	820	8.6e9	2.79	4.11	3	—
JSF10	lab	9.72	0.14	2.0	3.10	—	smooth	—	—	0.05	0.36	—	6.2e6	8.0	—	80	24
JSF12	lab	9.72	0.14	1.02	1.58	3.5e-4	8.4e-4	1880	0.006	0.04	0.26	44	1.6e6	6.21	5.8	80	24
JSF13	lab	9.72	0.14	2.0	3.10	3.5e-4	8.4e-4	3700	0.006	0.064	0.46	84	6.2e6	5.33	11.0	80	24
UKCRF	lab	180	0.48	0.1	2.86	0.01	0.02	140	0.042	0.1	0.22	240	2.9e5	14.1	1.2	6	40
UMTF	lab	60	0.10	0.09	0.86	0.01	0.01	86	0.1	0.035	0.35	90	7.7e4	17	0.9	60	33

Table 21: Test conditions for oscillatory flow experimental cases

Figures

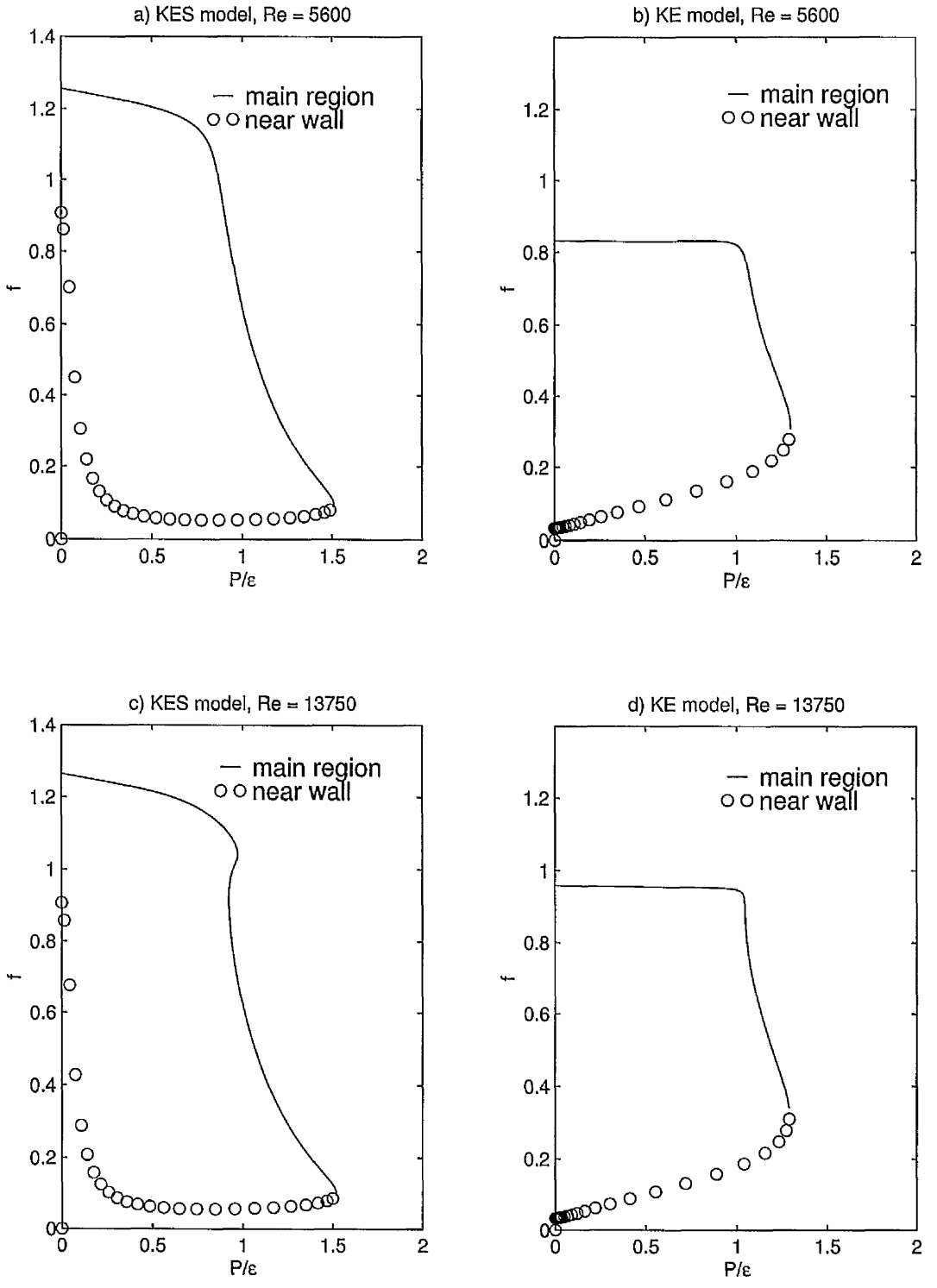

Figure 1: Plots of f against P/ϵ for channel flow at $Re = 5600$ and $Re = 13750$, where $f = f(Re_t)$ for the k-ϵ model, and $f = f(Re_t)f_S(S)$ for the k-ϵ-S model, for which the main region is distinguished from the near wall region

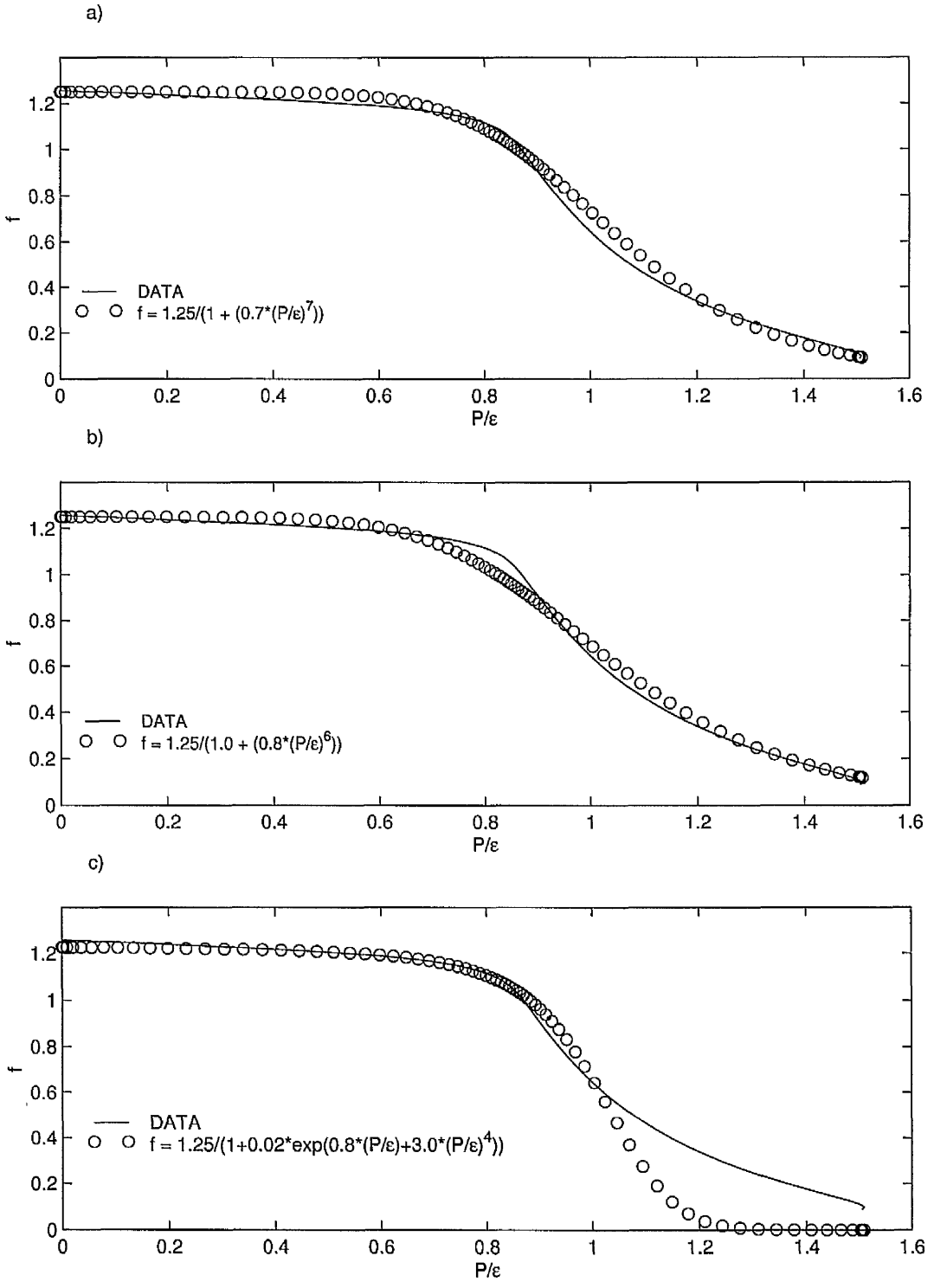

Figure 2: Three functions fitted against the plot of f against P/ϵ for channel flow at $Re = 5600$ for the k-ϵ-S model in the main region

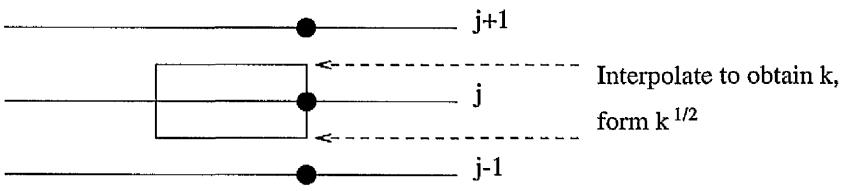

Figure 3: Schematic of control volume with 'staggered' interpolation of k.

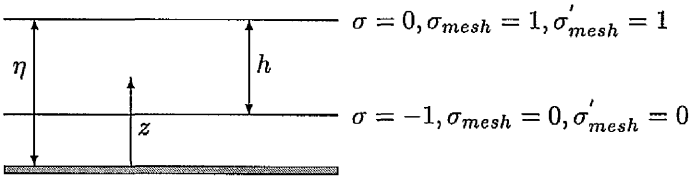

Figure 4: Sketch showing σ grid for SW1DV

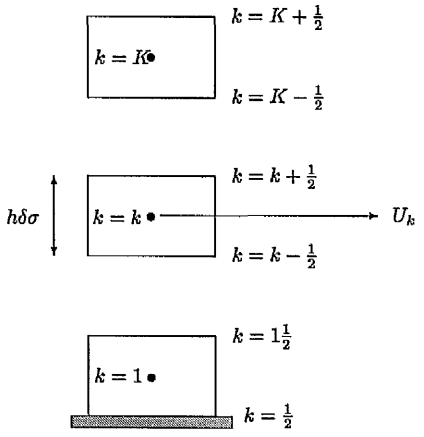

Figure 5: Sketch showing staggered mesh system for SW1DV

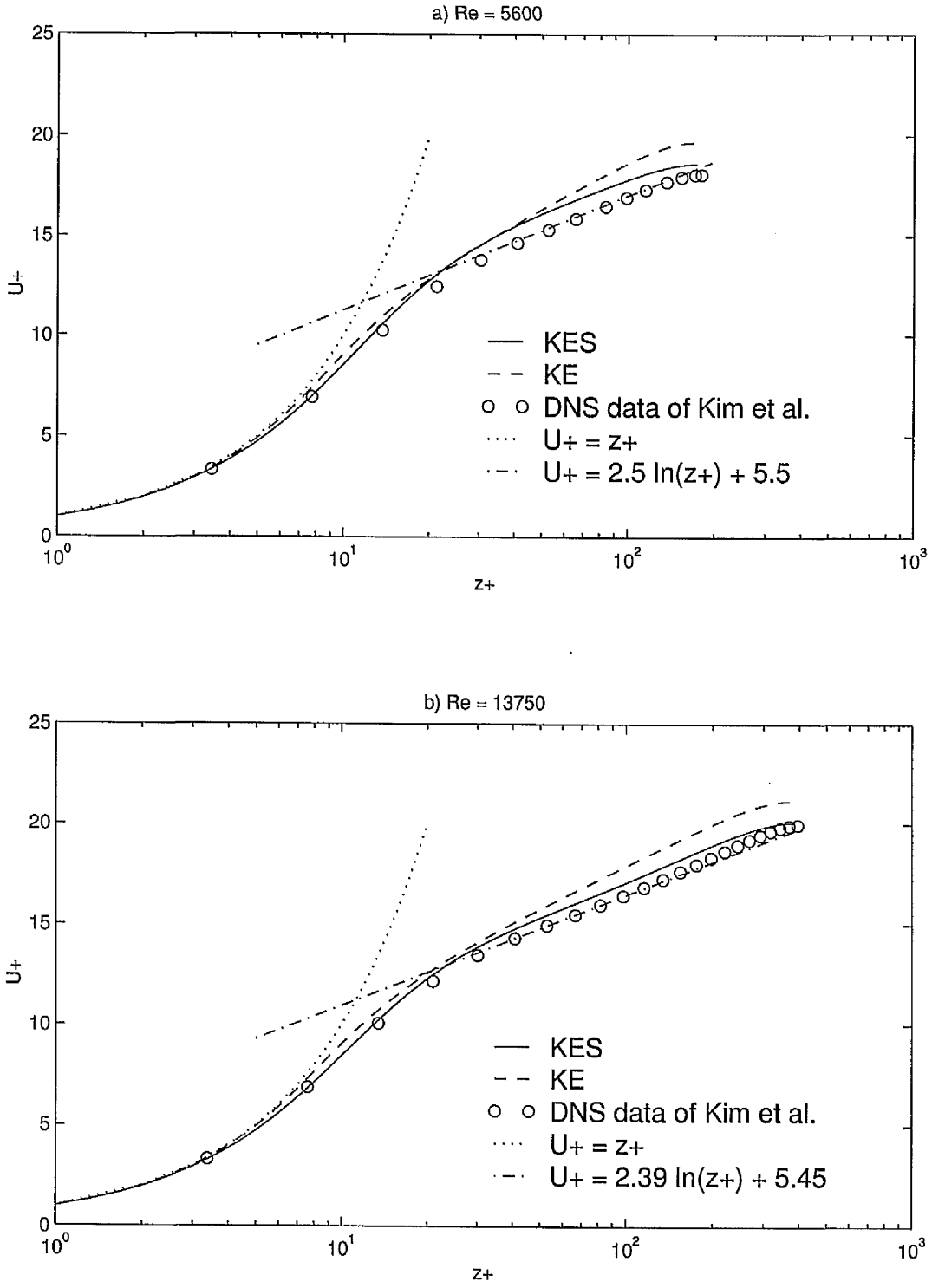

Figure 6: Mean velocity profiles in channel flow (a) $Re_b = 5600$, (b) $Re_b = 13750$: model solutions compared with DNS data of Kim *et al* (1987) and Kim (1990)

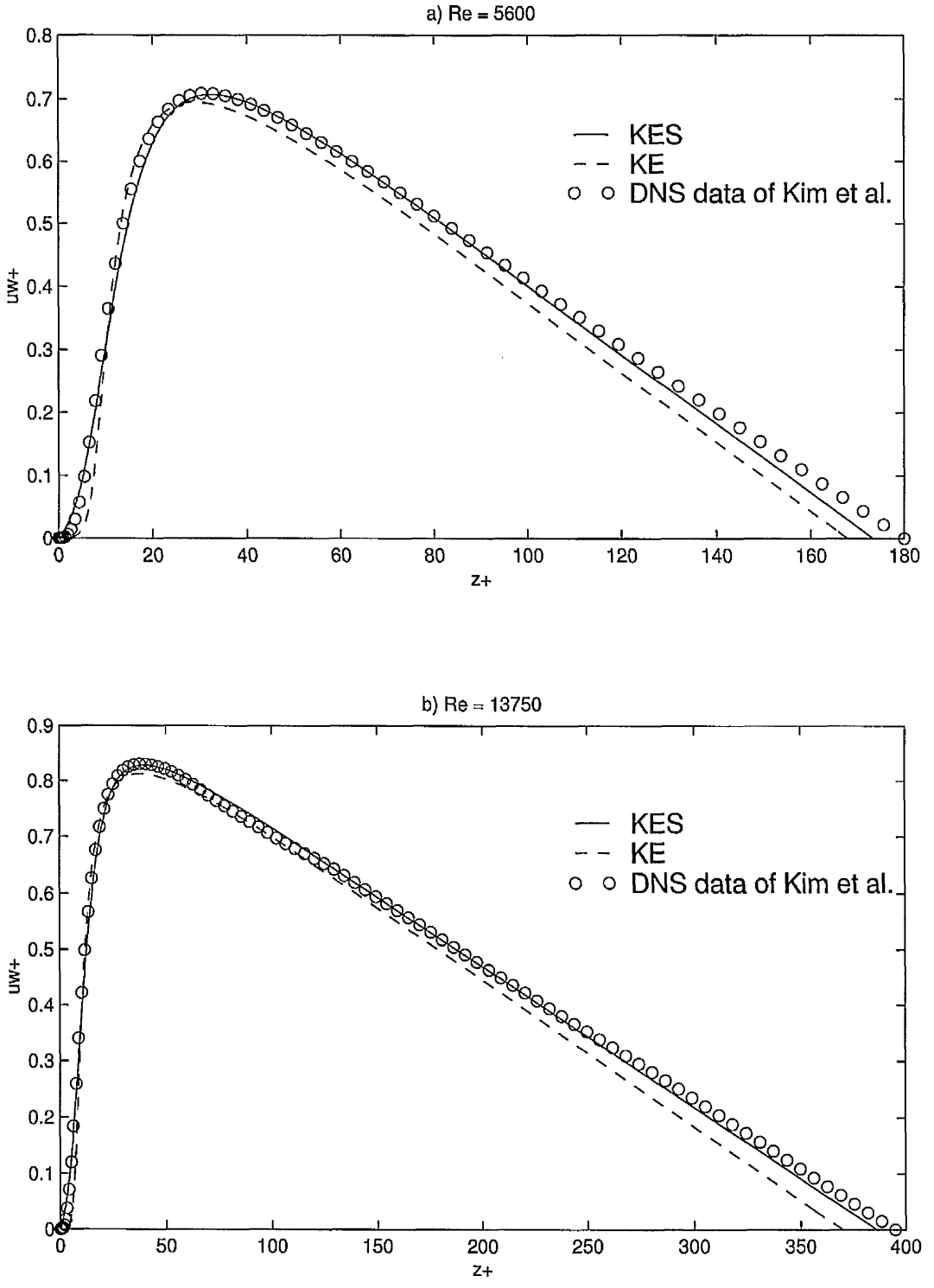

Figure 7: Reynolds shear stress profiles in channel flow (a) $Re_b = 5600$, (b) $Re_b = 13750$: model solutions compared with DNS data of Kim *et al* (1987) and Kim (1990)

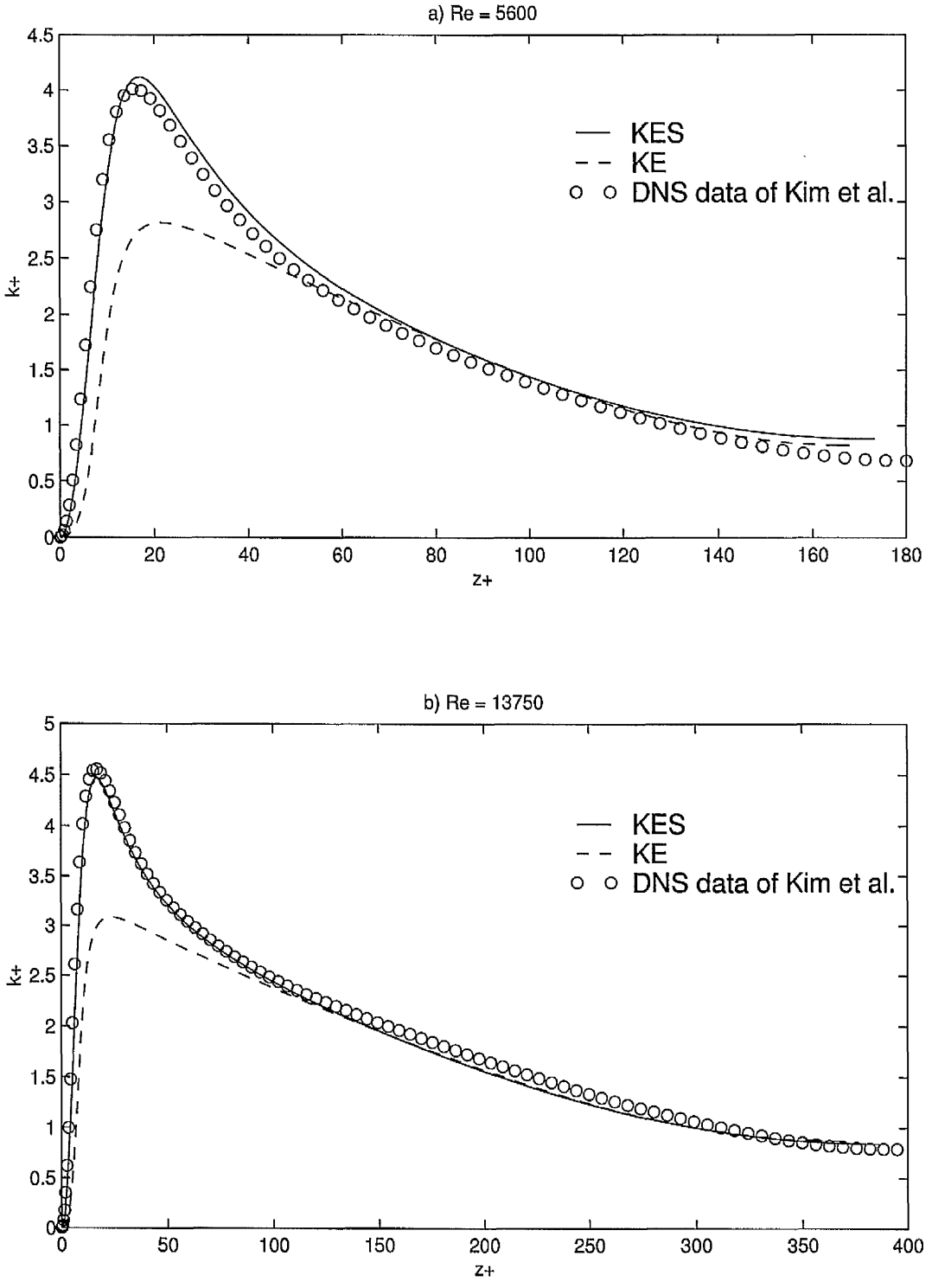

Figure 8: Turbulent kinetic energy profiles in channel flow (a) $Re_b = 5600$, (b) $Re_b = 13750$: model solutions compared with DNS data of Kim *et al* (1987) and Kim (1990)

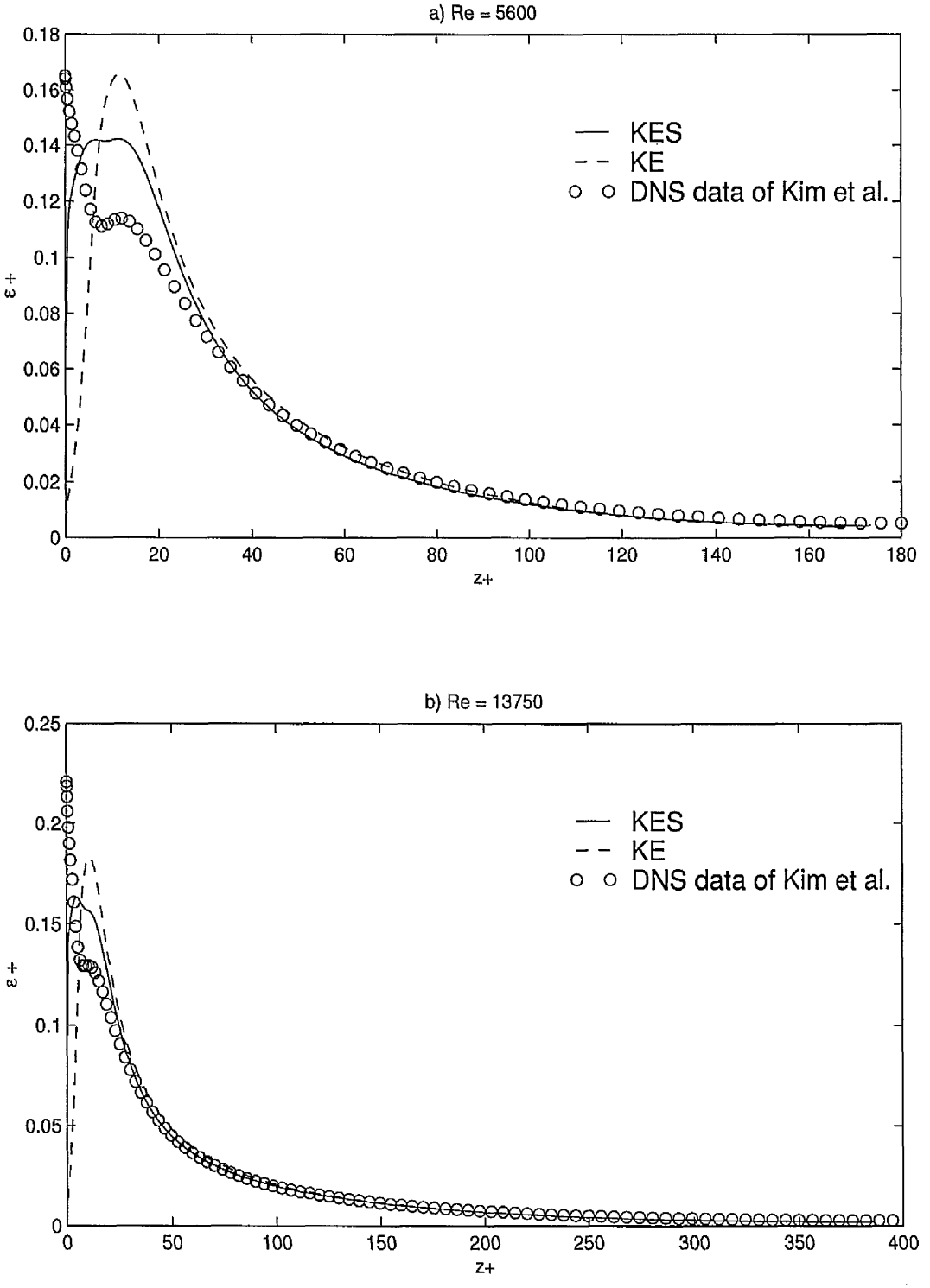

Figure 9: Turbulent dissipation rate profiles in channel flow (a) $Re_b = 5600$, (b) $Re_b = 13750$: model solutions compared with DNS data of Kim *et al* (1987) and Kim (1990)

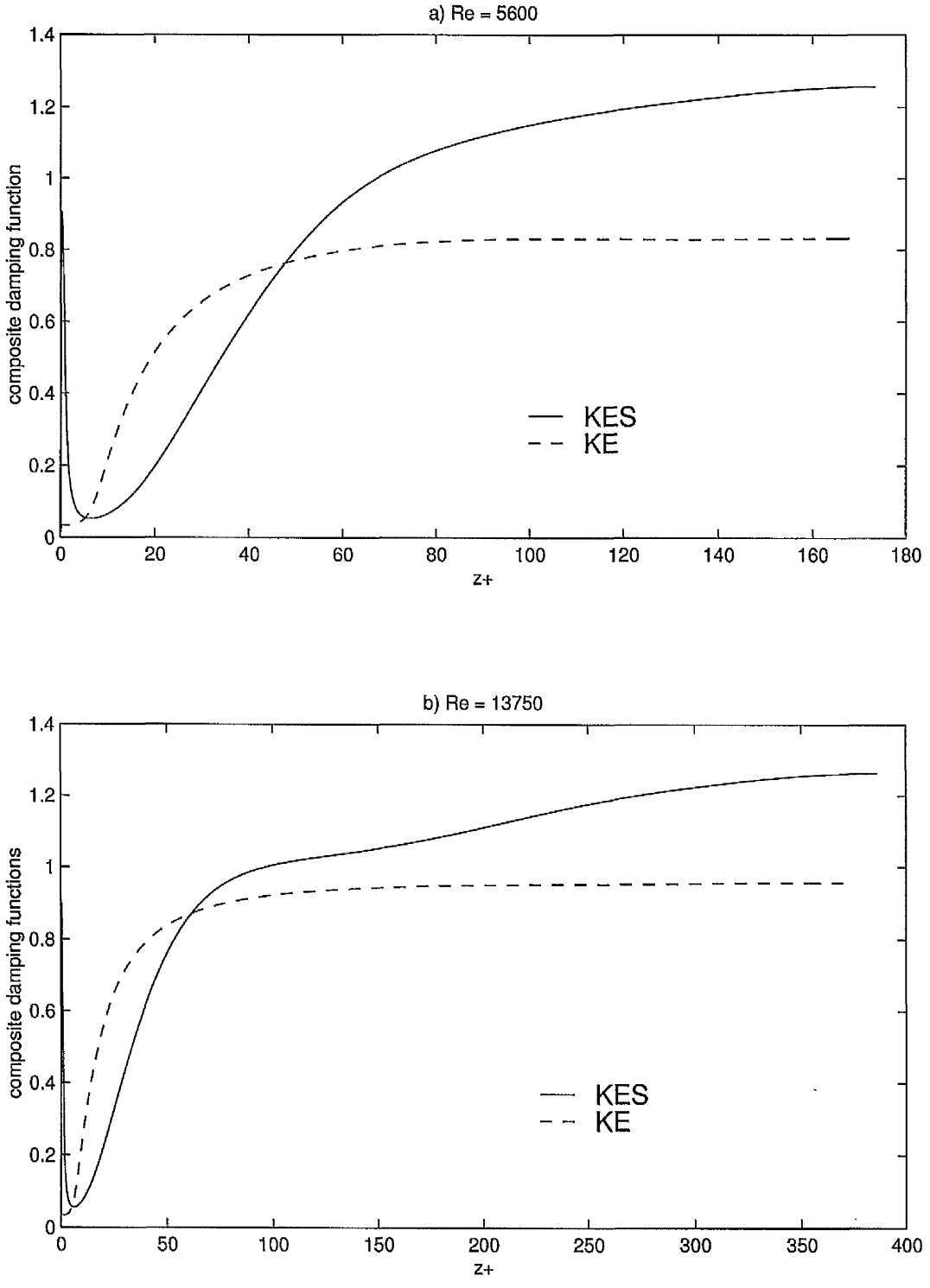

Figure 10: Composite damping functions in channel flow (a) $Re_b = 5600$, (b) $Re_b = 13750$

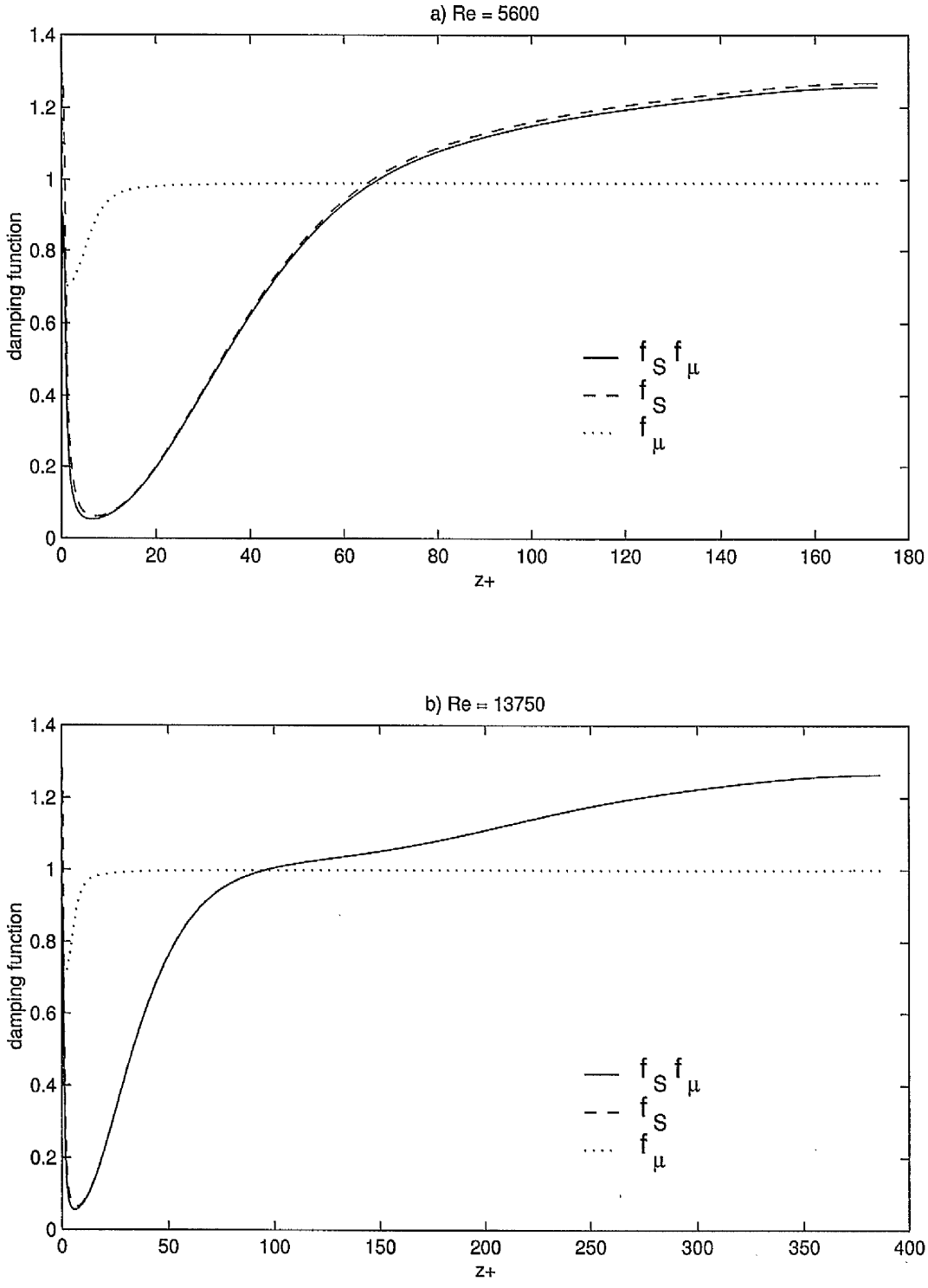

Figure 11: Damping functions for k-ϵ-S model in channel flow (a) $Re_b = 5600$, (b) $Re_b = 13750$

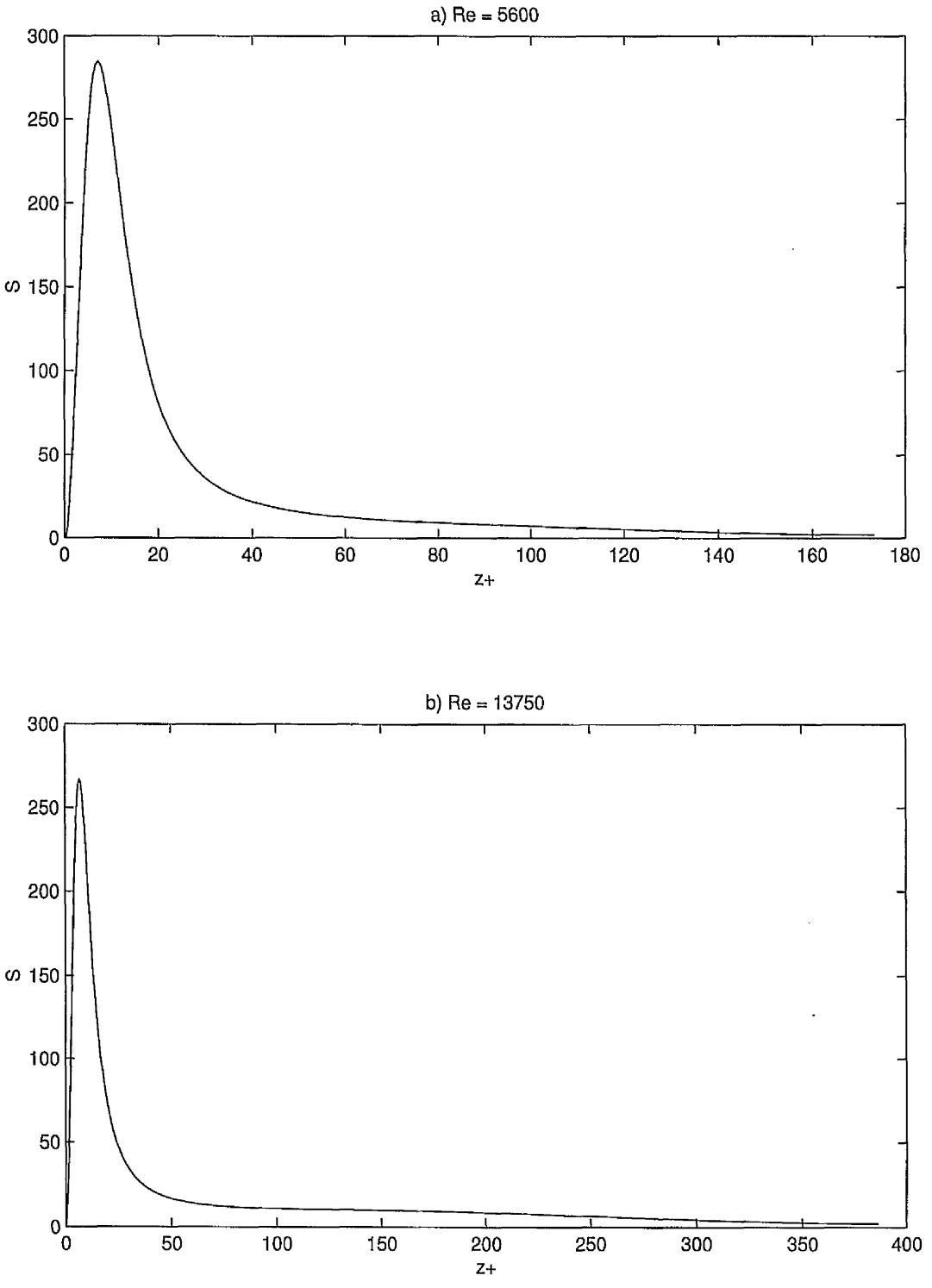

Figure 12: Strain parameter profiles for k-ϵ-S model in channel flow (a) $Re_b = 5600$, (b) $Re_b = 13750$

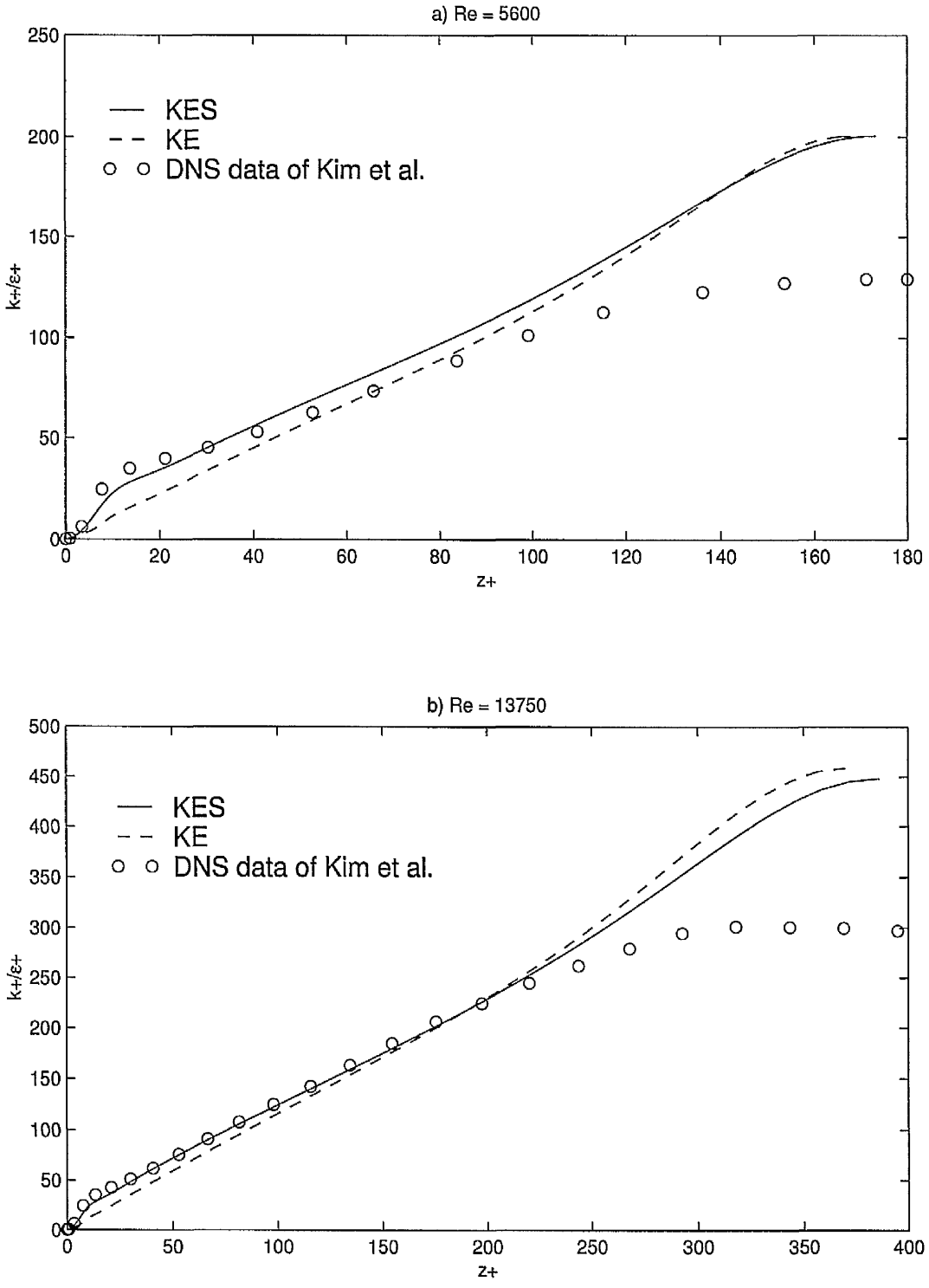

Figure 13: Turbulent time scale profiles in channel flow (a) $Re_b = 5600$, (b) $Re_b = 13750$: model solutions compared with DNS data of Kim *et al* (1987) and Kim (1990)

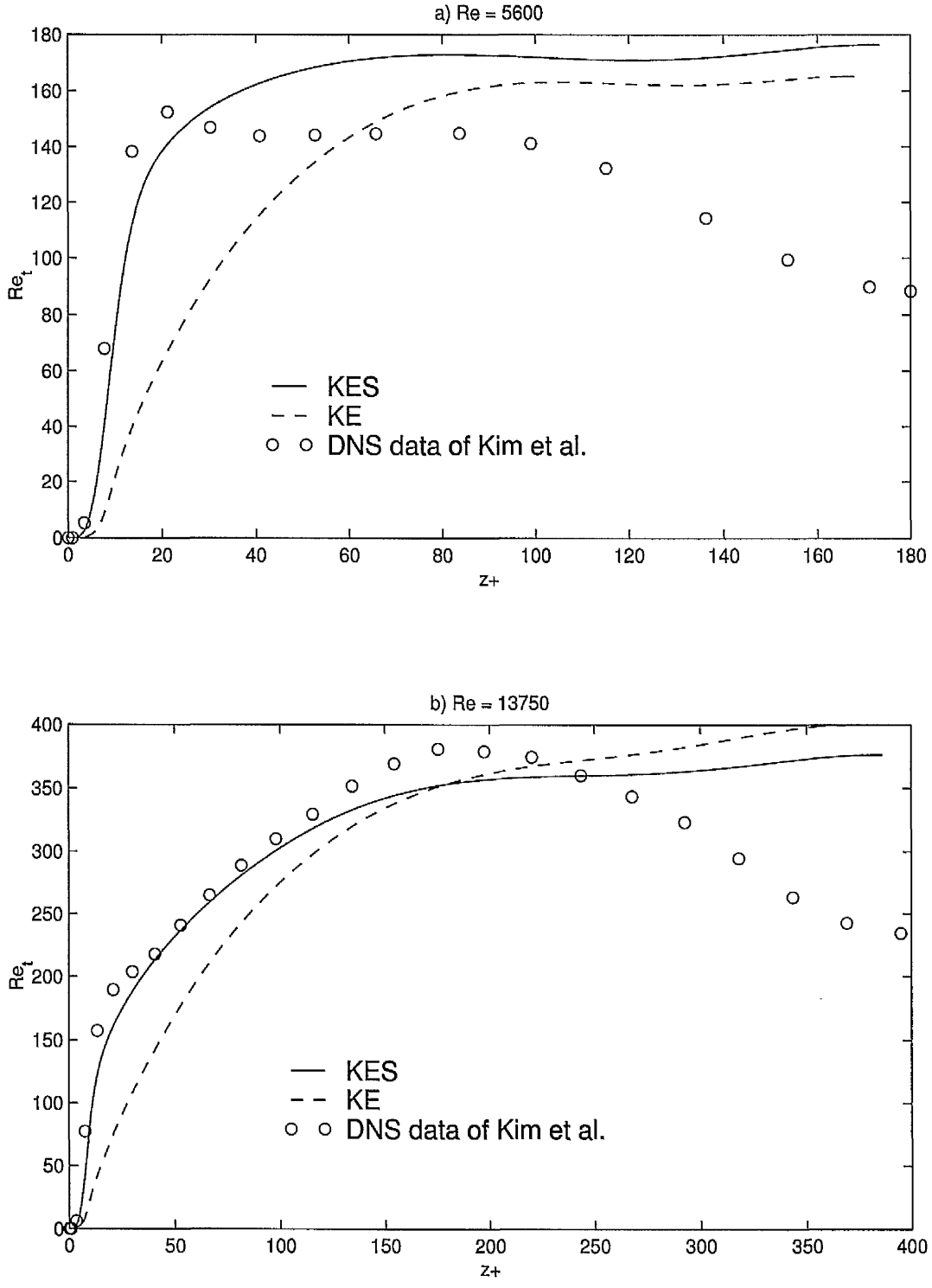

Figure 14: Turbulent Reynolds number profiles in channel flow (a) $Re_b = 5600$, (b) $Re_b = 13750$: model solutions compared with DNS data of Kim *et al* (1987) and Kim (1990)

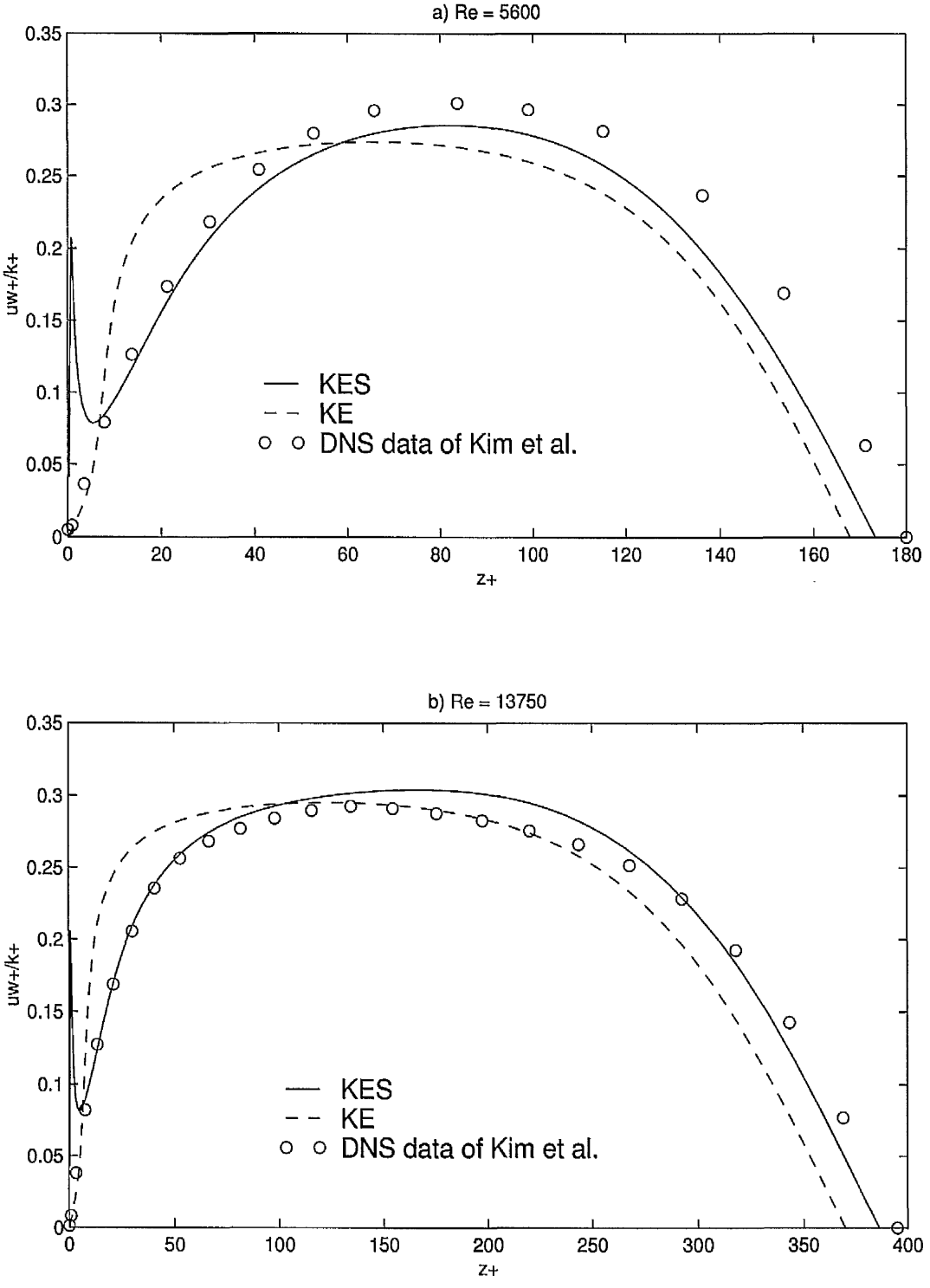

Figure 15: Anisotropic shear stress profiles in channel flow (a) $Re_b = 5600$, (b) $Re_b = 13750$: model solutions compared with DNS data of Kim *et al* (1987) and Kim (1990)

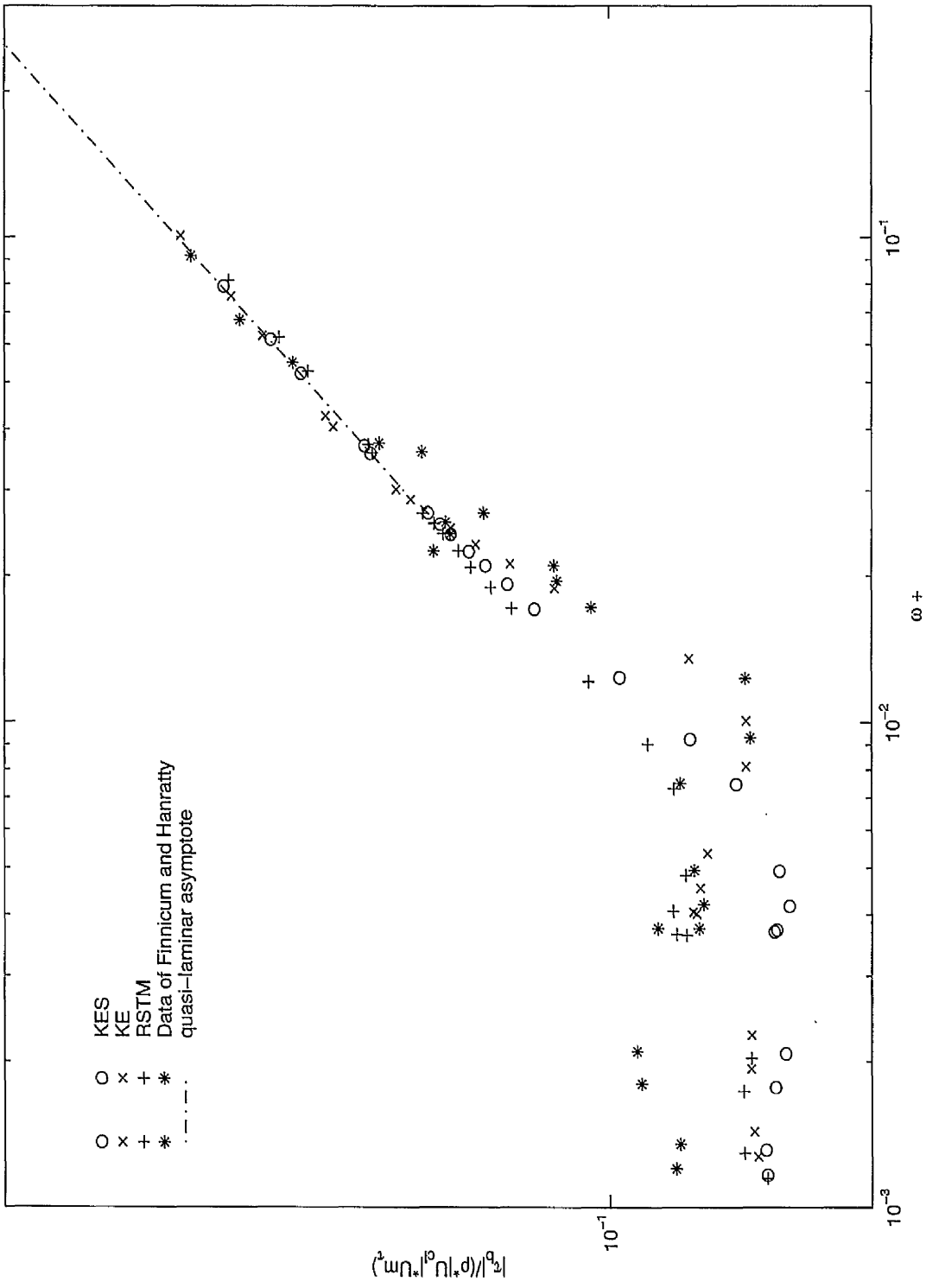

Figure 16: Relation between the dimensionless wall shear stress amplitude and dimensionless frequency parameter: model solutions compared with the experimental data of Finnicum and Hanratty (1988)

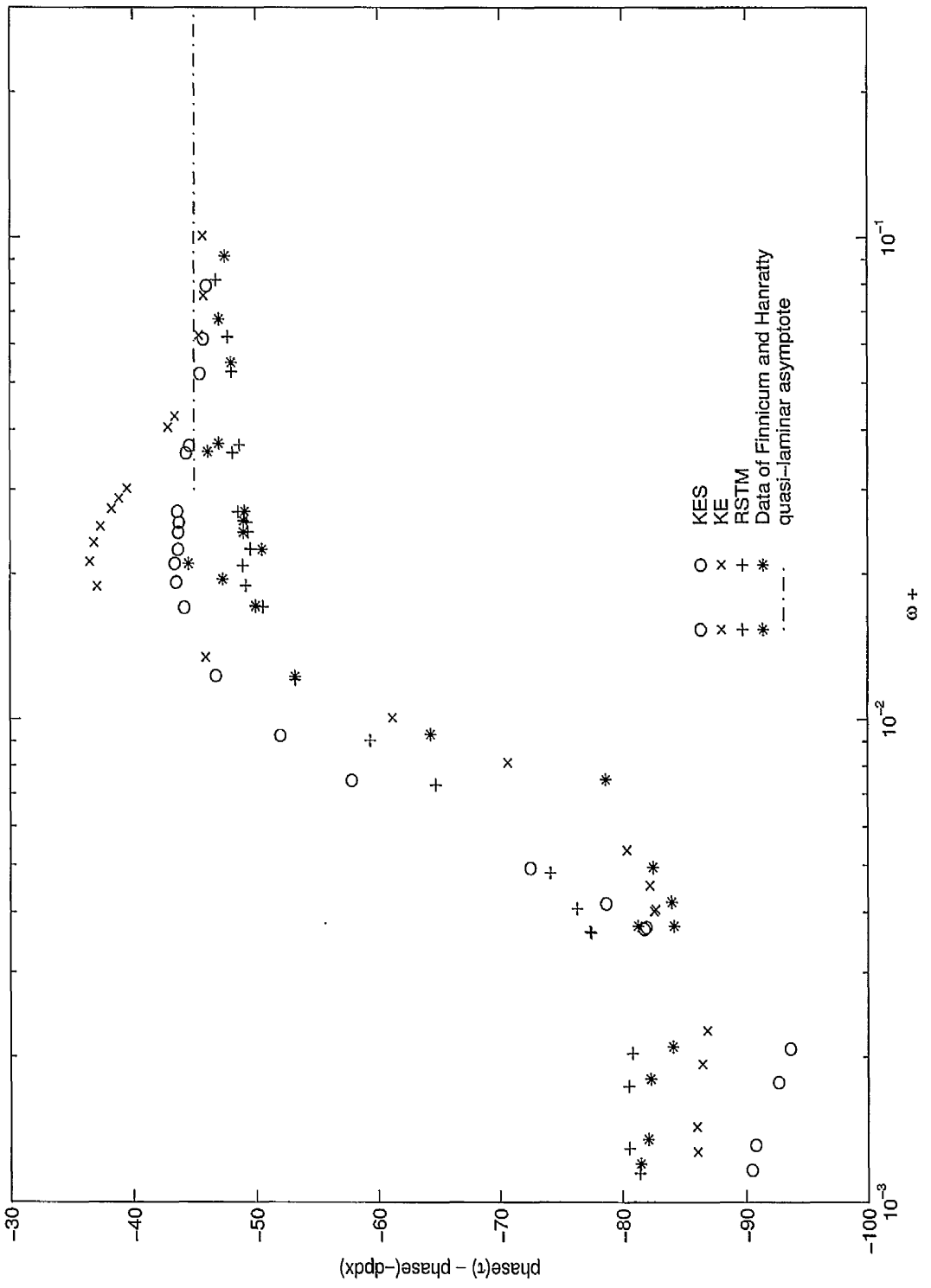

Figure 17: Relation between the dimensionless wall shear stress phase (with respect to pressure gradient) and dimensionless frequency parameter: model solutions compared with the experimental data of Finnicum and Hanratty (1988)

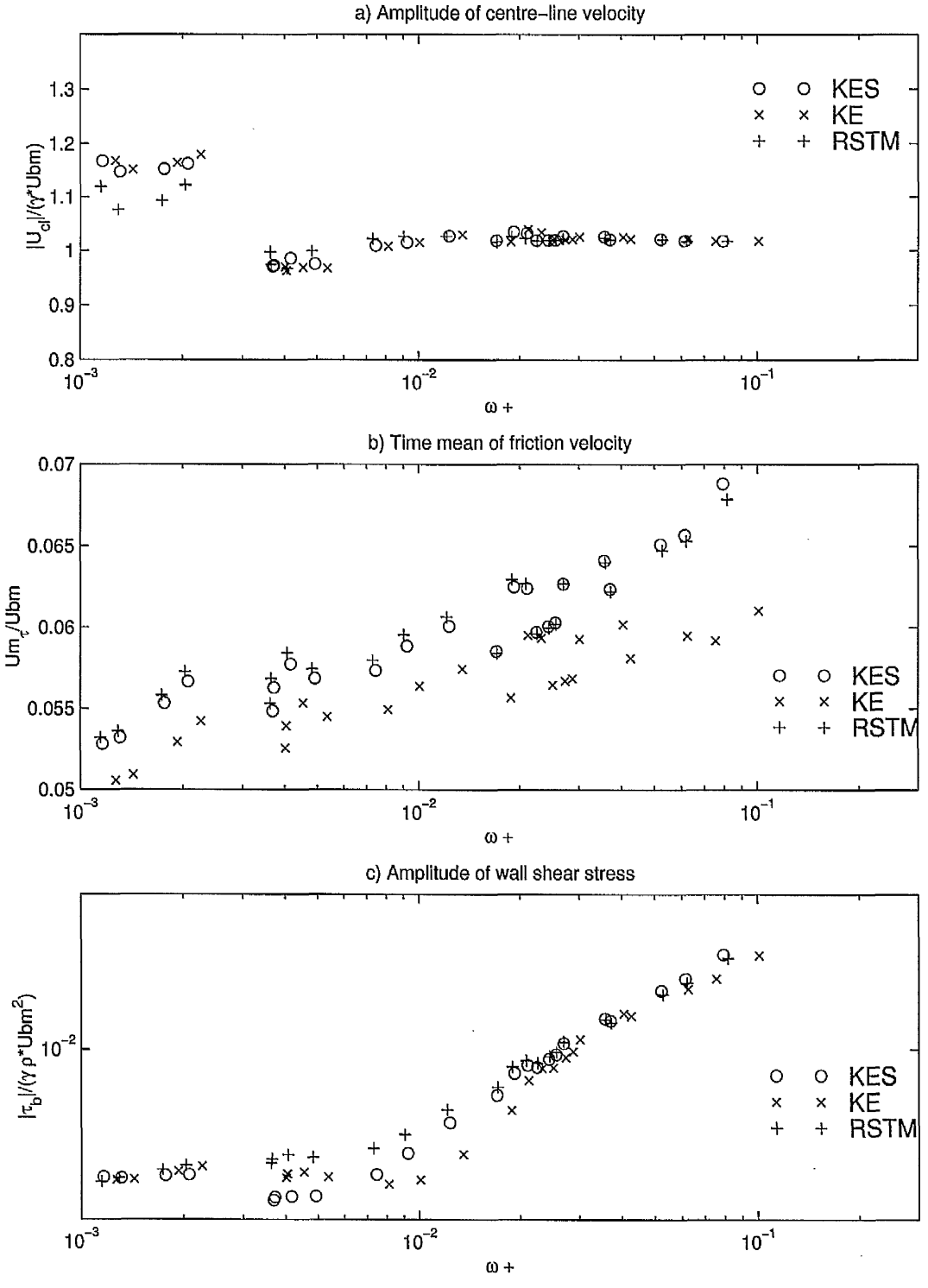

Figure 18: Model solutions for the frequency dependent variables of the dimensionless wall shear stress amplitude

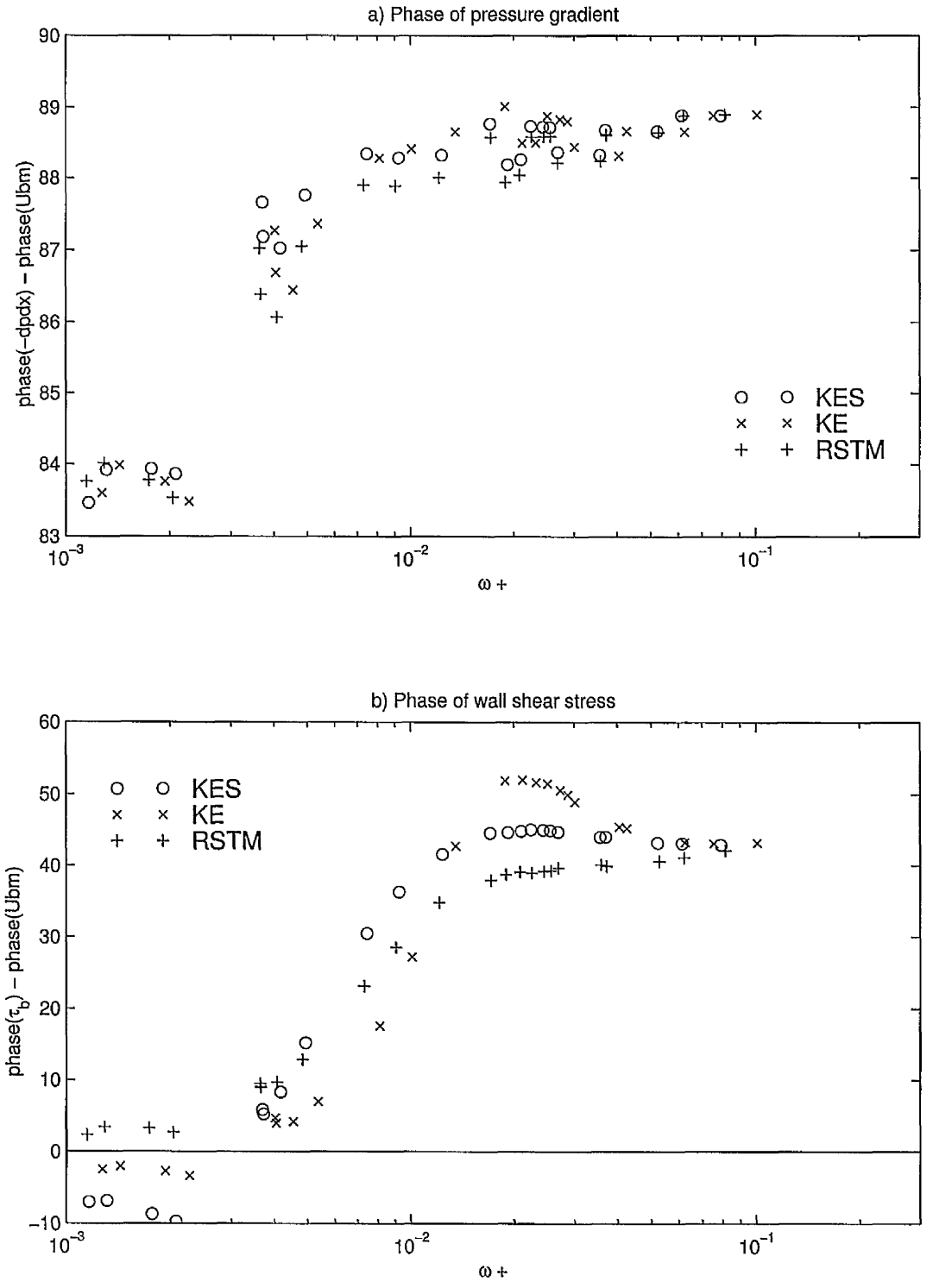

Figure 19: Model solutions for the frequency dependent variables of the dimensionless wall shear stress phase (with respect to bulk velocity)

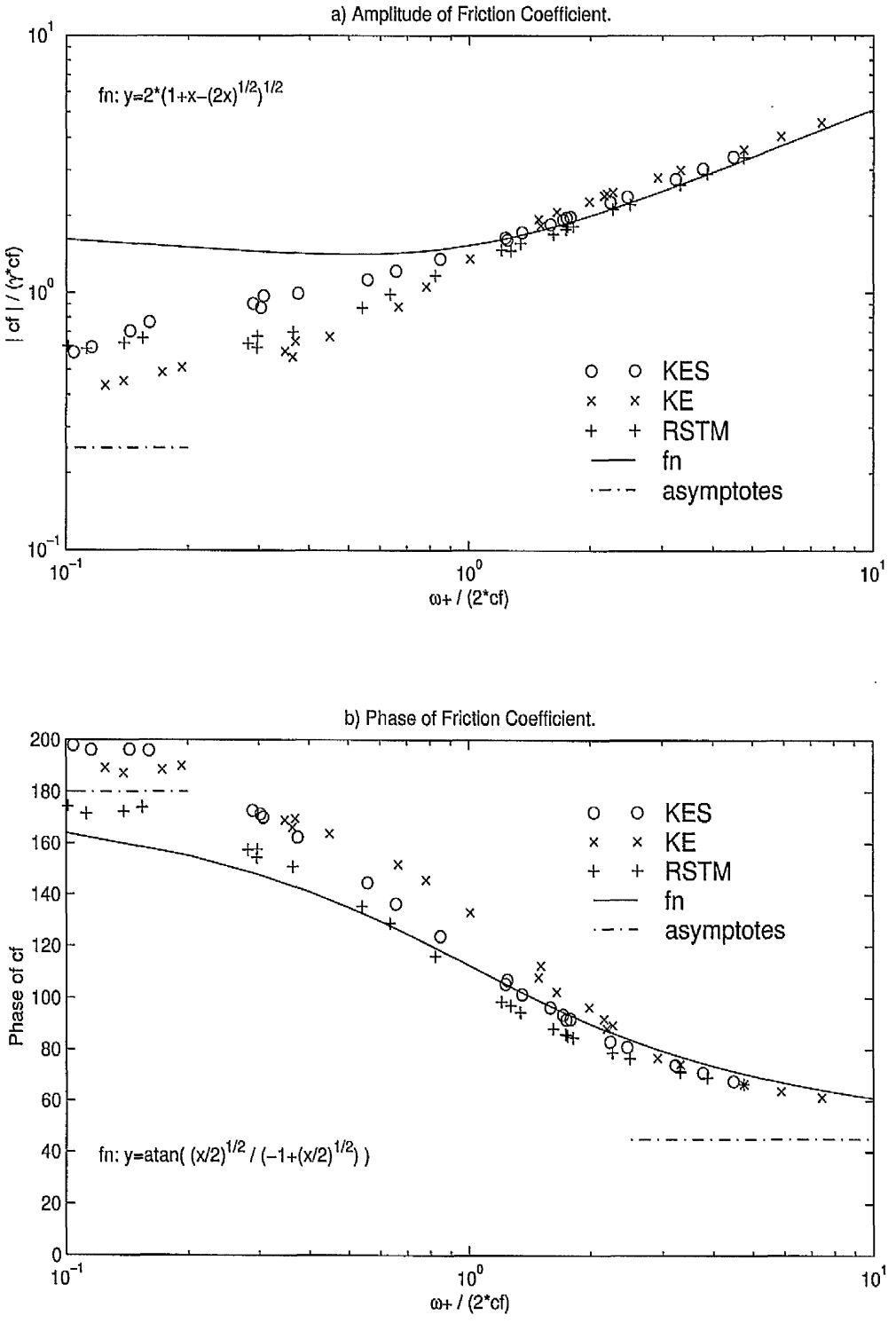

Figure 20: Comparison of model solutions for friction coefficient amplitude and phase with analytical functions and quasi-steady asymptotes

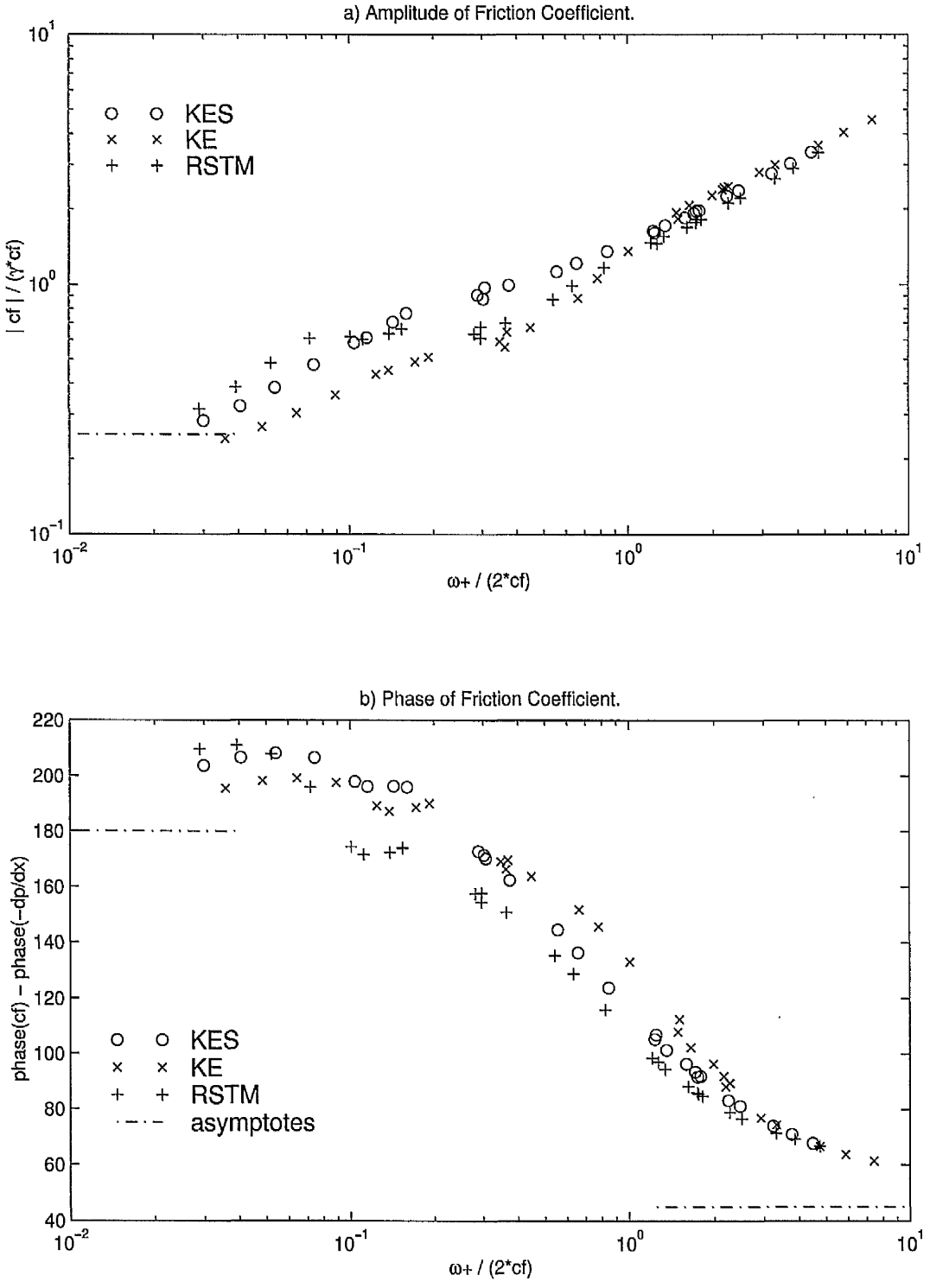

Figure 21: Comparison of model solutions for amplitude and phase of friction coefficient including extra data beyond the experimental runs of Finnicum and Hanratty (1988) to see behaviour near to the aymptotes

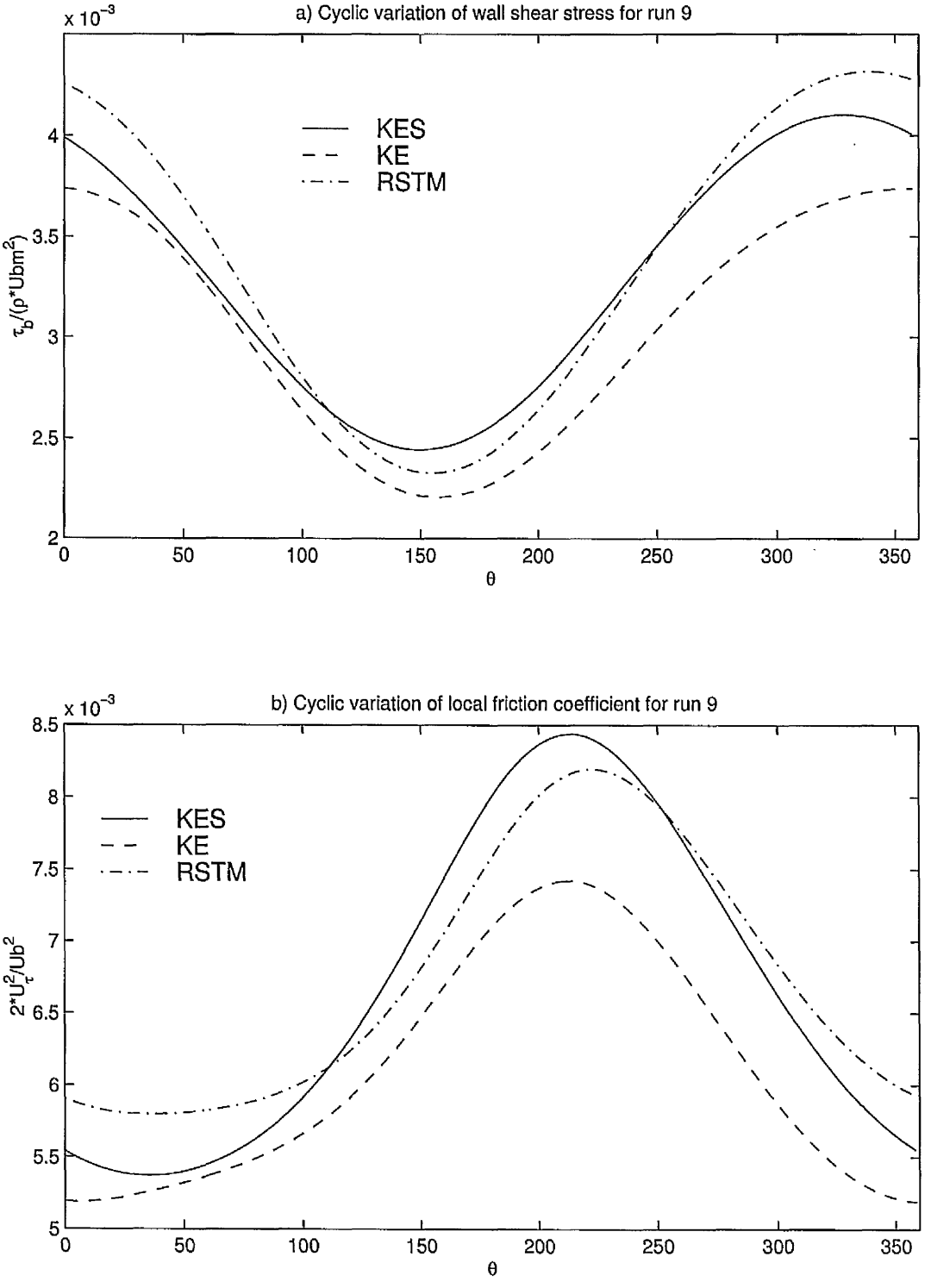

Figure 22: Cyclic variation of (a) wall shear stress and (b) local friction coefficient for $\overline{Re_b} = 21400$ and $f = 0.6$ (run 9): comparison of model solutions

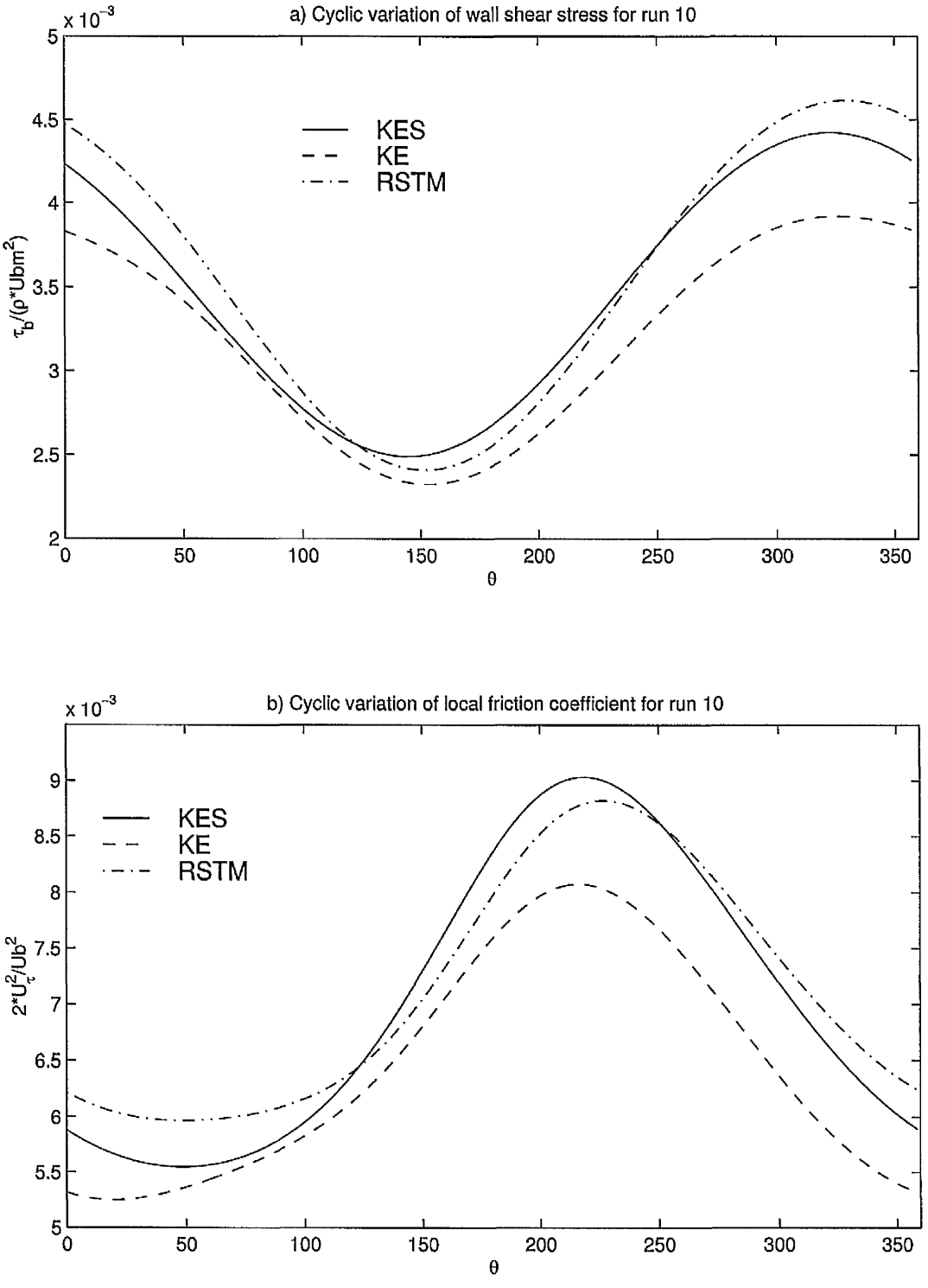

Figure 23: Cyclic variation of (a) wall shear stress and (b) local friction coefficient for $\overline{Re_b} = 17100$ and $f = 0.5$ (run 10): comparison of model solutions

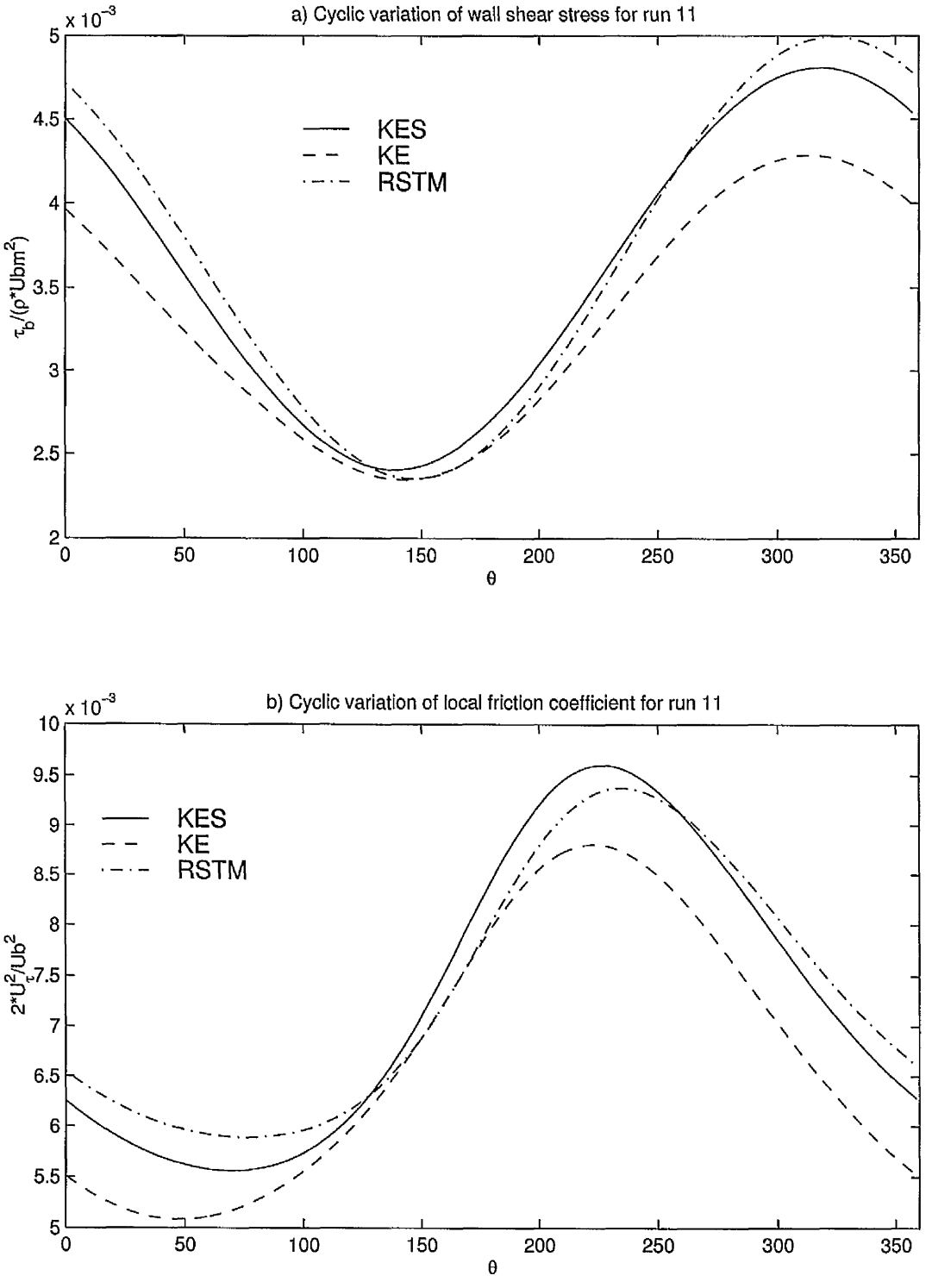

Figure 24: Cyclic variation of (a) wall shear stress and (b) local friction coefficient for $\overline{Re_b} = 14500$ and $f = 0.5$ (run 11): comparison of model solutions

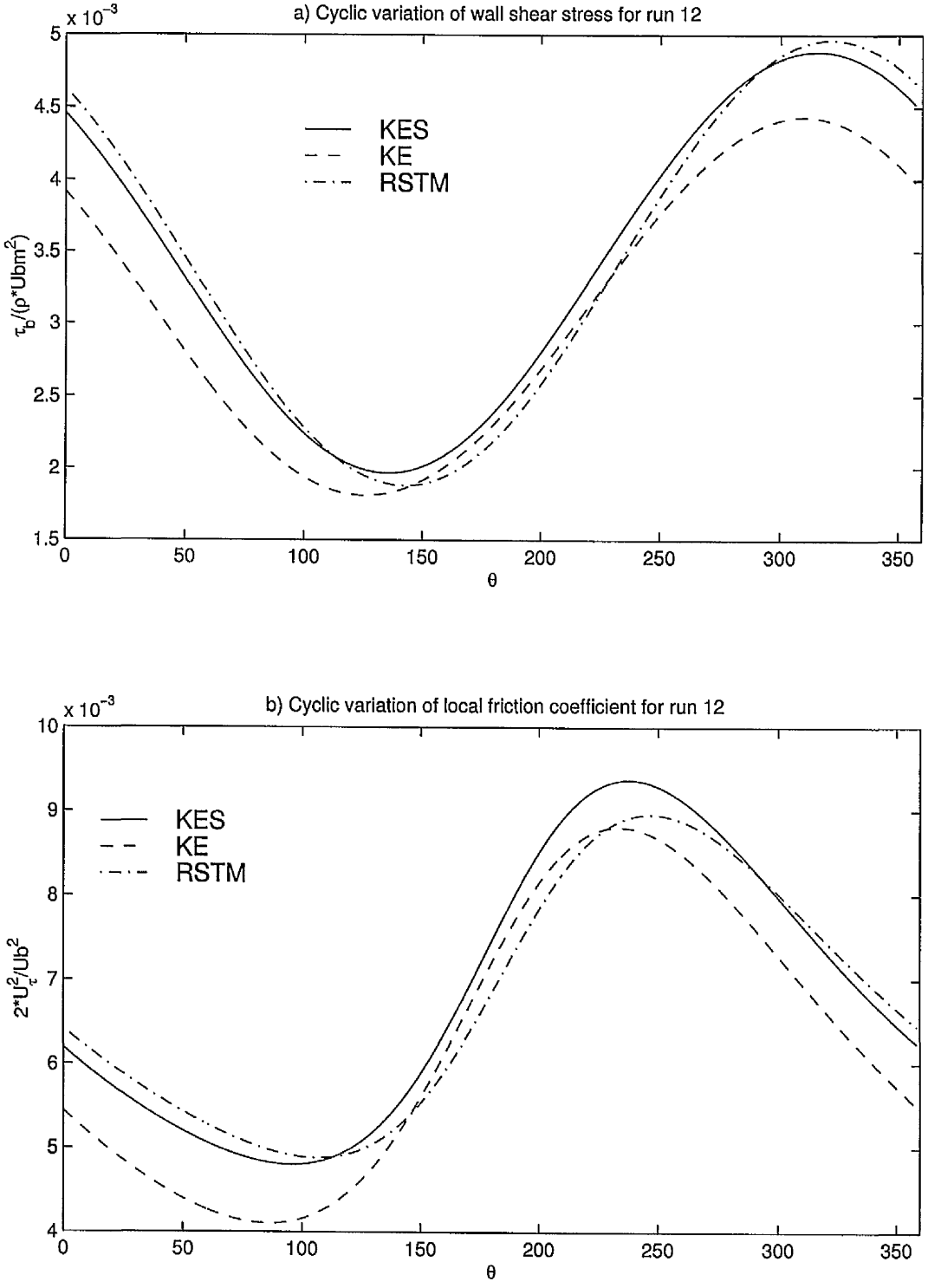

Figure 25: Cyclic variation of (a) wall shear stress and (b) local friction coefficient for $\overline{Re_b} = 17900$ and $f = 1.0$ (run 12): comparison of model solutions

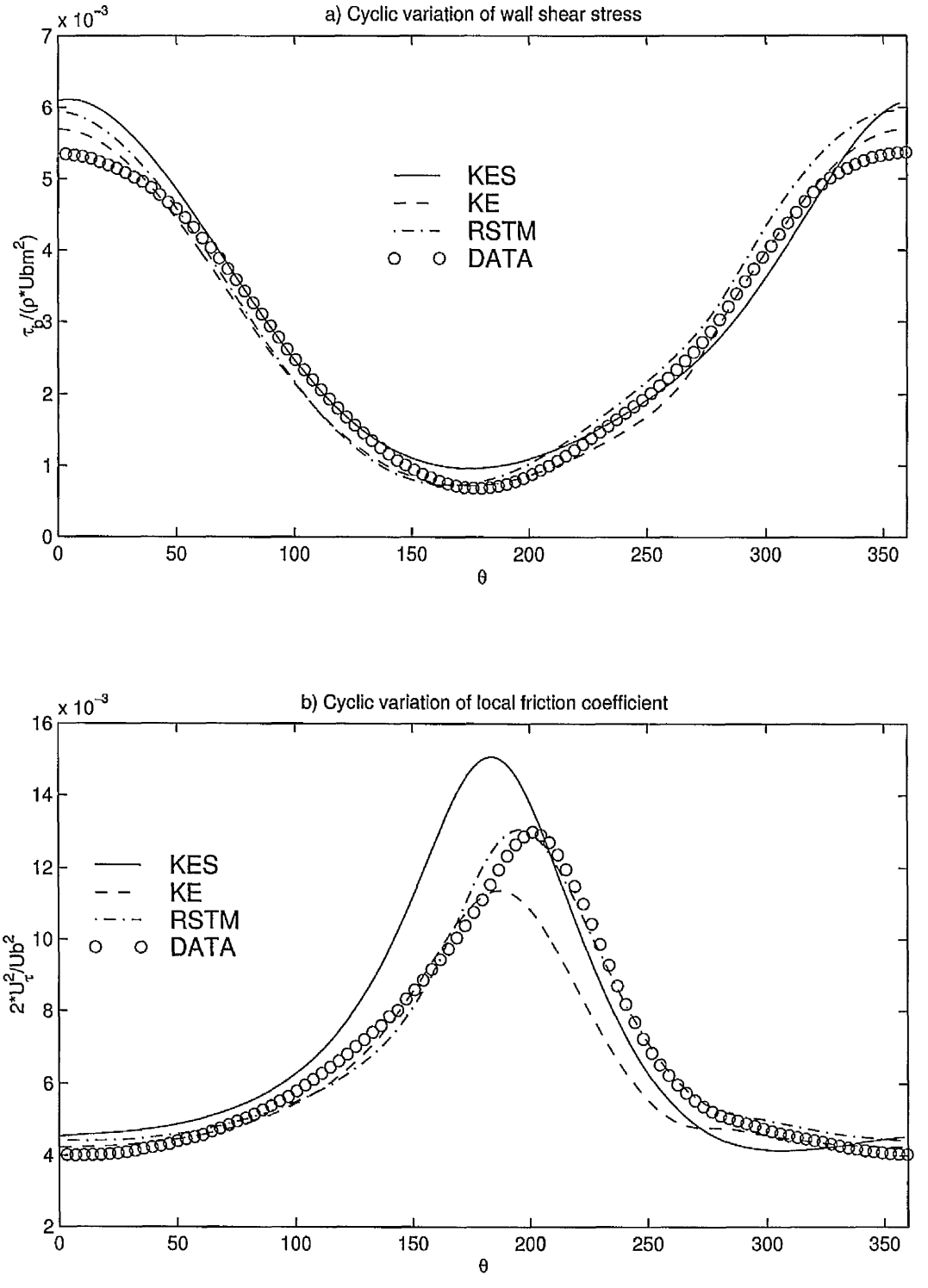

Figure 26: Cyclic variation of (a) wall shear stress, (b) local friction coefficient: model solutions compared with the experimental data of Tu and Ramaprian (1983)

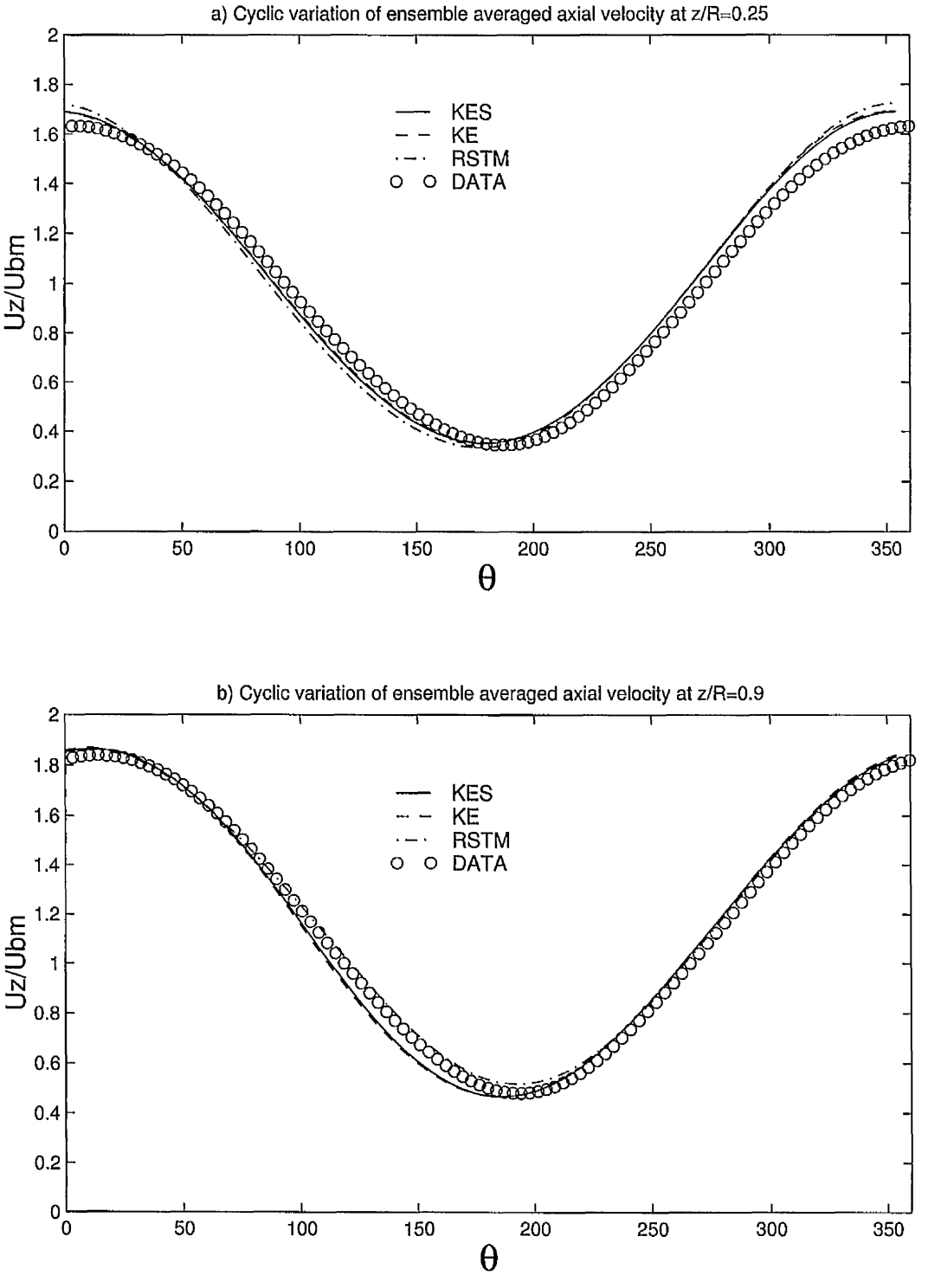

Figure 27: Cyclic variation of ensemble averaged axial velocity at (a) $z/R = 0.25$, (b) $z/R = 0.9$: model solutions compared with the experimental data of Tu and Ramaprian (1983)

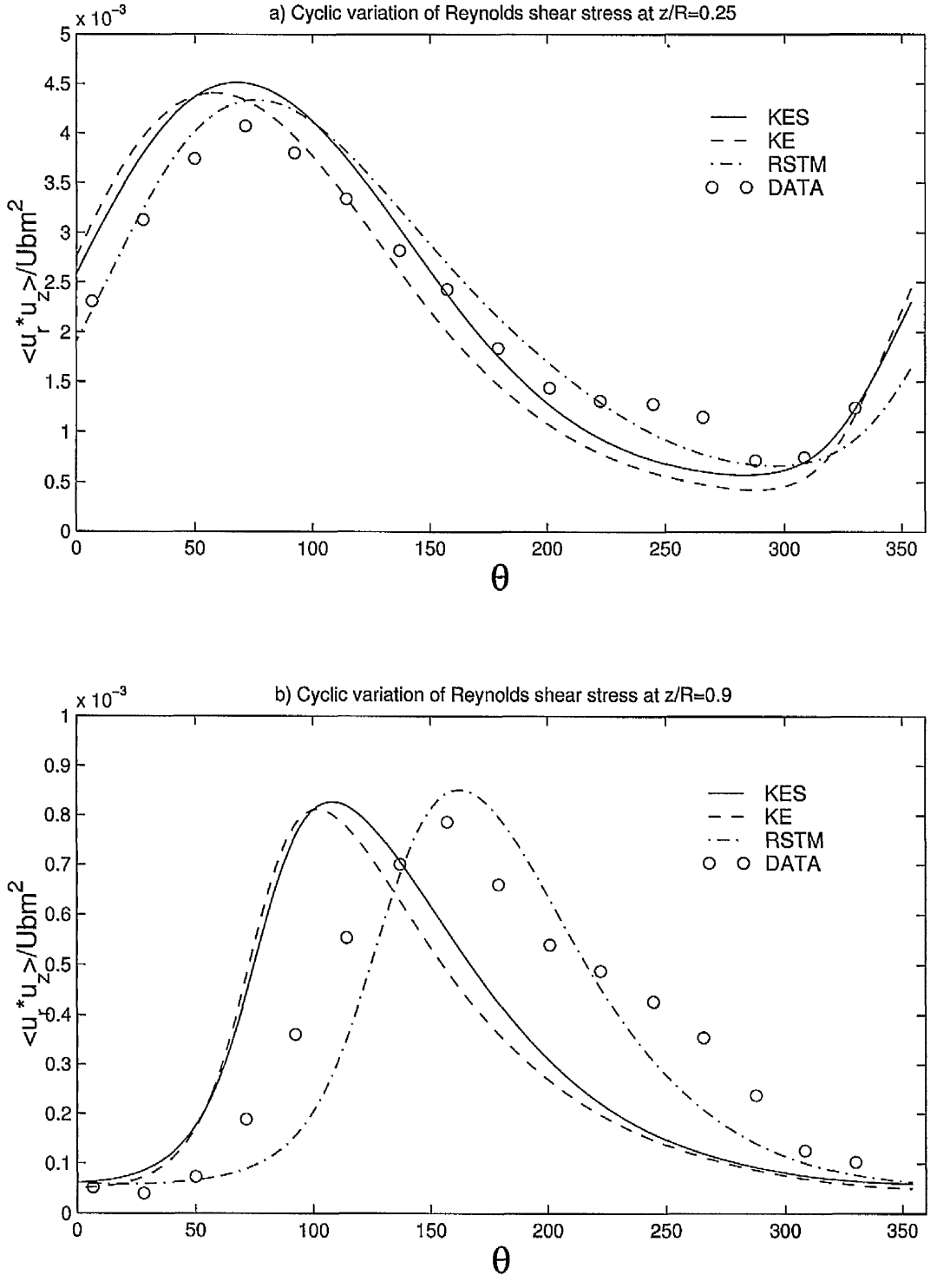

Figure 28: Cyclic variation of Reynolds shear stress at (a) $z/R = 0.25$, (b) $z/R = 0.9$: model solutions compared with the experimental data of Tu and Ramaprian (1983)

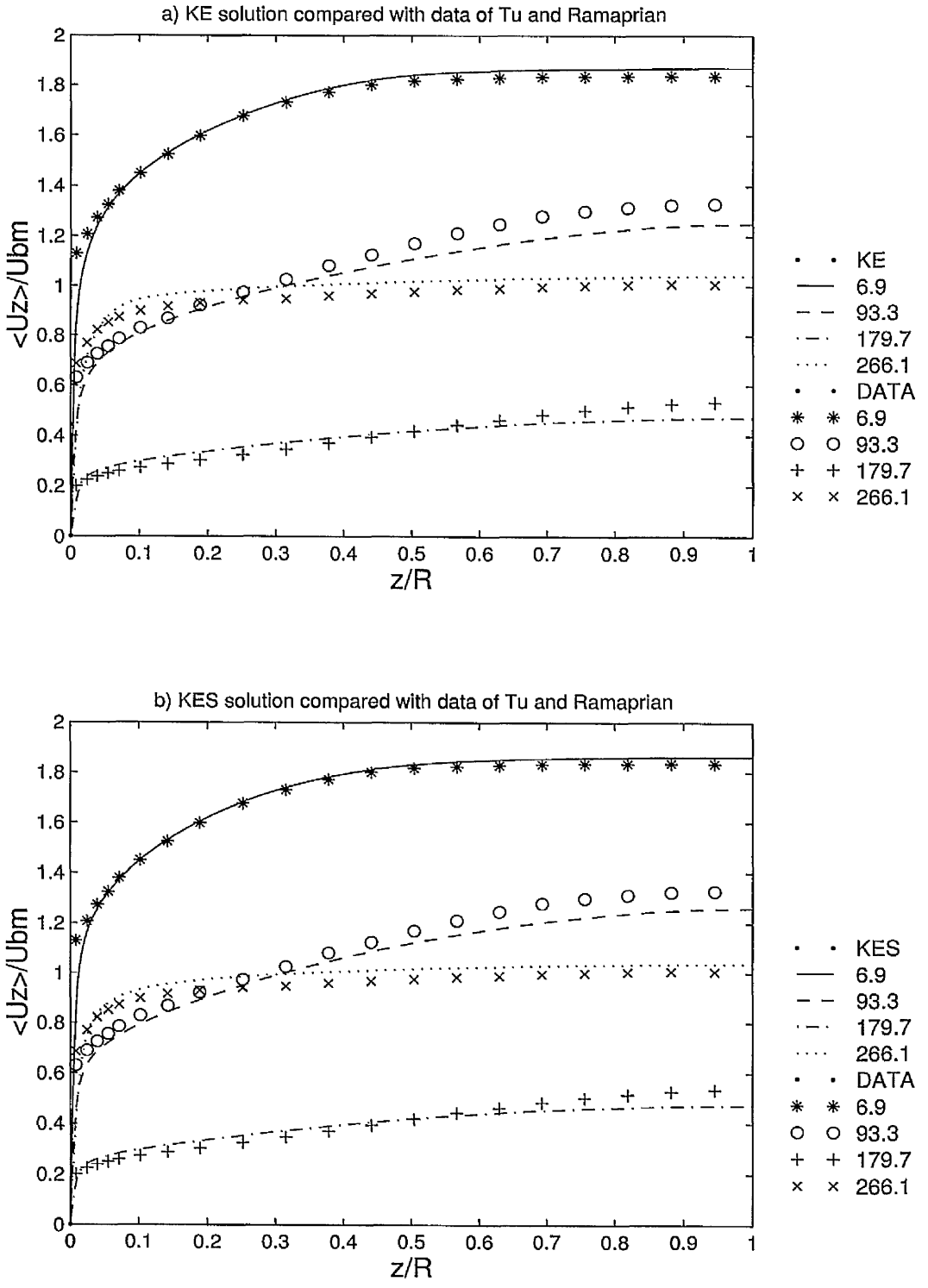

Figure 29: Development of ensemble averaged axial velocity profiles over a cycle: (a) k-ϵ, (b) k-ϵ-S solution compared with the experimental data of Tu and Ramaprian (1983)

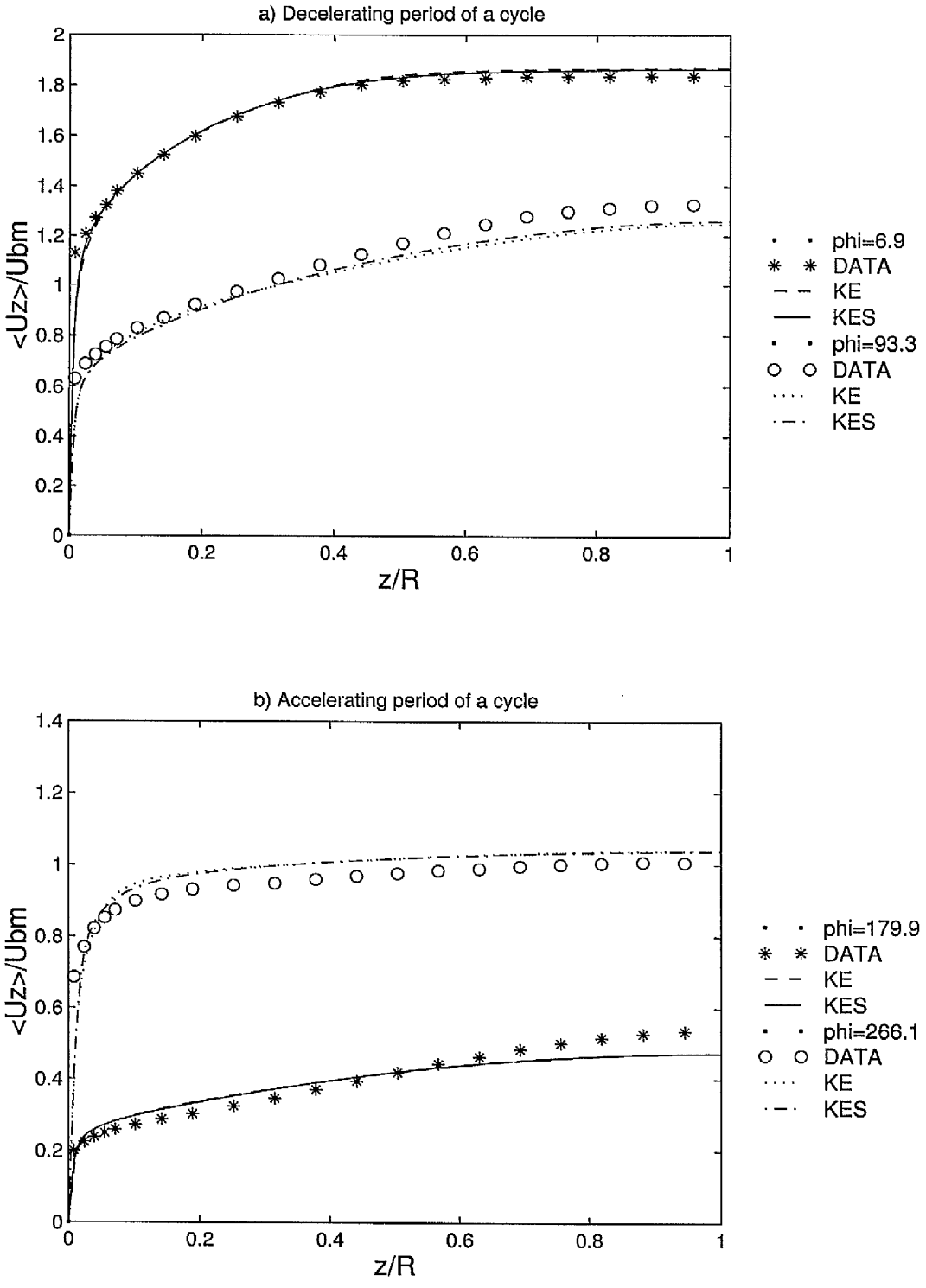

Figure 30: Development of ensemble averaged axial velocity profiles over (a) decelerating, (b) accelerating period of a cycle: model solutions compared with the experimental data of Tu and Ramaprian (1983)

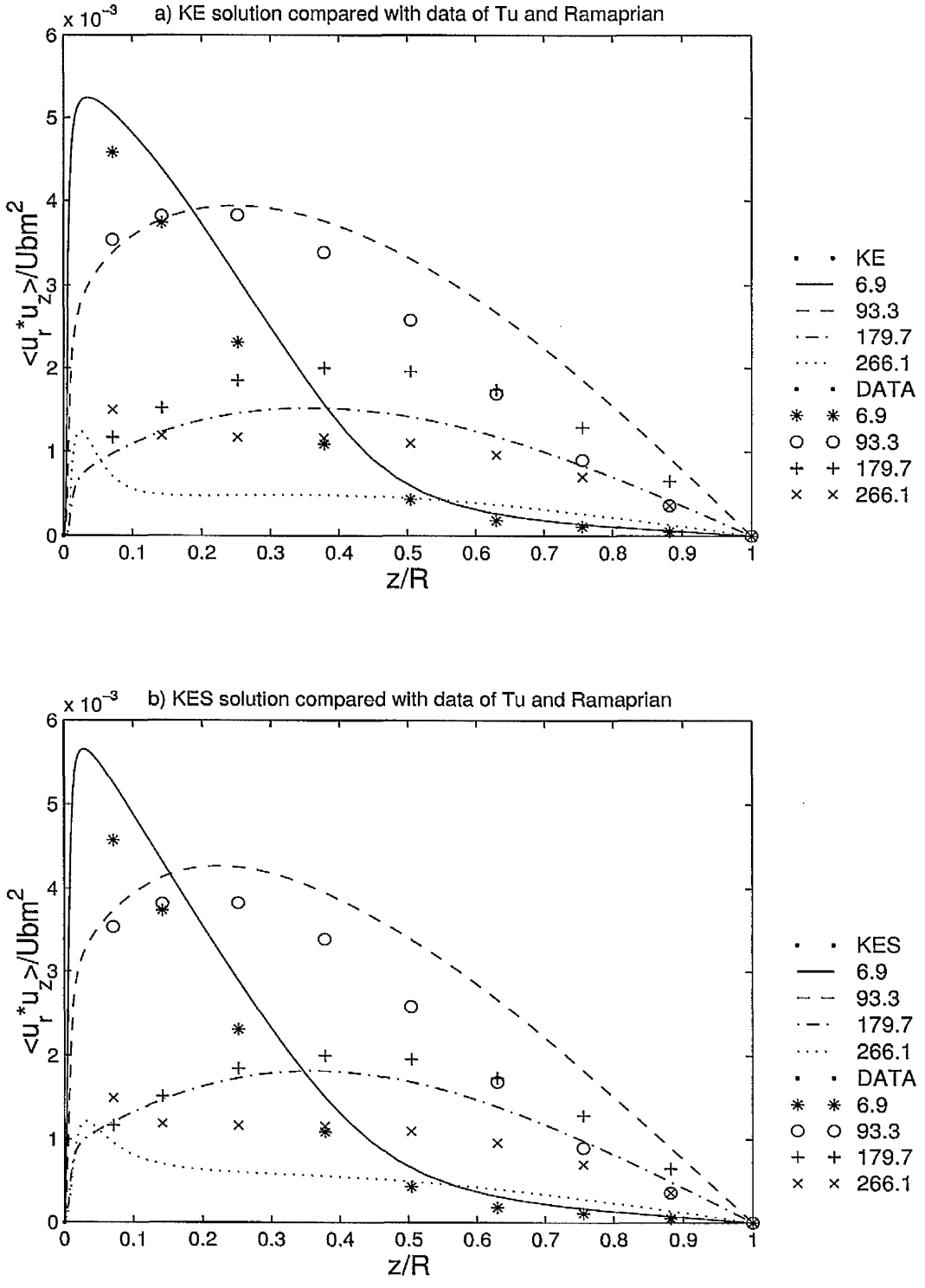

Figure 31: Development of Reynolds shear stress profiles over a cycle: (a) k-ϵ, (b) k-ϵ-S solution compared with the experimental data of Tu and Ramaprian (1983)

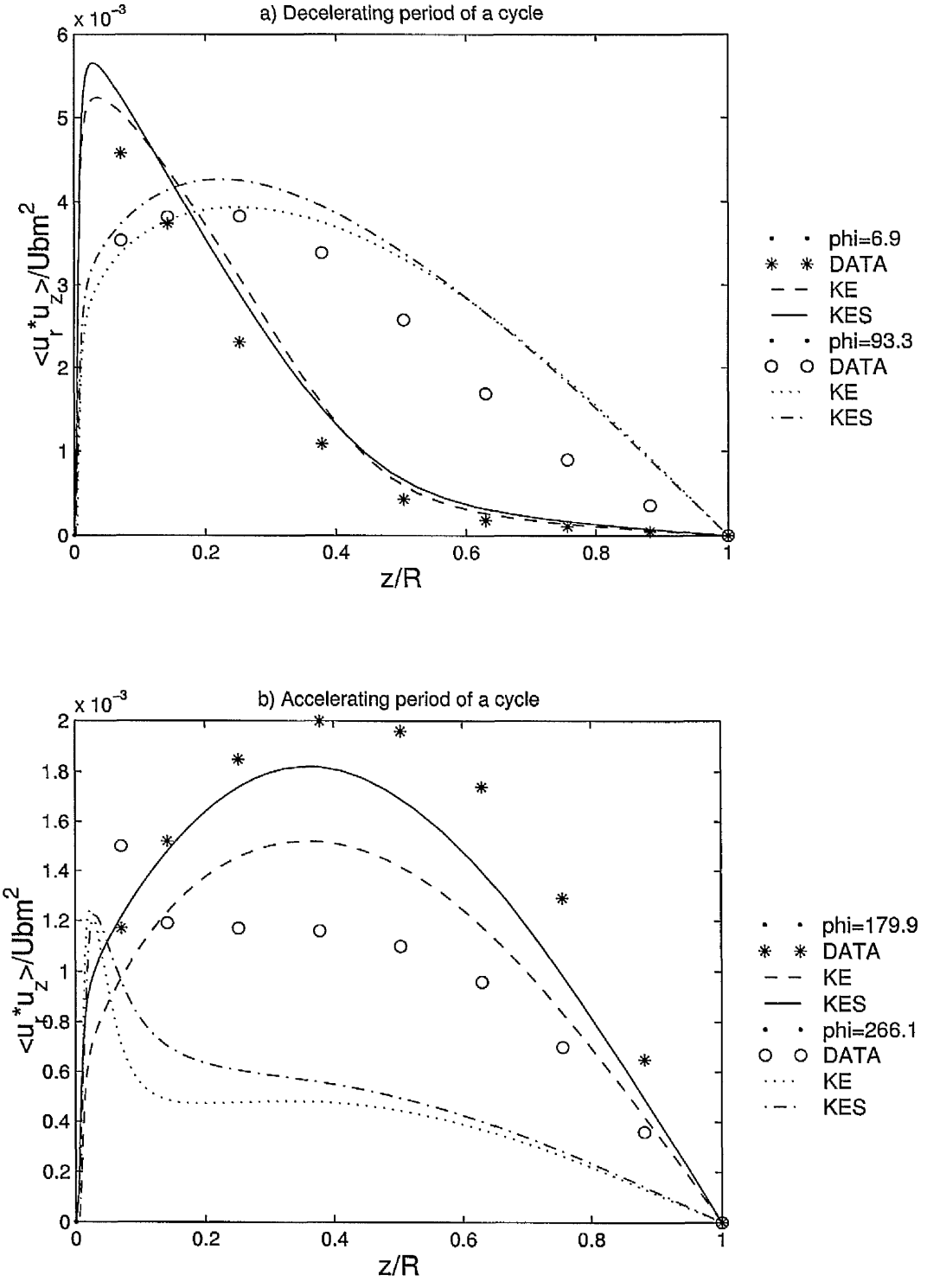

Figure 32: Development of Reynolds shear stress profiles over (a) decelerating, (b) accelerating period of a cycle: model solutions compared with the experimental data of Tu and Ramaprian (1983)

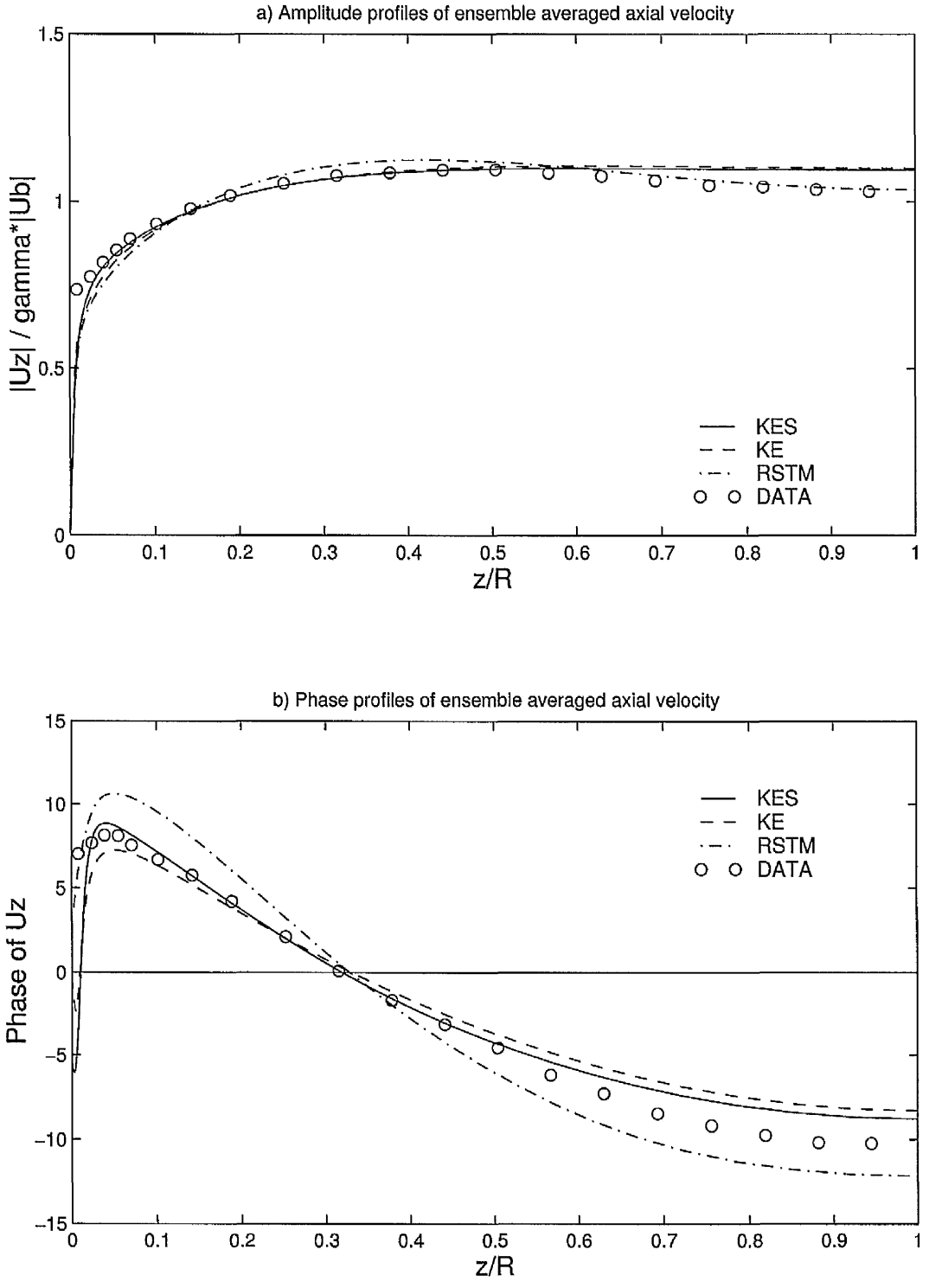

Figure 33: (a) Amplitude and (b) Phase profiles of ensemble averaged axial velocity: model solutions compared with the experimental data of Tu and Ramaprian (1983)

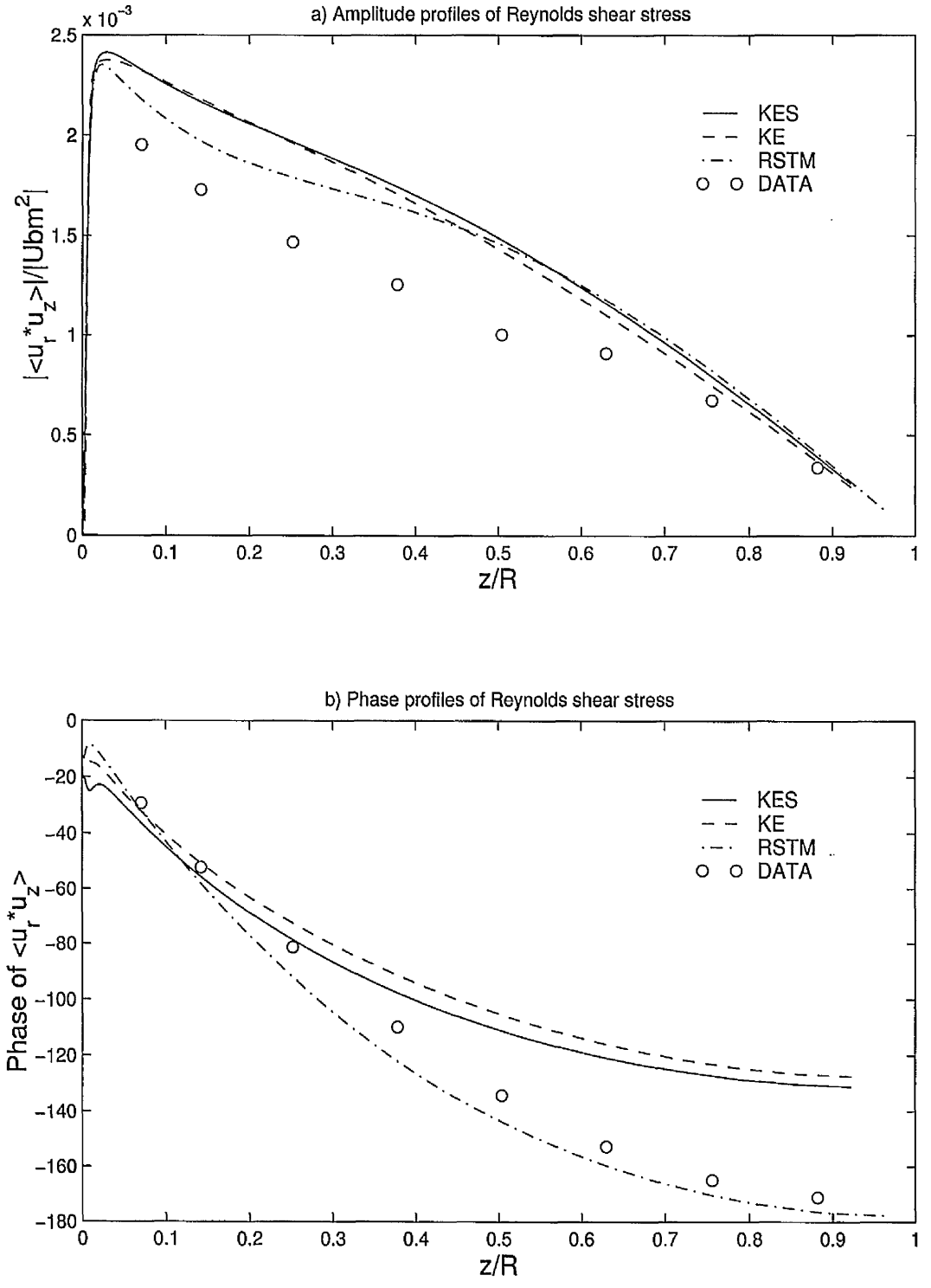

Figure 34: (a) Amplitude and (b) Phase profiles of Reynolds shear stress: model solutions compared with the experimental data of Tu and Ramaprian (1983)

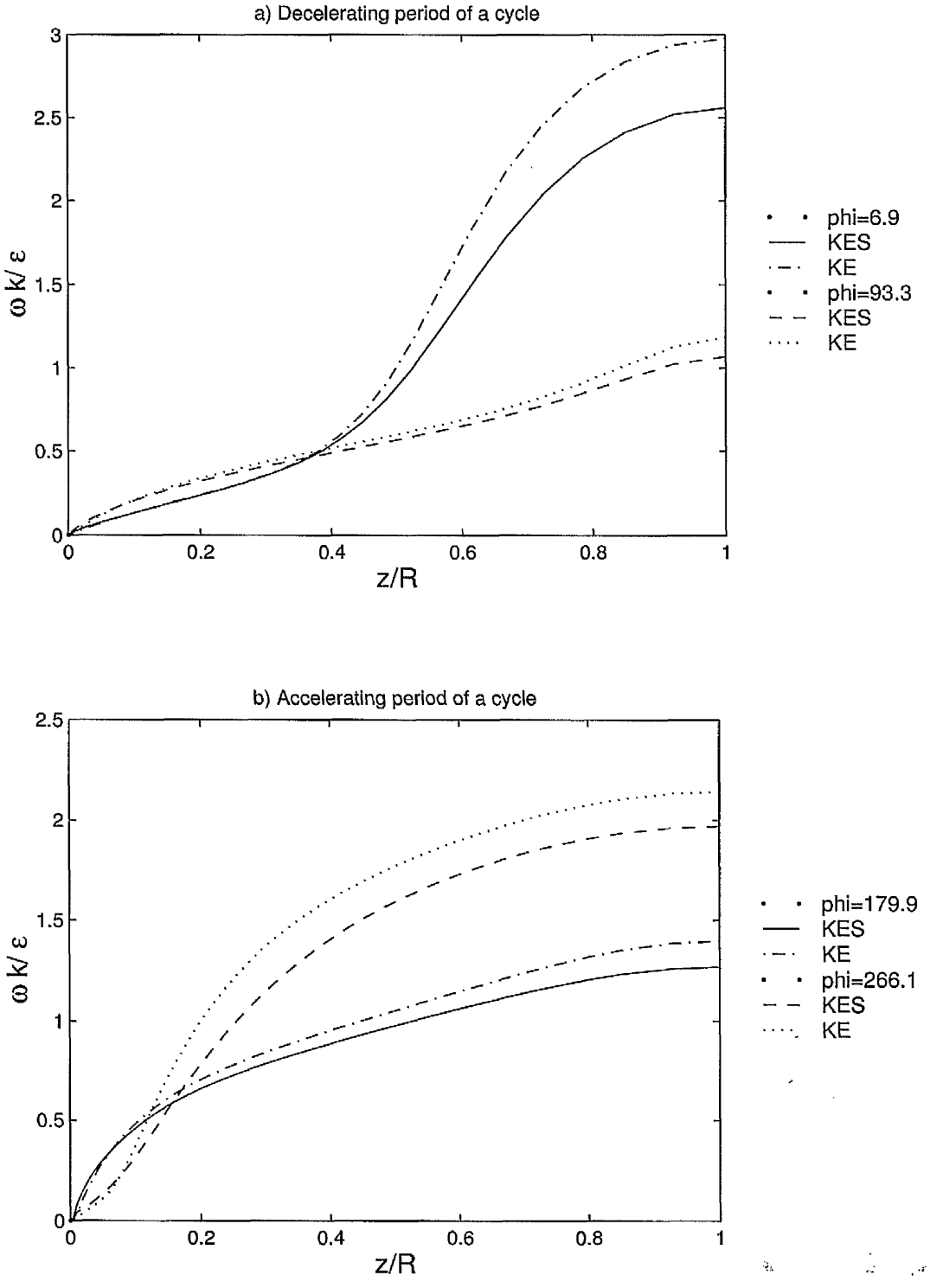

Figure 35: Turbulent time scale profiles over the (a) decelerating, (b) accelerating period of a cycle calculated by the k-ϵ-S and k-ϵ models

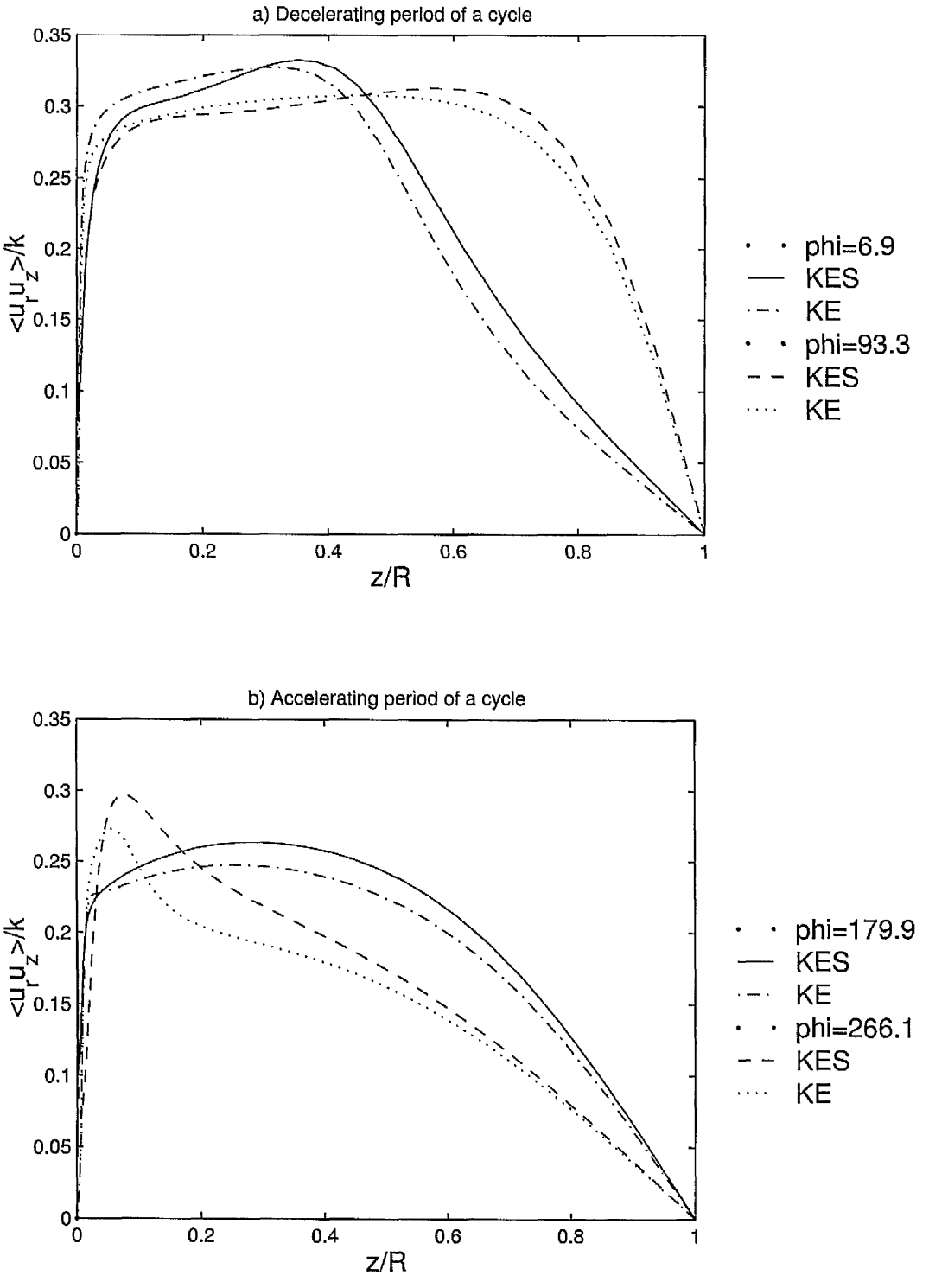

Figure 36: Anisotropic shear stress profiles over the (a) decelerating, (b) accelerating period of a cycle calculated the k-ϵ-S and k-ϵ models

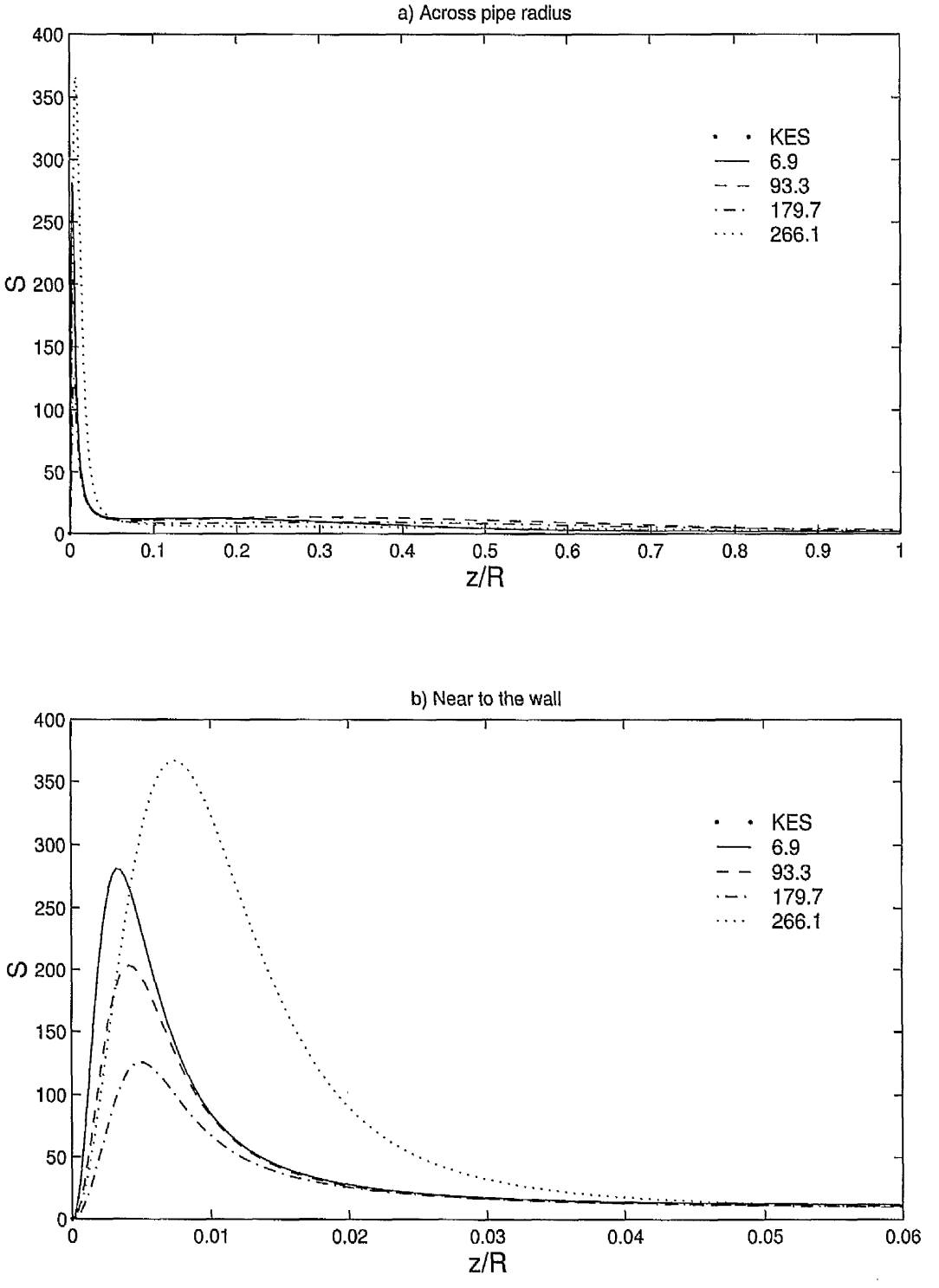

Figure 37: Strain parameter profiles (a) across the pipe radius, (b) near to the wall calculated by the k-ϵ-S model

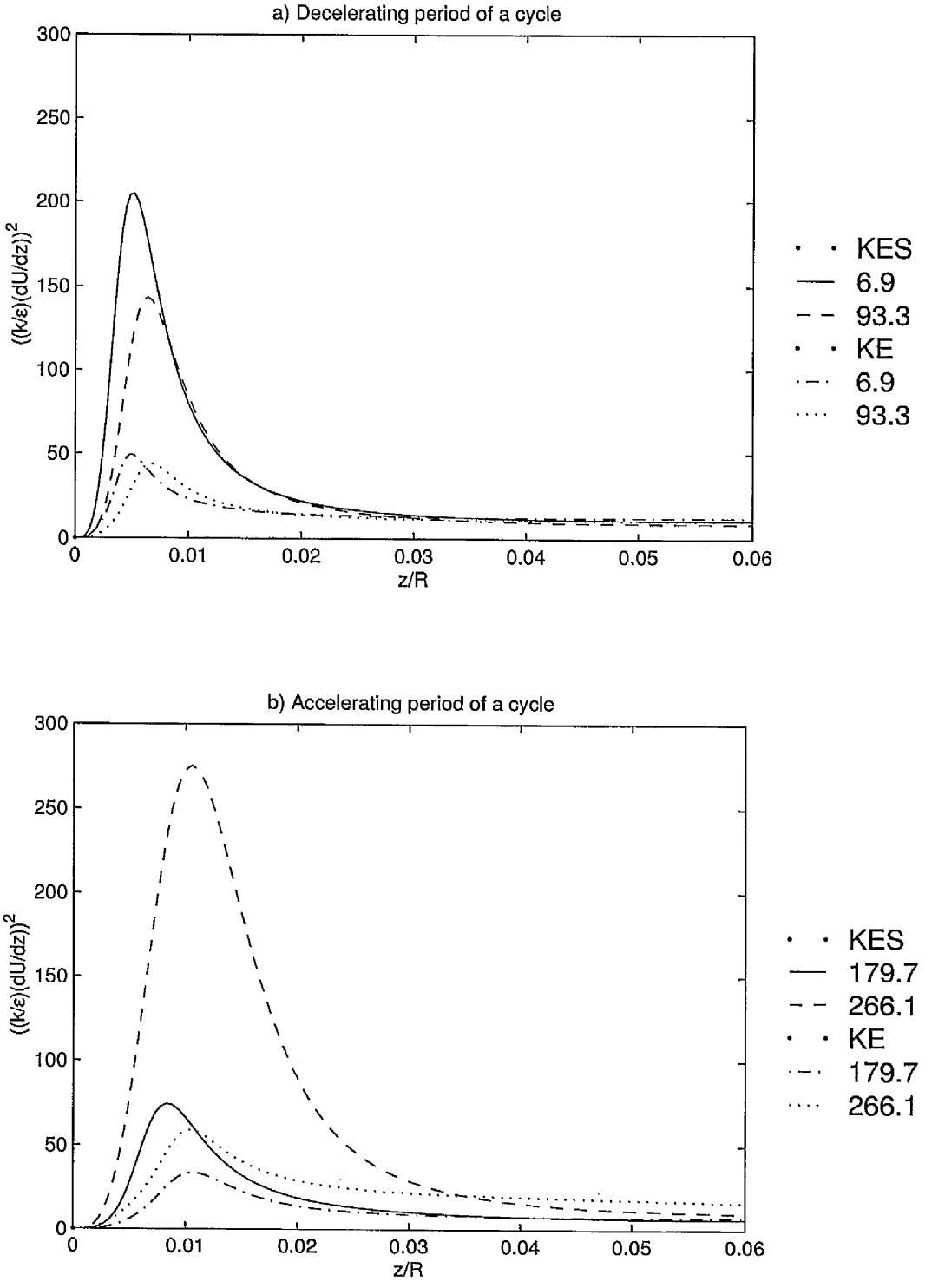

Figure 38: Strain parameter $\left(\frac{k}{\epsilon}\frac{\partial U}{\partial z}\right)^2$, profiles over the (a) decelerating, (b) accelerating period of a cycle near to the wall calculated by the k-ϵ-S and k-ϵ model

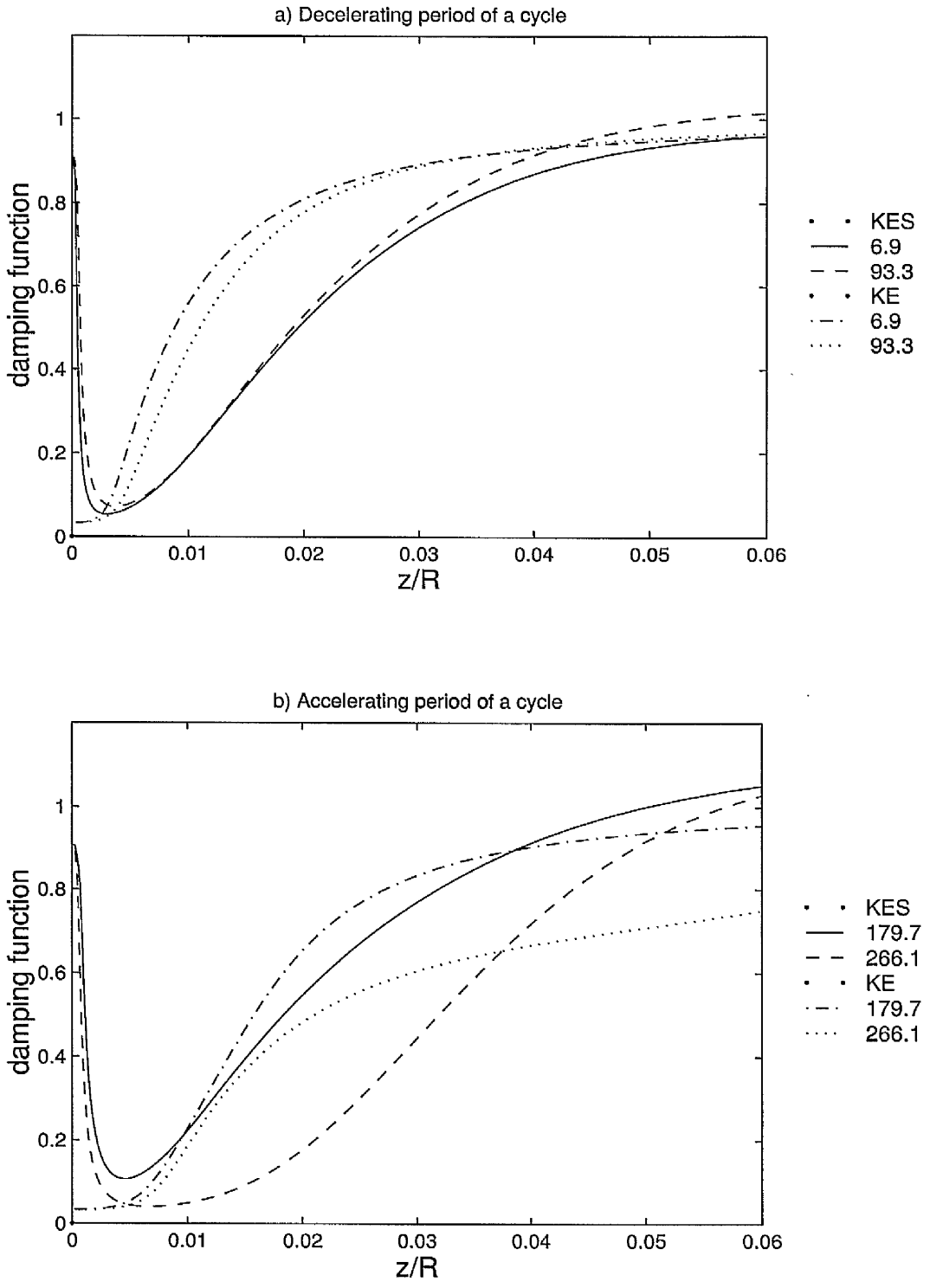

Figure 39: Composite damping function profiles over the (a) decelerating, (b) accelerating period of a cycle near to the wall calculated by the k-ϵ-S and k-ϵ model

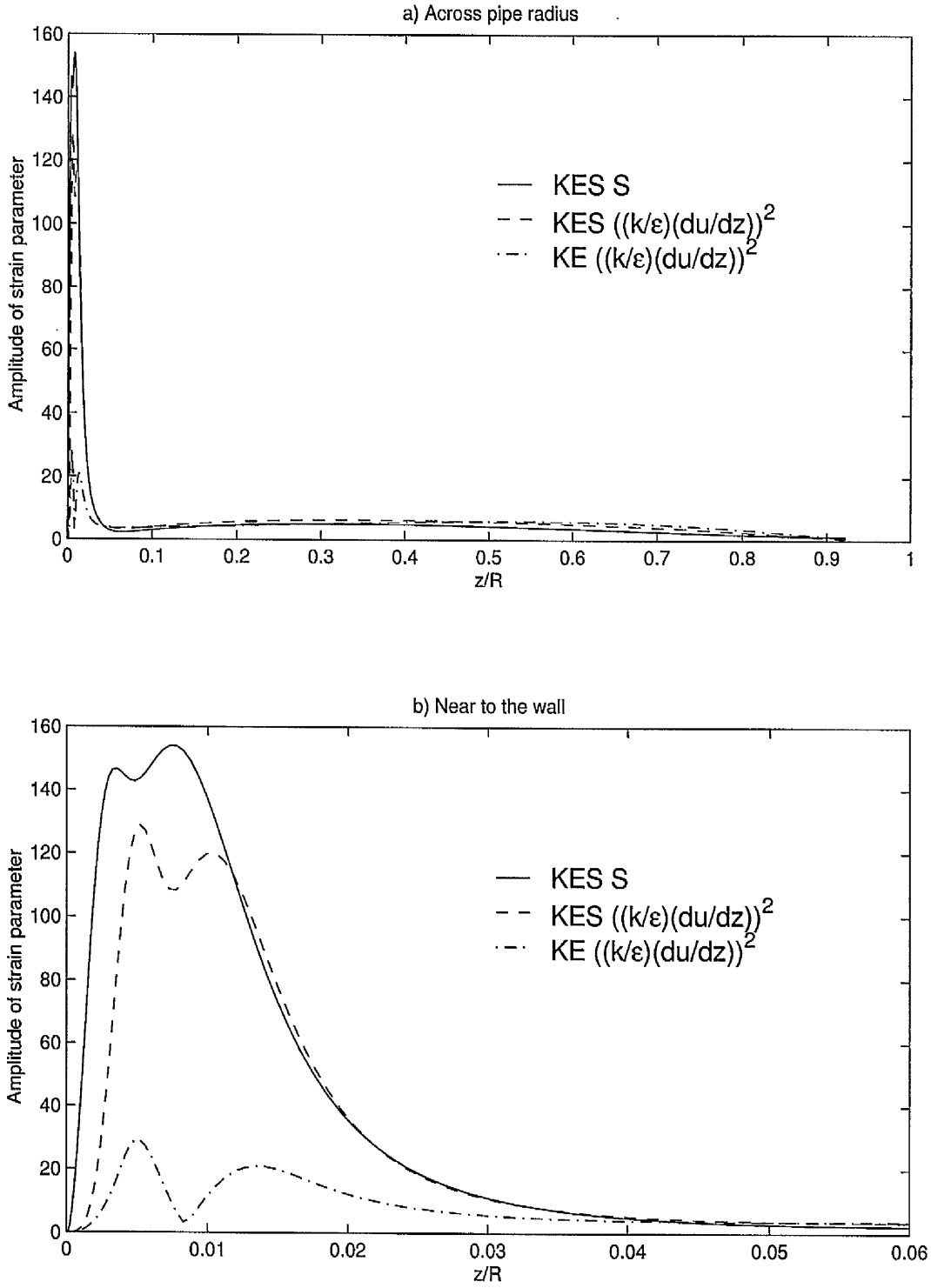

Figure 40: Amplitude of strain parameters (a) across the pipe radius, (b) near to the wall calculated by the k-ϵ-S and k-ϵ models

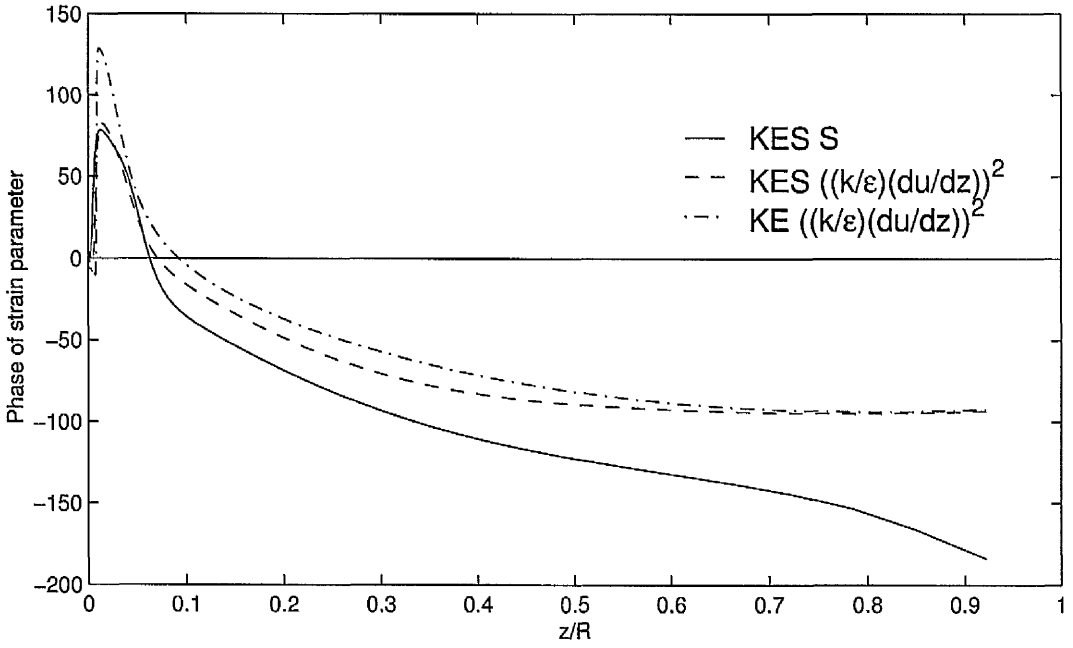

Figure 41: Phase of strain parameters calculated by the k-ϵ-S and k-ϵ model

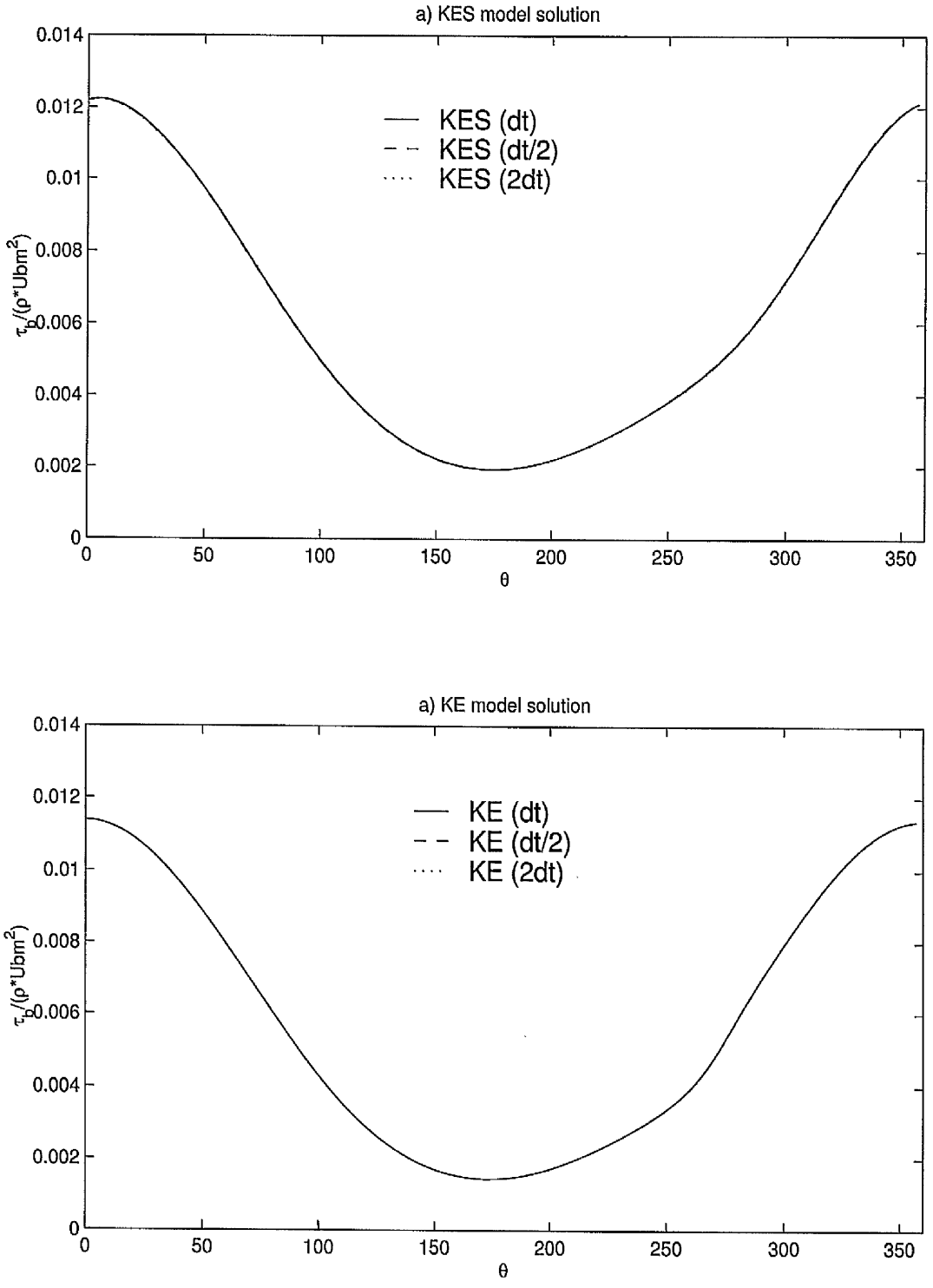

Figure 42: Sensitivity of (a) k-ϵ-S, (b) k-ϵ model to numerical time step: Cyclic variation of wall shear stress

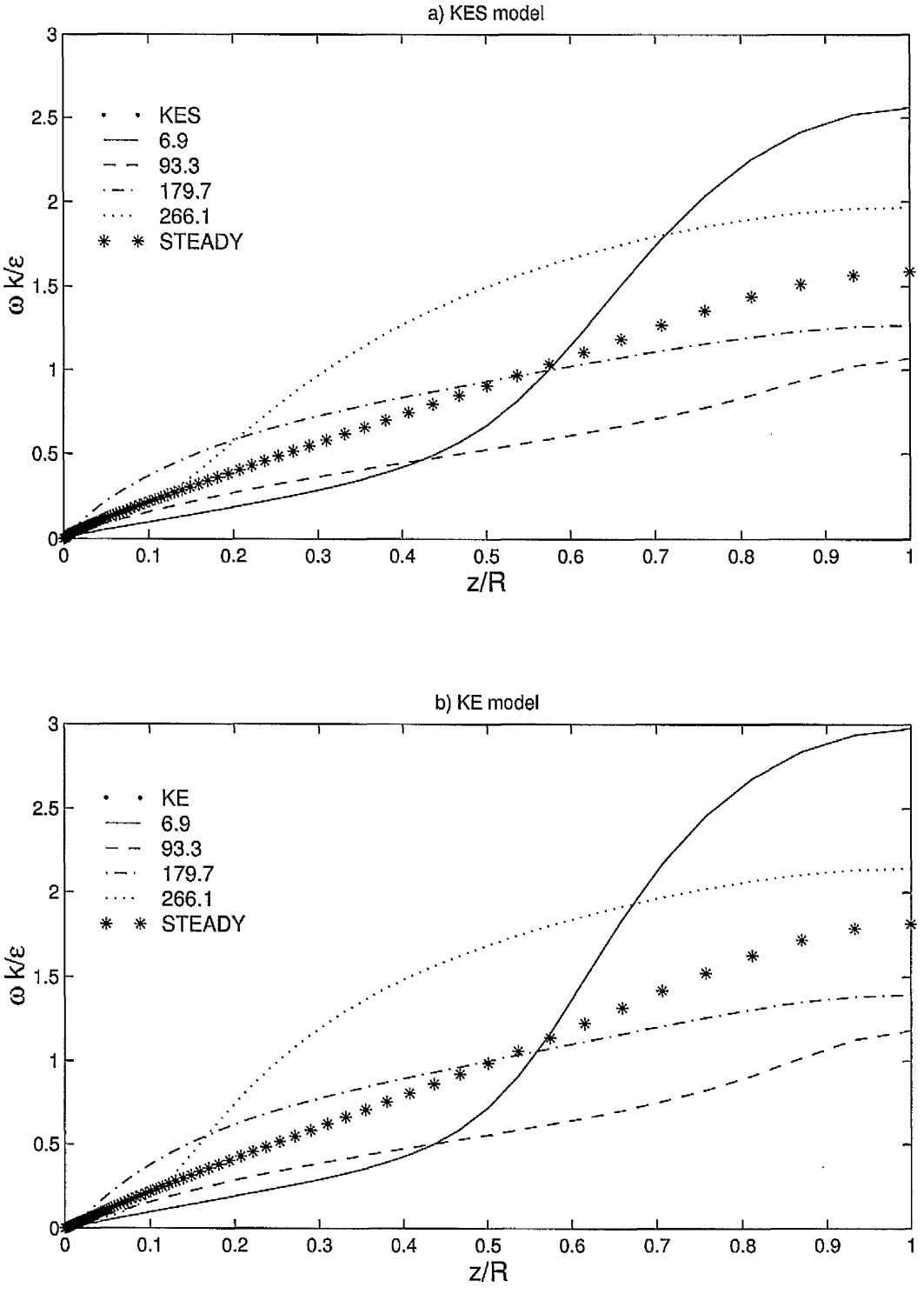

Figure 43: Turbulent time scale profiles: comparison of (a) k-ϵ-S, (b) k-ϵ model solutions with the steady flow case

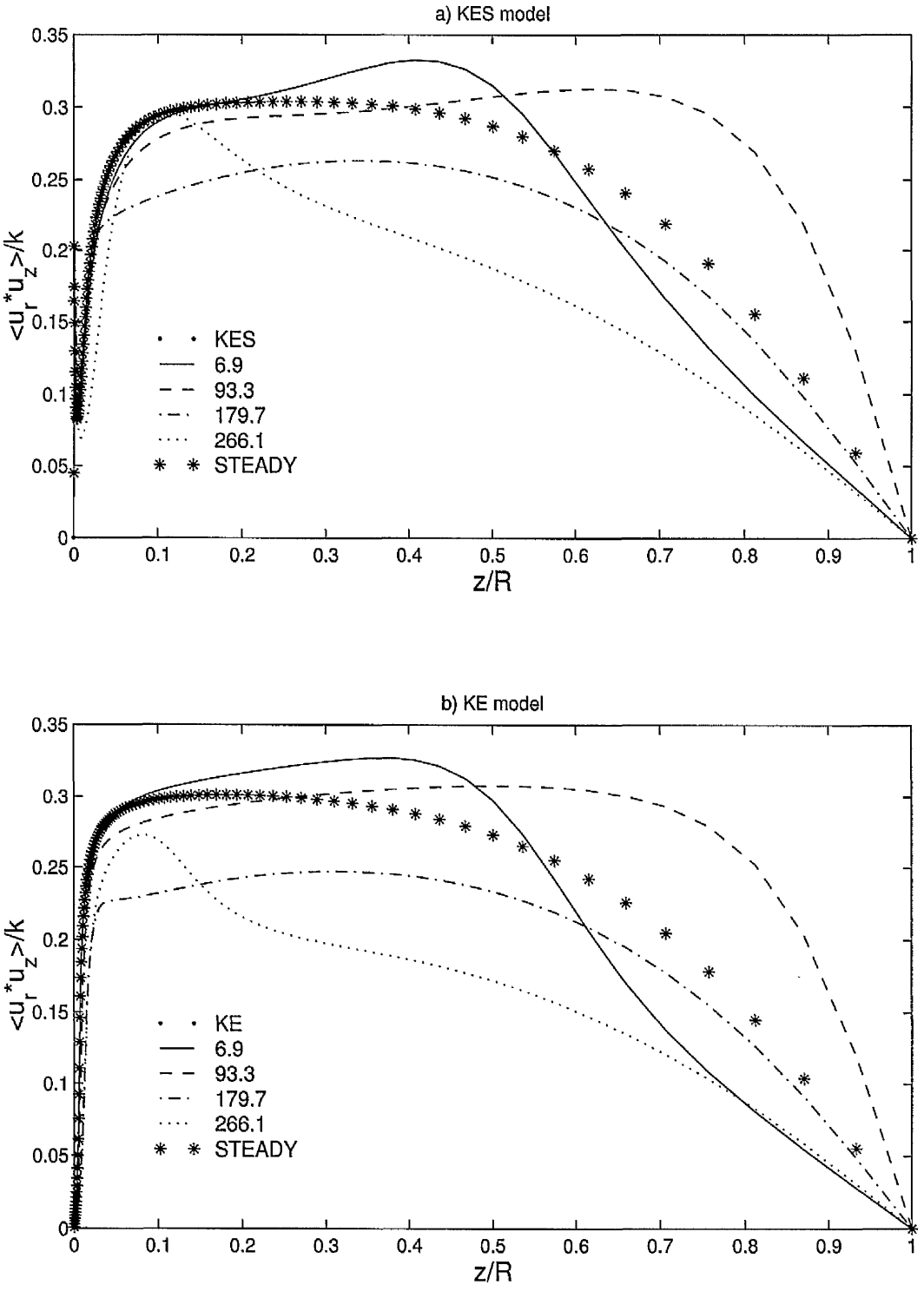

Figure 44: Anisotropic shear stress profiles: comparison of (a) k-ϵ-S, (b) k-ϵ model solutions with the steady flow case

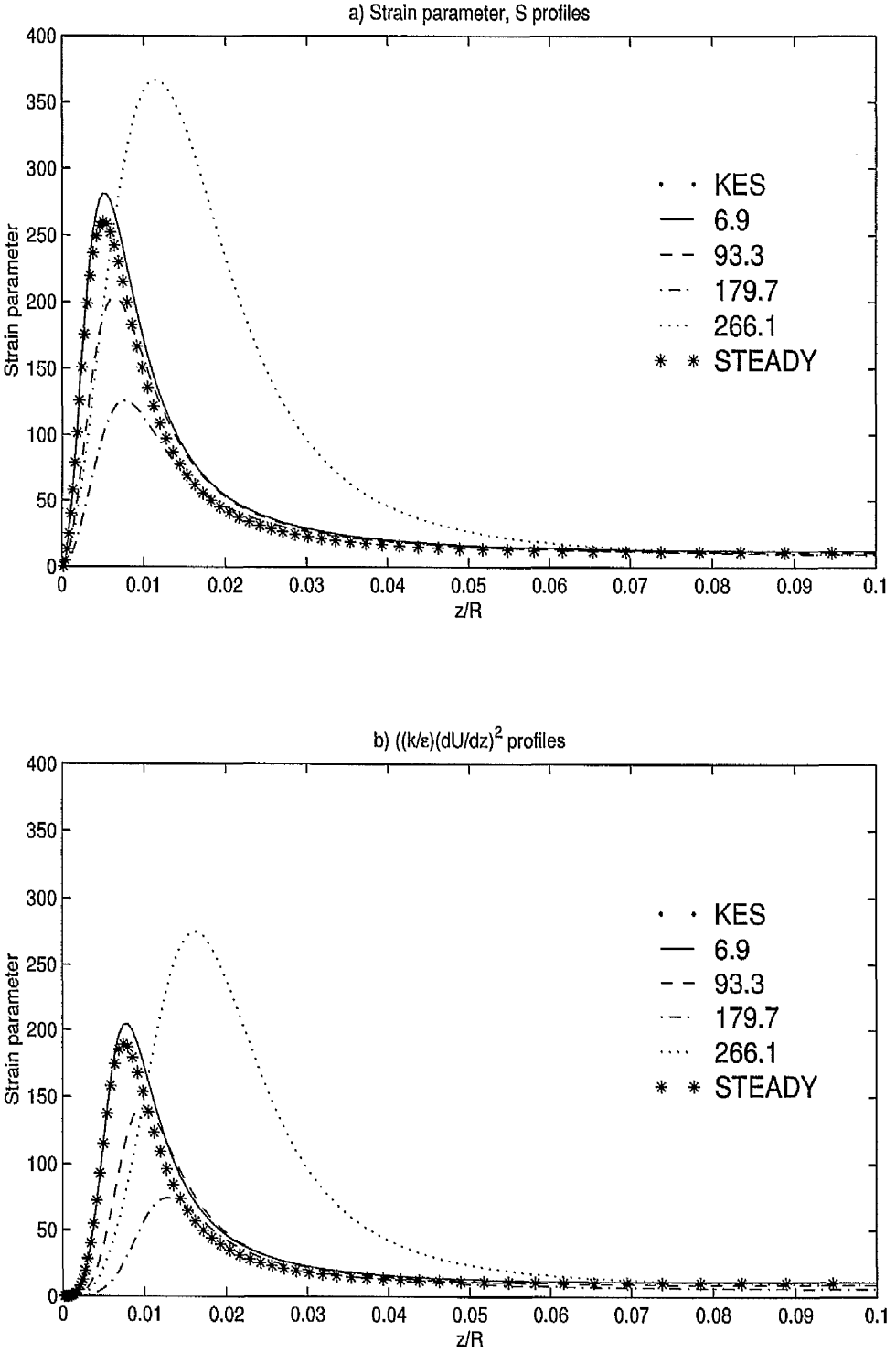

Figure 45: Strain parameter (a) S, (b) $\left(\frac{k}{\epsilon}\frac{\partial U}{\partial z}\right)^2$ profiles for the k-ϵ-S model near to the wall

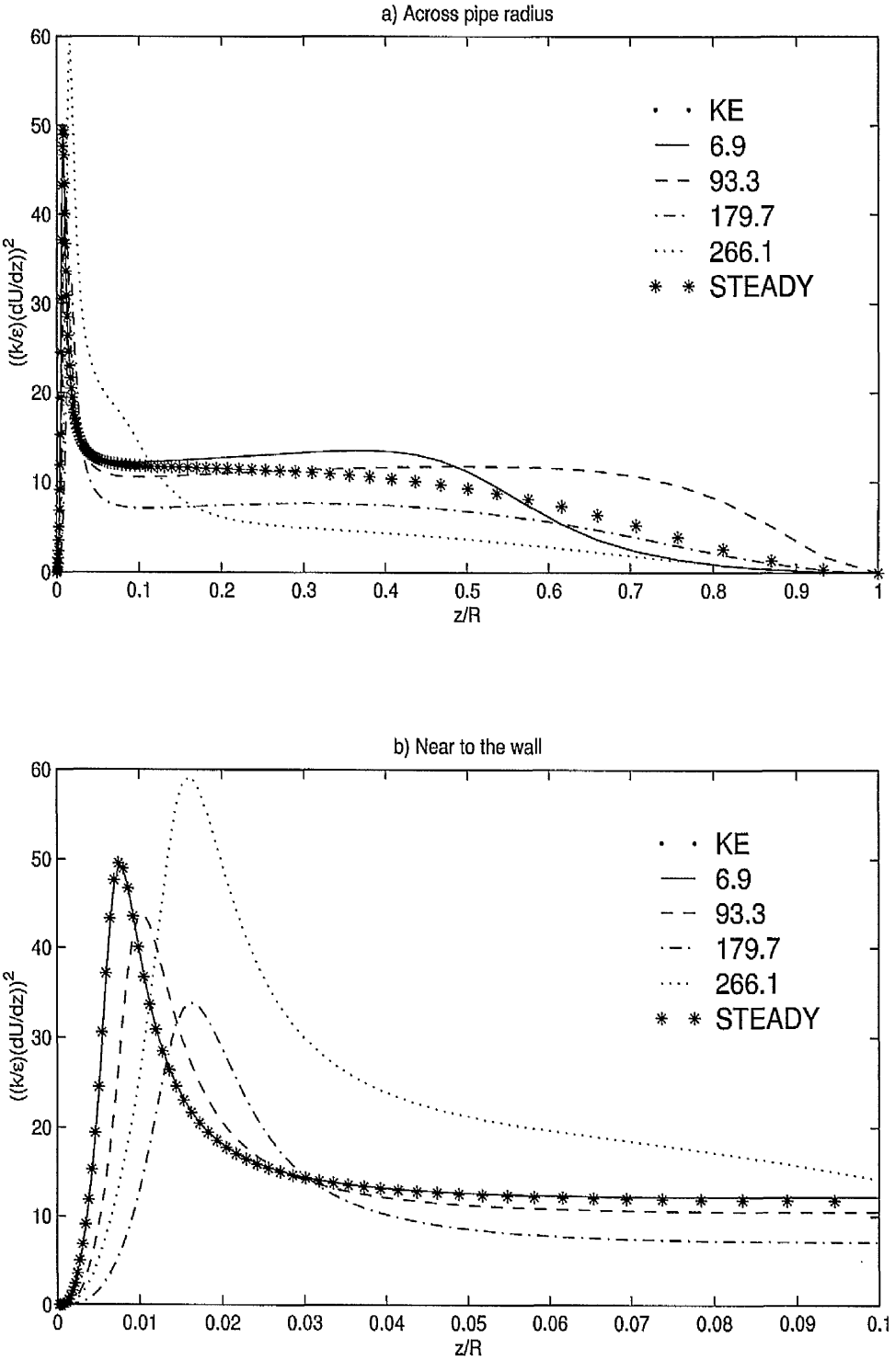

Figure 46: $\left(\frac{k}{\epsilon}\frac{\partial U}{\partial z}\right)^2$ profiles for the k-ϵ model (a) across the pipe radius, (b) near to the wall

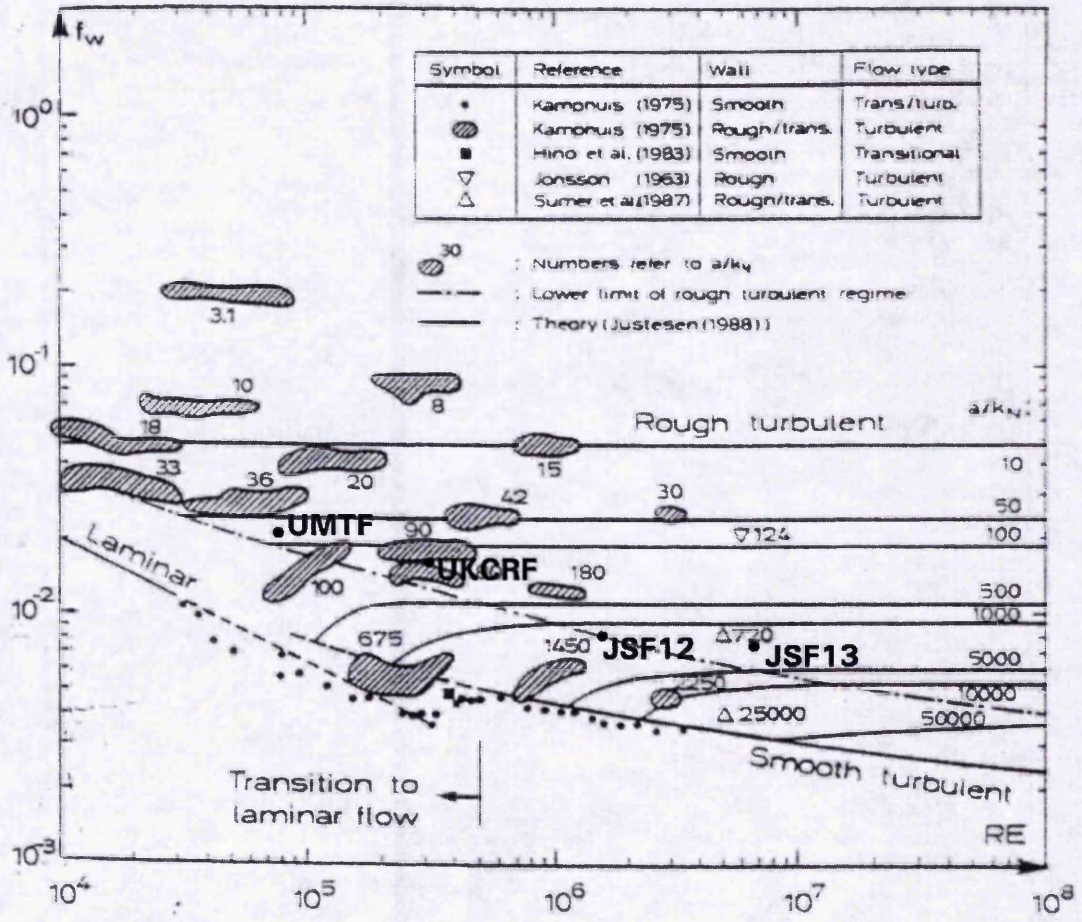

Figure 47: Diagram from Fredsøe and Deigaard (1992, p.33) showing experimental results of the relationship between Reynolds number and the roughness parameter with the additional experiments studied also marked on.

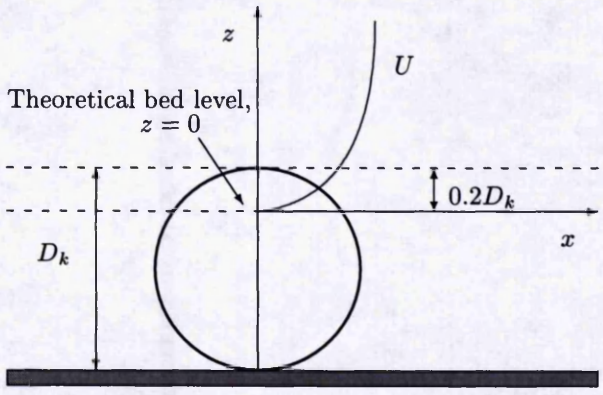

Figure 48: Schematic of theoretical bed level

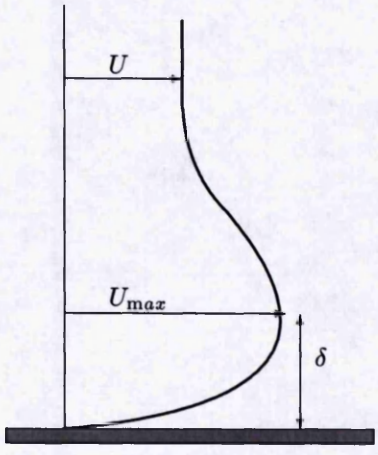

Figure 49: Schematic of boundary layer thickness estimation

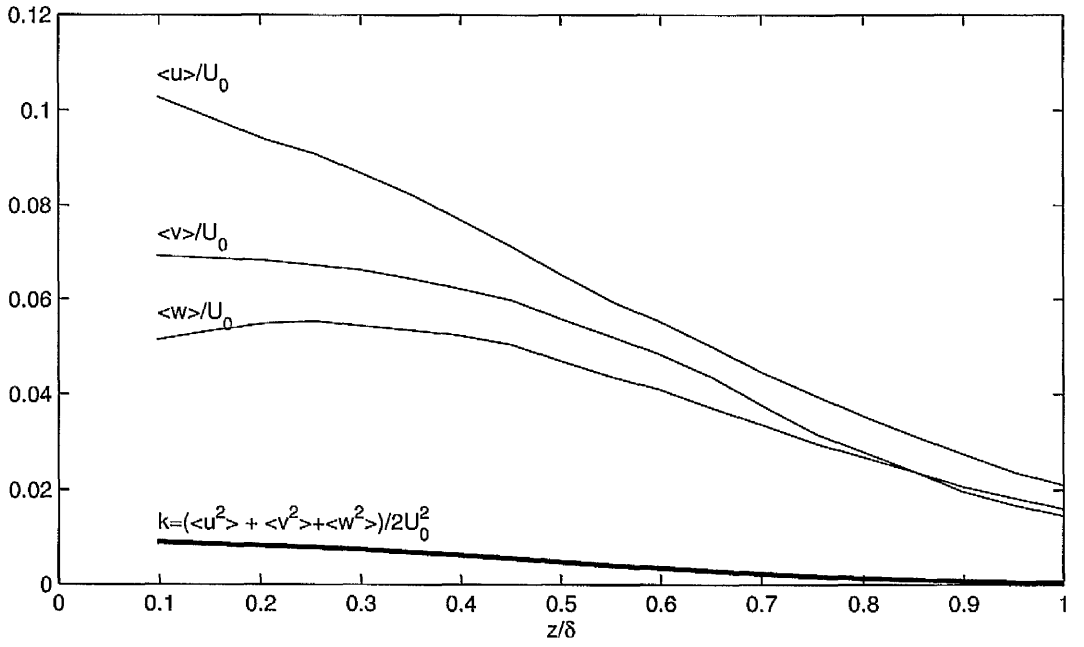

Figure 50: Relative turbulence intensities in a boundary layer along a rough wall and the resultant turbulent kinetic energy

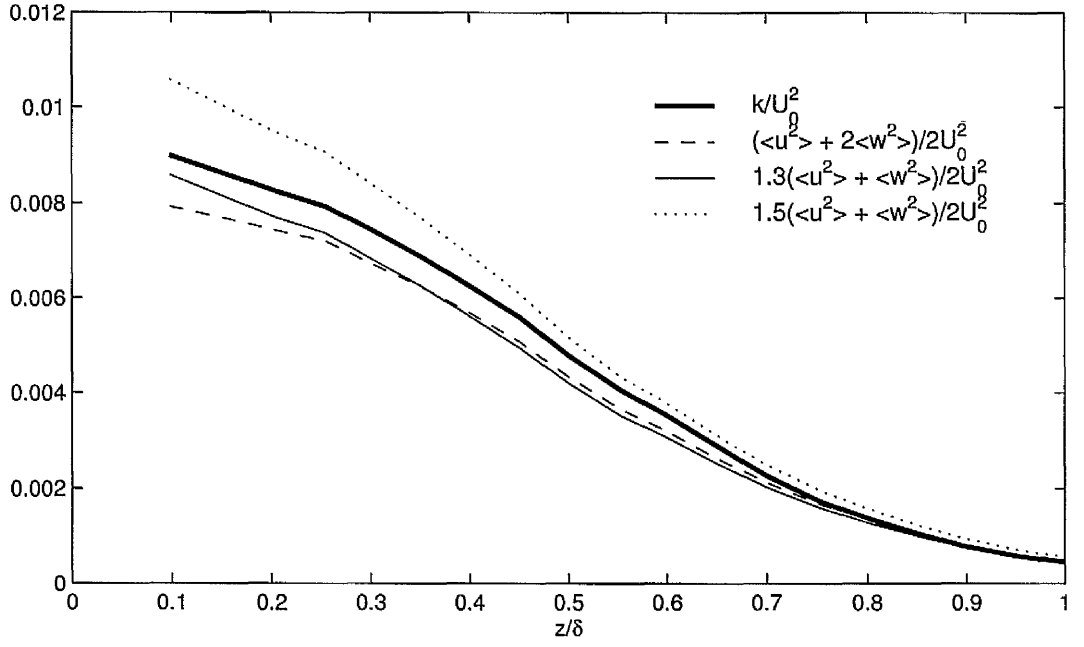

Figure 51: Comparison of approximate functions and exact turbulent kinetic energy

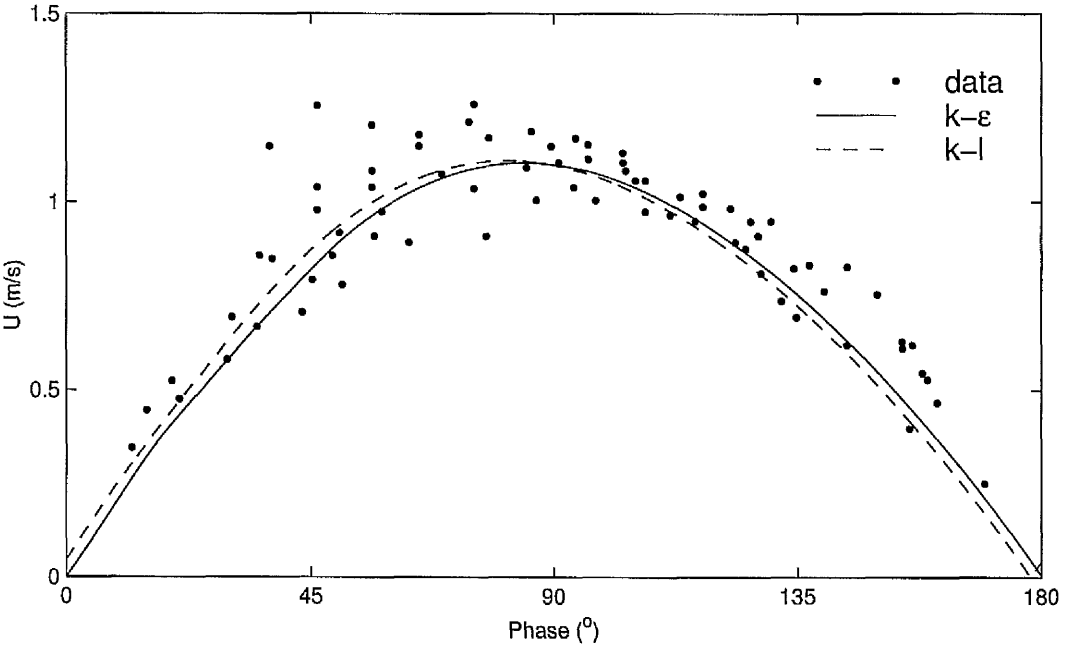

Figure 52: Cyclic variation of velocity in the Jade estuary at 2.14 m above the bed

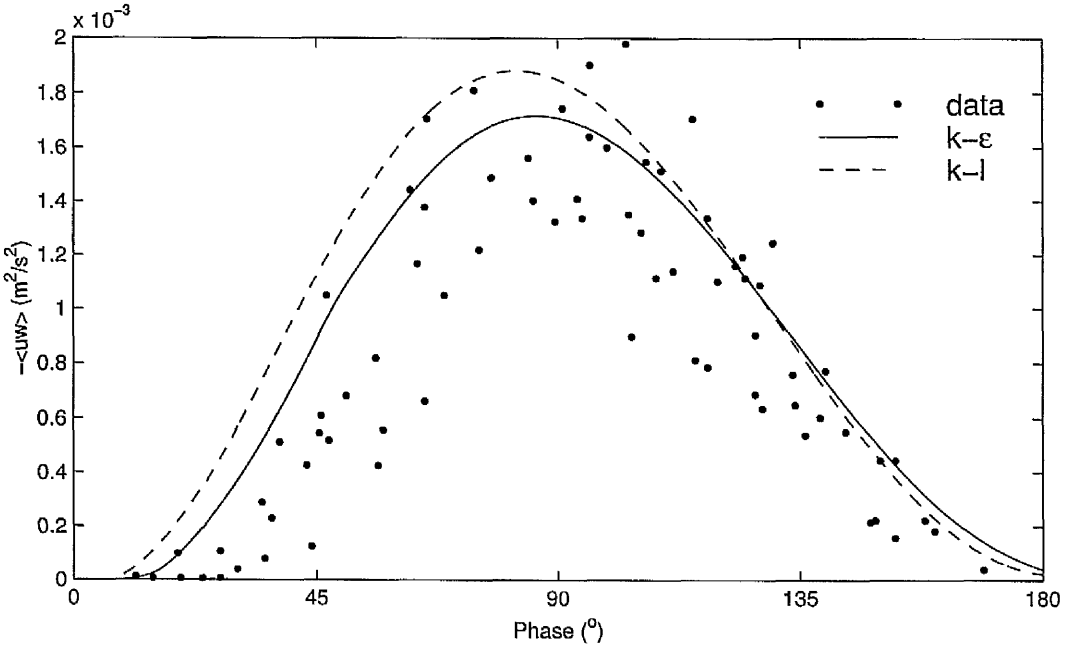

Figure 53: Cyclic variation of Reynolds shear stress in the Jade estuary at 2.14 m above the bed

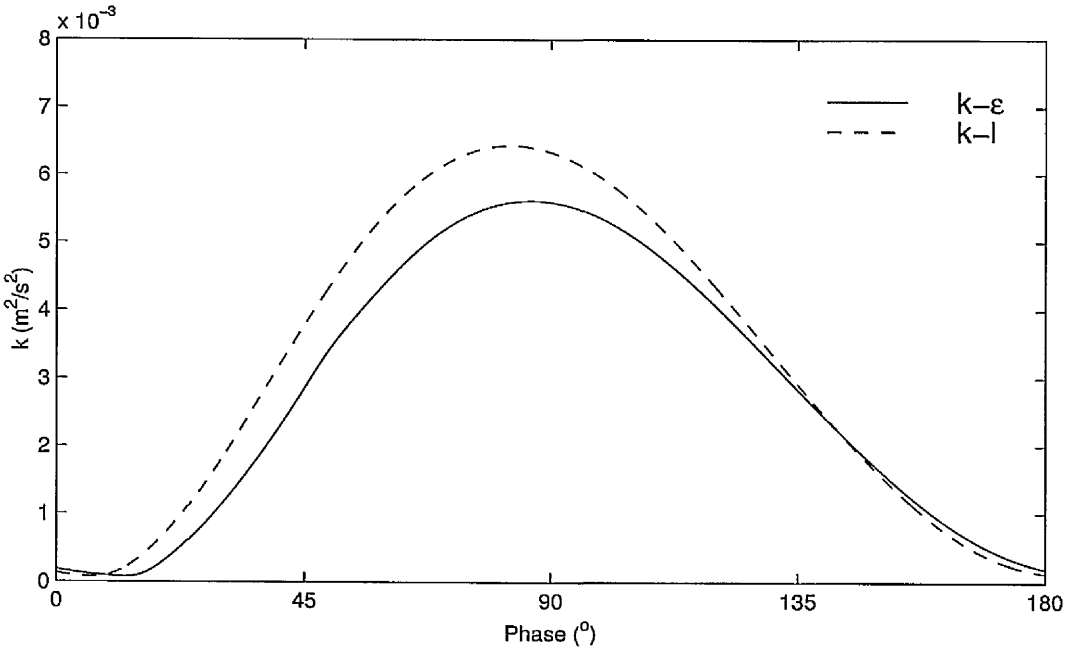

Figure 54: Cyclic variation of turbulent kinetic energy in the Jade estuary at 2.14 m above the bed

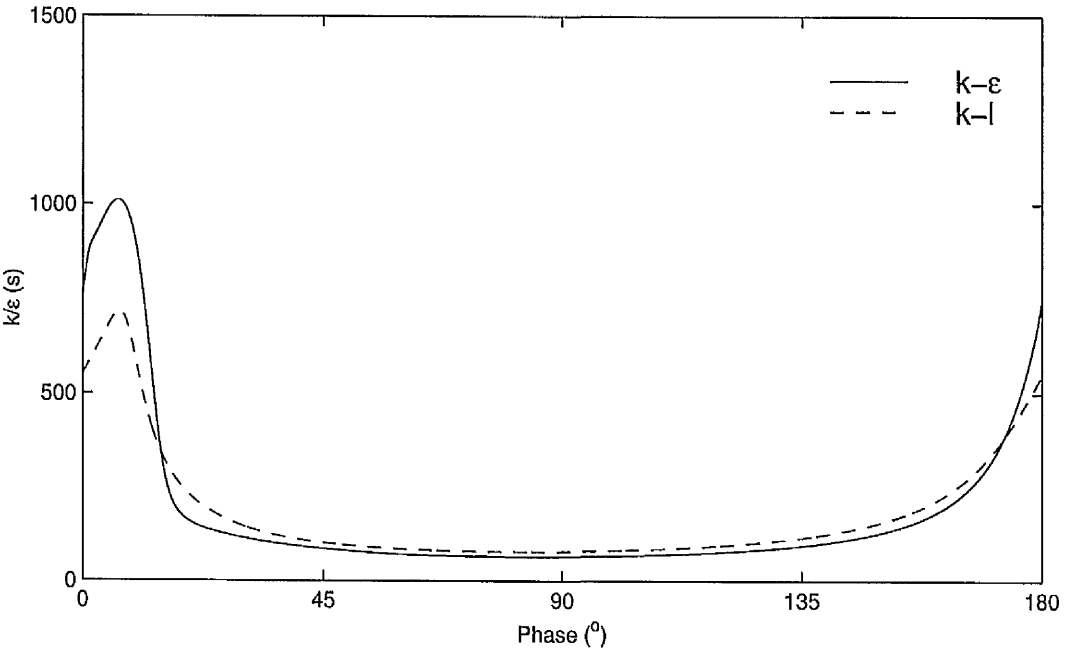

Figure 55: Cyclic variation of turbulent time scale in the Jade estuary at 2.14 m above the bed

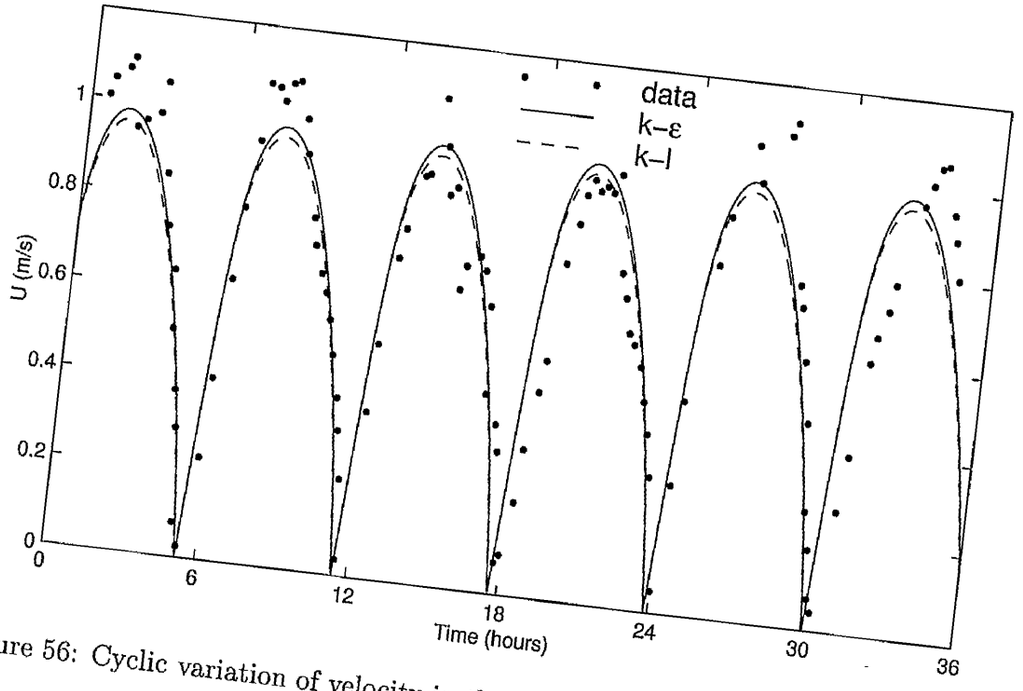

Figure 56: Cyclic variation of velocity in the Elbe estuary at 1.9 m above the bed

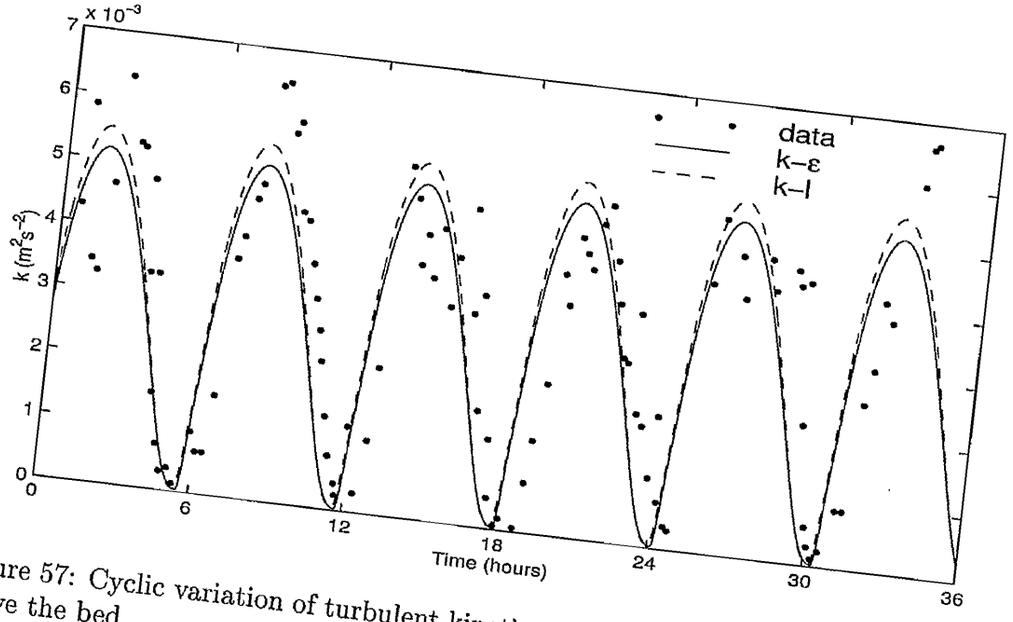

Figure 57: Cyclic variation of turbulent kinetic energy in the Elbe estuary at 1.9 m above the bed

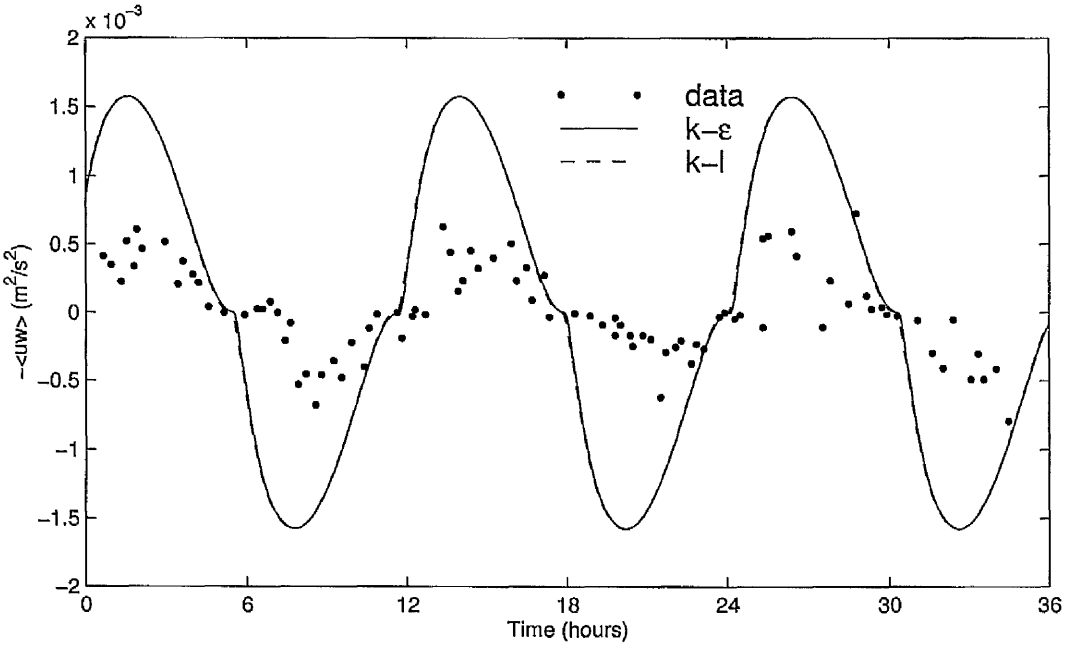

Figure 58: Cyclic variation of Reynolds shear stress in the Elbe estuary at 1.9 m above the bed

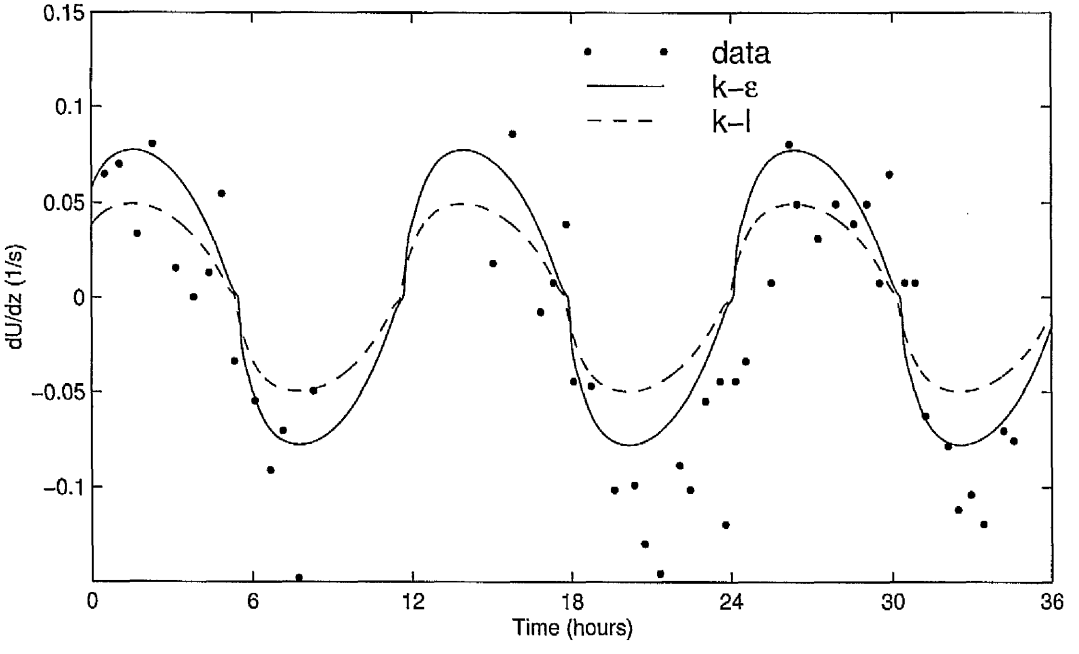

Figure 59: Cyclic variation of velocity gradient in the Elbe estuary at 1.9 m above the bed

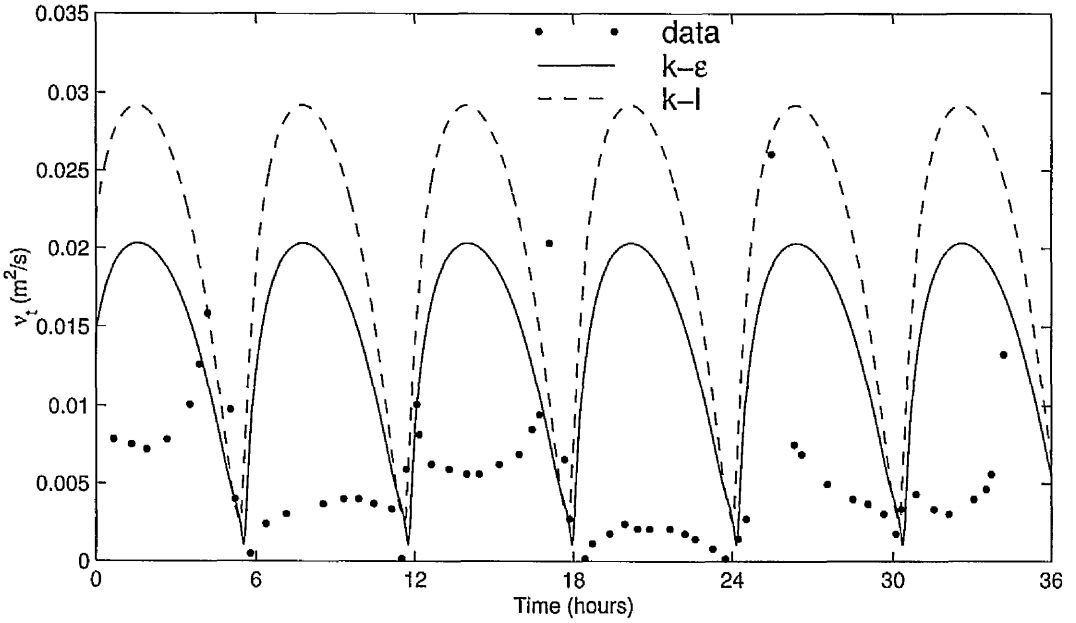

Figure 60: Cyclic variation of turbulent eddy viscosity in the Elbe estuary at 1.9 m above the bed

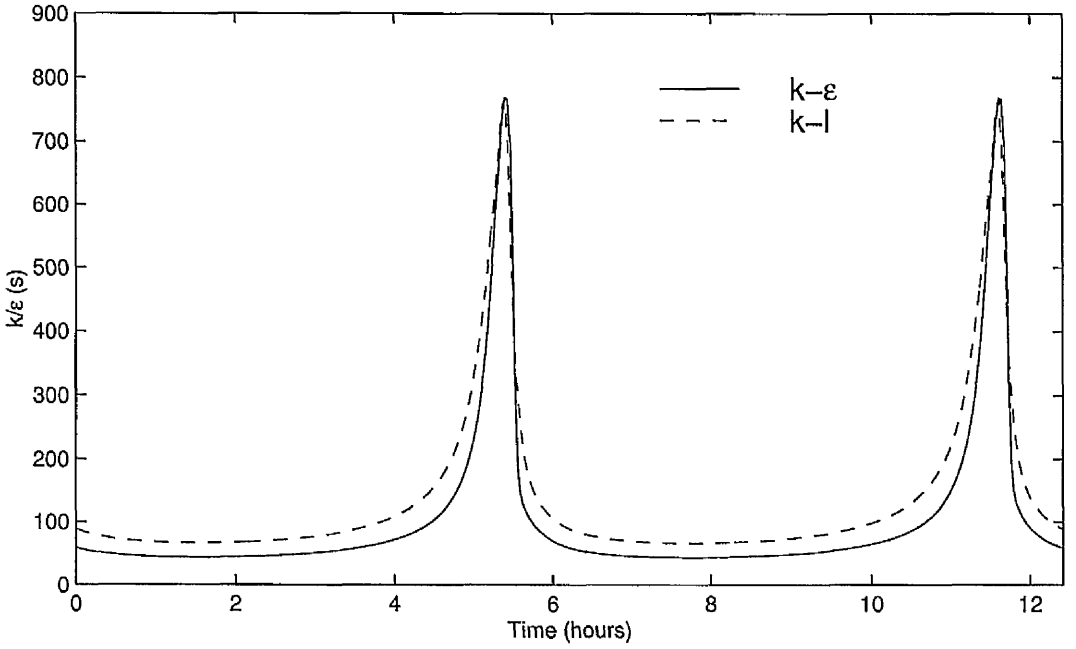

Figure 61: Cyclic variation of turbulent time scale in the Elbe estuary at 1.9 m above the bed

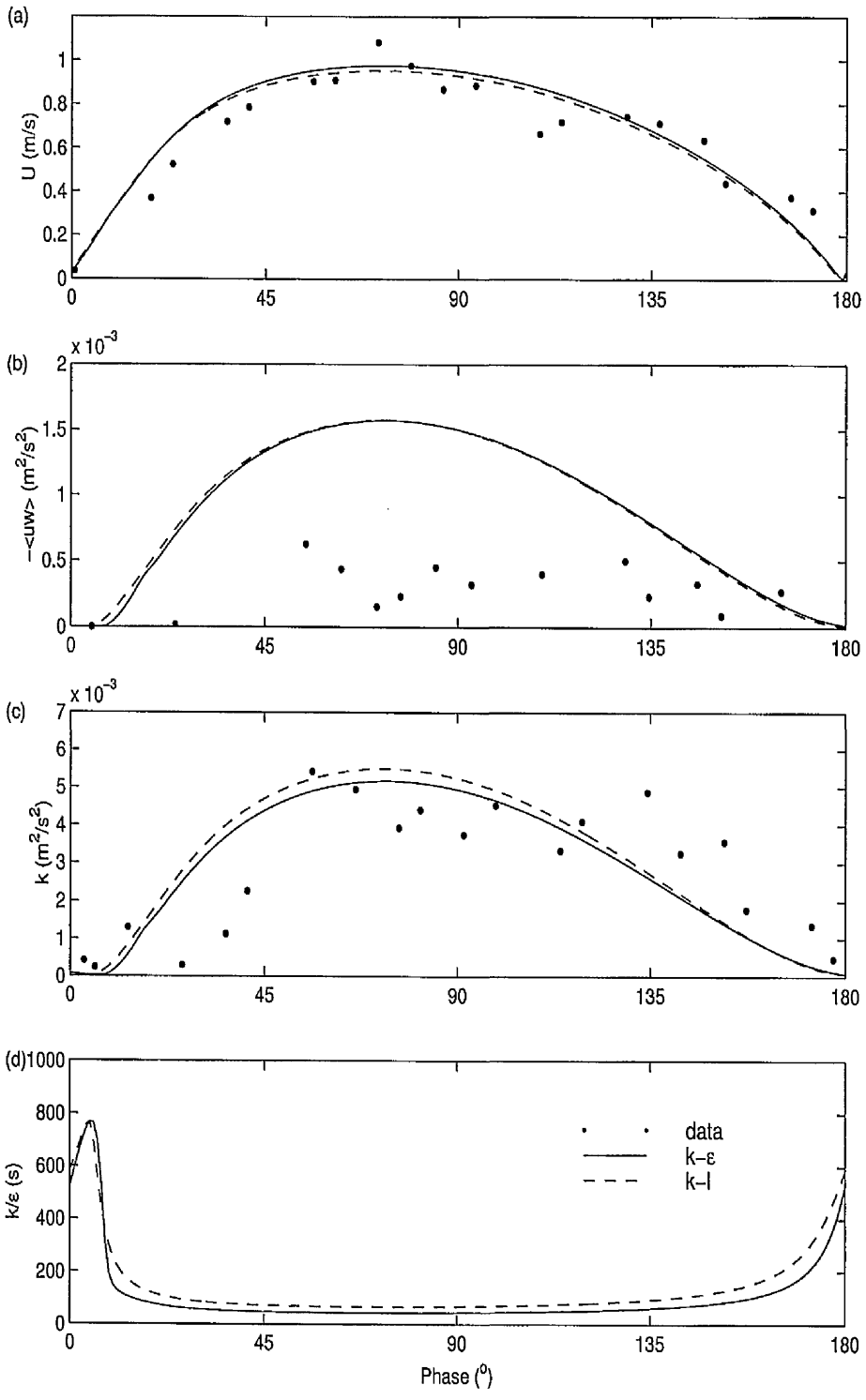

Figure 62: Variation of (a) velocity (b) Reynolds shear stress (c) turbulent kinetic energy and (d) turbulent time scale in the Elbe estuary over half cycle of oscillation at 1.9 m above the bed

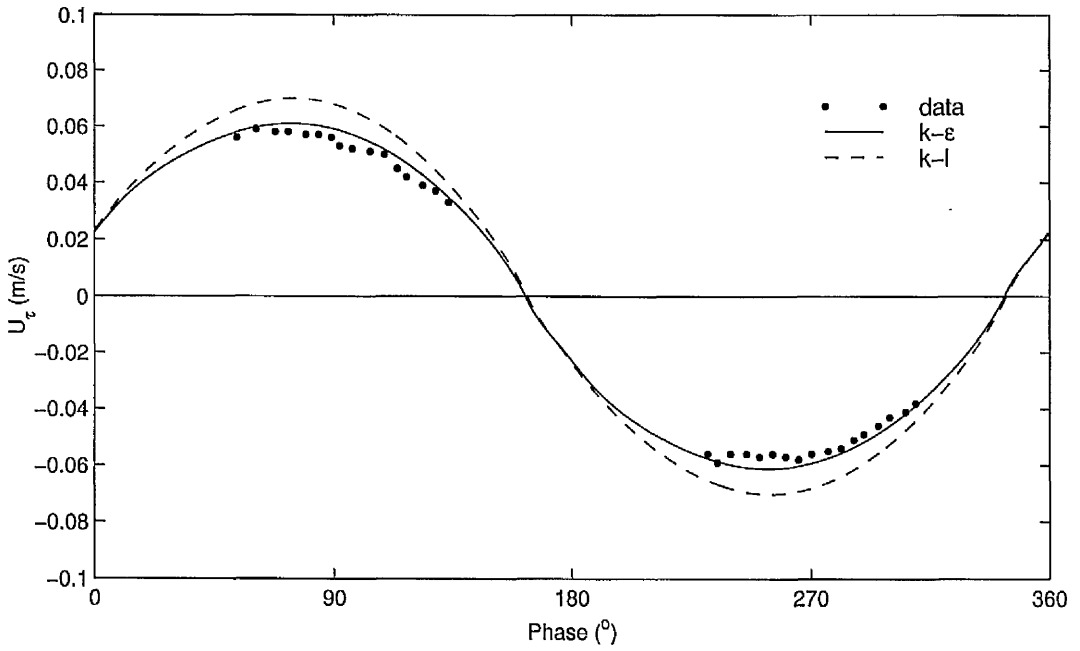

Figure 63: Cyclic variation of bed friction velocity for the JSF12 case

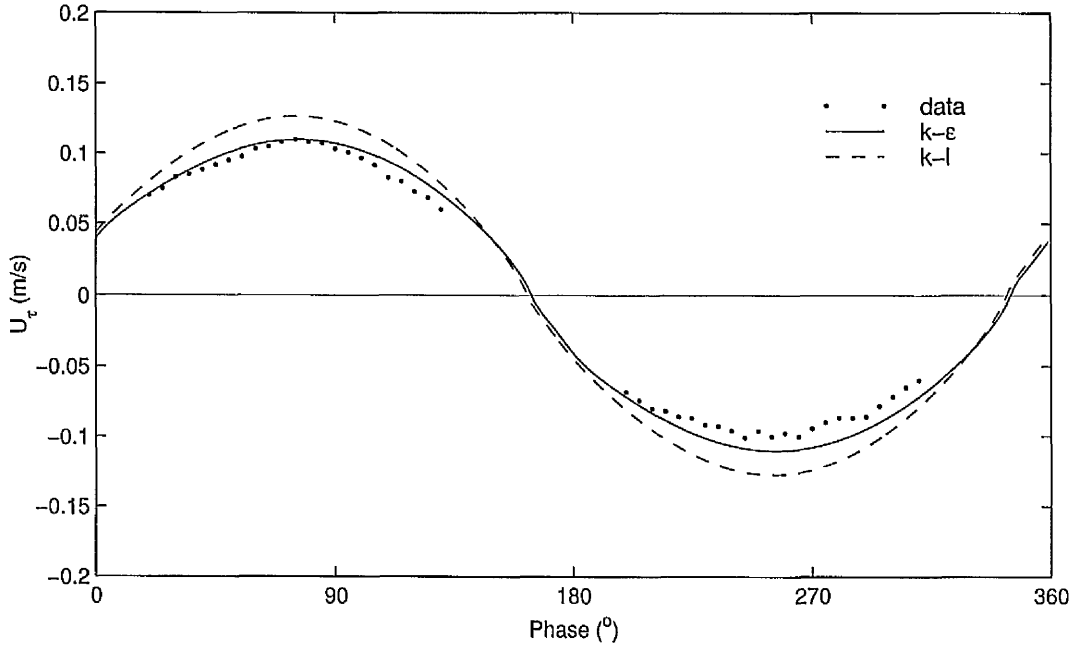

Figure 64: Cyclic variation of bed friction velocity for the JSF13 case

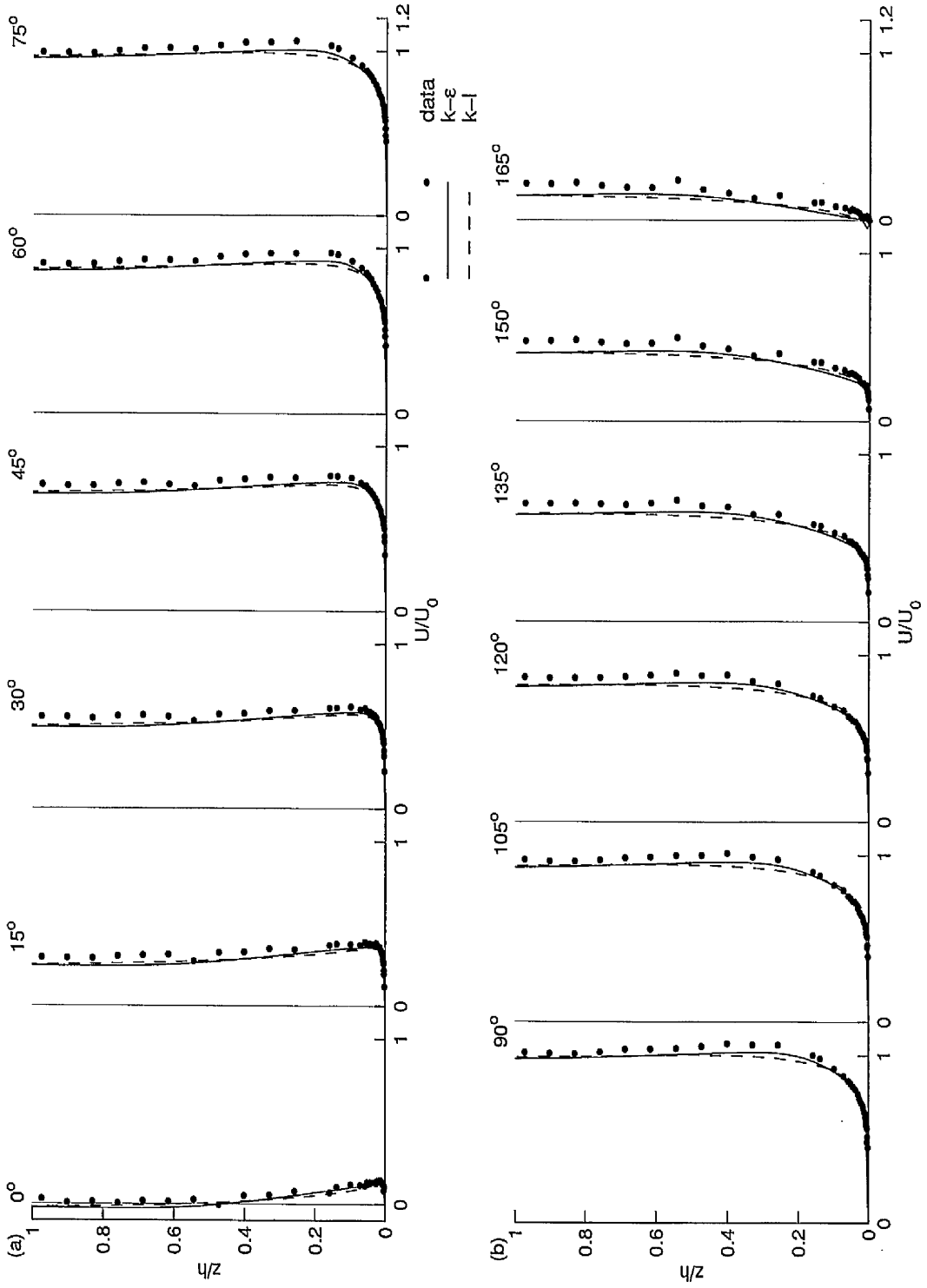

Figure 65: Profiles of velocity for the JSF10 case

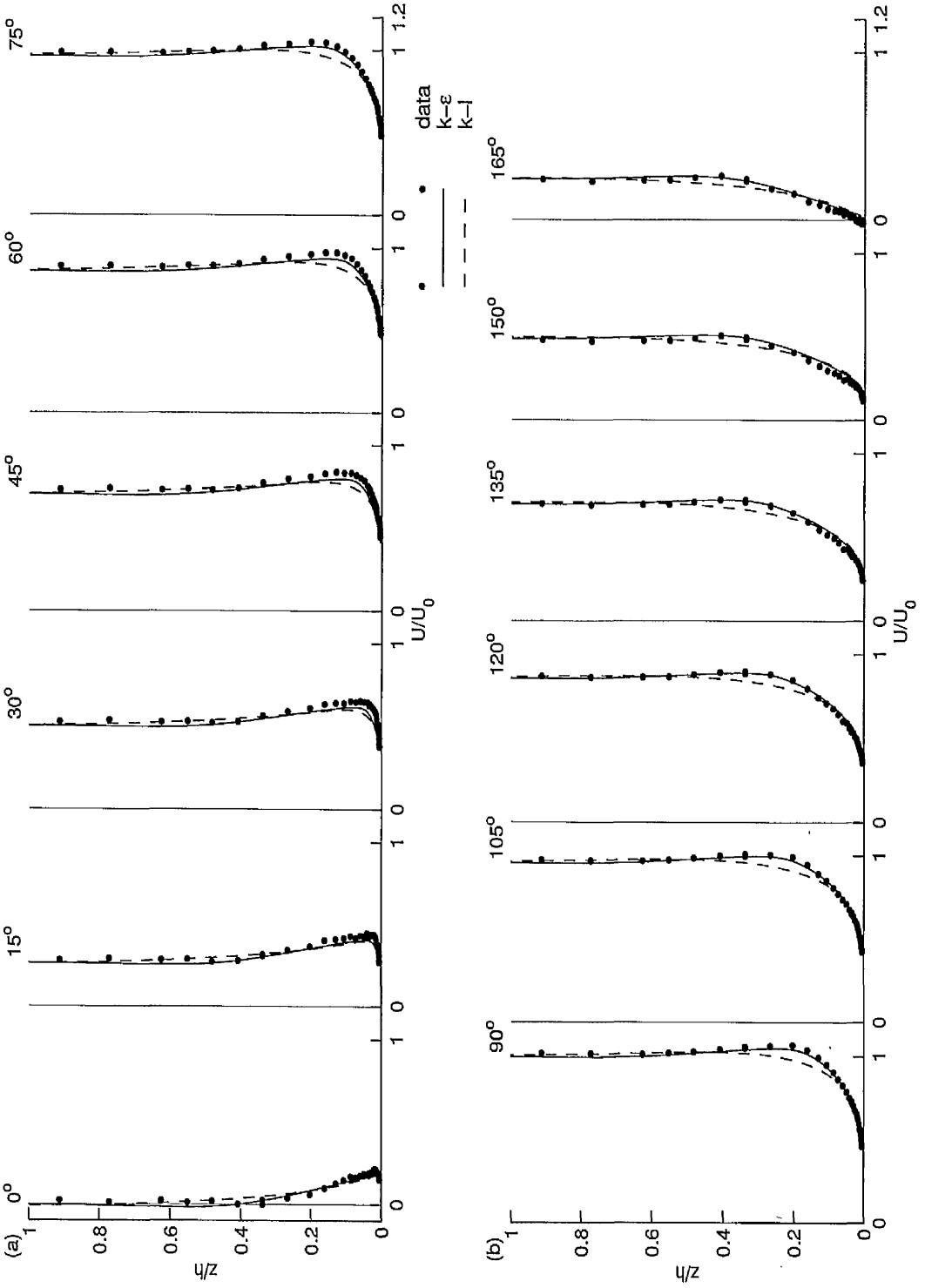

Figure 66: Profiles of velocity for the JSF12 case

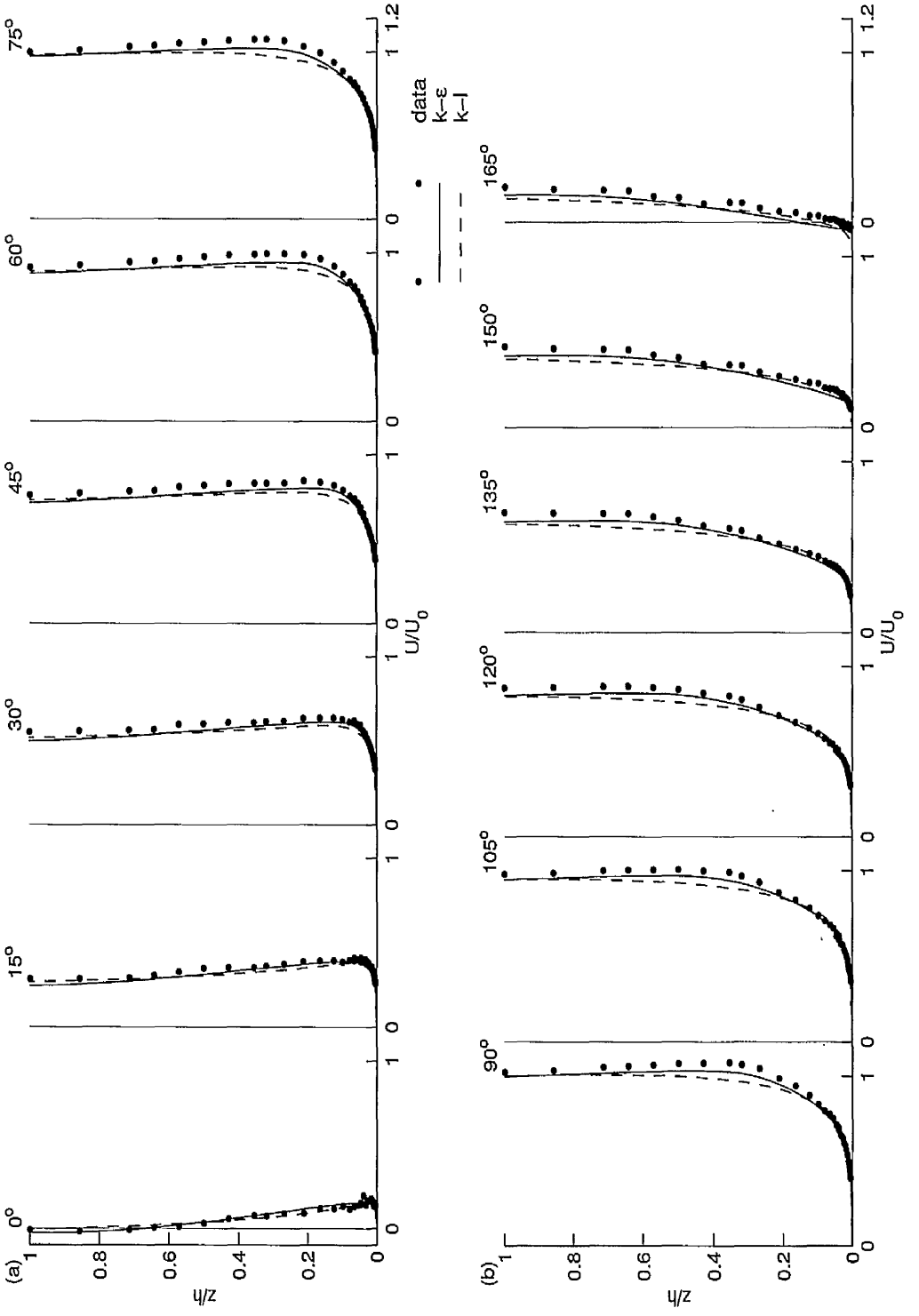

Figure 67: Profiles of velocity for the JSF13 case

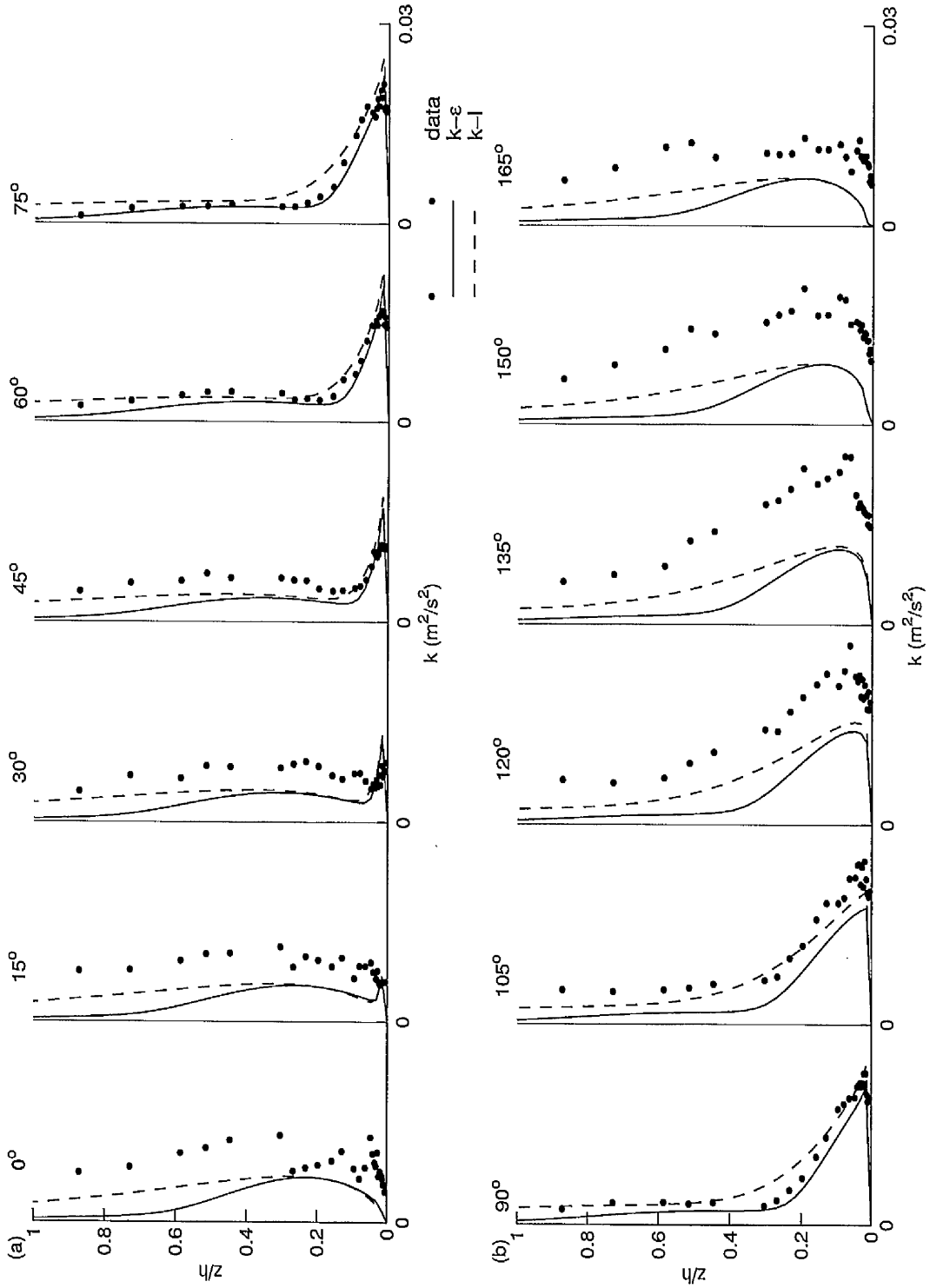

Figure 68: Profiles of turbulent kinetic energy for the JSF10 case

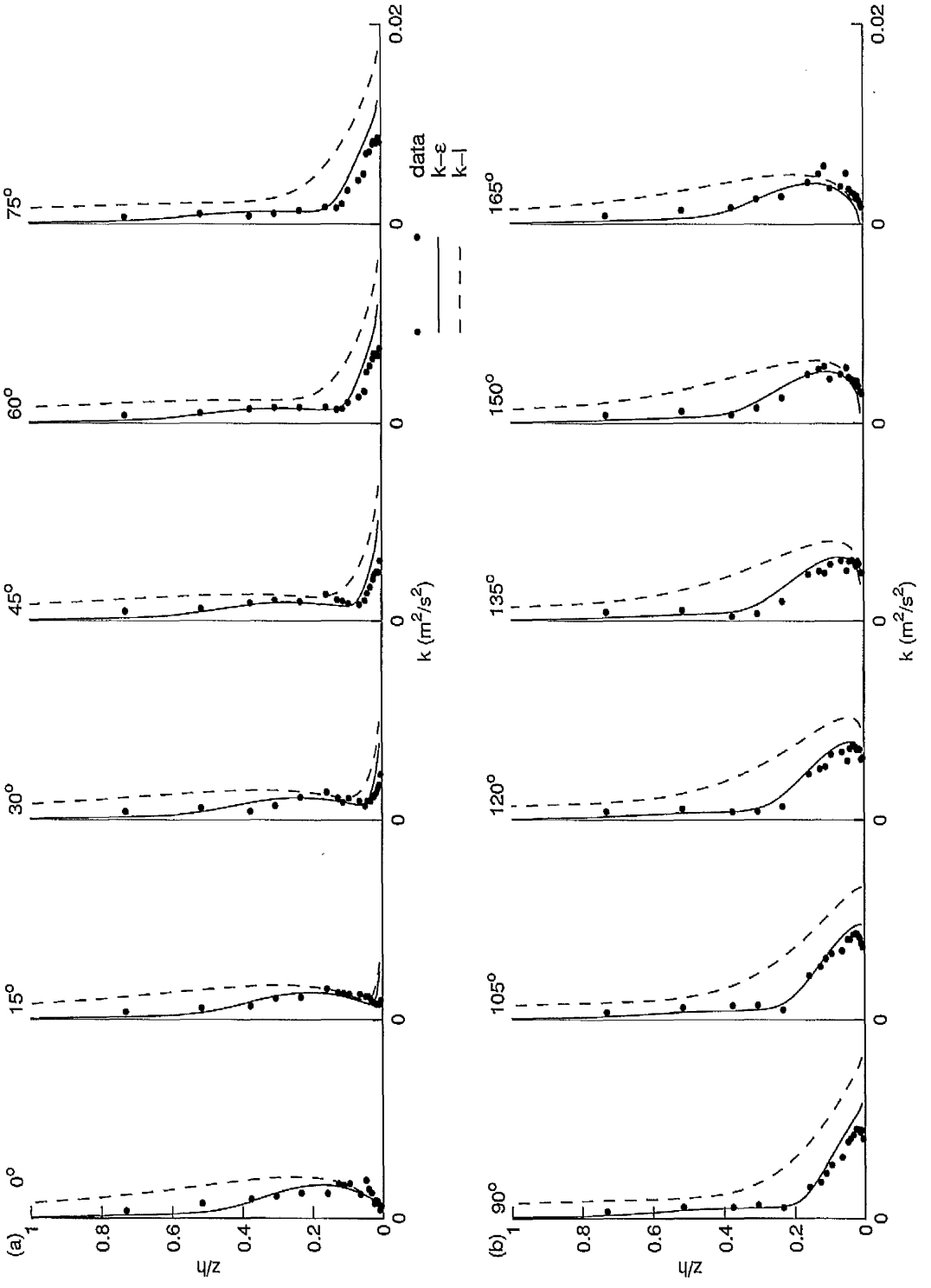

Figure 69: Profiles of turbulent kinetic energy for the JSF12 case

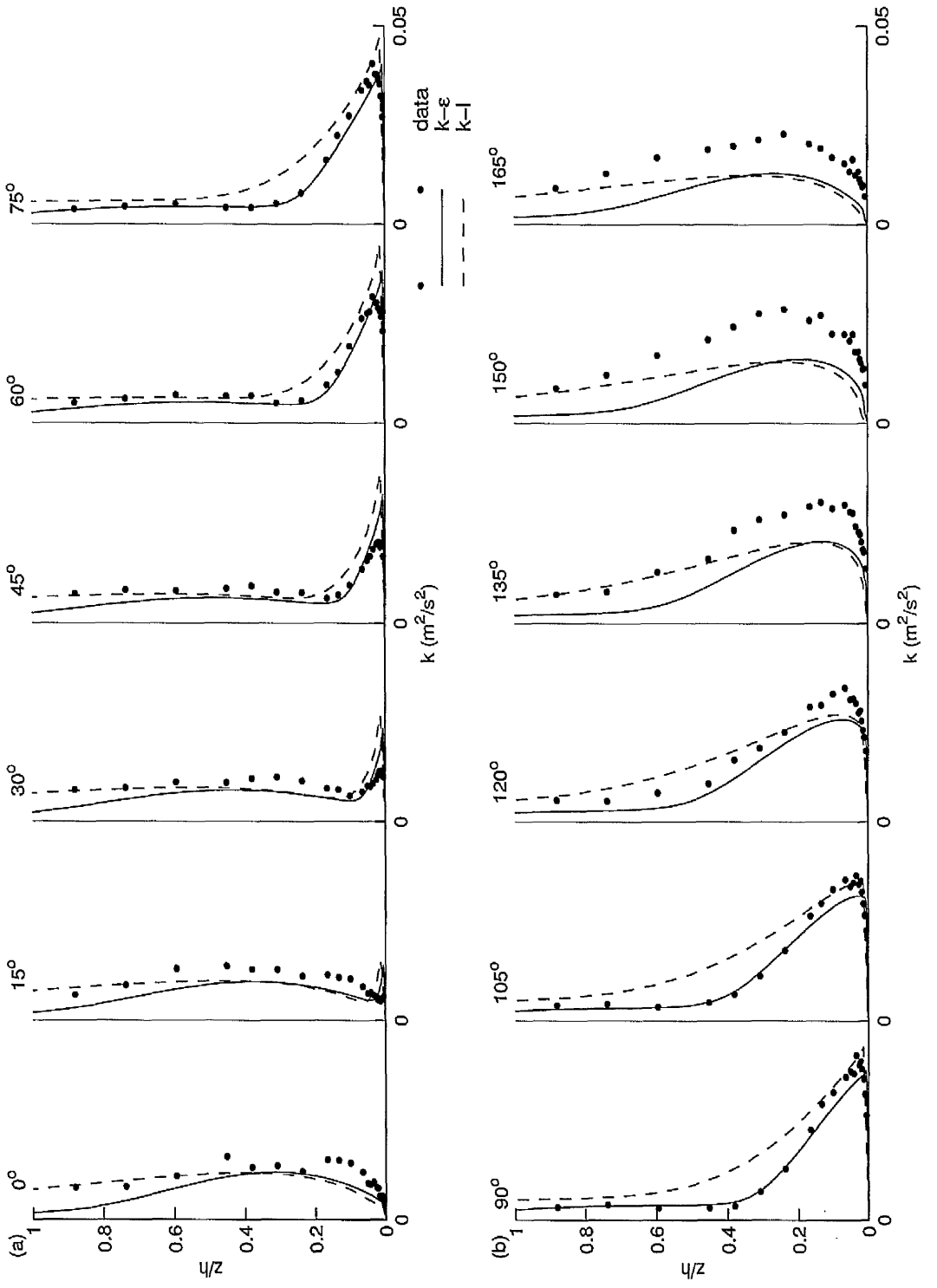

Figure 70: Profiles of turbulent kinetic energy for the JSF13 case

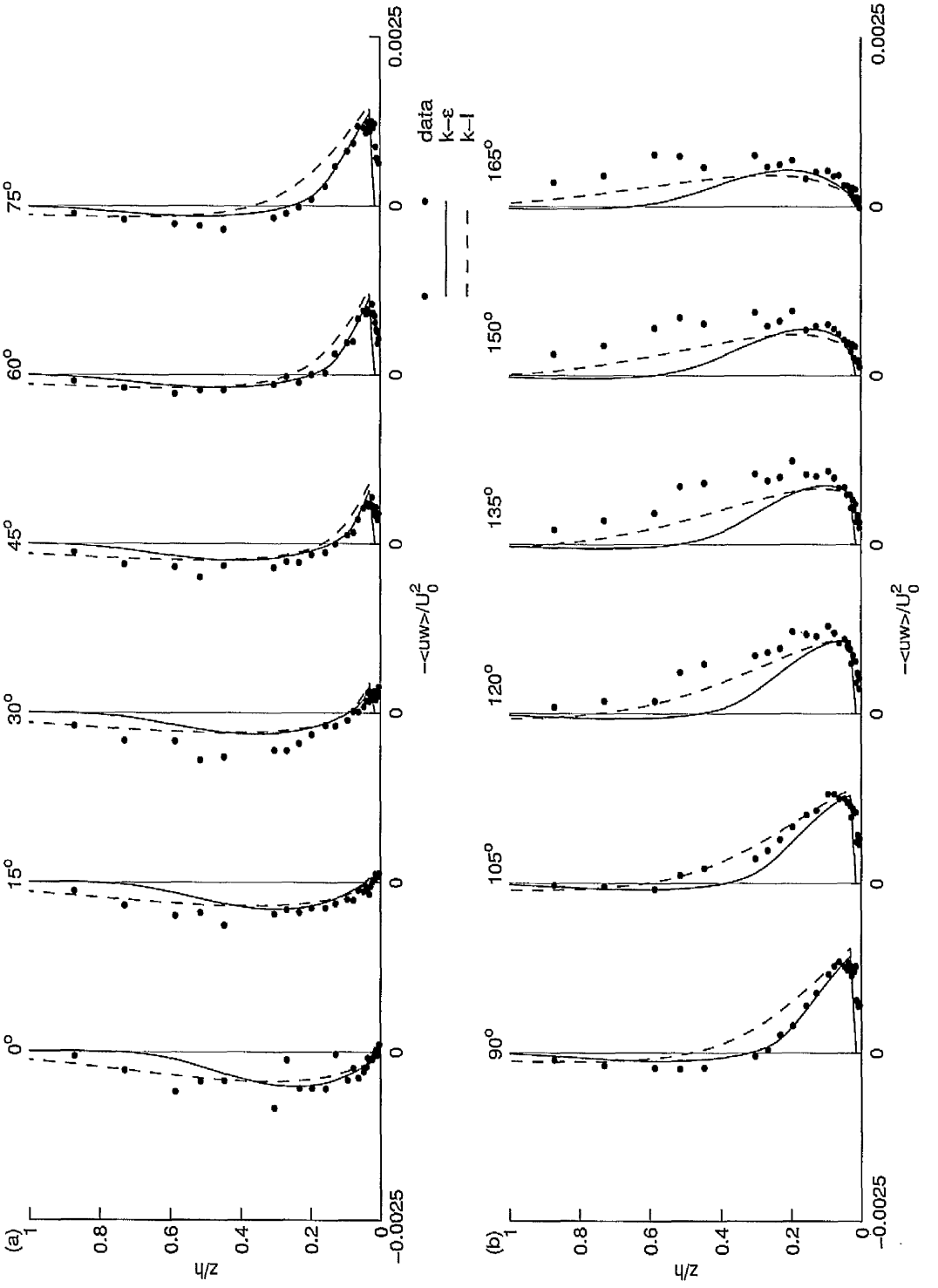

Figure 71: Profiles of Reynolds shear stress for the JSF10 case

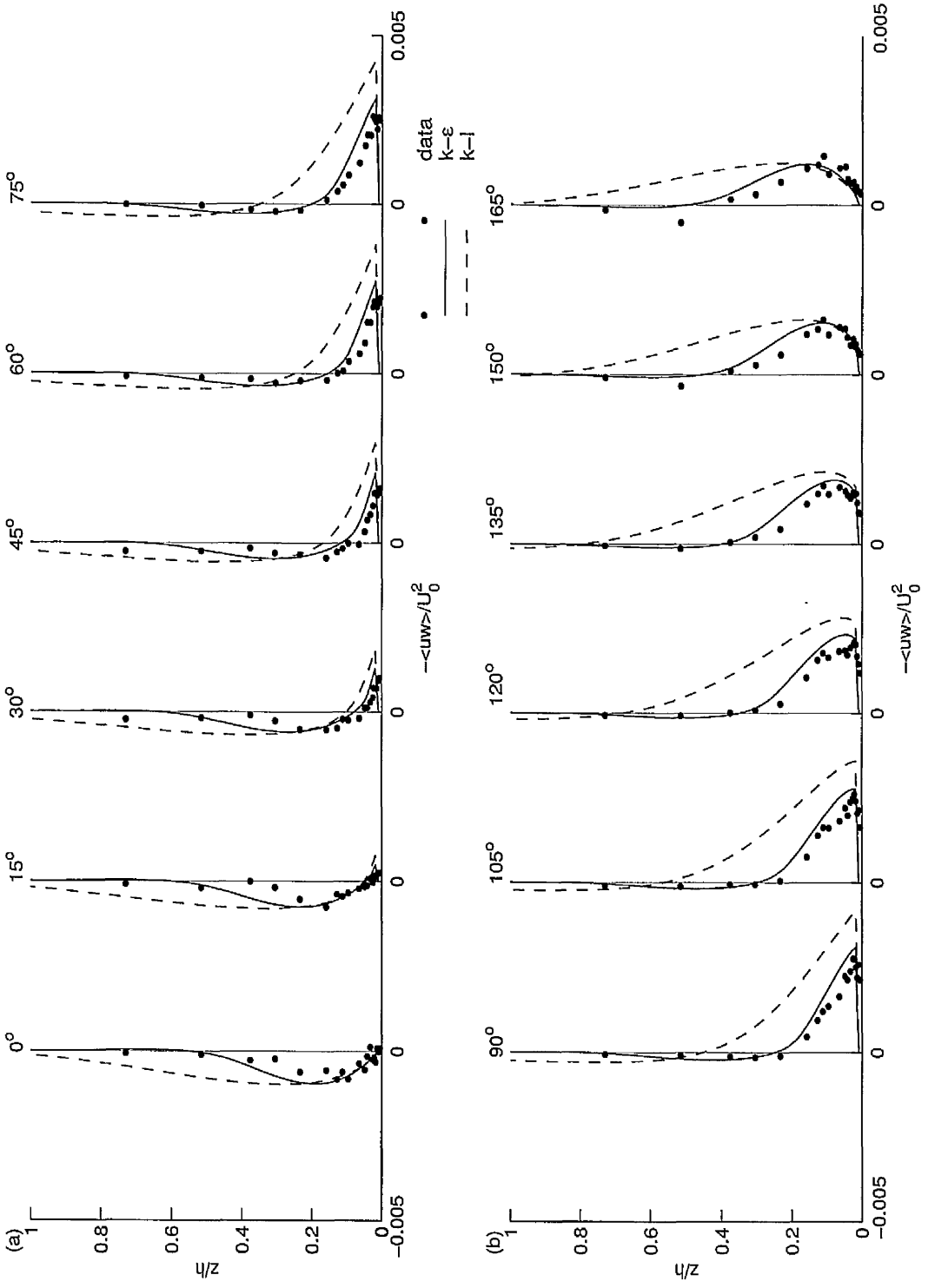

Figure 72: Profiles of Reynolds shear stress for the JSF12 case

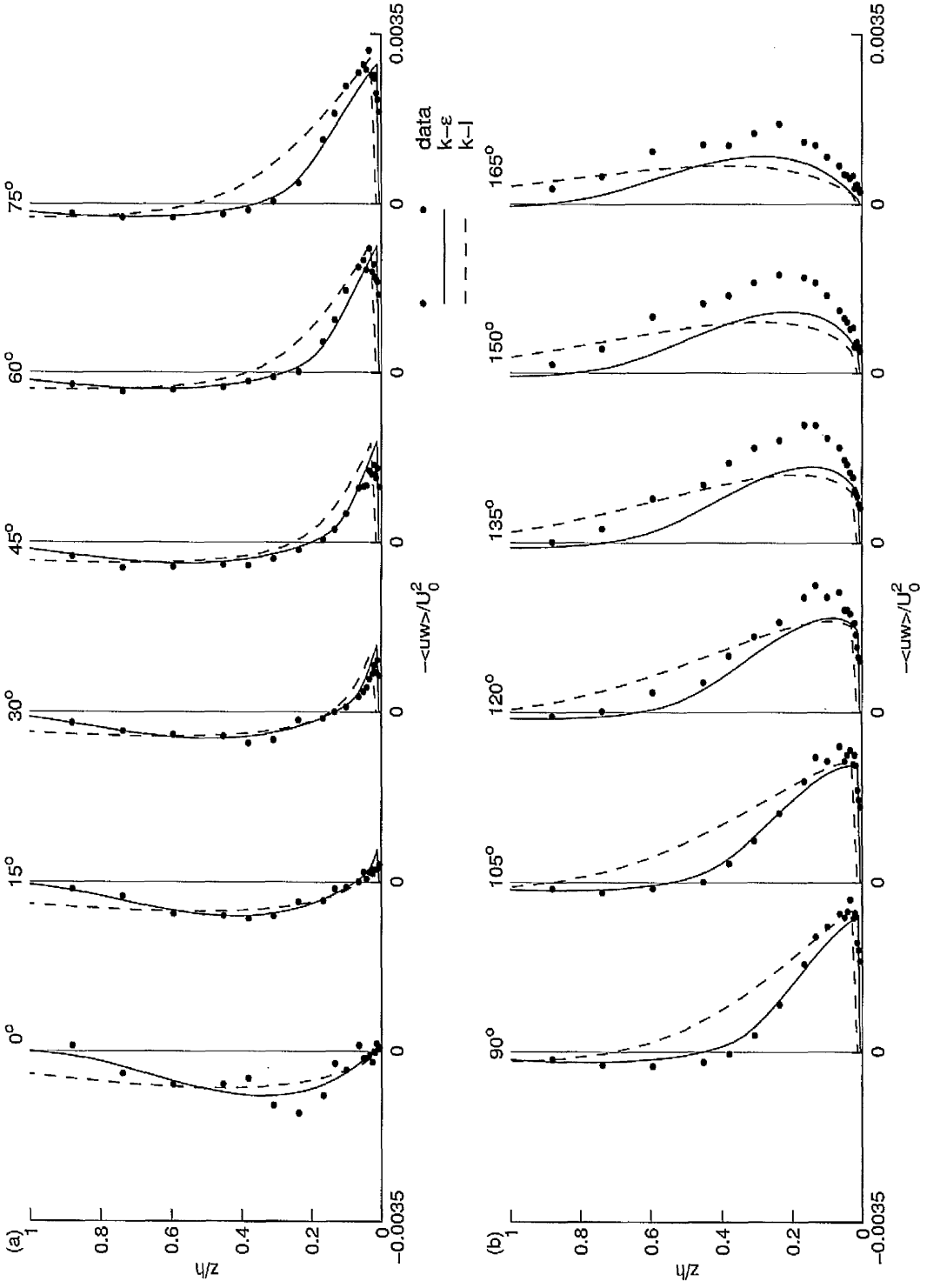

Figure 73: Profiles of Reynolds shear stress for the JSF13 case

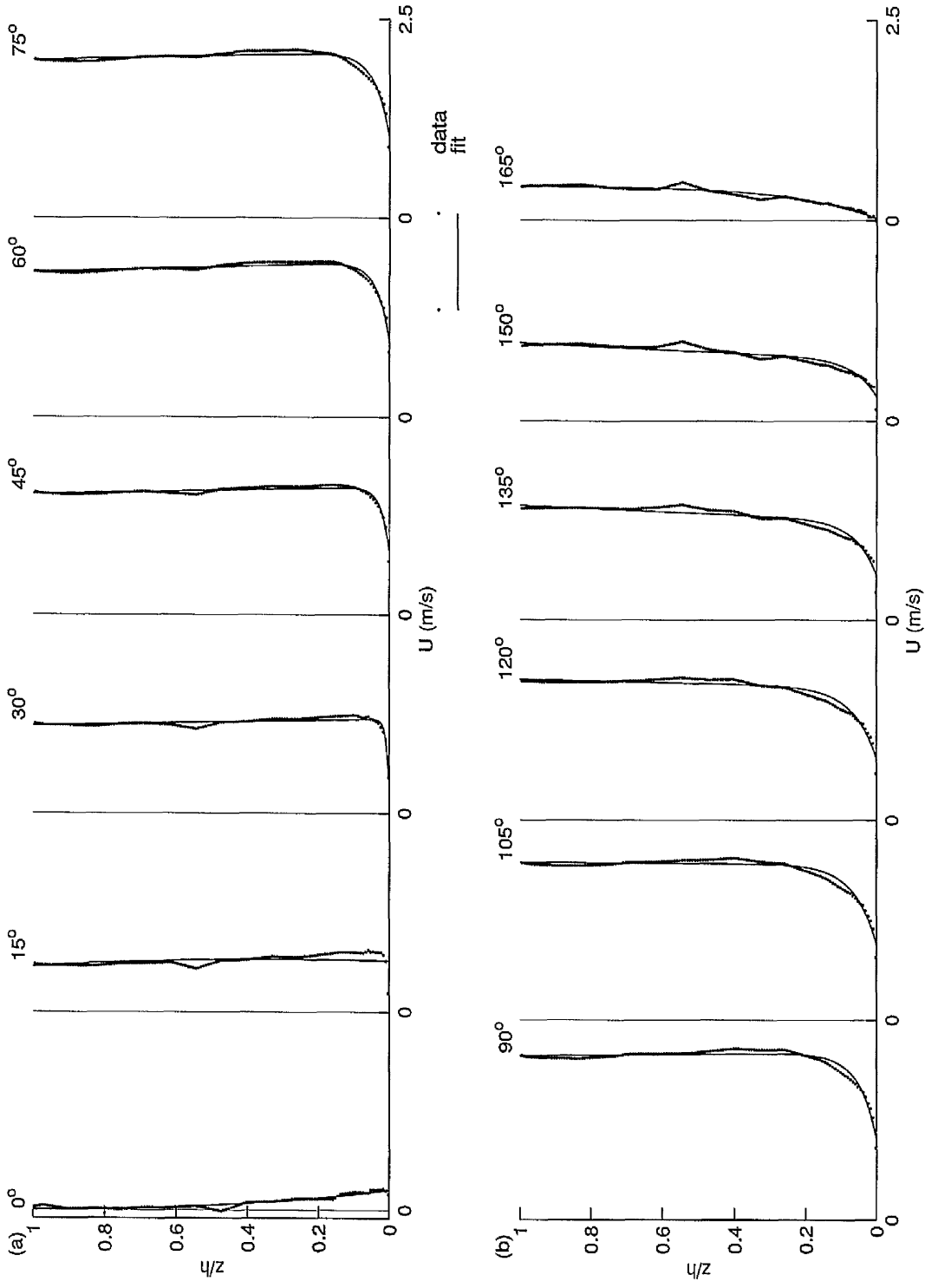

Figure 74: Profiles of experimental velocity data with least squares fit for the JSF10 case

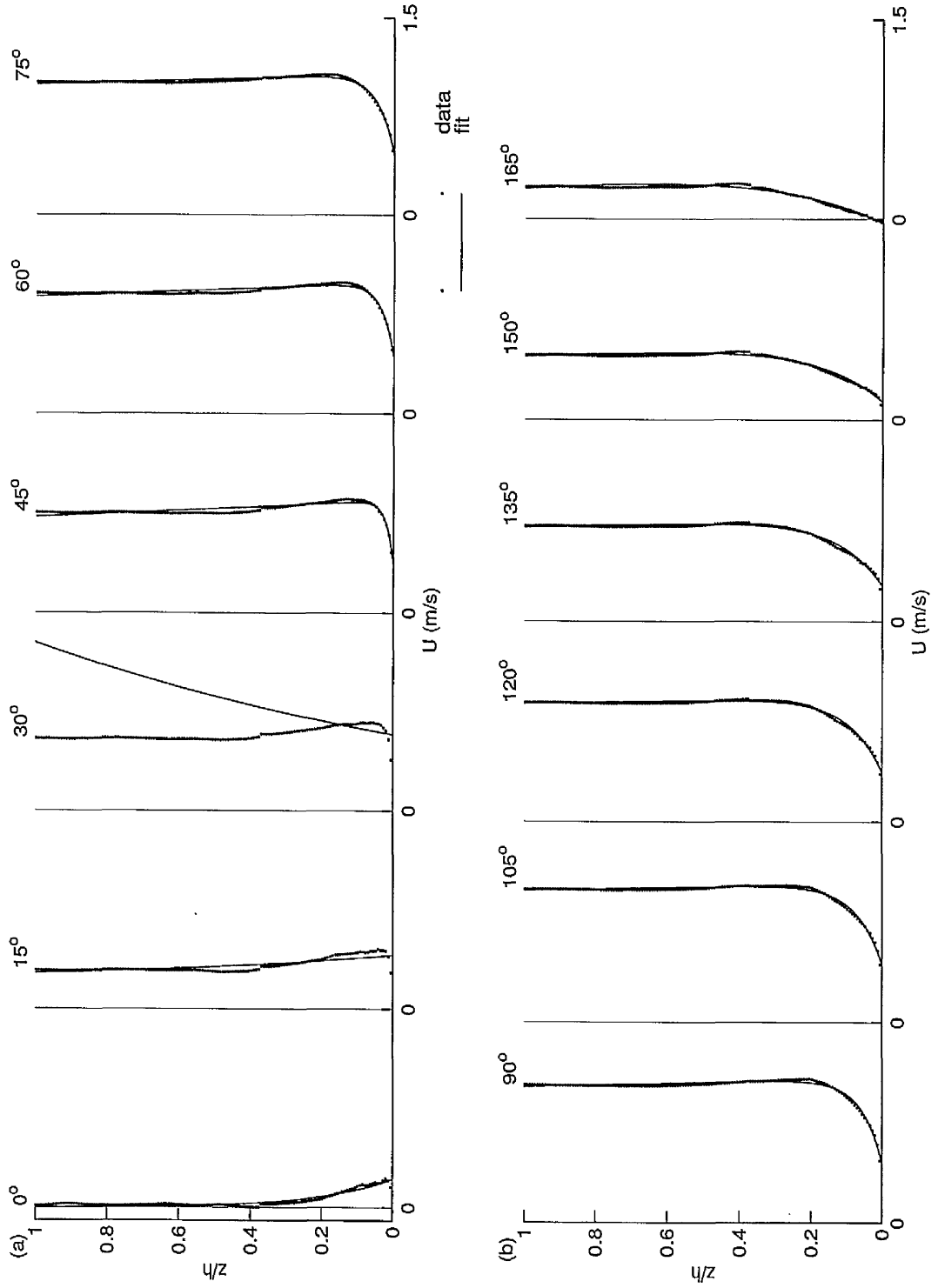

Figure 75: Profiles of experimental velocity data with least squares fit for the JSF12 case

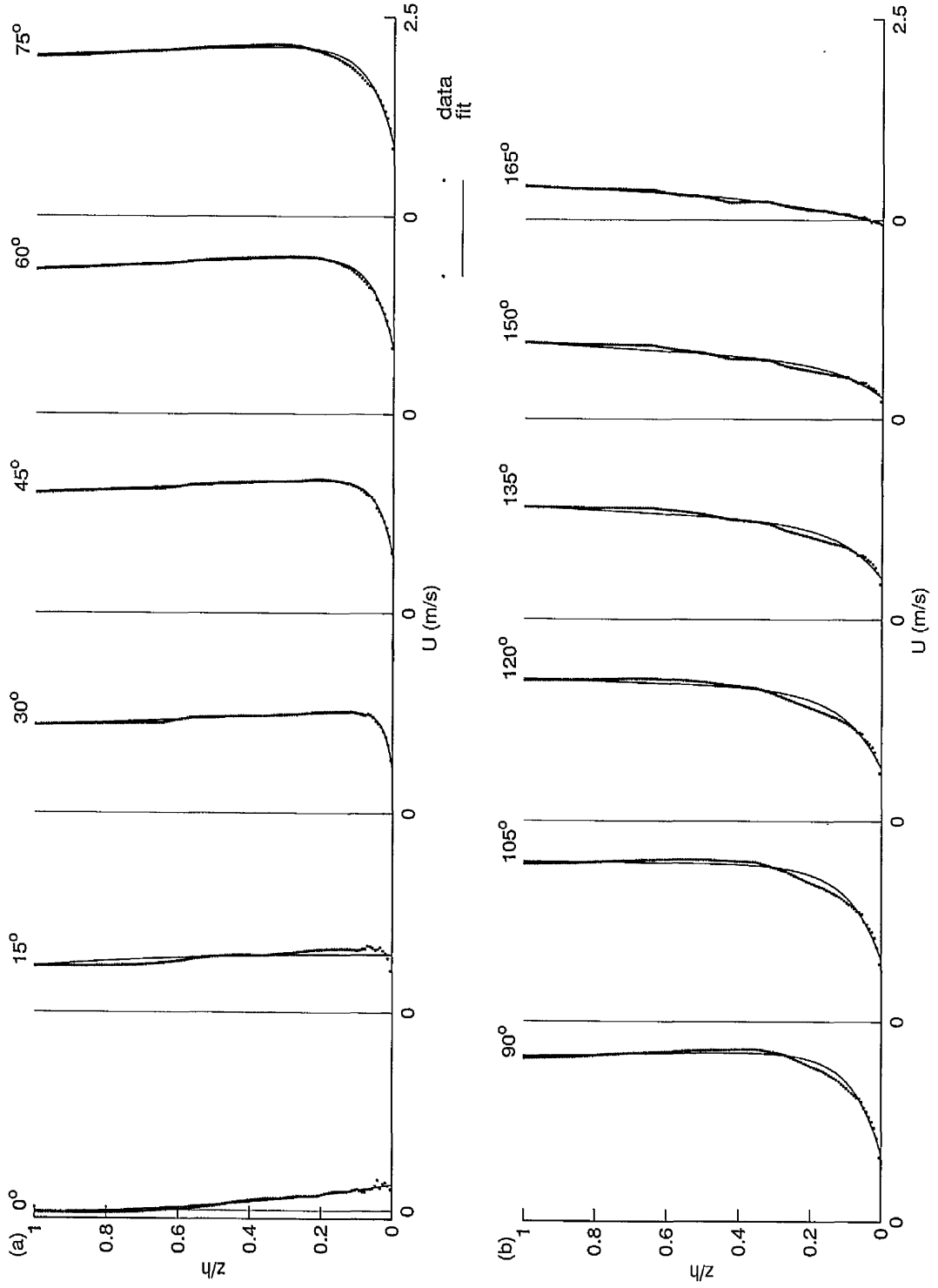

Figure 76: Profiles of experimental velocity data with least squares fit for the JSF13 case

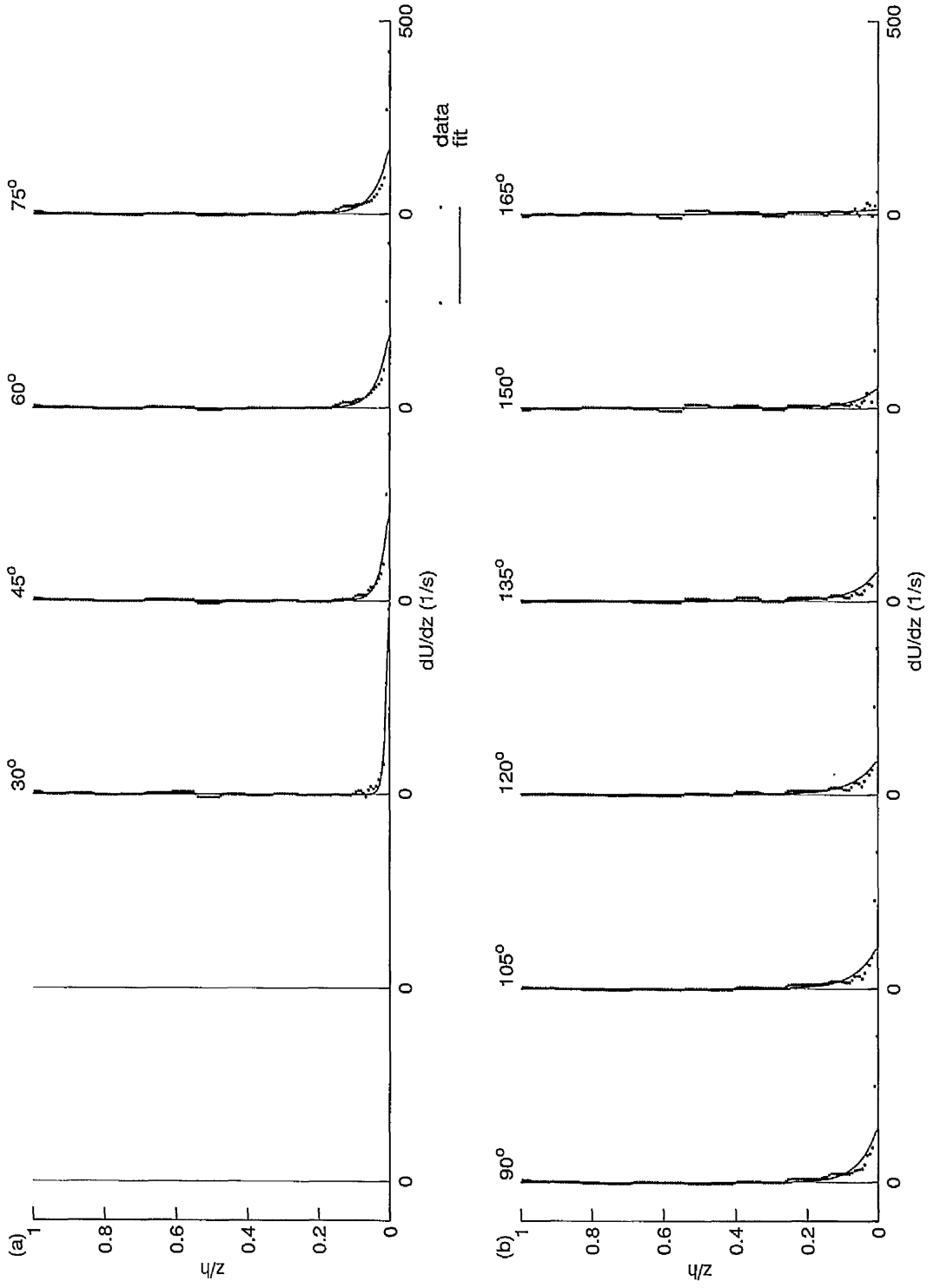

Figure 77: Profiles of velocity gradient data with gradient of least squares fit for the JSF10 case

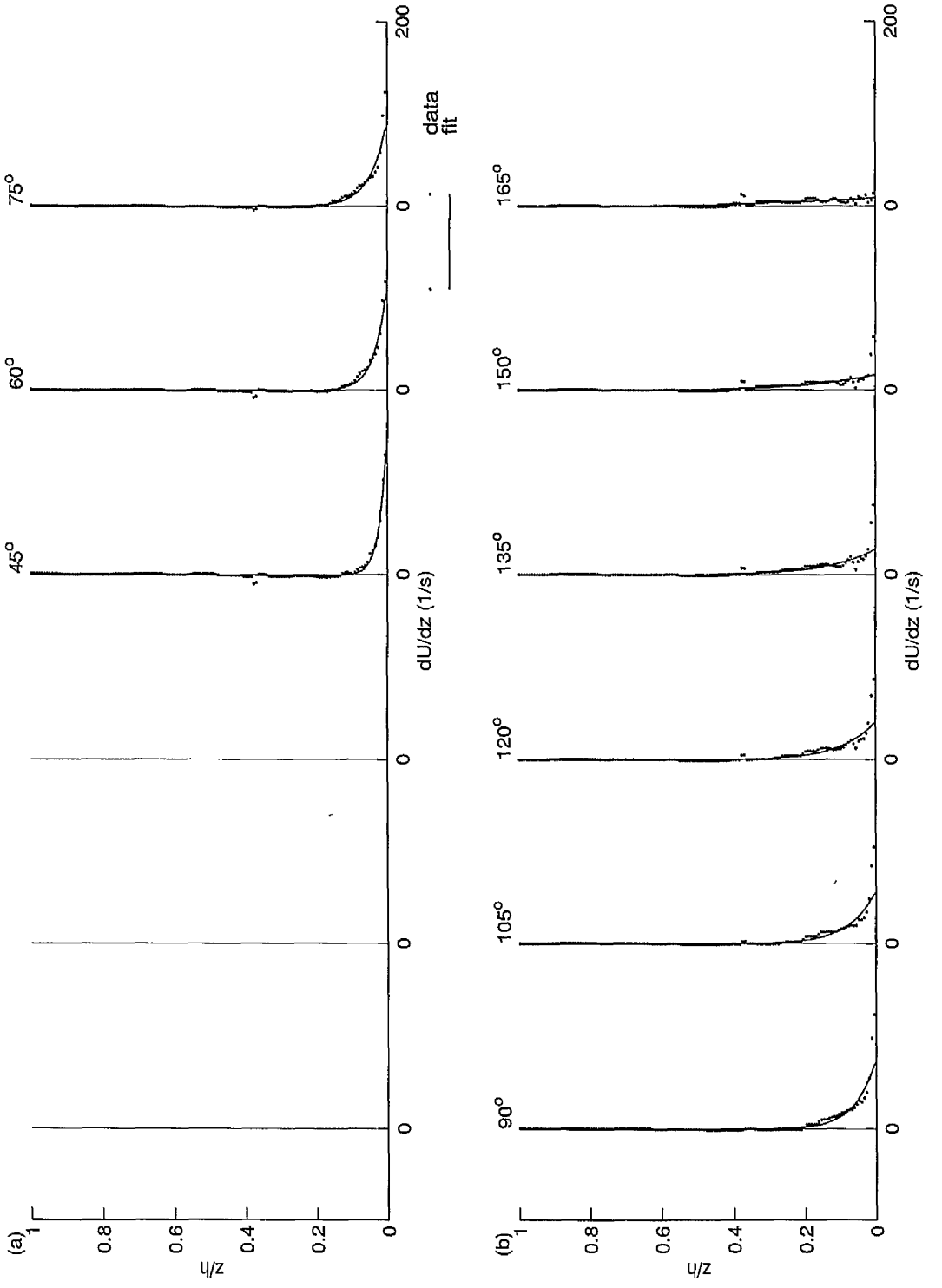

Figure 78: Profiles of velocity gradient data with gradient of least squares fit for the JSF12 case

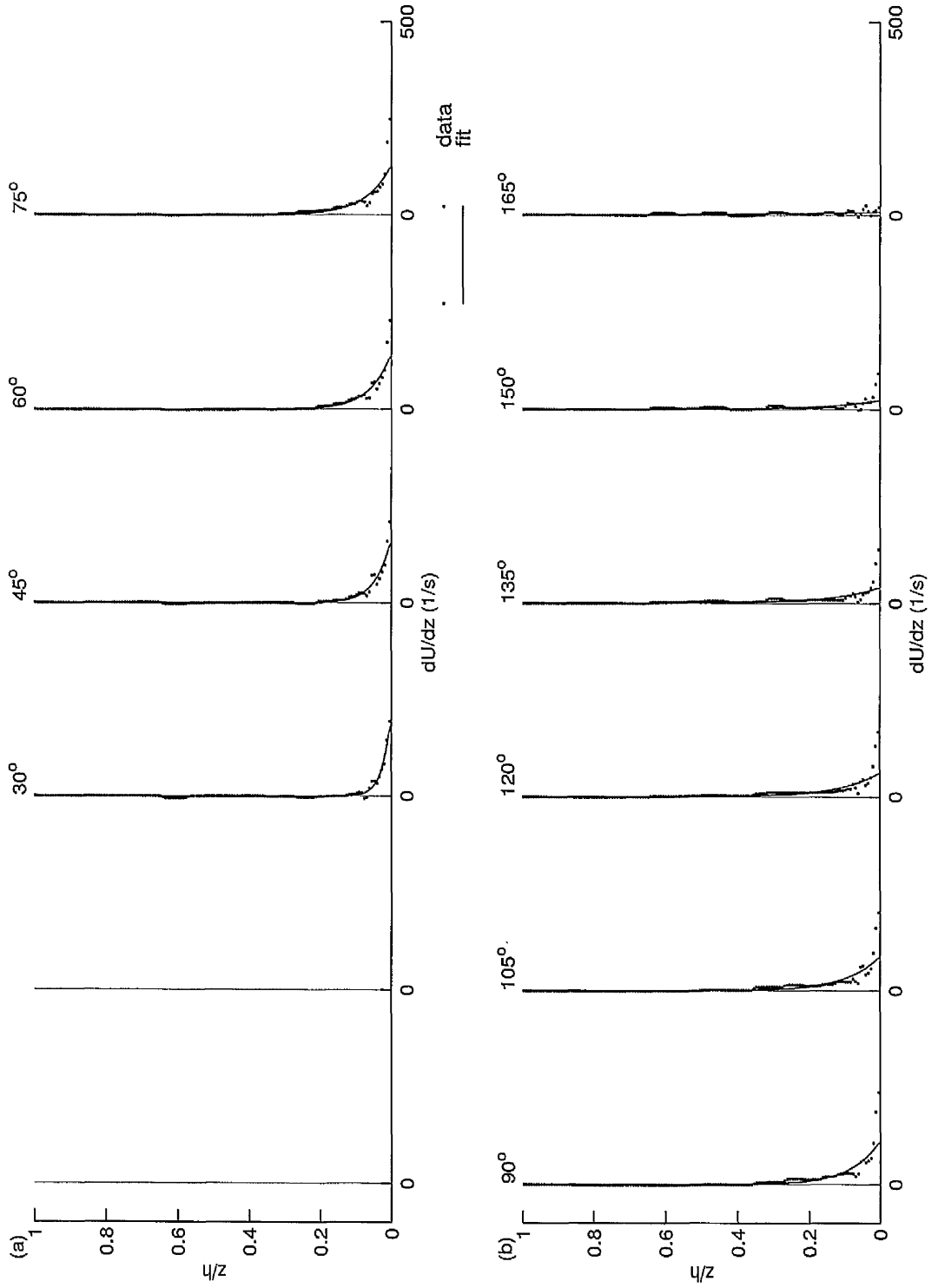

Figure 79: Profiles of velocity gradient data with gradient of least squares fit for the JSF13 case

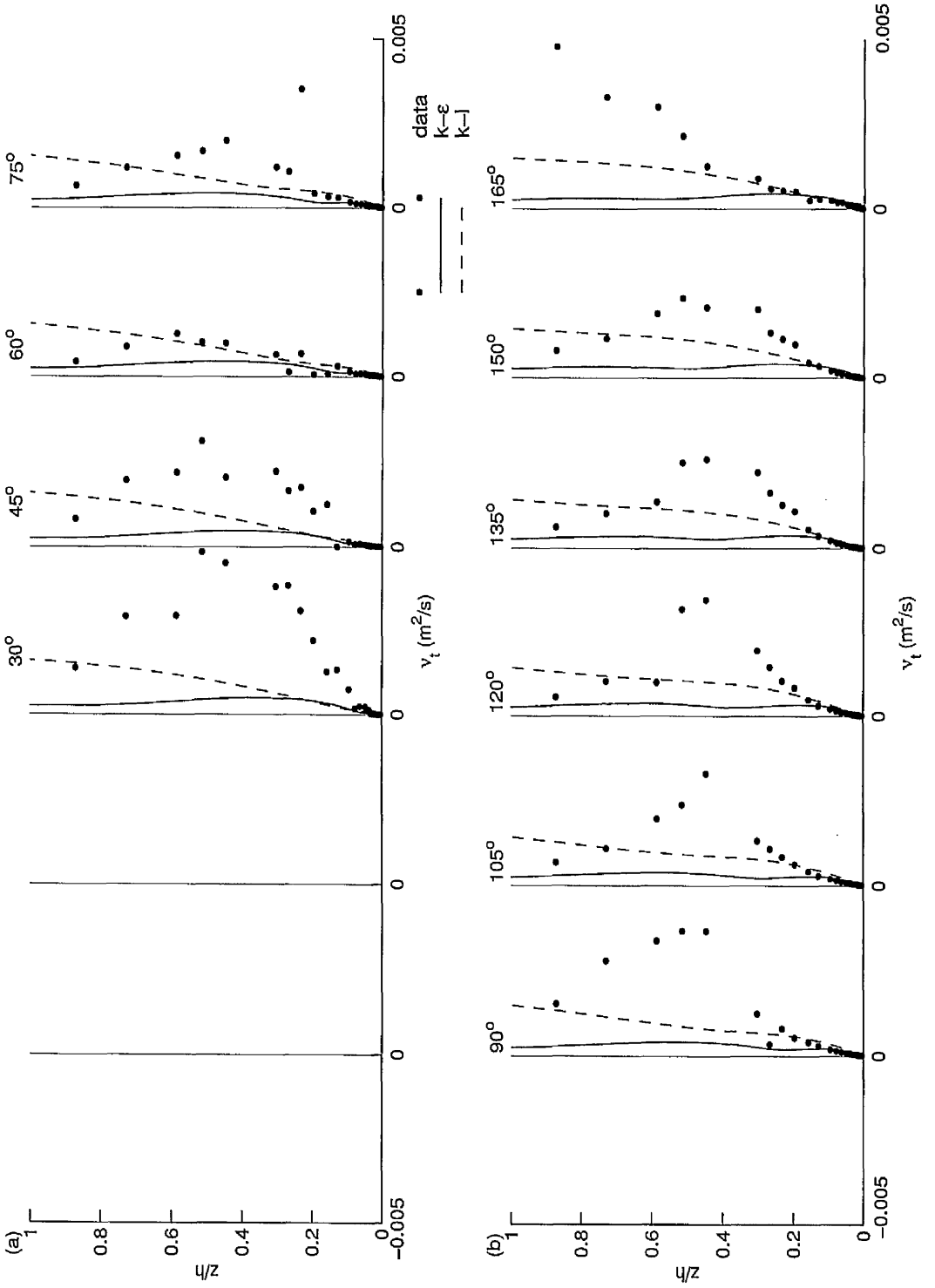

Figure 80: Profiles of turbulent eddy viscosity for the JSF10 case

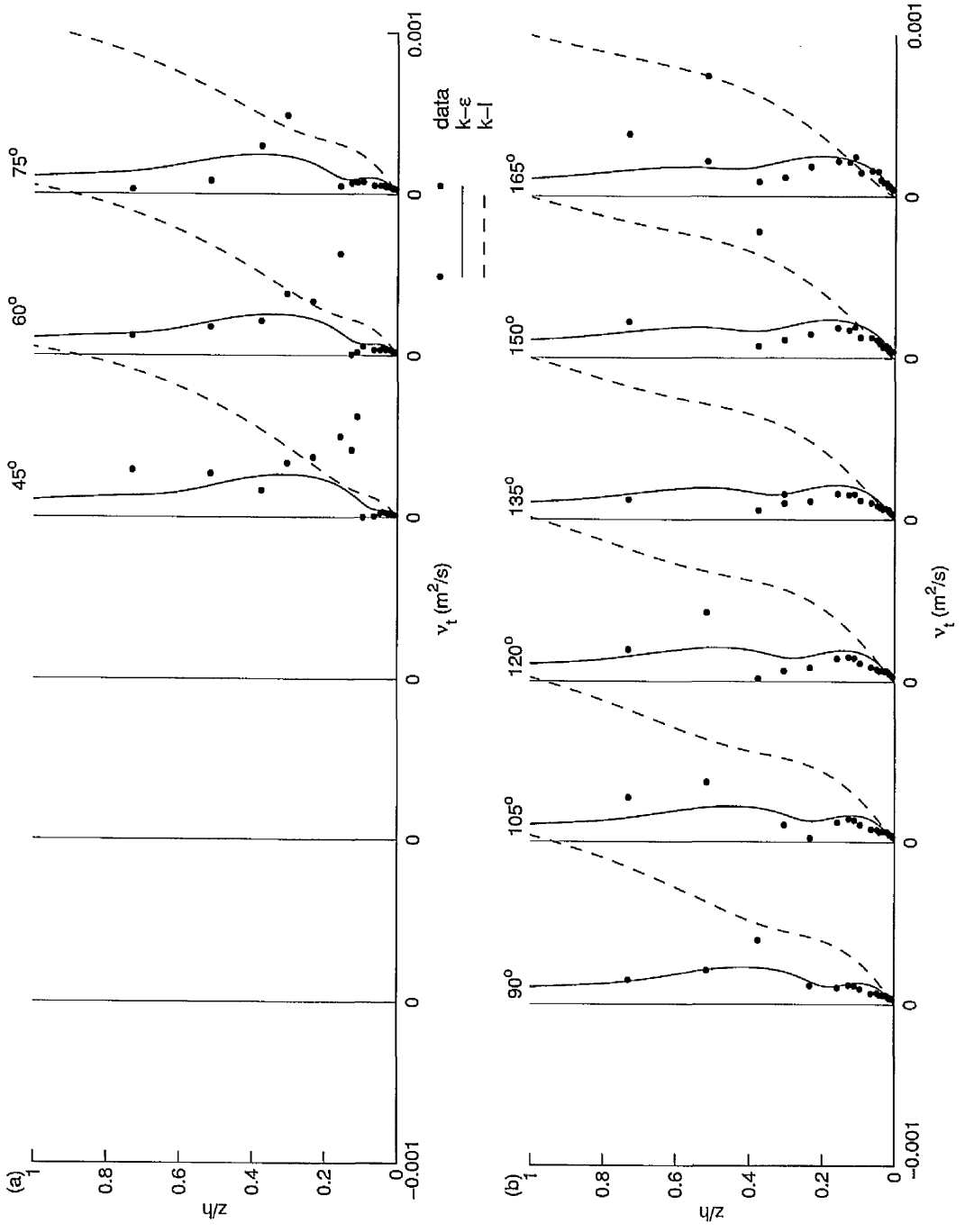

Figure 81: Profiles of turbulent eddy viscosity for the JSF12 case

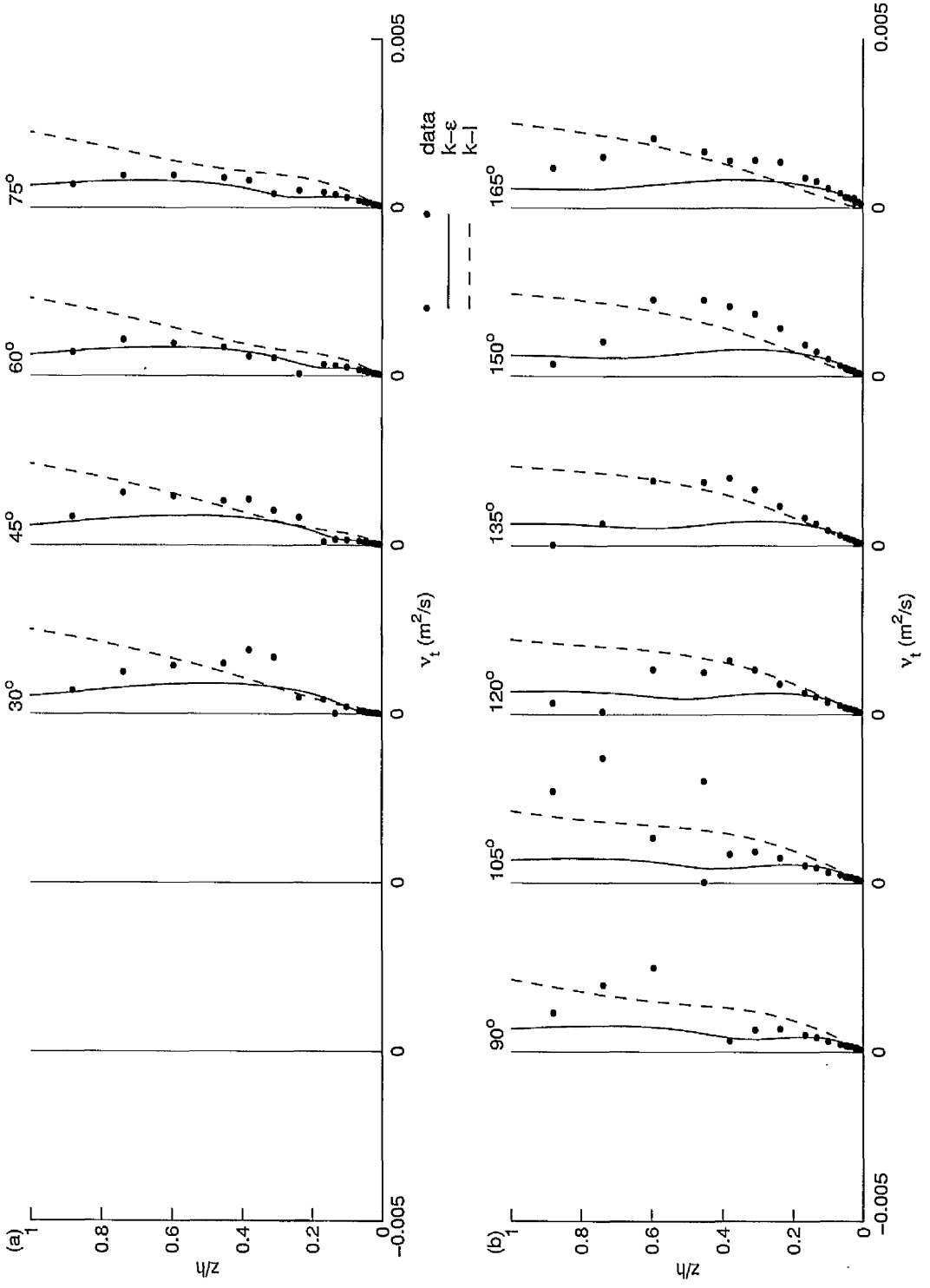

Figure 82: Profiles of turbulent eddy viscosity for the JSF13 case

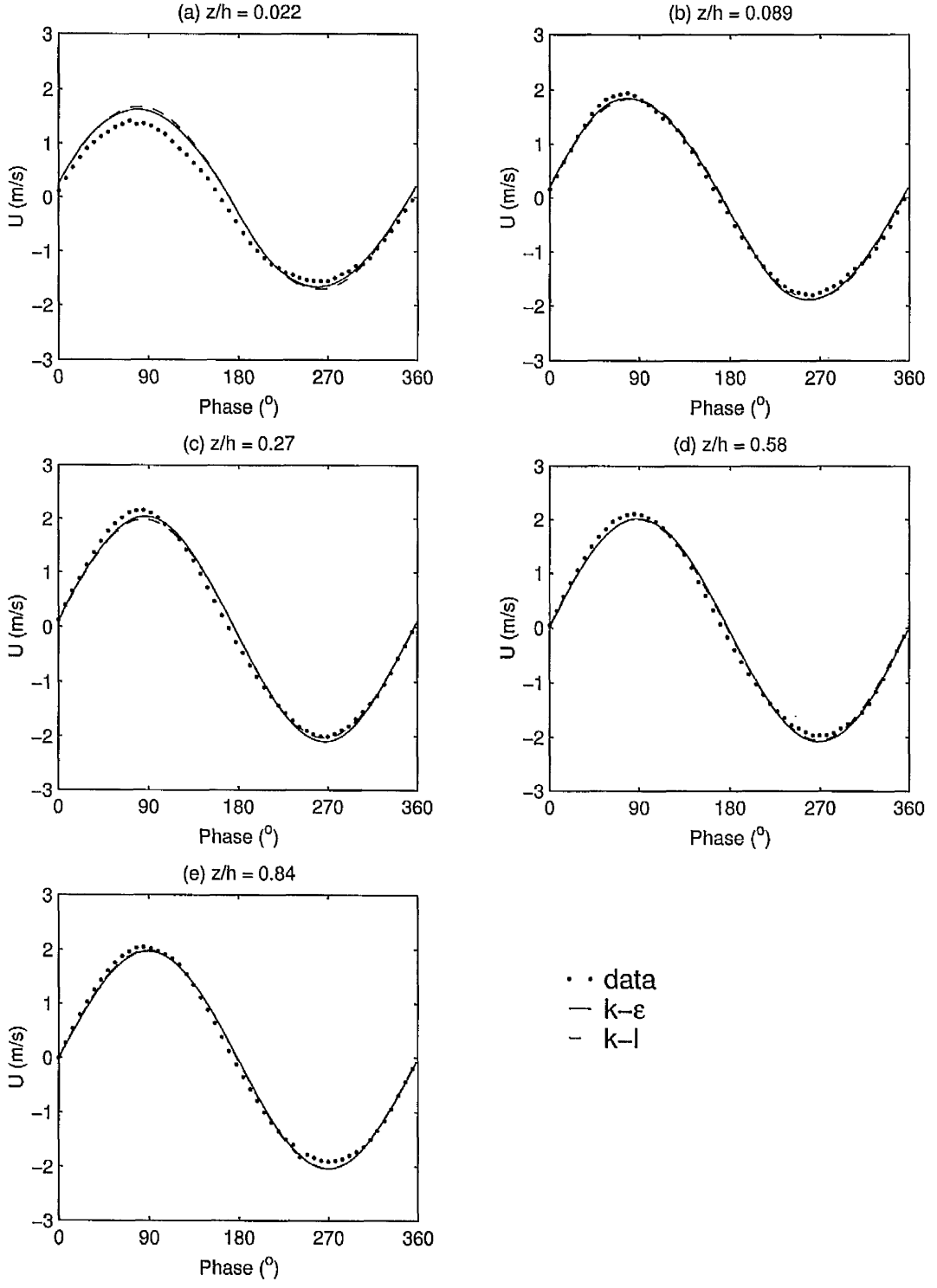

Figure 83: Cyclic variation of velocity at 5 heights above the bed for JSF10 case

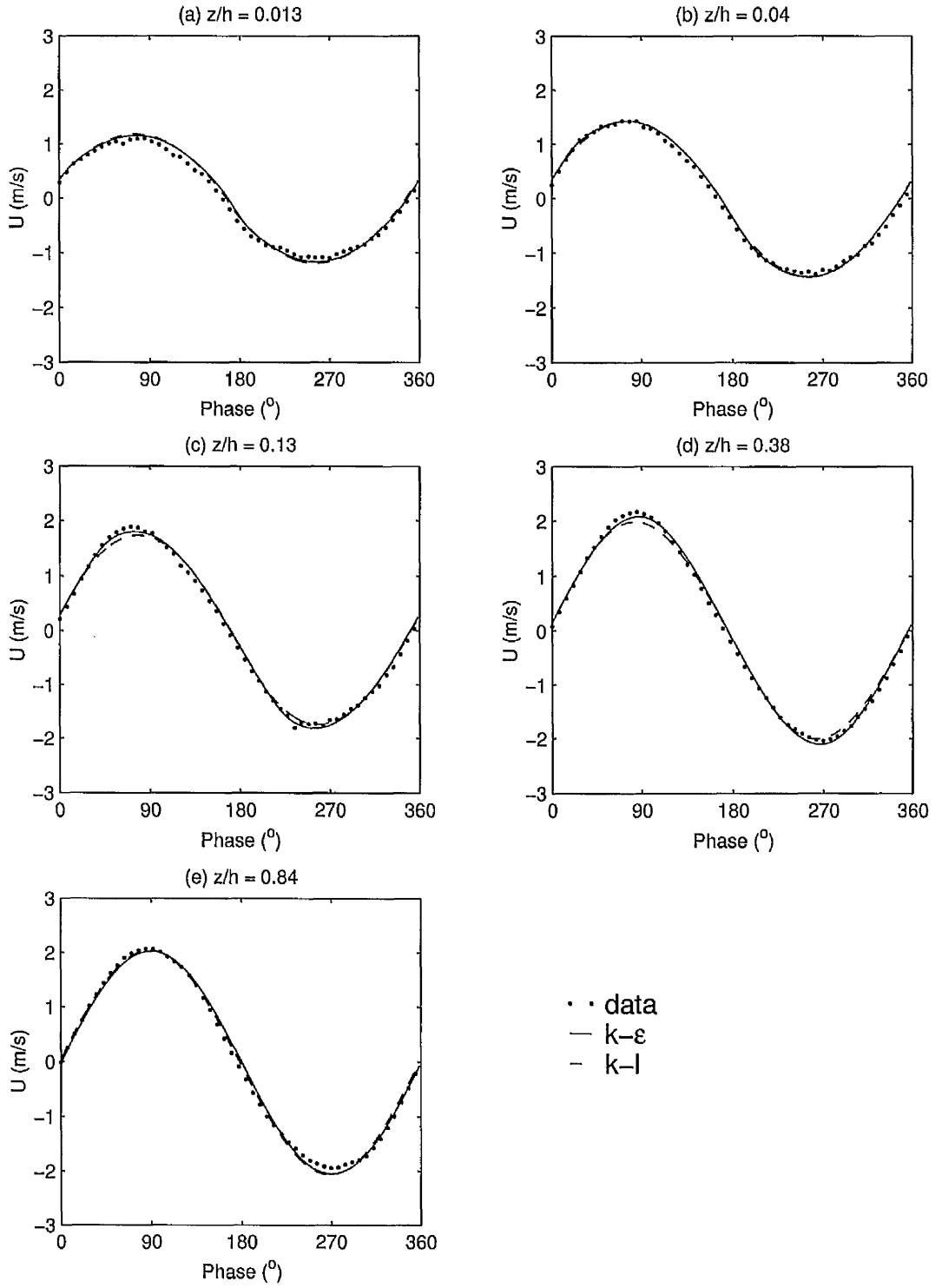

Figure 84: Cyclic variation of velocity at 5 heights above the bed for JSF13 case

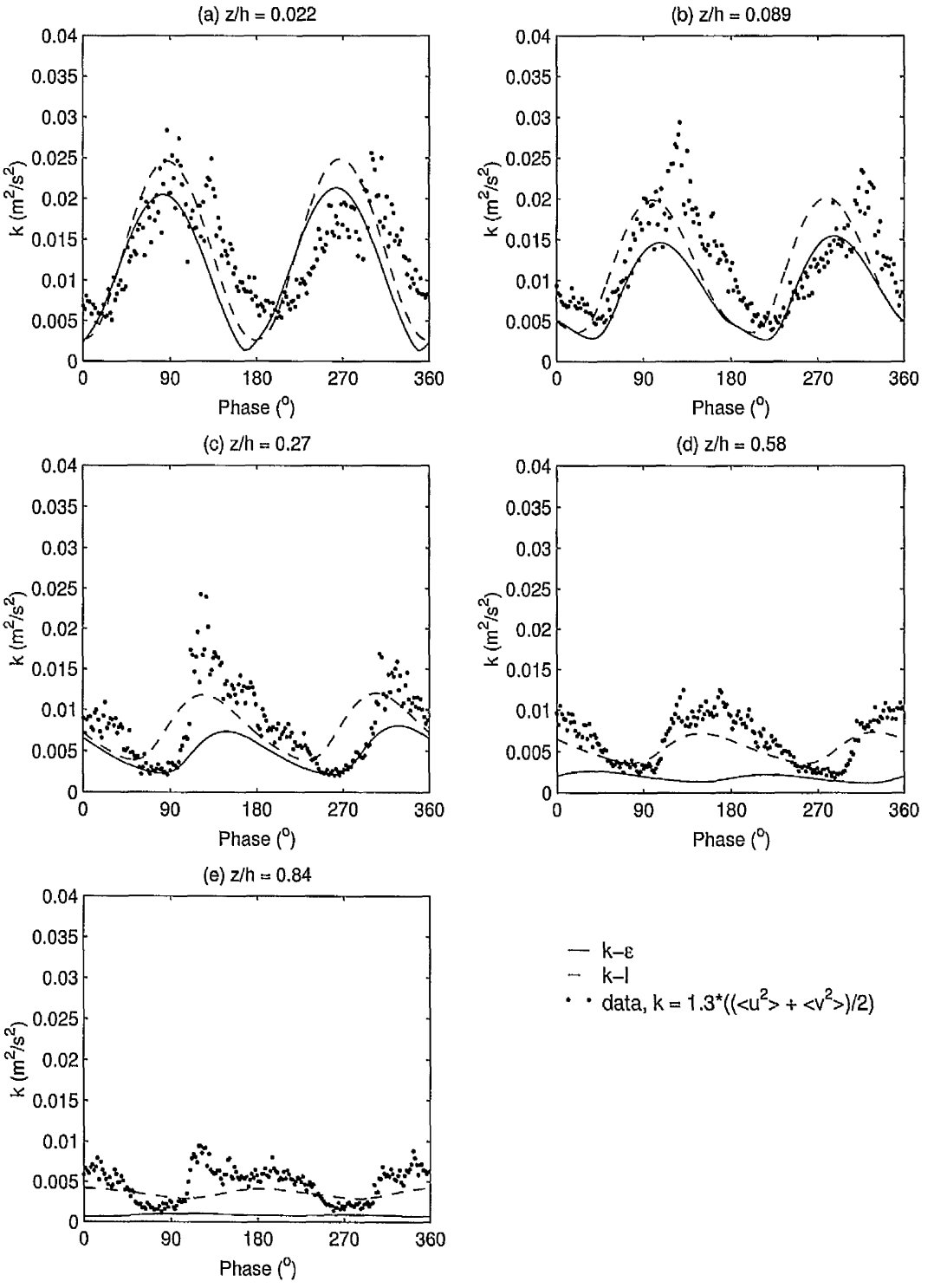

Figure 85: Cyclic variation of turbulent kinetic energy at 5 heights above the bed for JSF10 case

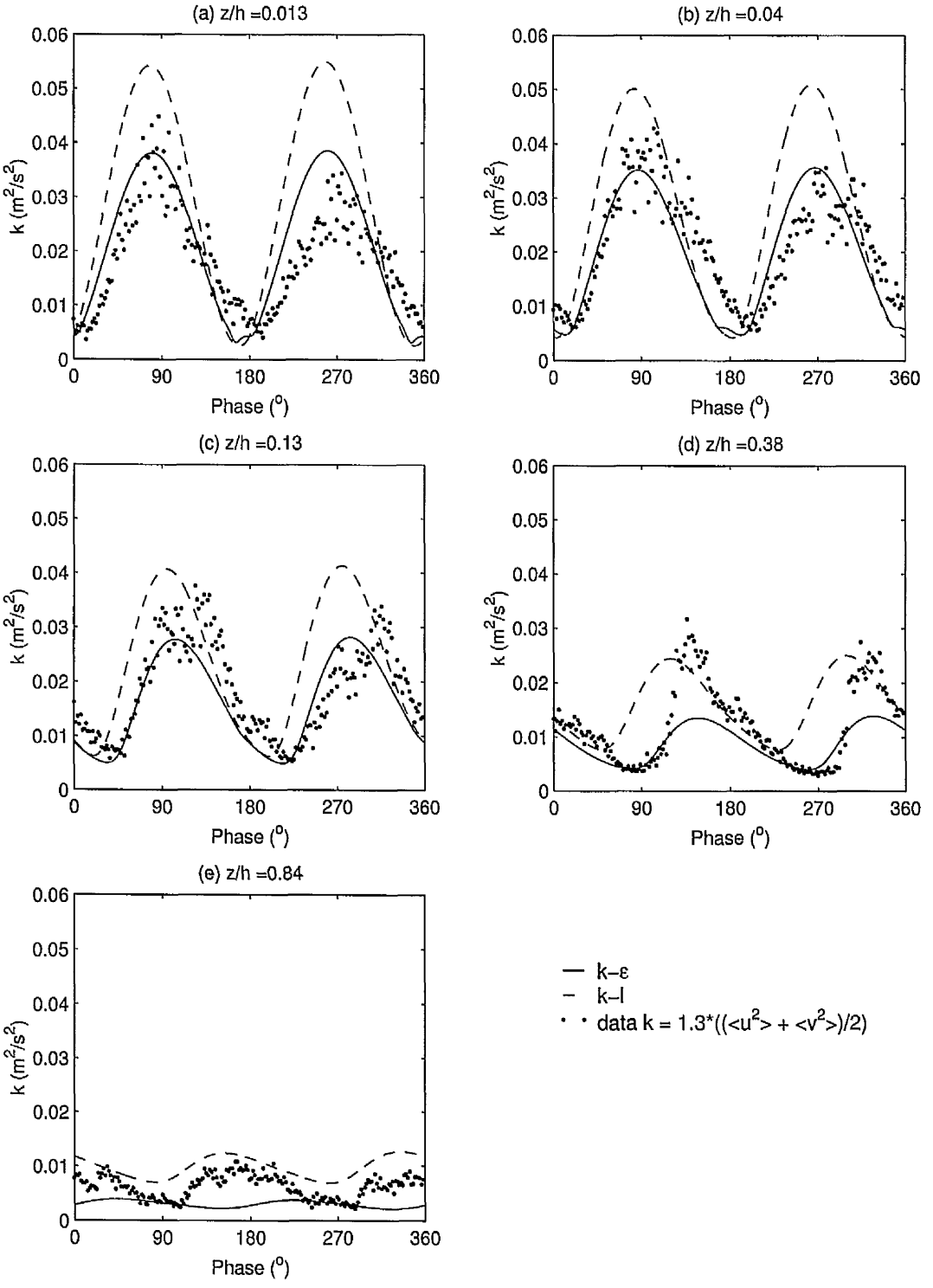

Figure 86: Cyclic variation of turbulent kinetic energy at 5 heights above the bed for JSF13 case

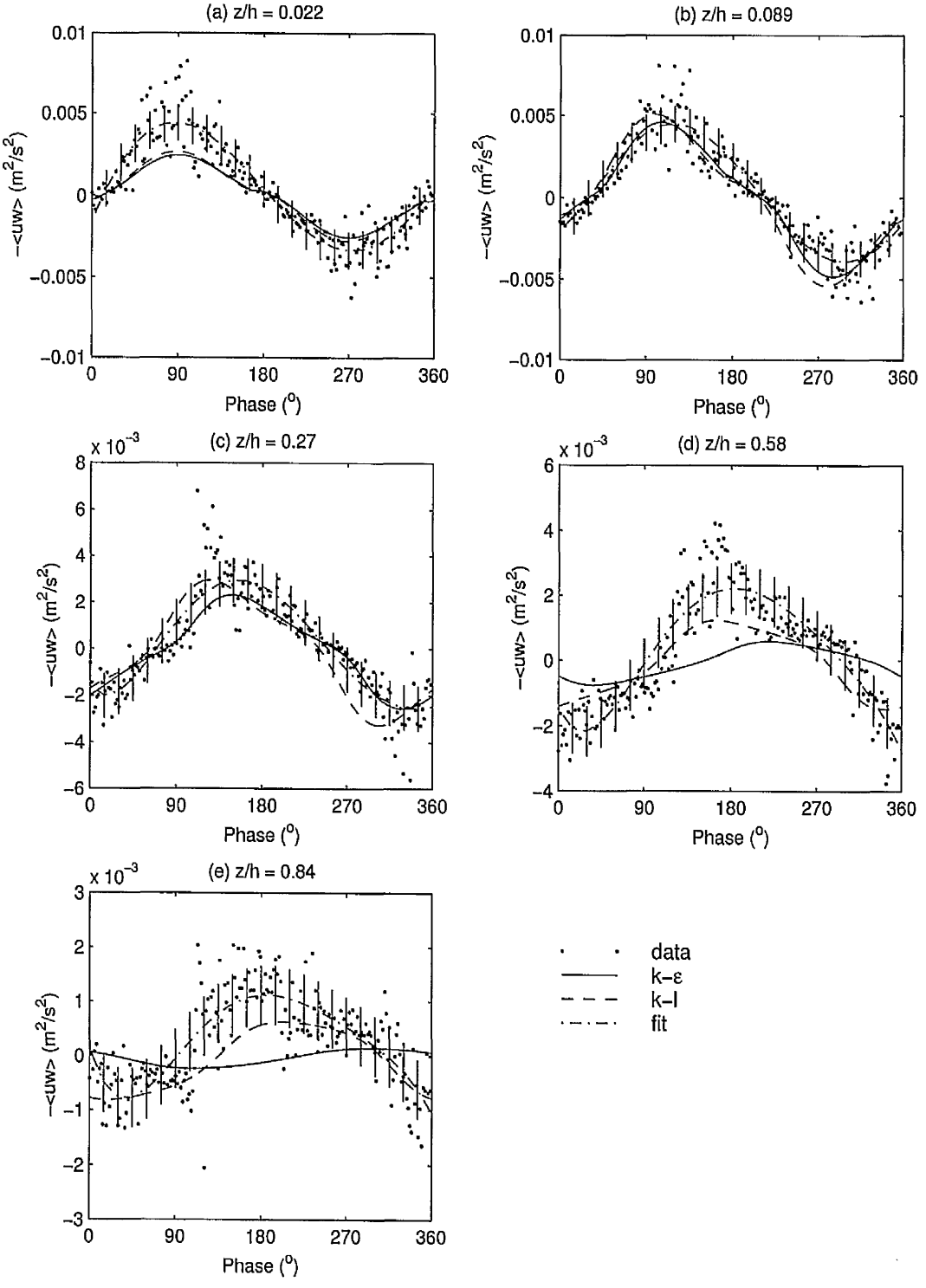

Figure 87: Cyclic variation of Reynolds shear stress at 5 heights above the bed for JSF10 case: 'fit' denotes a polynomial fit to the data of order 5 and the vertical lines give the uncertainty range of the fit

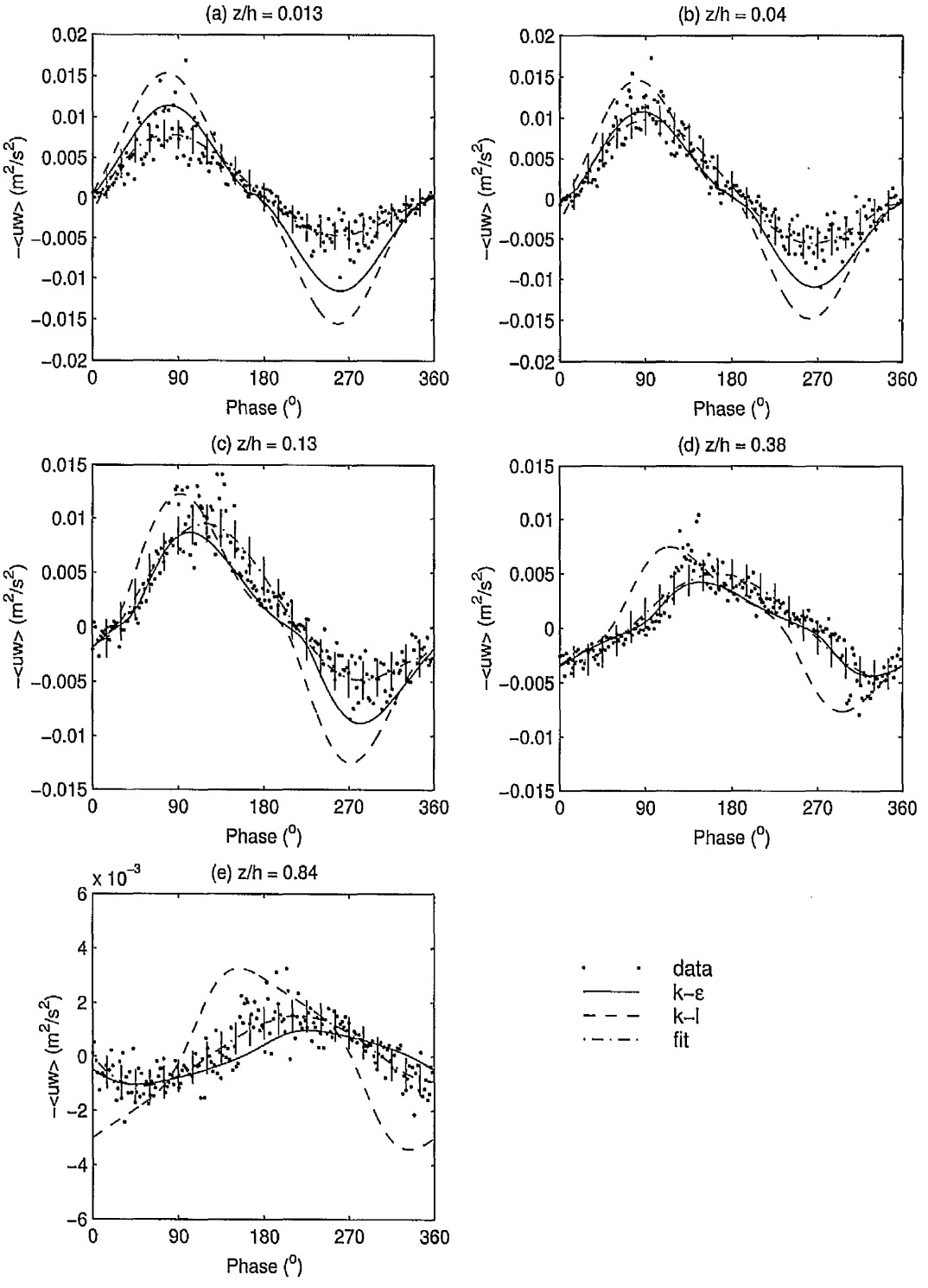

Figure 88: Cyclic variation of Reynolds shear stress at 5 heights above the bed for JSF13 case: 'fit' denotes a polynomial fit to the data of order 5 and the vertical lines give the uncertainty range of the fit

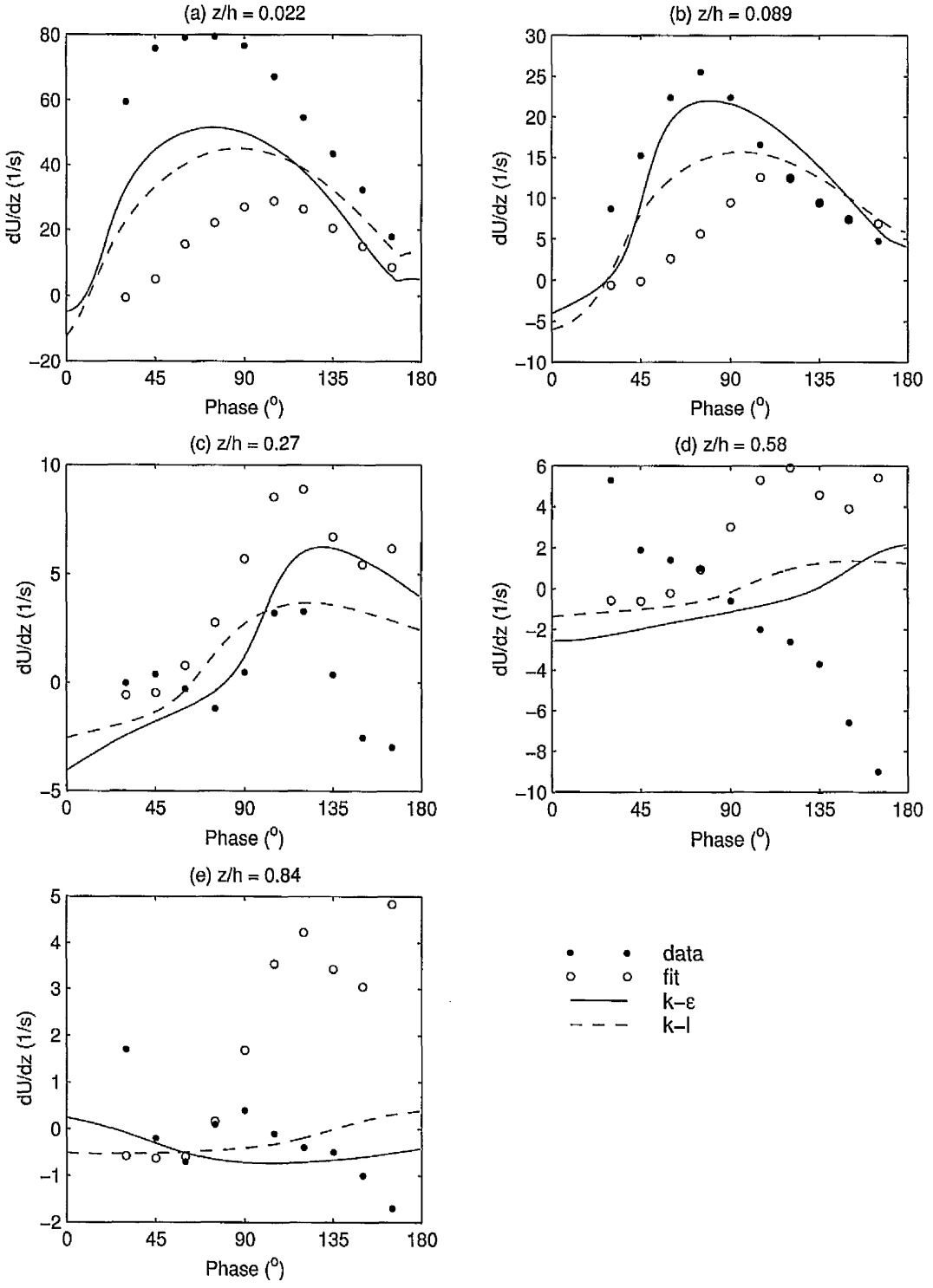

Figure 89: Cyclic variation of the velocity gradient at 5 heights above the bed for JSF10 case: 'data' denotes the gradient formed from the experimental velocity data and 'fit' denotes the gradient formed from a least squares fit to the experimental velocity data

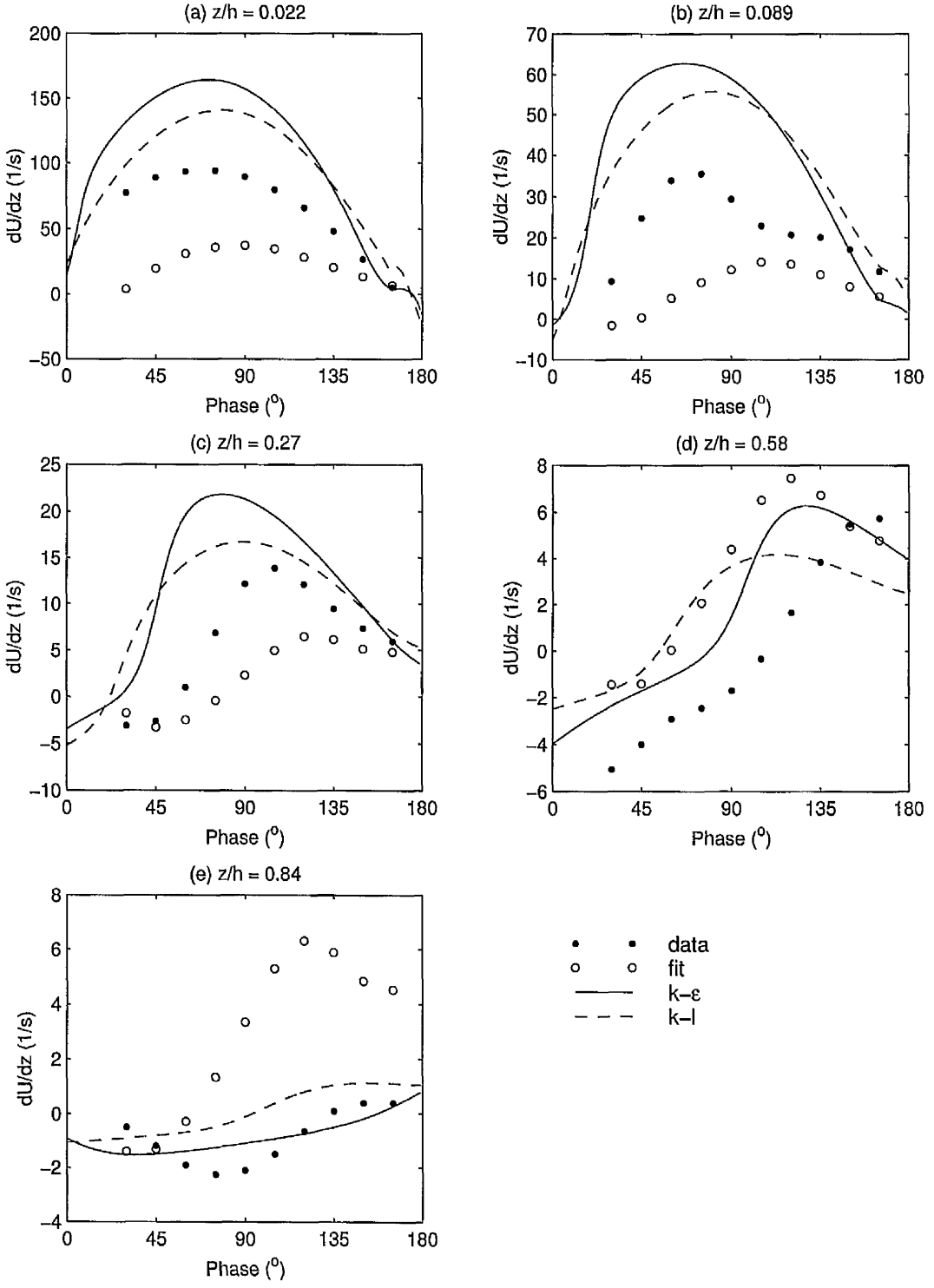

Figure 90: Cyclic variation of the velocity gradient at 5 heights above the bed for JSF13 case: 'data' denotes the gradient formed from the experimental velocity data and 'fit' denotes the gradient formed from a least squares fit to the experimental velocity data

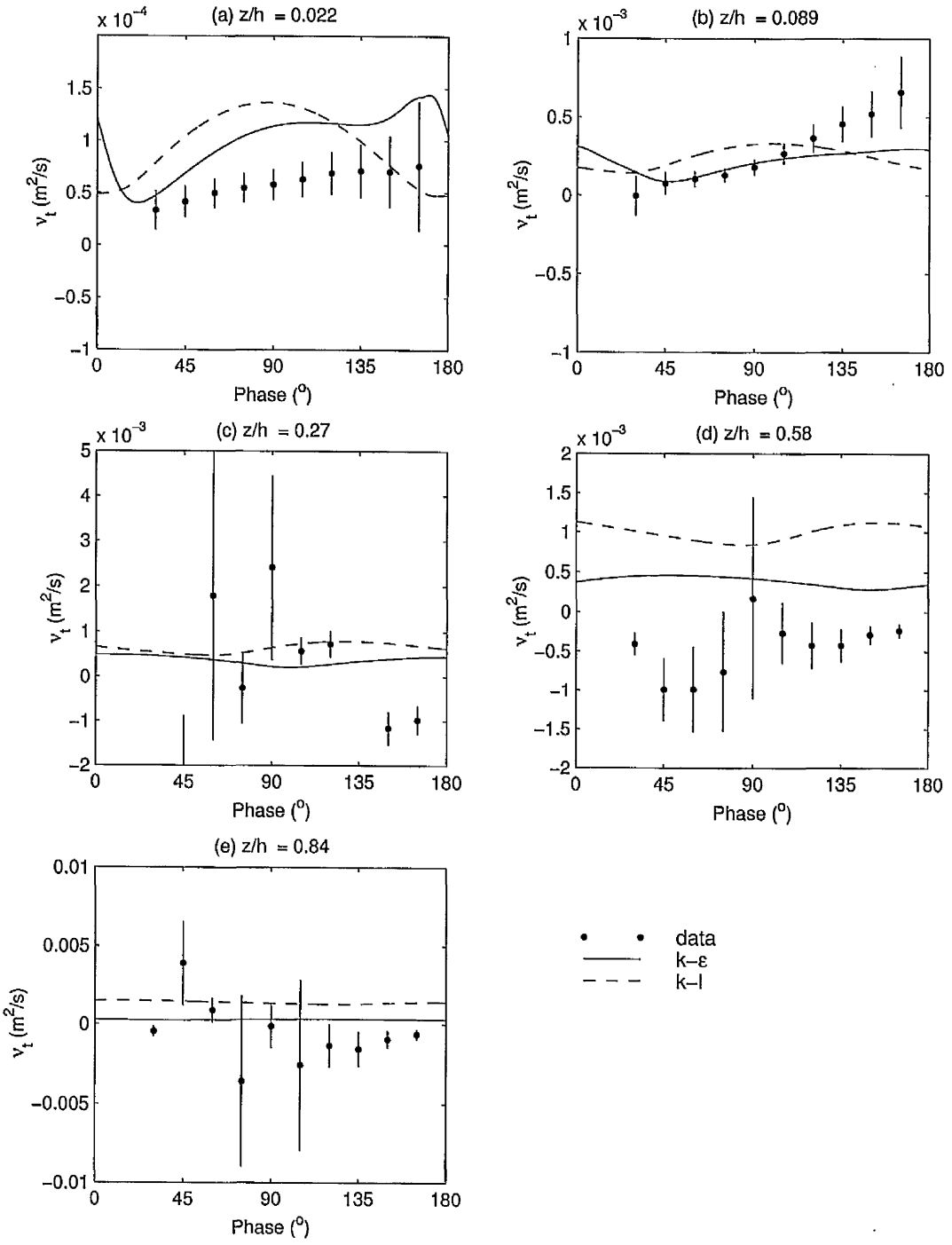

Figure 91: Cyclic variation of turbulent eddy viscosity at 5 heights above the bed for JSF10 case: the vertical lines give the uncertainty range of the experimental data

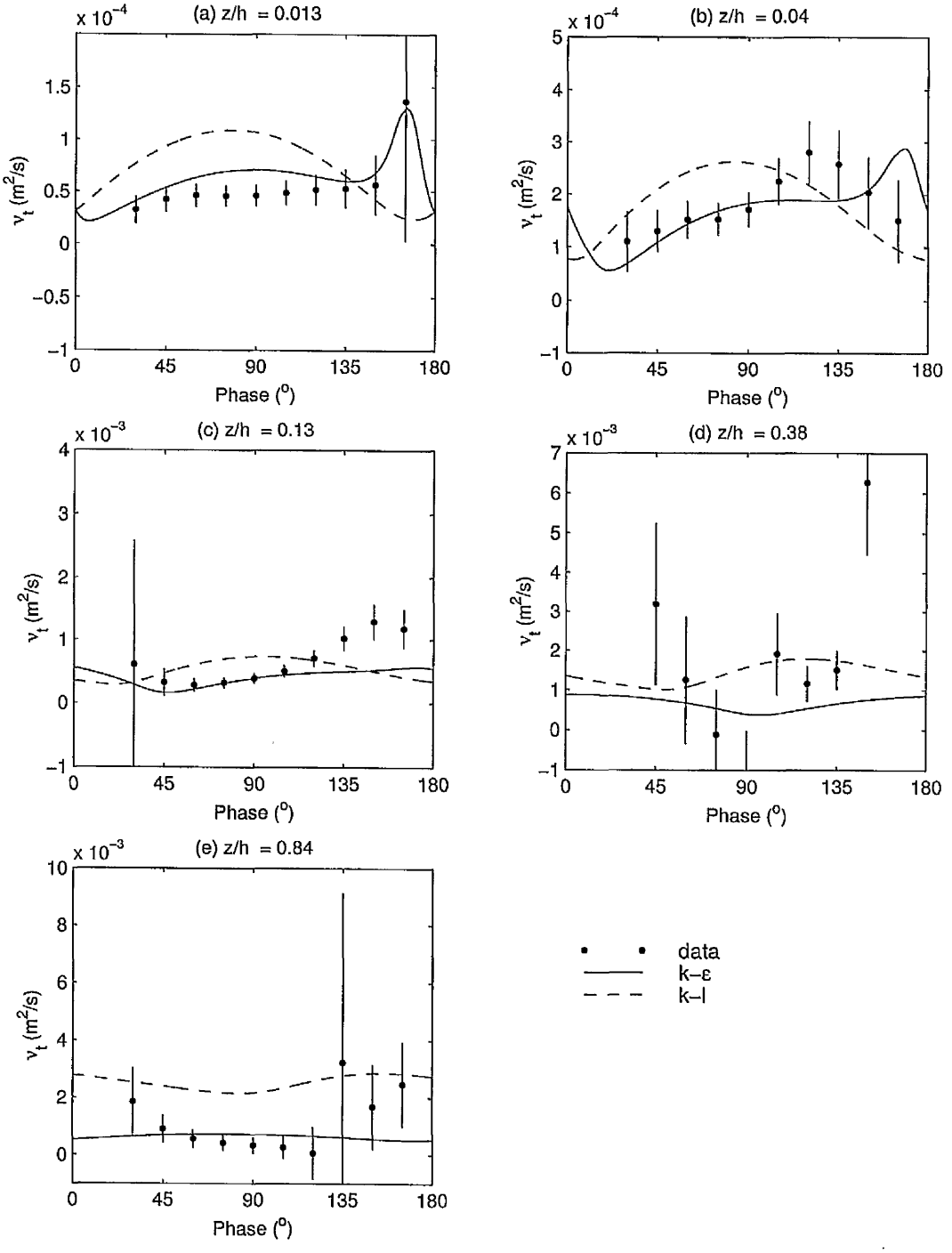

Figure 92: Cyclic variation of turbulent eddy viscosity at 5 heights above the bed for JSF13 case: the vertical lines give the uncertainty range of the experimental data

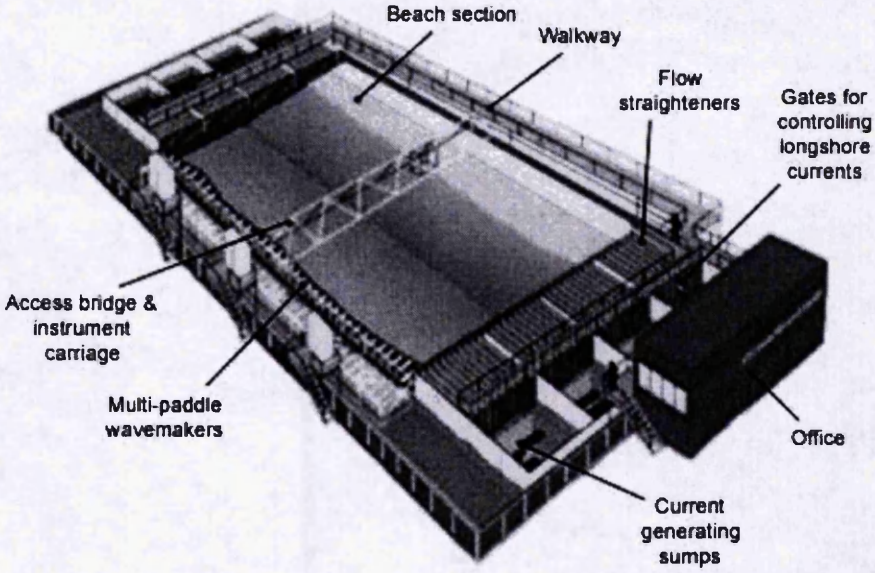

Figure 93: Photograph of UK Coastal Research Facility at HR Wallingford, Oxfordshire (Lloyd *et al* 1997)

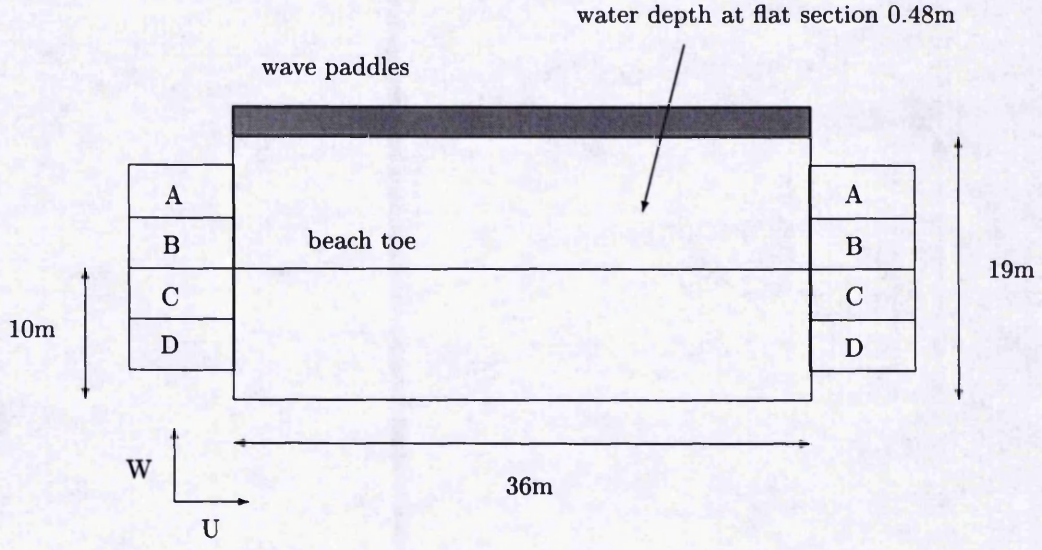

Figure 94: Experimental set-up of the UK Coastal Research Facility (Lloyd *et al* 1997)

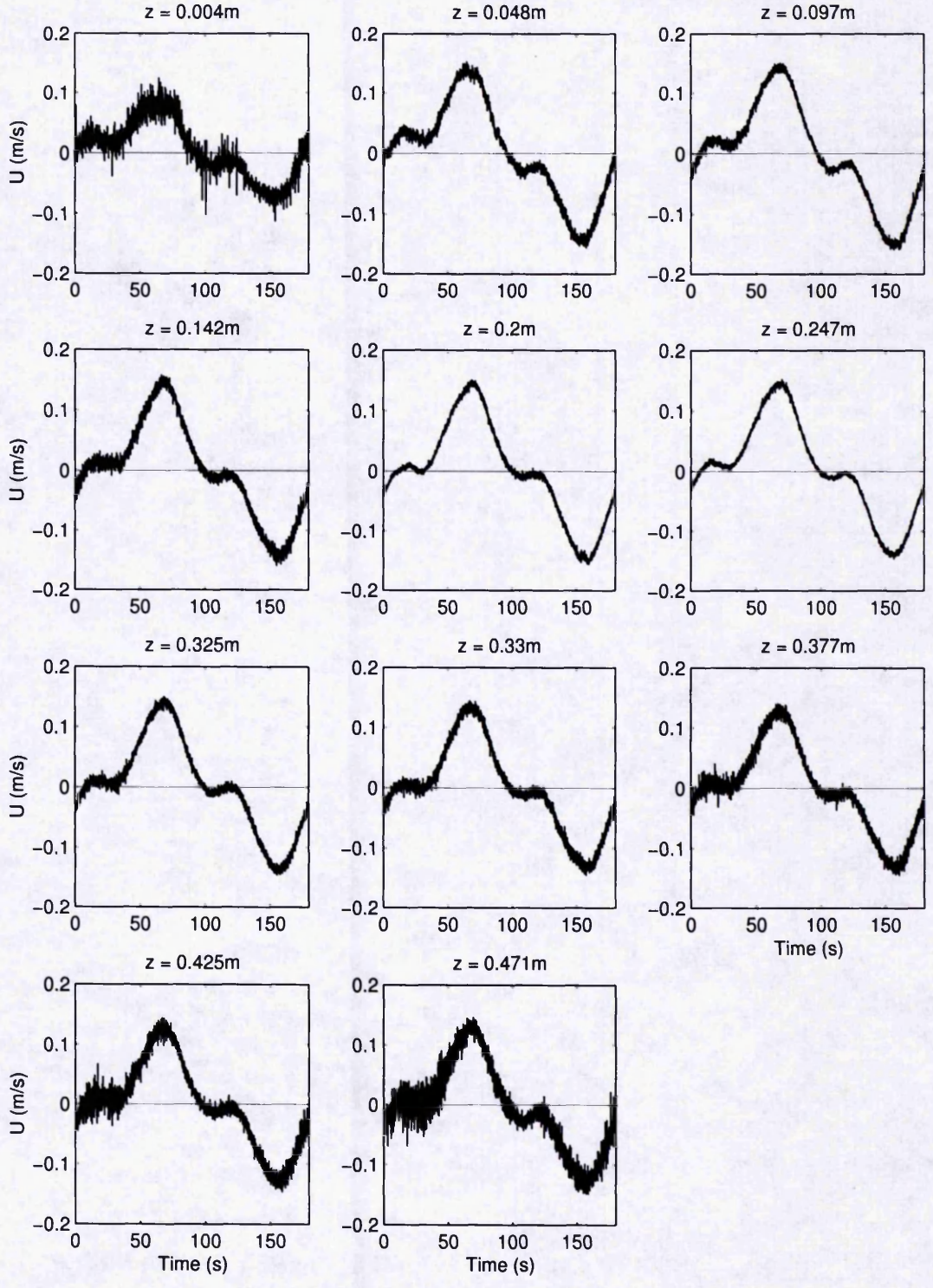

Figure 95: Cyclic variation of raw velocity ensemble averaged over 6 cycles at 11 heights above the bed for the UKCRF case

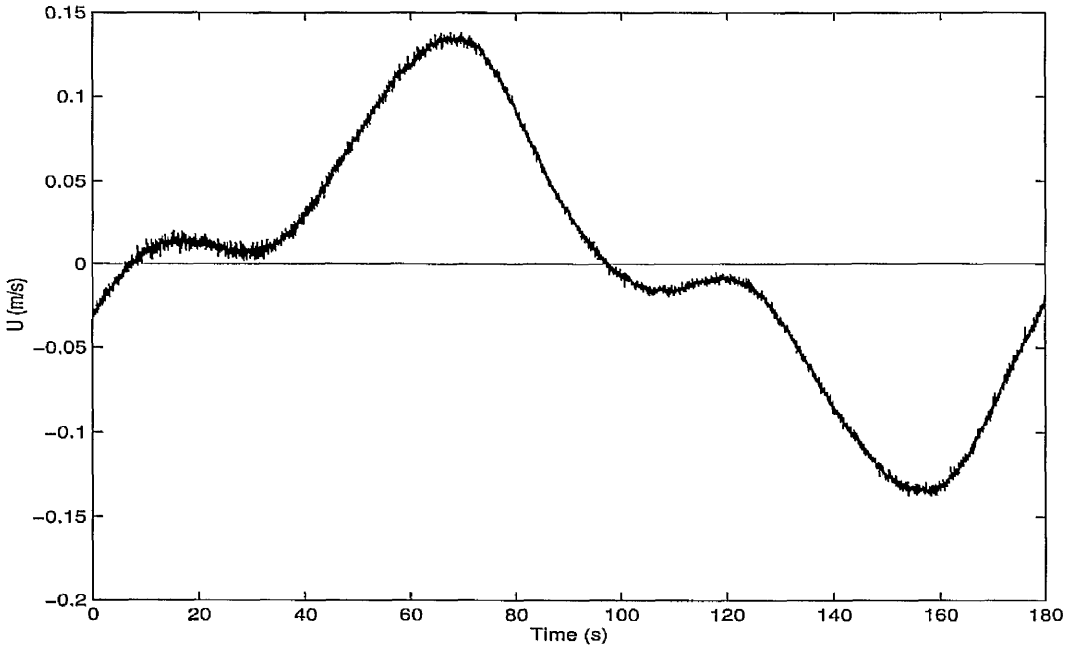

Figure 96: Cyclic variation of bulk velocity ensemble averaged over 6 cycles of oscillation for the UKCRF case

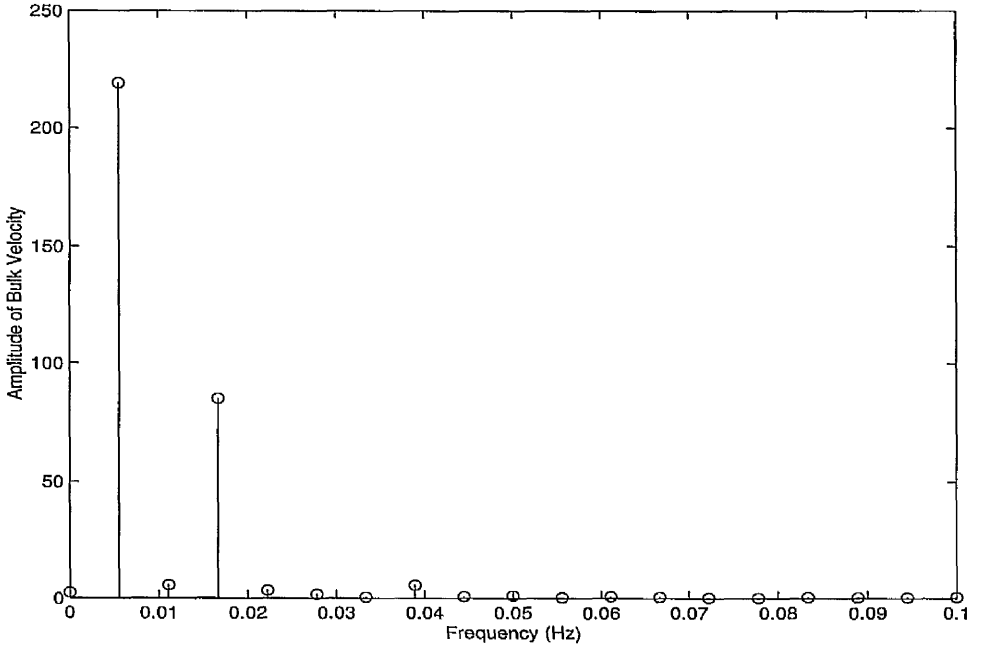

Figure 97: Fourier transform of bulk velocity for the UKCRF case

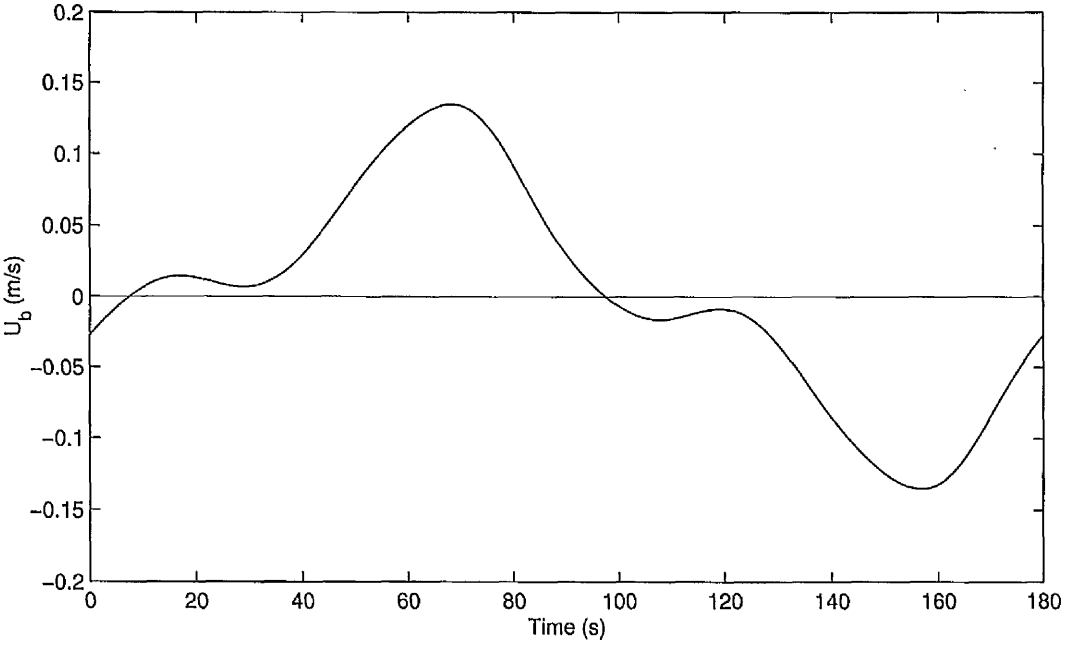

Figure 98: Smoothed bulk velocity across one cycle of oscillation for the UKCRF case

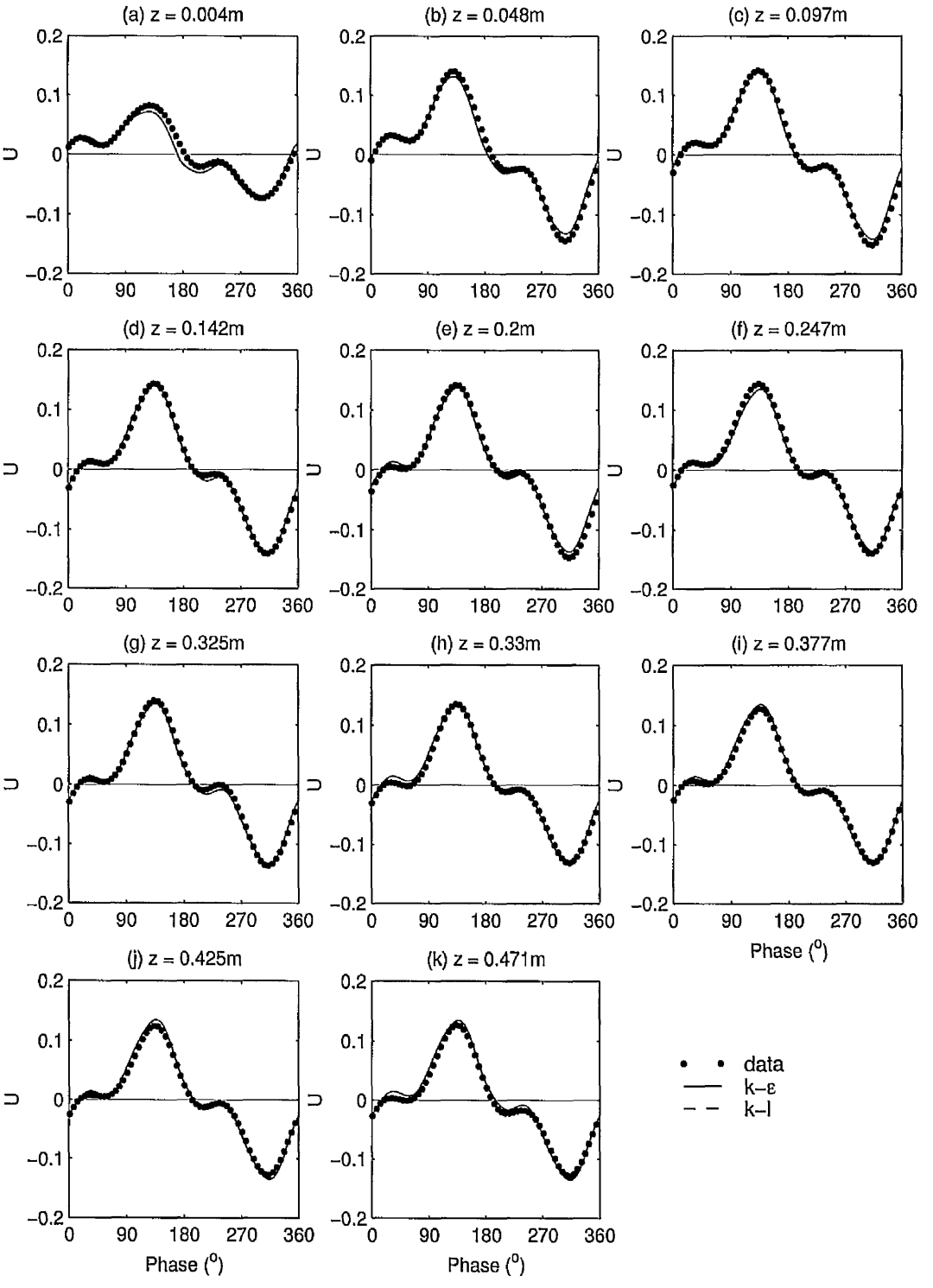

Figure 99: Cyclic variation of smoothed experimentalvelocity data at 11 heights above the bed compared with model calculations for the UKCRF case

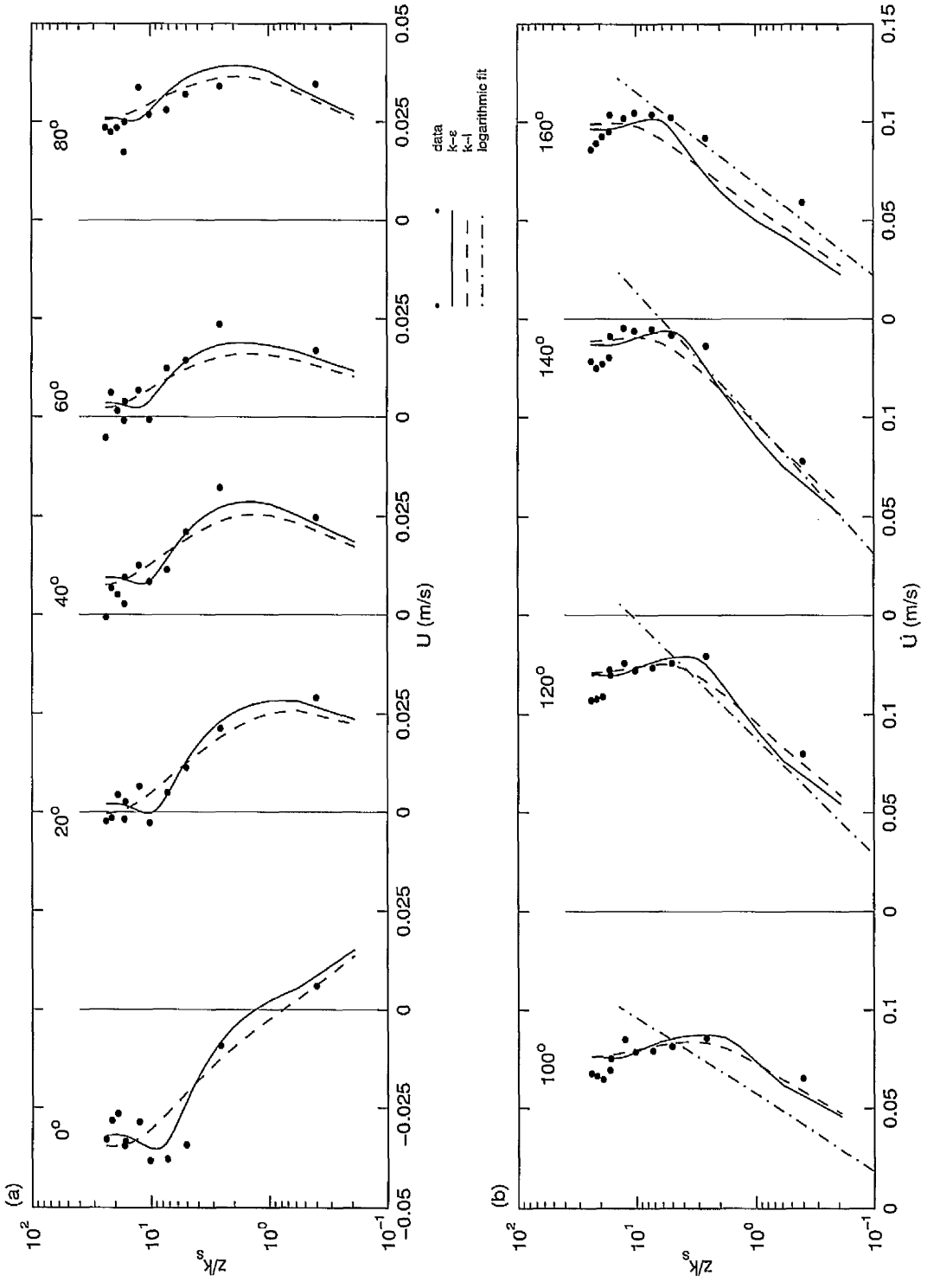

Figure 100: Profiles of velocity data compared with model calculations on semi-logarithmic axis for the UKCRF case, with logarithmic fit to velocity data

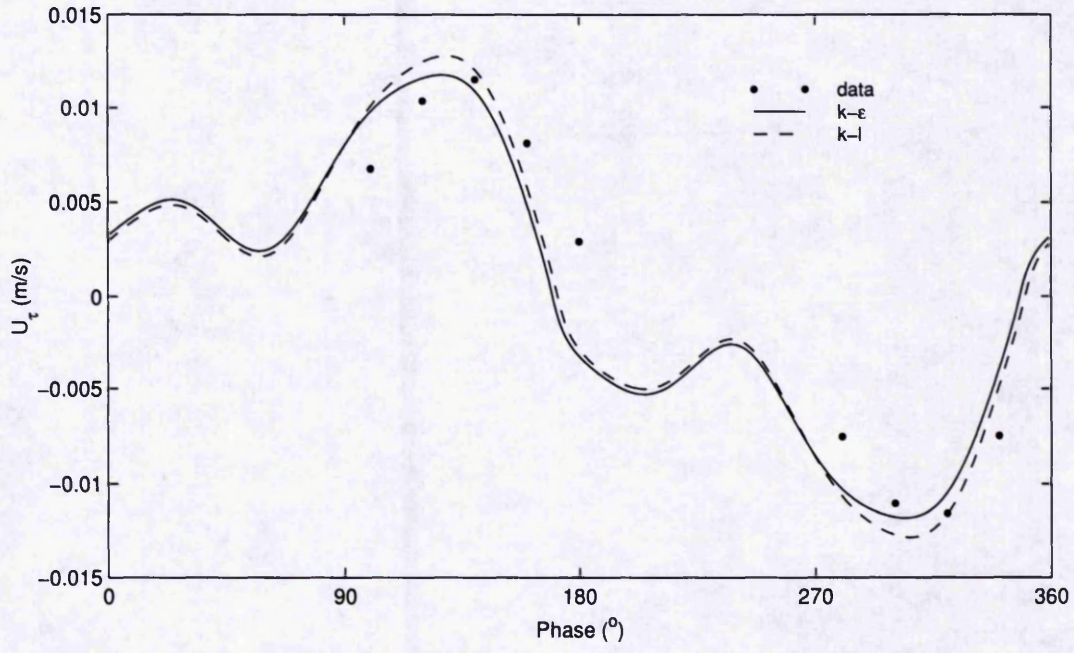

Figure 101: Cyclic variation of fricion velocity compared to model calculations for the UKCRF case

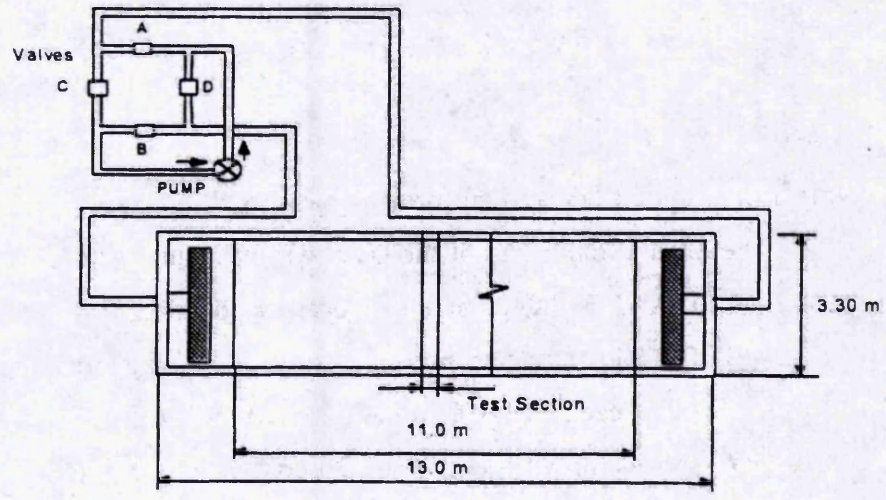

Figure 102: Schematic of the experimental set-up of the University of Manchester tidal flume

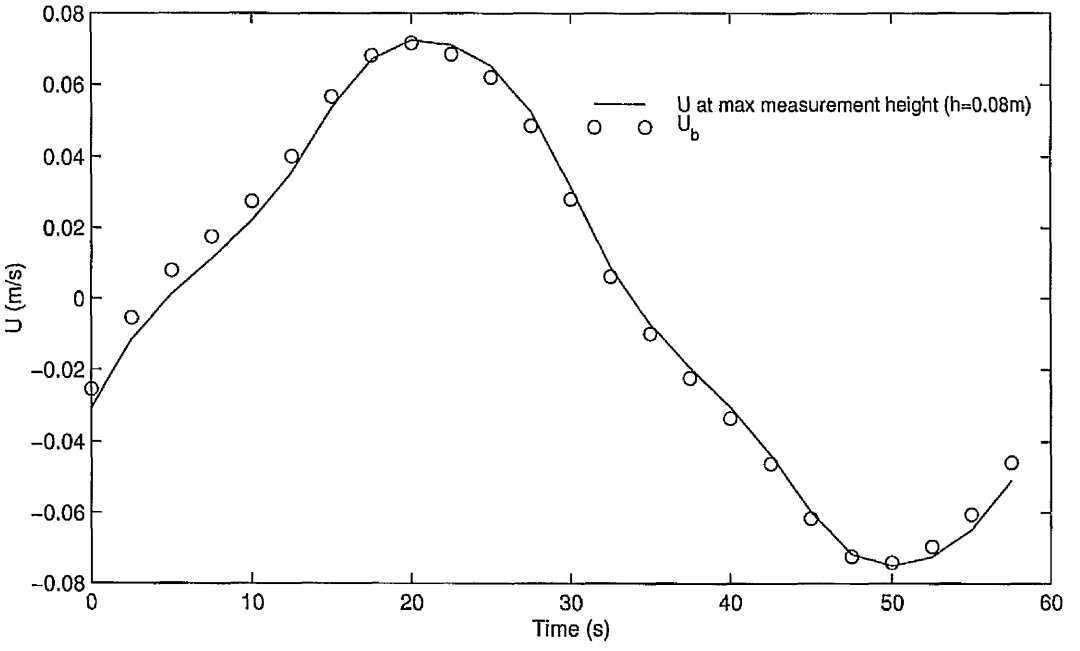

Figure 103: Cyclic variation of bulk velocity data and the streamwise velocity near to the surface in the UMTF case

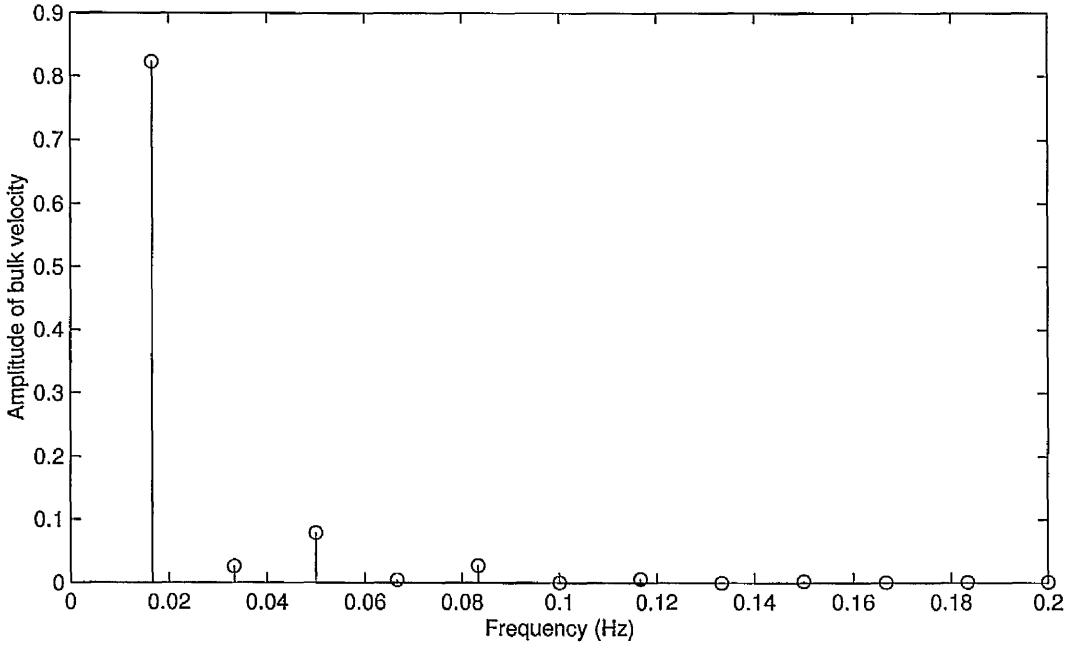

Figure 104: Variation of amplitude against frequency of the bulk velocity in the UMTF case

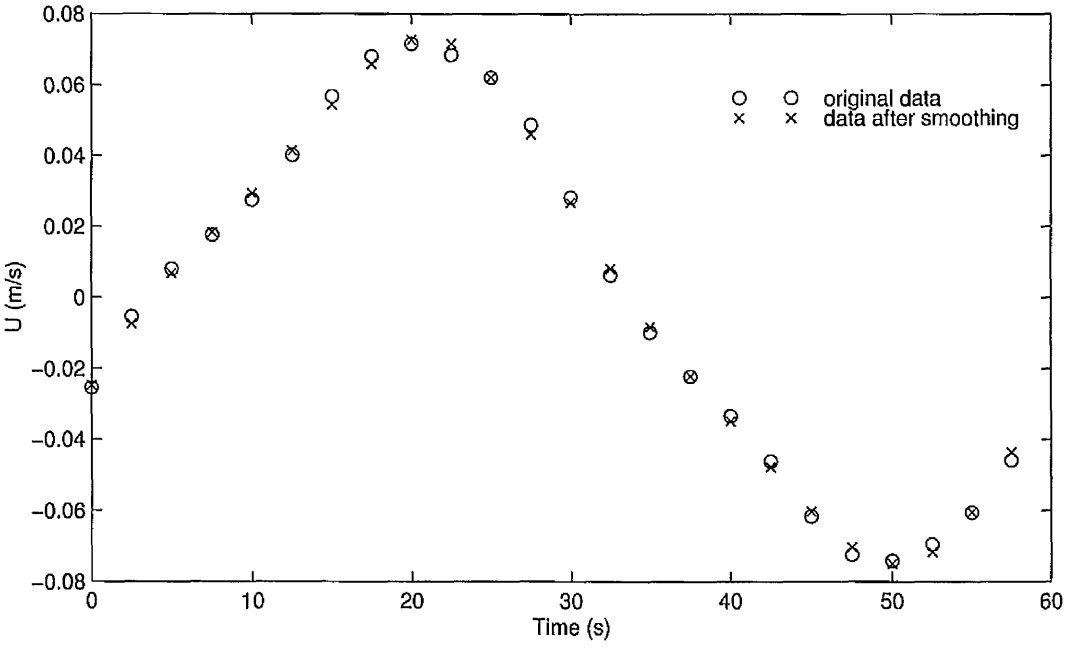

Figure 105: Comparison of the cyclic variation of raw and smoothed bulk velocity data for the UMTF case

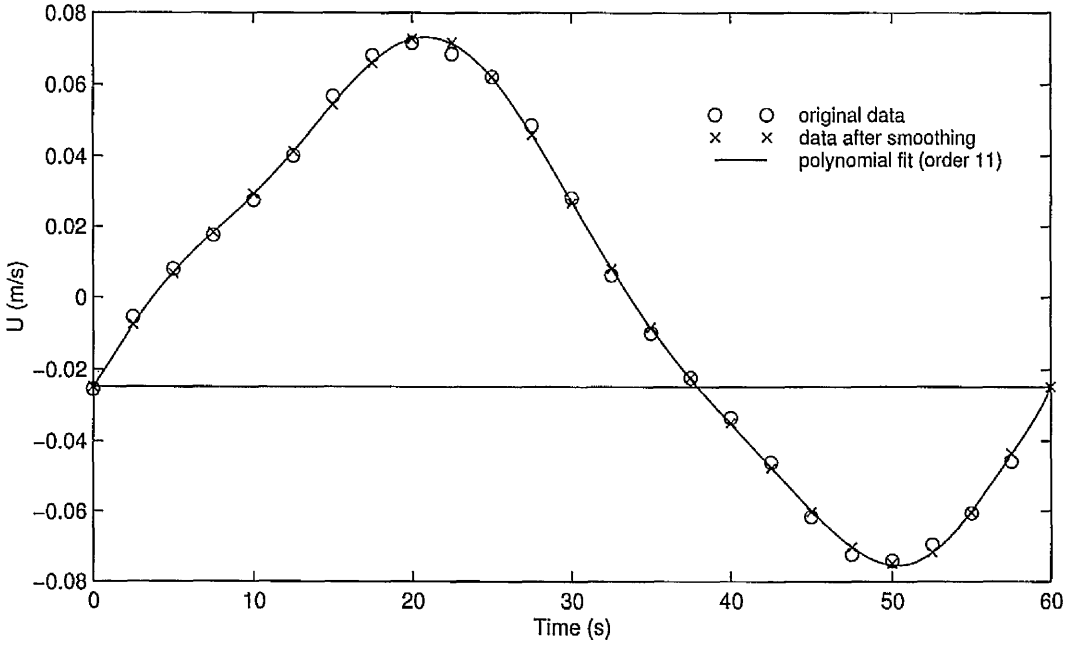

Figure 106: Comparison of the cyclic variation of raw and smoothed bulk velocity data for the UMTF case with the polynomial fit used as input to the code

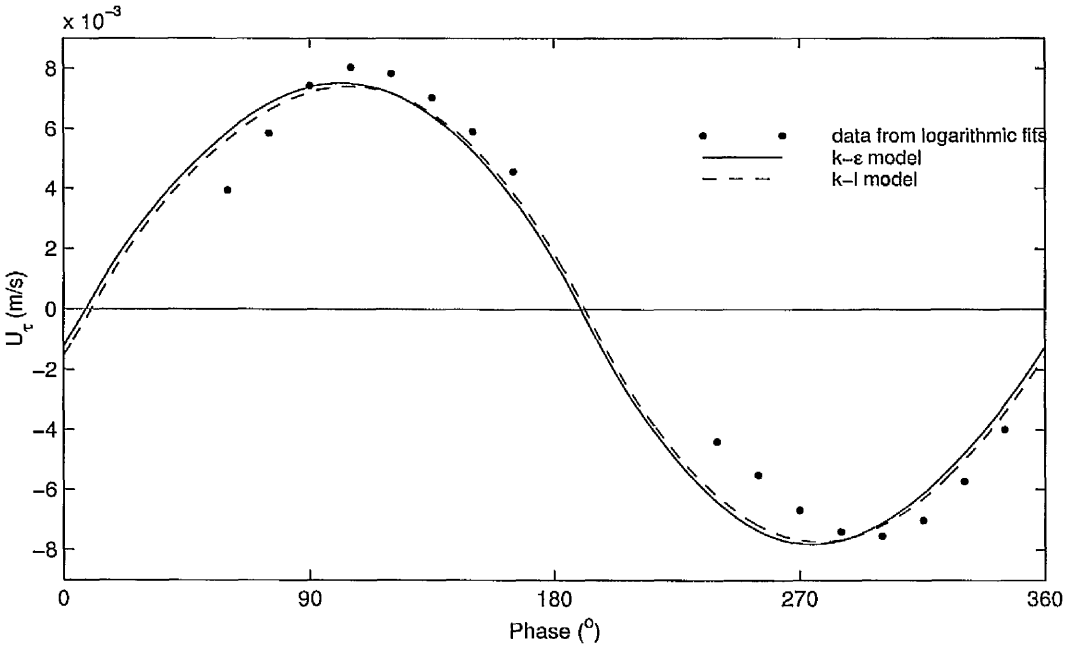

Figure 107: Friction velocity across a cycle of oscillation: model solutions compared with the data obtained by logarithmic fits to the mean velocity.

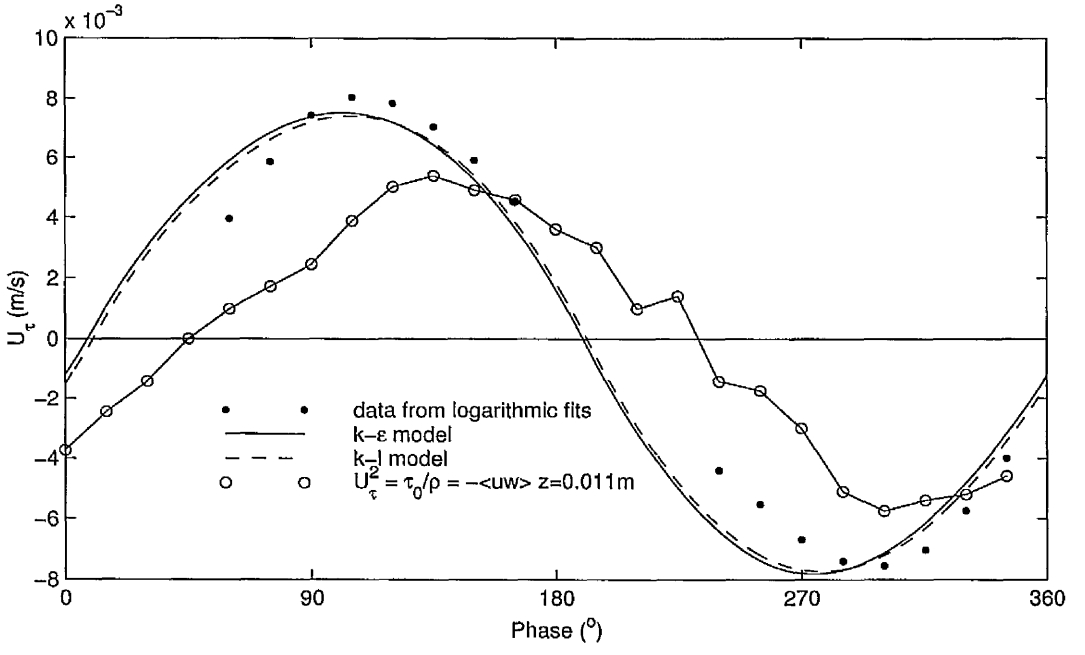

Figure 108: Friction velocity across a cycle of oscillation: model solutions compared with the data obtained by logarithmic fits to the mean velocity and with data derived from the Reynolds stress in the log layer

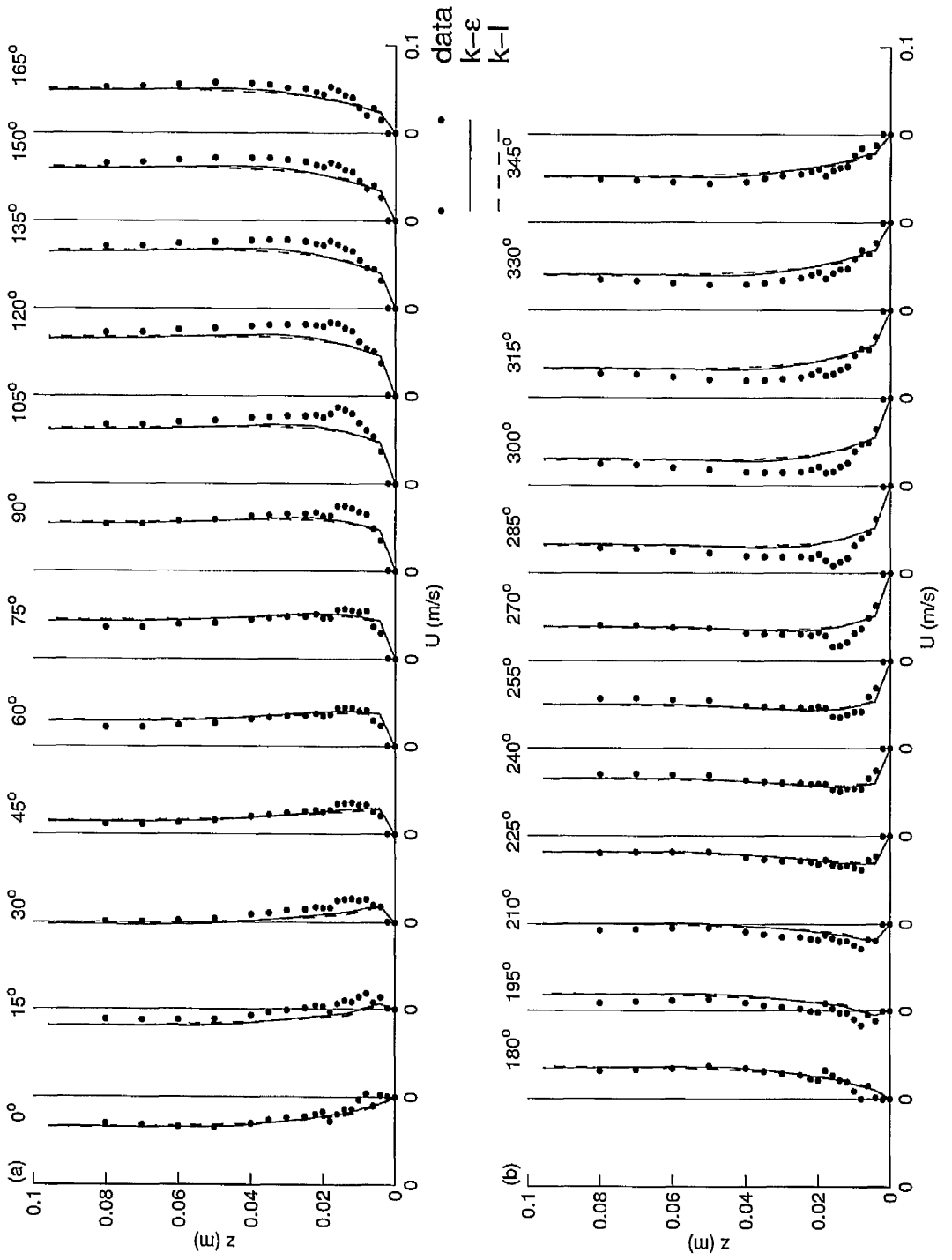

Figure 109: Profiles of velocity for the UMTF case

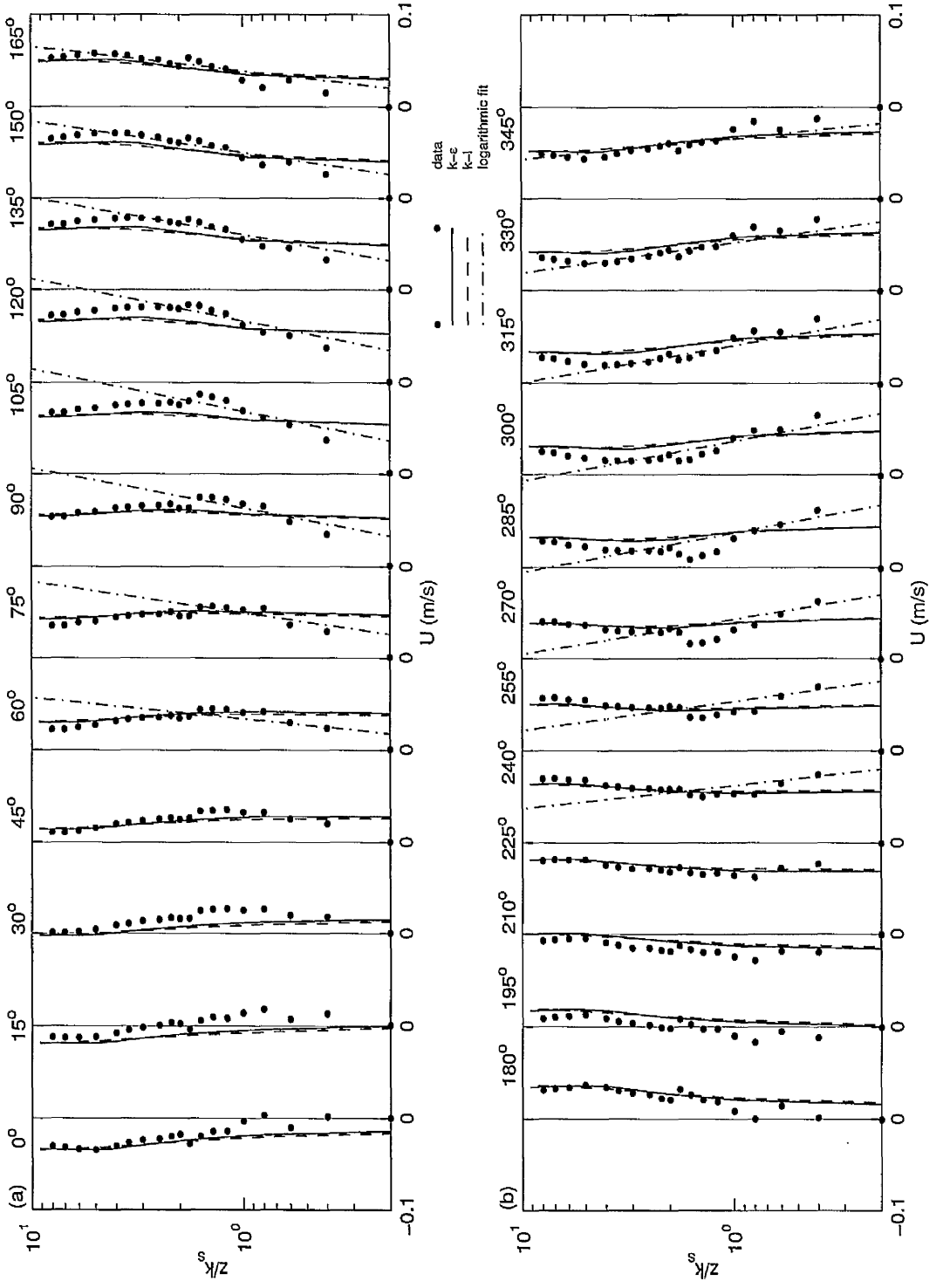

Figure 110: Profiles of velocity and the semi-logarithmic fits for the UMTF case

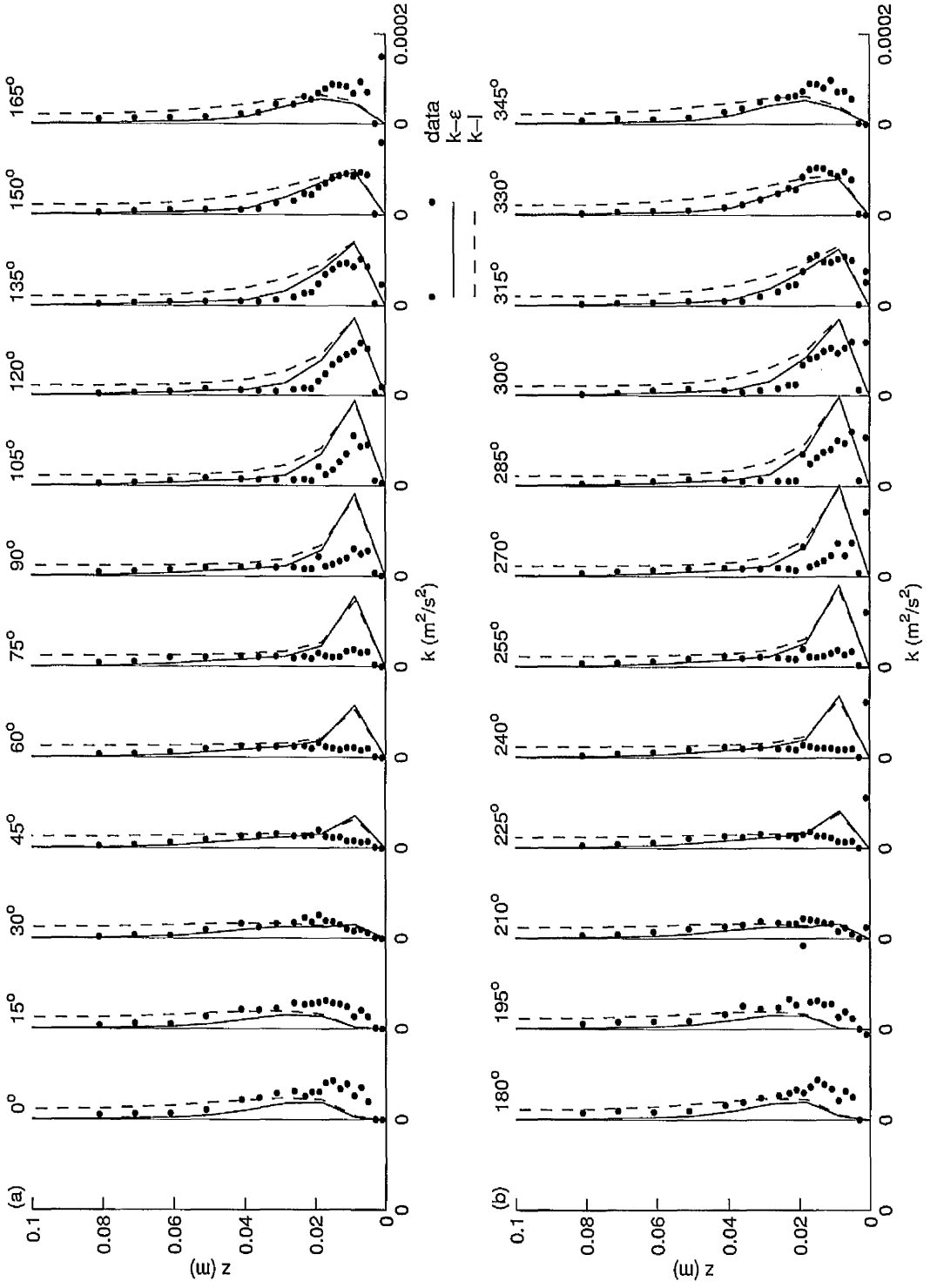

Figure 111: Profiles of turbulent kinetic energy for the UMTF case

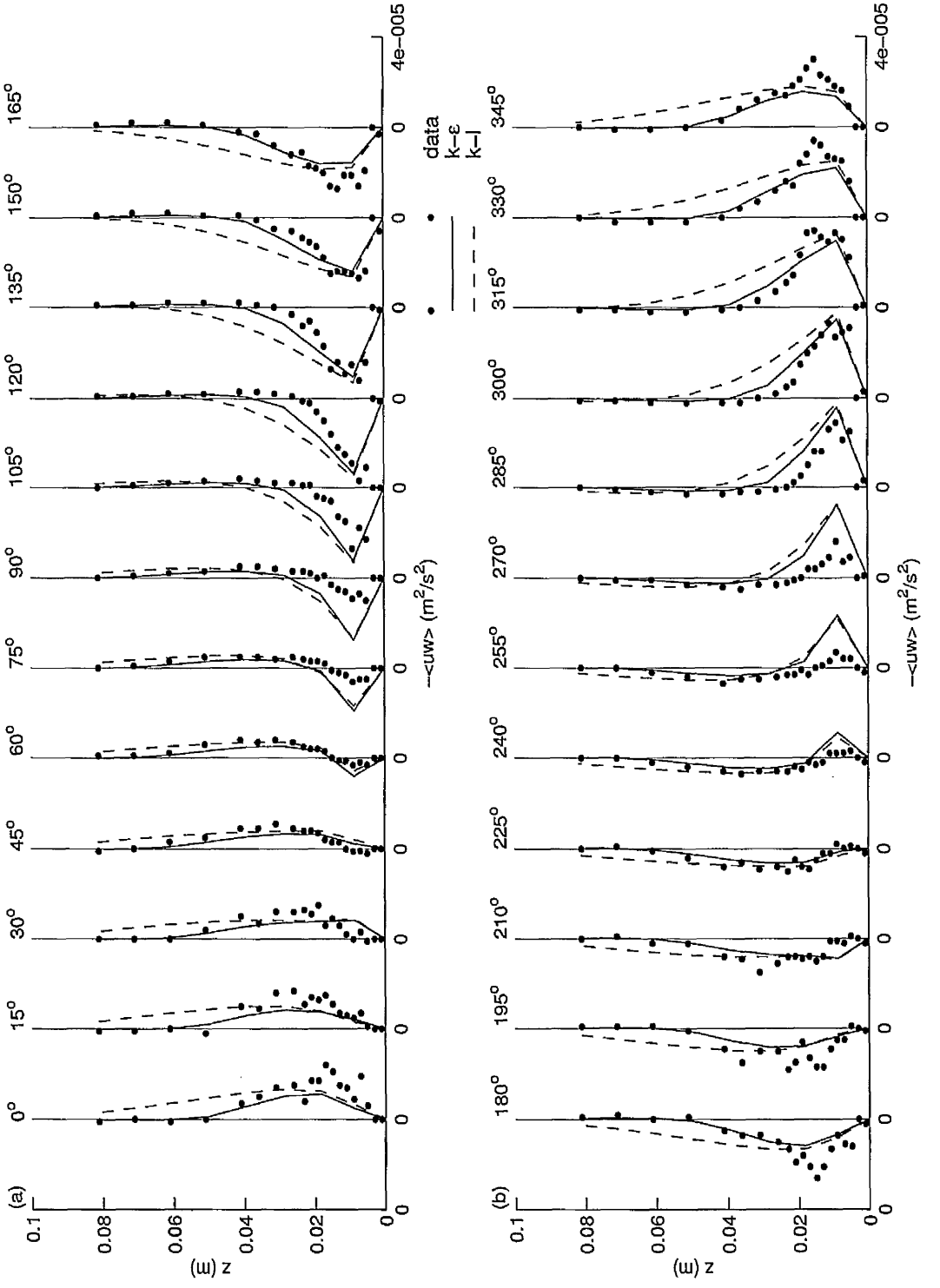

Figure 112: Profiles of Reynolds shear stress for the UMTF case

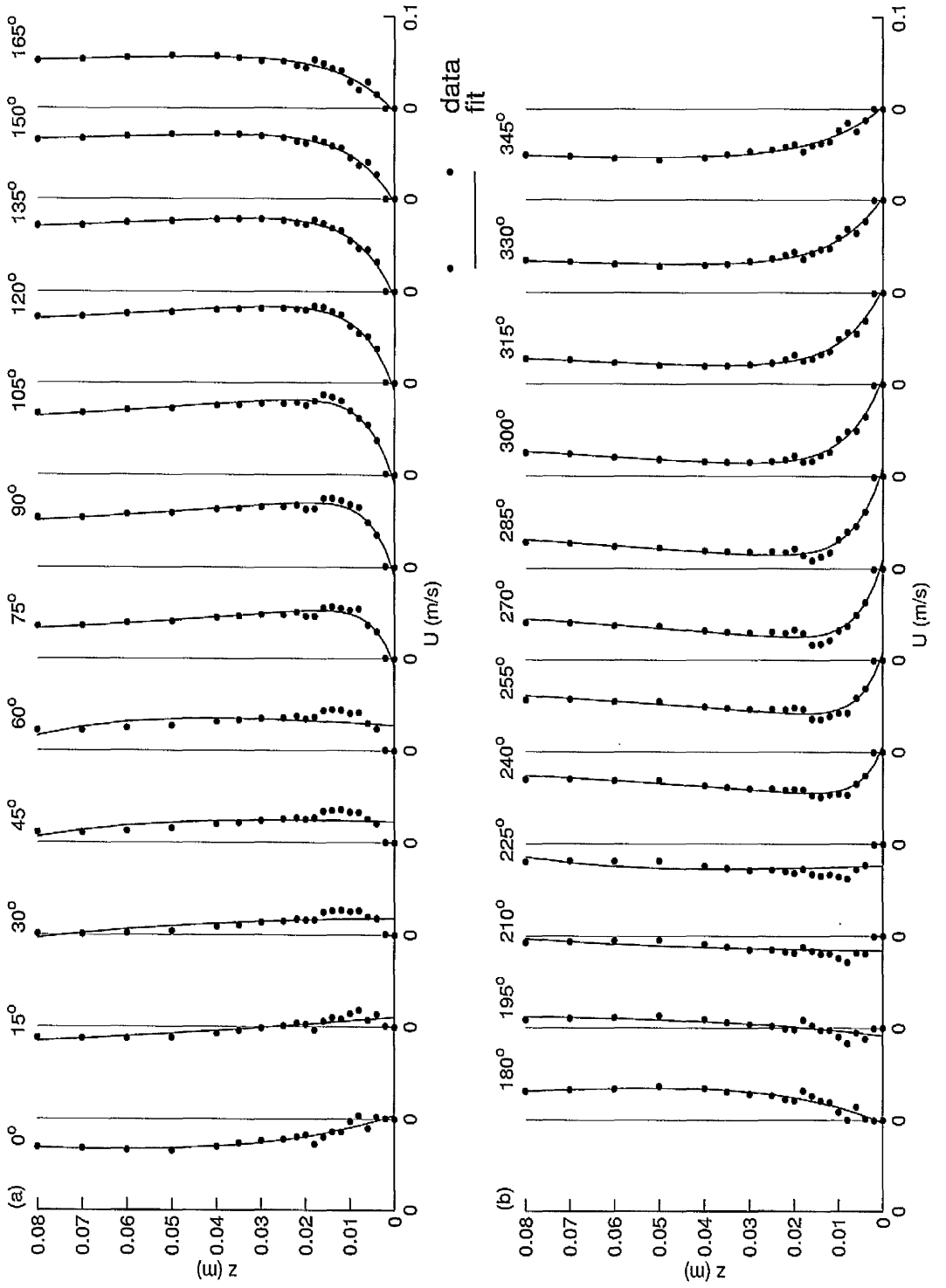

Figure 113: Profiles of velocity and the least squares fit to the data for the UMTF case

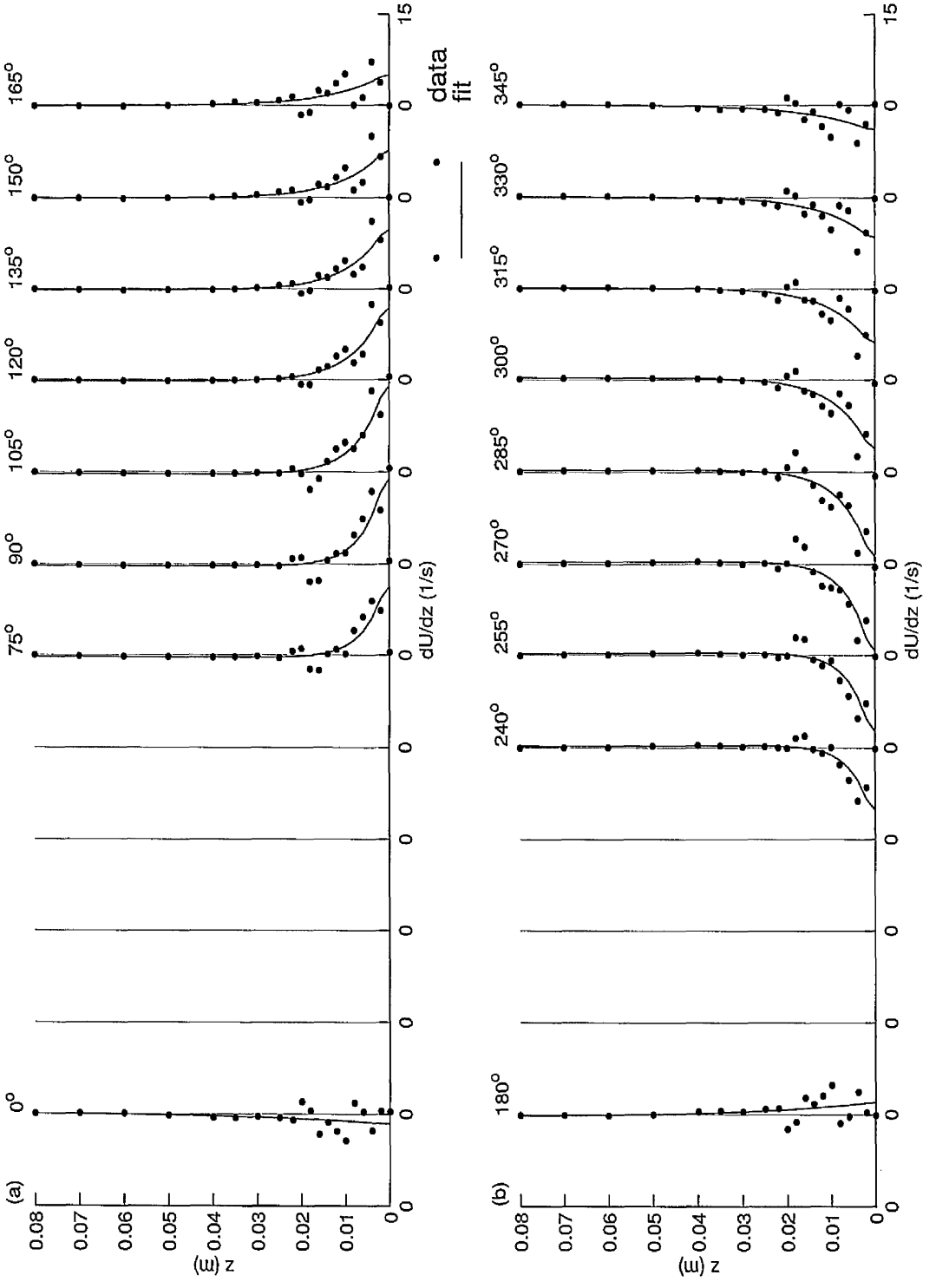

Figure 114: Profiles of velocity gradient and the least squares fit to the data for the UMTF case

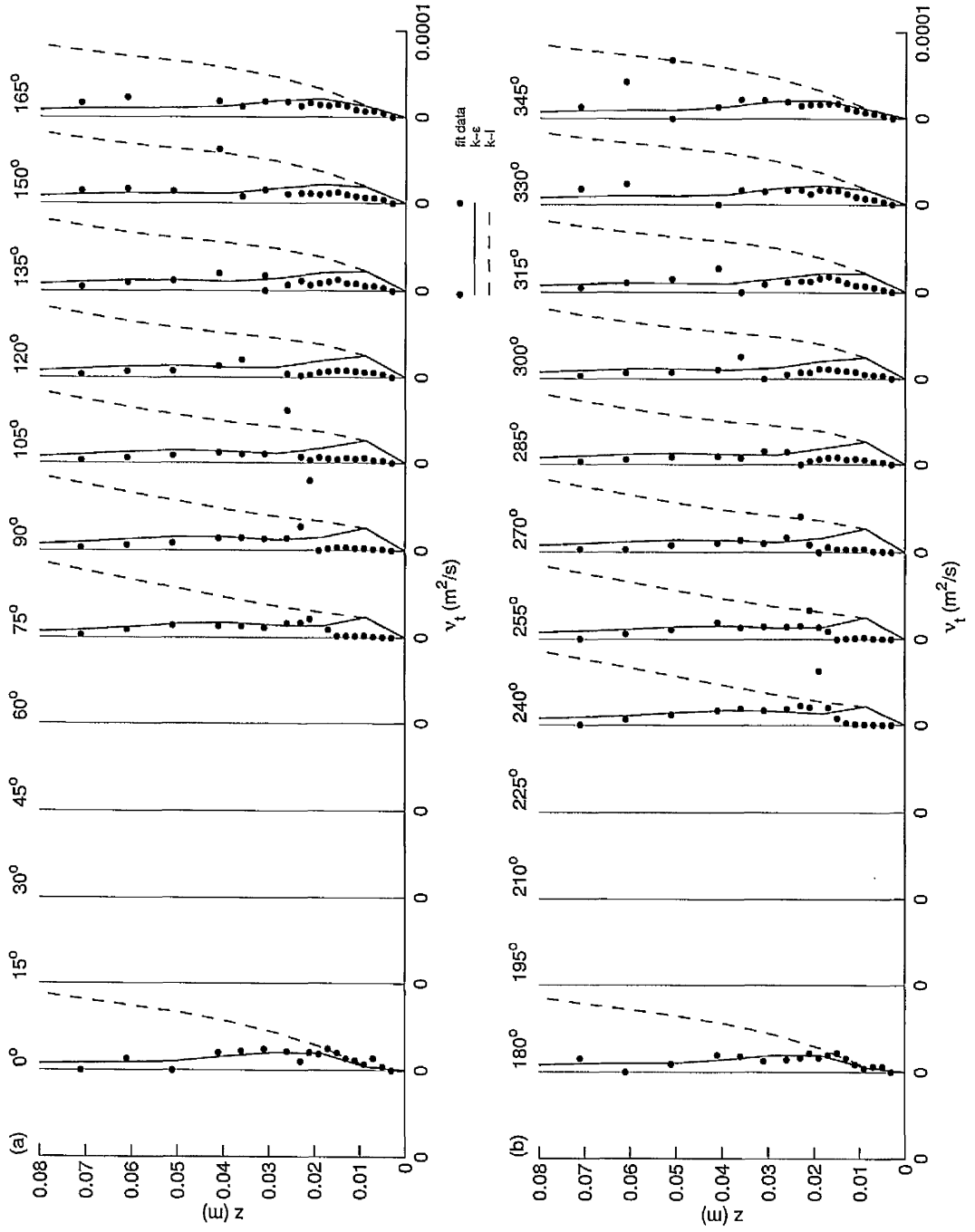

Figure 115: Profiles of turbulent eddy viscosity for the UMTF case

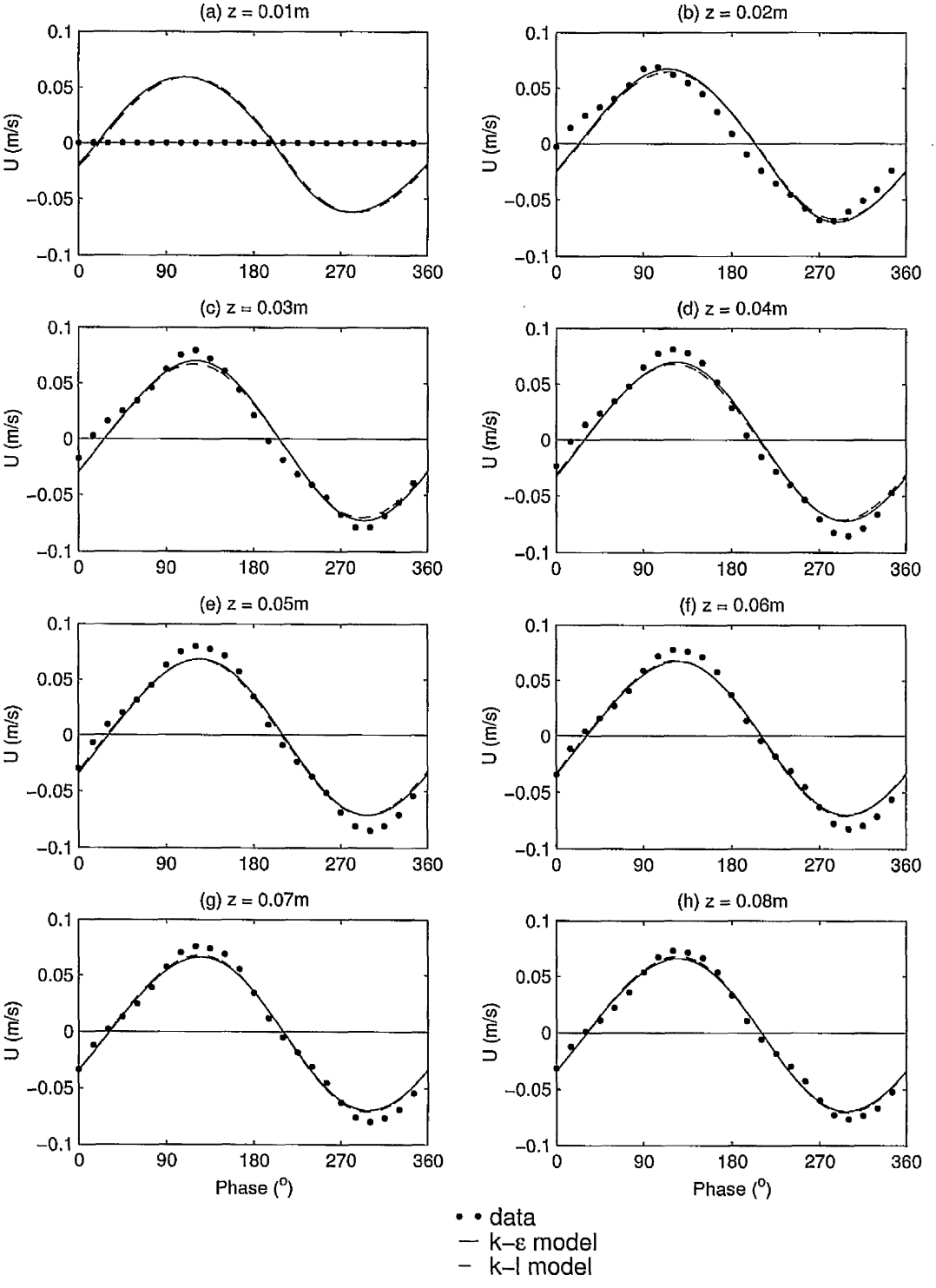

Figure 116: Cyclic variation of velocity for the UMTF case

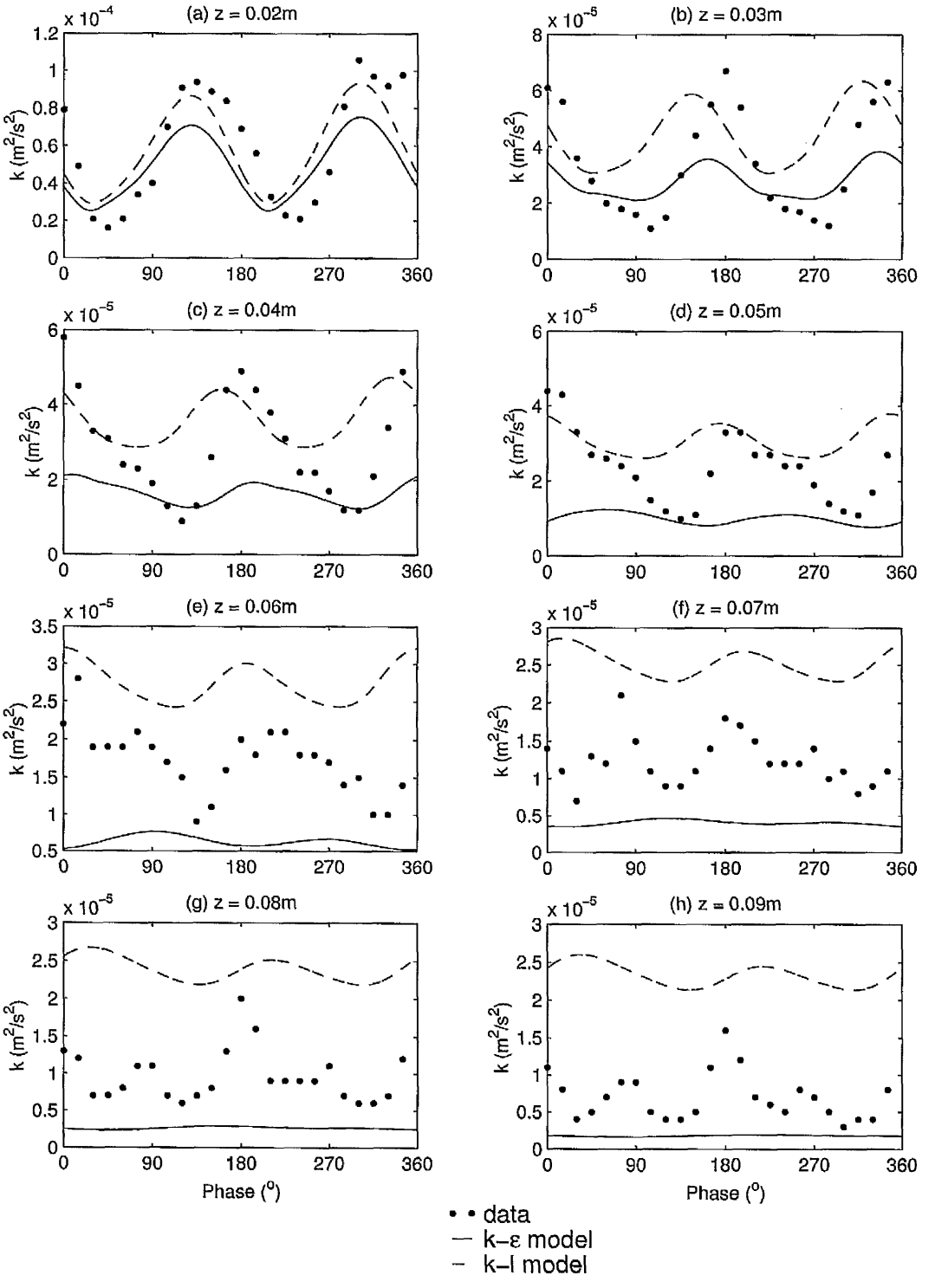

Figure 117: Cyclic variation of turbulent kinetic energy for the UMTF case

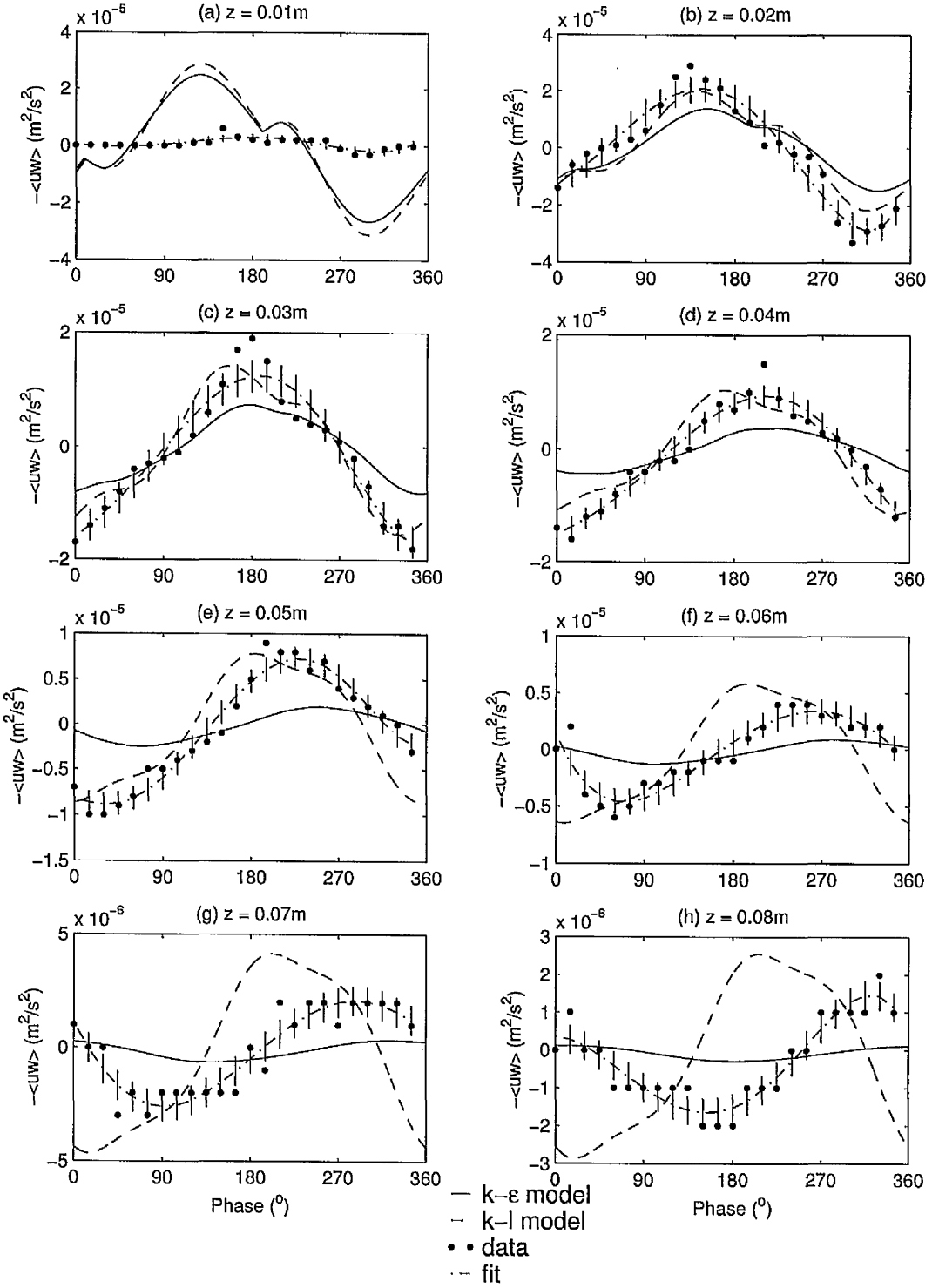

Figure 118: Cyclic variation of Reynolds shear stress for the UMTF case

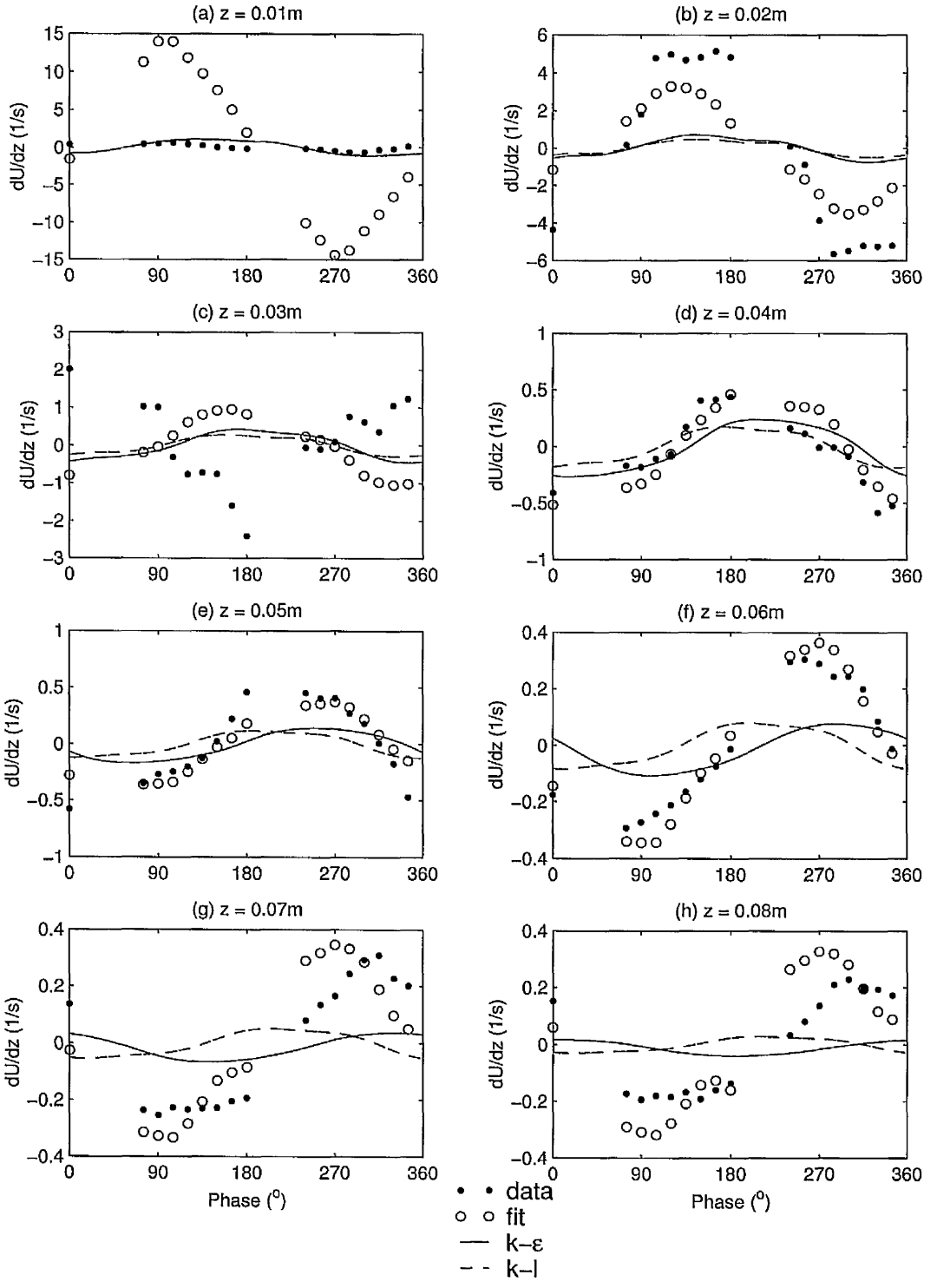

Figure 119: Cyclic variation of velocity gradient comparing model results with data and least squares fit for the UMTF case

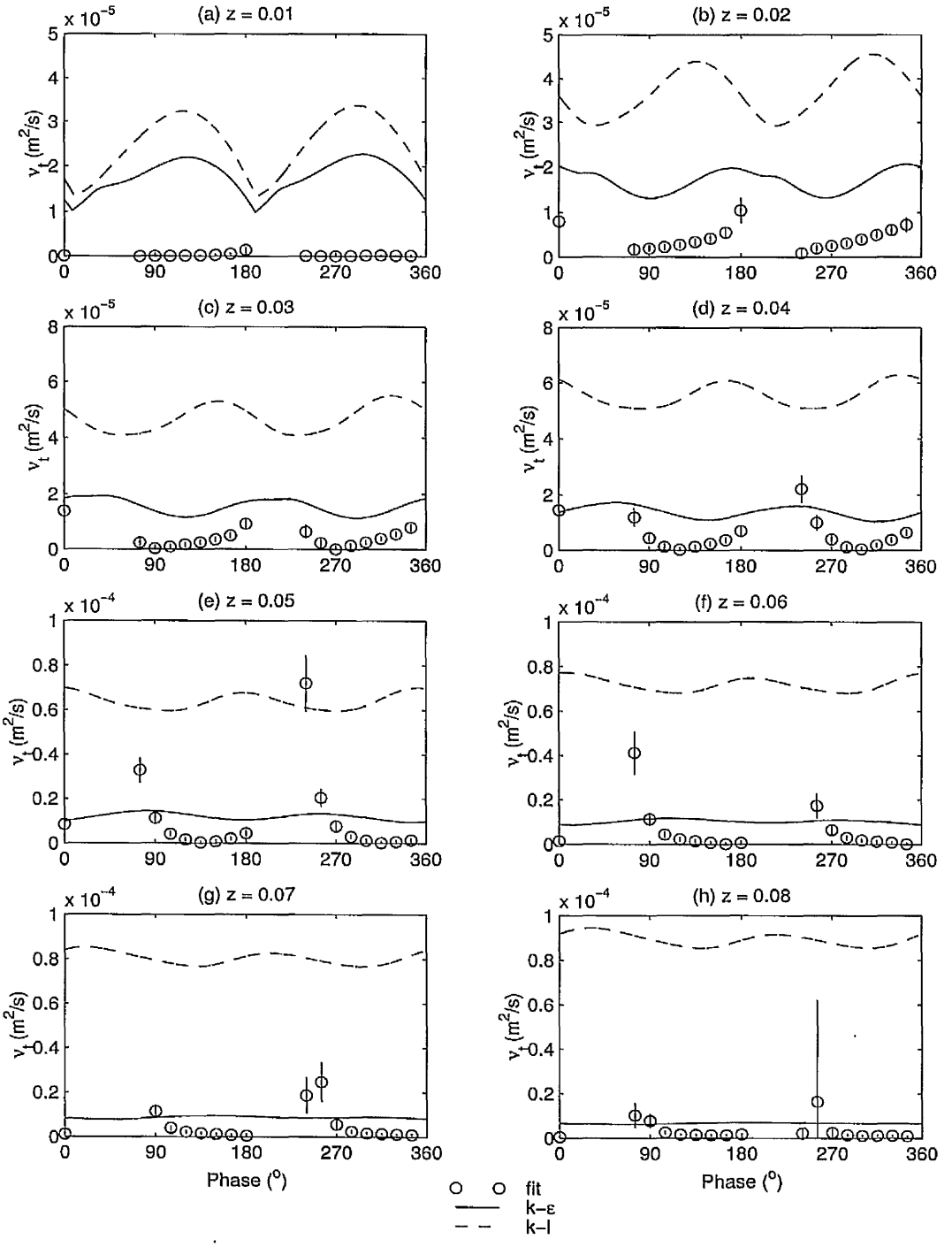

Figure 120: Cyclic variation of turbulent eddy viscosity for the UMTF case

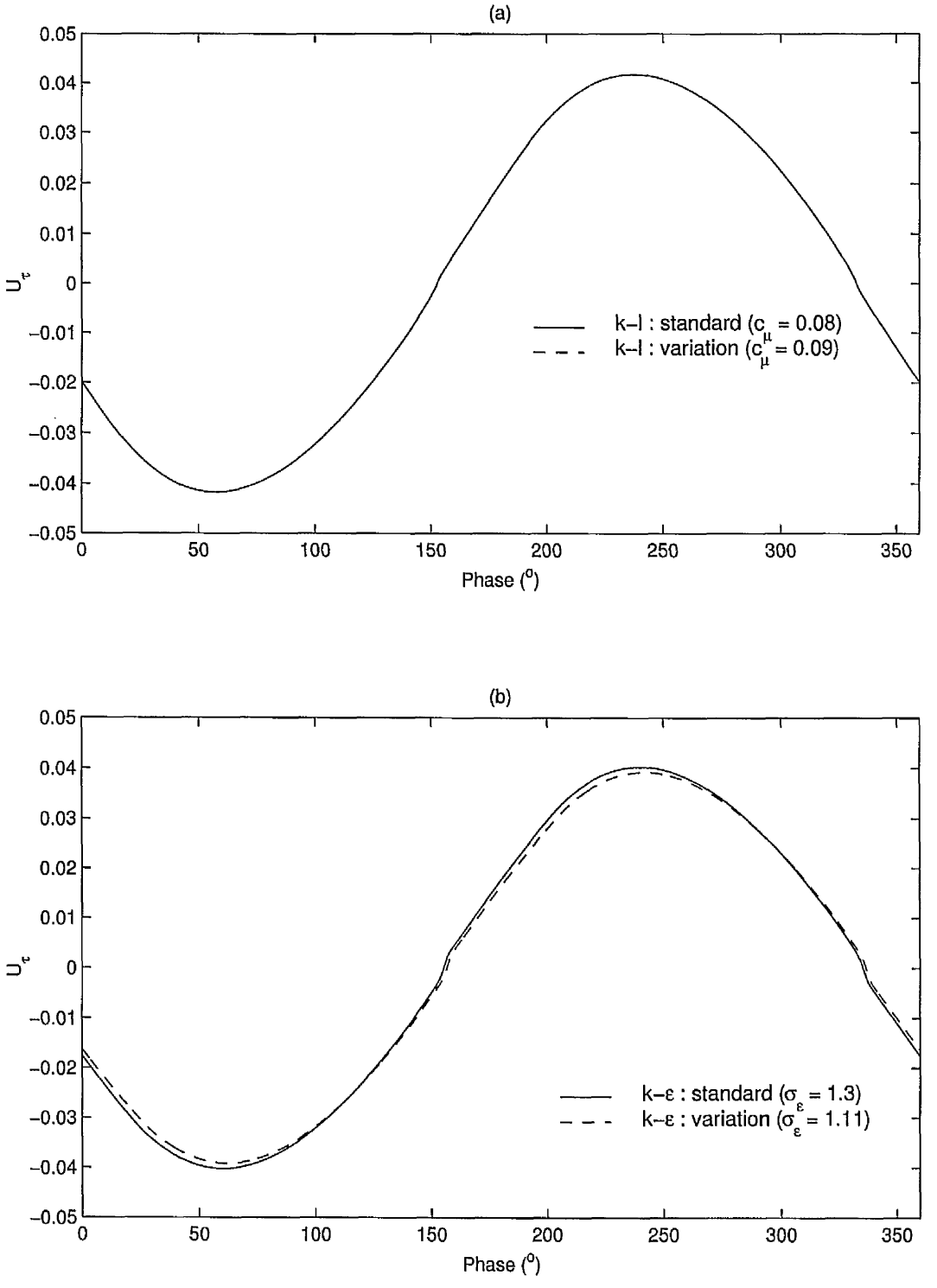

Figure 121: Cyclic variation of friction velocity for the Jade estuary comparing the standard and variation values of the constants for the (a) k-l model and (b) k-ϵ model

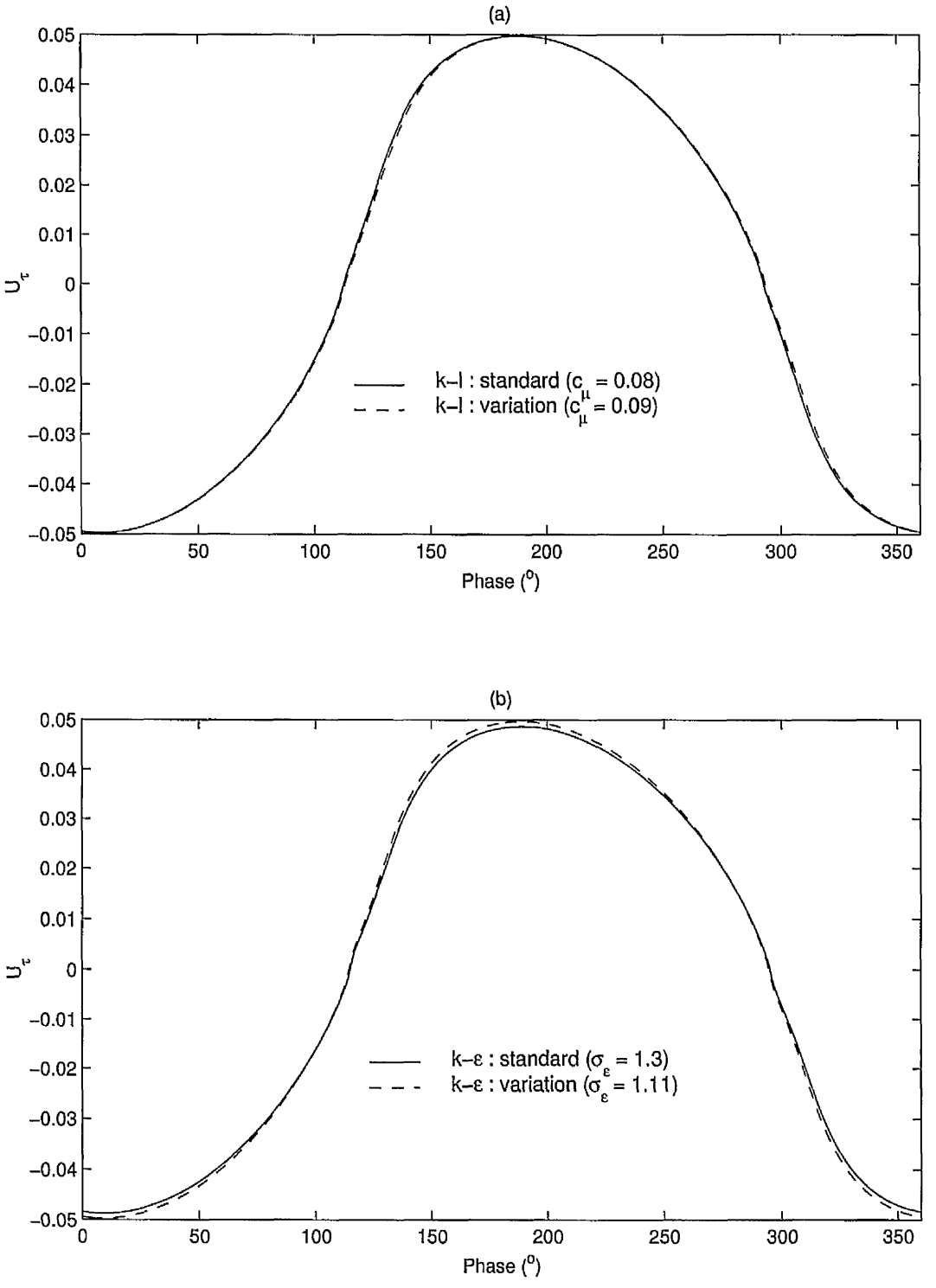

Figure 122: Cyclic variation of friction velocity for the Elbe estuary comparing the standard and variation values of the constants for the (a) k-l model and (b) k-ϵ model

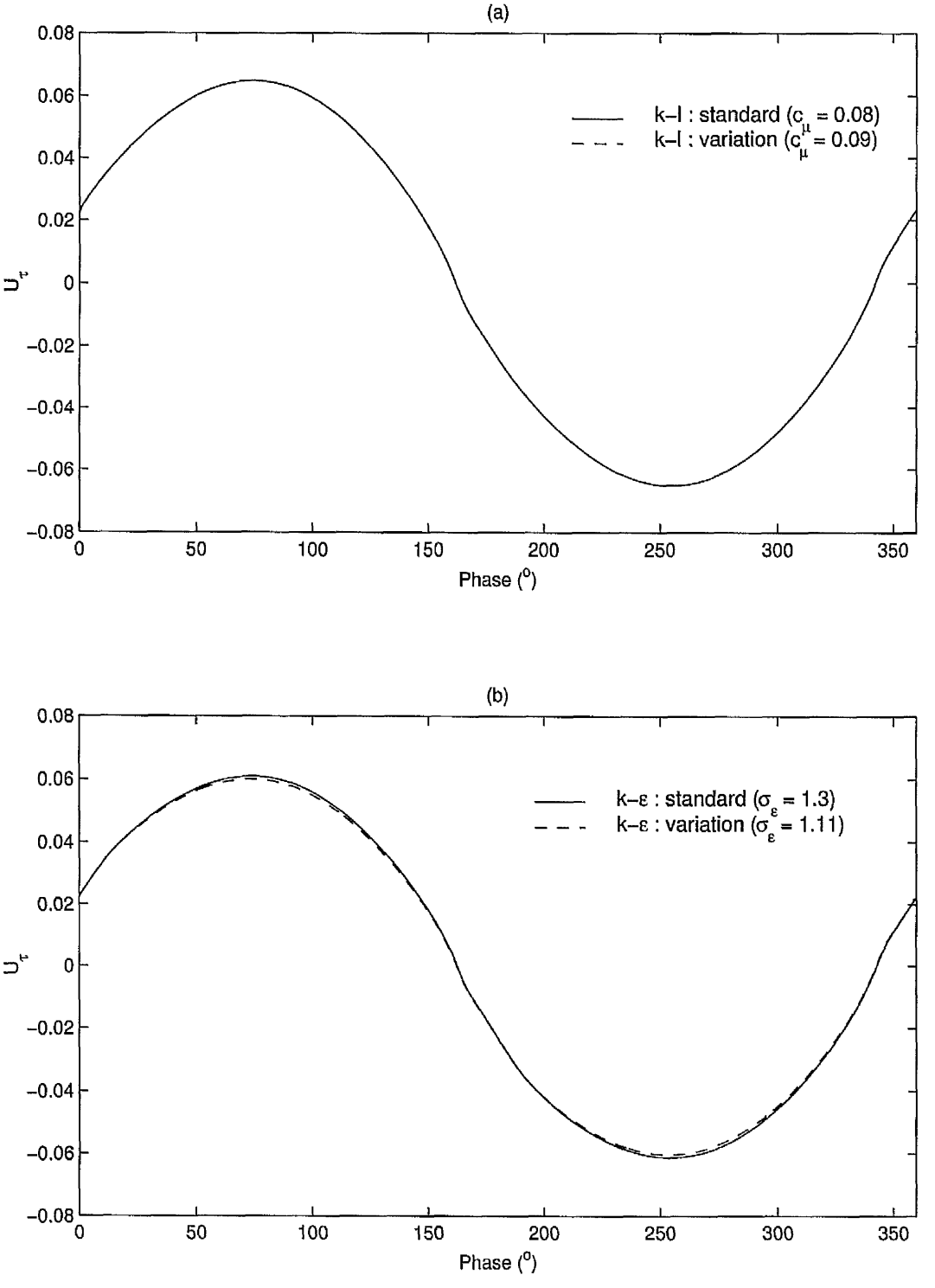

Figure 123: Cyclic variation of friction velocity for the JSF12 case comparing the standard and variation values of the constants for the (a) k-l model and (b) k-ϵ model

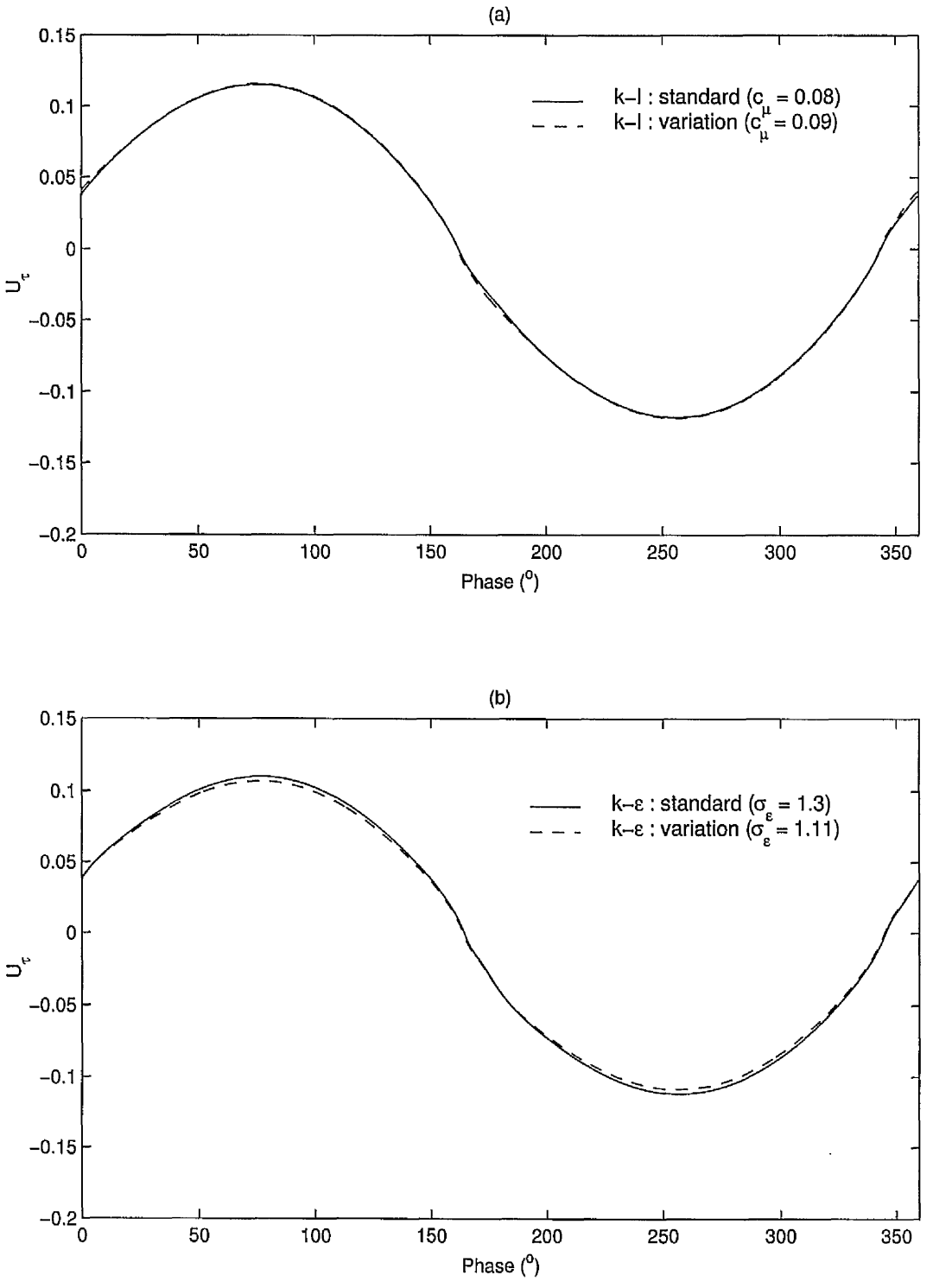

Figure 124: Cyclic variation of friction velocity for the JSF13 case comparing the standard and variation values of the constants for the (a) k-l model and (b) k-ϵ model

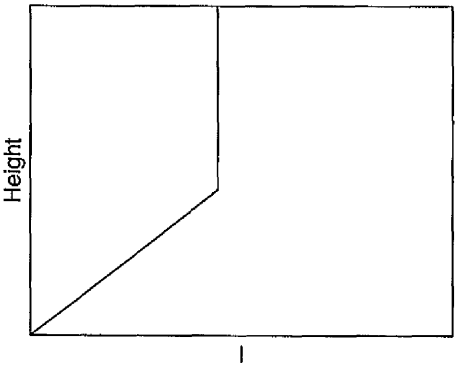

Figure 125: Schemtic diagram of proposed variation of length scale against height for the k-l model

Appendix A

Publication

Paper published in the proceedings of the XXVIIIth Biennial IAHR congress, Graz, Austria in August 1999. This paper was presented as part of the John F. Kennedy student paper competition.

k-ϵ and k-l Modelling in Oscillatory Flow over Rough Beds

S. B. Letherman
Hydrodynamics Research Group, School of Engineering, University of Manchester, U.K.

Correspondence to: School of Engineering, University of Manchester, Manchester, M13 9PL, U.K.
Telephone: +44 (0)161 275 4406, email: mbgmhsbl@fs1.eng.man.ac.uk

ABSTRACT
A new assessment is made of two-equation (k-ϵ) and one-equation (k-l) turbulence models in oscillatory flow. The turbulence models are compared with the data of Jensen, Sumer and Fredsøe [1]. An attempt is made to quantify the uncertainties in the Reynolds shear stress measurements. The results show that the k-ϵ model performs well, and considerably better than the k-l model.

KEYWORDS
Turbulence model, oscillatory flow, rough bed, k-ϵ, k-l.

1. INTRODUCTION

The motivation for this study is to assess two-equation (k-ϵ) and one-equation (k-l) turbulence models (and eventually others) for oscillatory flow over rough beds. The equations are solved using a semi-implicit finite volume scheme. The parabolic spacing in the numerical grid was selected in order to give high resolution near to the bed and the surface to resolve the large gradients of velocity, k and ϵ. Wall functions for fully rough turbulent boundary layers are used at the bed. Here the Jensen, Sumer and Fredsøe (JSF) experimental data [1,2] is used in comparison with the numerical models. In the future data for the Elbe [3] and also Manchester experimental data will also be used. Comparisons of the models with data for the bed shear stress are presented. The Reynolds shear stress and turbulent eddy viscosity are also examined. In order to obtain data for the eddy viscosity, the JSF experimental data for the Reynolds stress and velocity has been processed. The eddy viscosity therefore inherits an estimated error from the processing of the data.

2. MODEL EQUATIONS

The boundary layer equation in the streamwise direction is

$$\frac{\partial u}{\partial t} = -\frac{1}{\rho}\frac{\partial p}{\partial x} + \frac{\partial}{\partial z}\left(\nu_E \frac{\partial u}{\partial z}\right), \quad (2.1)$$

where x and z represent the horizontal and vertical directions, respectively. Given that the freestream velocity is independent of the distance from the bed, the flow outside the boundary layer varies sinusoidally with time as

$$u_\infty(t) = u_M \sin(\omega t) \quad (2.2)$$

where u_M is the amplitude of u_∞ and $\omega = 2\pi/T$ where T is the period of oscillation. In this region outside the boundary layer the unsteady Euler equation applies

$$\frac{\partial u_\infty}{\partial t} = -\frac{1}{\rho}\frac{\partial p}{\partial x}. \quad (2.3)$$

The Reynolds shear stress, $-\overline{uw}$, the turbulent eddy viscosity ν_t, and the effective total viscosity ν_E, are defined by

$$-\overline{uw} = \nu_t \frac{\partial u}{\partial z} \quad (2.4)$$

$$\nu_E = \nu + \nu_t = \nu + c_\mu \frac{k^2}{\epsilon} \quad (2.5)$$

where ν is the kinematic viscosity. For the two-equation k-ϵ model the kinetic energy, k and the dissipation rate, ϵ are governed by the following transport equations [4]

$$\frac{\partial k}{\partial t} = \nu_t \left(\frac{\partial u}{\partial z}\right)^2 + \frac{\partial}{\partial z}\left[\left(\nu + \frac{\nu_t}{\sigma_k}\right)\frac{\partial k}{\partial z}\right] - \epsilon \quad (2.6)$$

$$\frac{\partial \epsilon}{\partial t} = c_{\epsilon 1}\frac{\epsilon}{k}\nu_t \left(\frac{\partial u}{\partial z}\right)^2 + \frac{\partial}{\partial z}\left[\left(\nu + \frac{\nu_t}{\sigma_\epsilon}\right)\frac{\partial \epsilon}{\partial z}\right] - c_{\epsilon 2}\frac{\epsilon^2}{k} \quad (2.7)$$

For the one-equation k-l model, k is calculated using the above transport equation (2.6), and ϵ is supplied by the relation

$$\epsilon = c_\mu^{3/4}\frac{k^{1/2}}{\kappa z}. \quad (2.8)$$

The value of σ_ϵ may be related to the other model constants by considering the flow in the bed region. Following Rodi [4], the ϵ-equation (2.7) reduces to

$$\sigma_\epsilon = \frac{\kappa^2}{c_\mu^{1/2}(c_{\epsilon 2} - c_{\epsilon 1})} \quad (2.9)$$

Thus taking the standard values of the other model constants: $c_\mu = 0.09, c_{\epsilon 1} = 1.44, c_{\epsilon 2} = 1.92, \sigma_k = 1.0$ and von Kármán's constant $\kappa = 0.4$, relation (2.9) gives $\sigma_\epsilon = 1.11$. At the bed the boundary conditions used are standard wall functions. The law of the wall for fully rough turbulent boundary layers gives the bed boundary condition [5]

$$u^+ = \frac{u}{u_\tau} = \frac{1}{\kappa}\left(\frac{z}{k_s}\right) + 8.5 \quad (2.10)$$

where the bed friction velocity $u_\tau = \sqrt{\tau_b/\rho}$ and k_s is the roughness height. The bed region is taken to be $30 < z^+_{\max} < 100$ where $z^+ = z u_\tau/\nu$. In the bed region the Reynolds stresses are assumed to be constant and equal to the bed shear stress and turbulence production is taken to be equal to dissipation. Thus the boundary conditions on k and ϵ are

$$k = \frac{u_\tau^2}{\sqrt{c_\mu}}, \quad \epsilon = \frac{u_\tau^3}{\kappa z} \quad (2.11)$$

At the surface the shear stress is zero, and thus the velocity gradient $\partial u/\partial z = 0$. The surface boundary conditions for k and ϵ are set to $\partial k/\partial z = \partial \epsilon/\partial z = 0$.
For details of the numerical procedures refer to Stansby [6] since the method is based upon a one-dimensional version of the 3-D semi-implicit finite volume flow and solute transport solver.

3. RESULTS AND DISCUSSION

The turbulence model results are compared to the JSF data for $a/k_s = 3700$ [1,2], where a is the freestream particle amplitude. The period of oscillation was $T = 9.72$ s , the roughness height $k_s = 8.4 \times 10^{-4}$ m, the maximum value of the freestream velocity $u_M = 2.0$ m/s and the kinematic viscosity $\nu = 1.14 \times 10^{-6}$ m^2/s. The

number of vertical grid points was 100. The mesh spacing was varied parabolically to give fine resolution near the bed and the free surface, motivated by the presence of large gradients in these regions. Sensitivity tests (not shown here due to lack of space) show that the solutions are independent of the mesh.

Following Justesen [7] we consider the two key quantities of bed shear stress and eddy viscosity. Figure (1) shows the bed friction velocity u_τ, normalized by u_M against time. The k-ϵ model gives good agreement with the data and the k-l model overpredicts the data. The Reynolds shear stress and turbulent eddy viscosity are also examined over half a cycle at five distances from the bed: z/a 0.0006, 0.0018, 0.0058, 0.017 and 0.038. Relative to the boundary layer, taken to be of thickness $\delta \approx 0.02$ m [1], these heights are $z/\delta \approx 0.03$, 0.09, 0.3, 0.85 and 1.9.

A polynomial fit of order 16 to the velocity data was taken to obtain the velocity gradient. Another polynomial fit to the Reynolds shear stress of order 5 was taken to overcome the scatter in the data (Figure (2)). For a given parameter ϕ, the following equation provides a measure of uncertainty:

$$\Delta\phi = \left[\frac{1}{n}\sum(\phi_{\text{data pt}} - \phi_{\text{fit pt}})^2\right]^{1/2}, \quad \phi = \phi_{\text{fit pt}} \pm \Delta\phi \quad (3.1)$$

where n is the total number of points. Equation (3.1) was used to estimate the possible error in the polynomial fits of both the JSF Reynolds shear stress and the velocity data. In fact, the error of the velocity fit compared to the JSF data was negligible. For the Reynolds stress 71% of all JSF data points are within the fit uncertainty range. Figures 2(a-e) show the $-\overline{uw}$ data at the five heights given above, the polynomial fit and also the uncertainty range from equation (3.1). The Reynolds shear stress calculated by the turbulence models is also shown. At all heights the scatter of the data is large. The k-ϵ model gives good agreement. The k-l model at heights near to the bed (figures 2(a-c)) is in good agreement at phases 0^o-50^o and 125^o-180^o, but in the range 50^o-125^o where the velocity is largest, the k-l model overpredicts the data. This trend is also seen towards the edge of the boundary layer in figure 2(d). In figure 2(e) at $z/a = 0.038$ in the notional freestream region, the k-l model is in very poor agreement with the data. Figures 3(a-e) show the turbulent eddy viscosity for the experimental data and the turbulence models over half a cycle at the five heights from the bed given above. The Reynolds stress fit and the uncertainty was divided by the velocity gradient using equation (2.4) to obtain the eddy viscosity data. Equation (2.5) was used to calculate the turbulent eddy viscosity for both turbulence models. As with the Reynolds stress, the k-ϵ model is in general in good agreement. The k-l model again gives poor agreement in the range 50^o-125^o, although the model generally predicts the eddy viscosity fairly well at the other phases in the lower boundary layer. However figure 3(e) shows that ν_t predicted by the k-l model is very large compared to both the data and the k-ϵ model in the freestream.

4. CONCLUSIONS

In order to evaluate the turbulence models the bed shear stress, Reynolds shear stress and eddy viscosity have been compared to the JSF experimental data. Polynomial fits have been taken to obtain the eddy viscosity in suitable form for comparison. Certain assumptions have been made to give a measure of possible error in the data

fits, namely that the error in the Reynolds stress data is independent of phase position and has a normal distribution, enabling an average error to be determined for a cycle. Improving these assumptions would require much more detailed data but this approach gives a useful indication of scatter. Nevertheless, the results show that the k-ϵ model predicts the Reynolds shear stress and eddy viscosity well. The k-l model does not do so well, particularly in the region towards the edge of the boundary layer. It would be interesting to compare with the results of a more complex model and indeed a simpler mixing length approach.

ACKNOWLEDGMENTS
The guidance of Prof. P. K. Stansby and Dr. M. A. Cotton is gratefully acknowledged. The assistance of Prof. B. M. Sumer in providing the experimental data is also greatly appreciated. This work was funded by a research studentship from the EPSRC.

REFERENCES

[1] B. L. Jensen, B. M. Sumer, and J. Fredsøe, Turbulent oscillatory boundary layers at high Reynolds numbers, J. Fluid Mech., v.206, pp. 265-297, 1989.
[2] Private correspondence with B. M. Sumer.
[3] M. Schröder, Messung des turbulenten Impuls- und Salztransports in der Mischungszone der Elbe, Tech. Rep. GKSS 87/E/16, GKSS-Forchungszentrum Geesthacht, 1987.
[4] W. Rodi, Turbulence Models and Their Application in Hydraulics. A-State-of-the-Art Review, 3rd ed., Balkema, Netherlands.
[5] H. Schlichting, Boundary-Layer Theory, 7th ed., McGraw-Hill, New York, 1979.
[6] P. K. Stansby, Semi-implicit finite volume shallow-water flow and solute transport solver with k-ϵ turbulence model, Int. J. Num. Meth. Fluids, v.25, pp.285-313, 1997.
[7] P. Justesen, A note on turbulence calculations in the wave boundary layer, J. Hyd. Research, v.29, no.5, 1991.

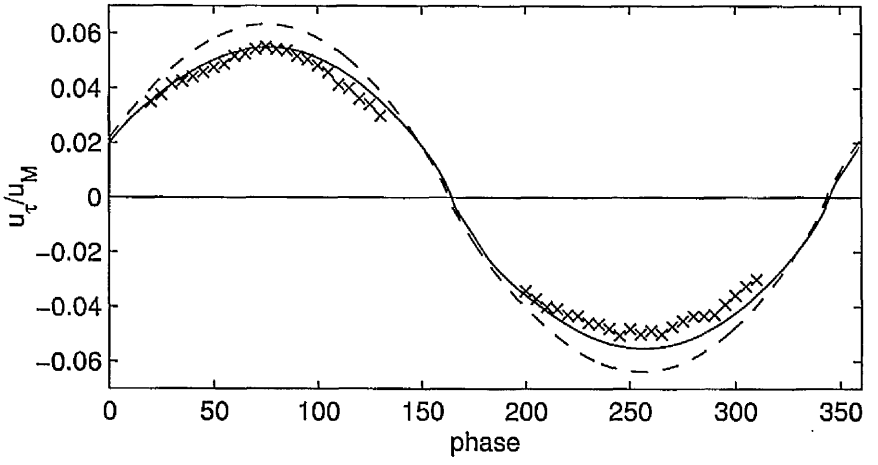

Figure (1): Friction velocity at the bed against phase position over one cycle, × JSF experimental data from a log fit [1], —— k-ϵ model, - - - - k-l model.

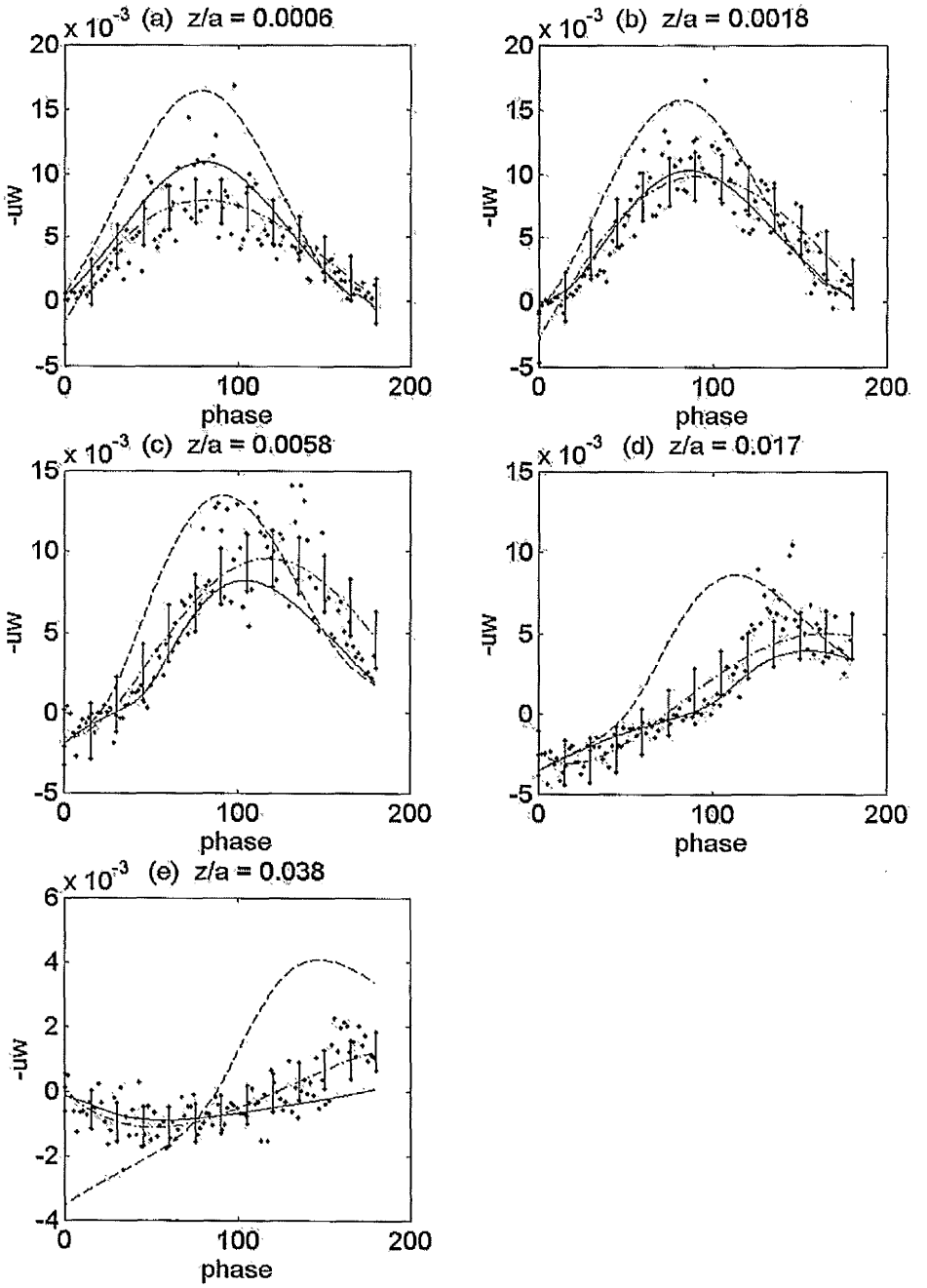

Figure (2): Reynolds shear stress as a function of time at five distances from the bed, • experimental data from JSF [2], – . – . polynomial fit, —— k-ϵ model, - - - - k-l model; the vertical lines give a measure of uncertainty in the polynomial fit.

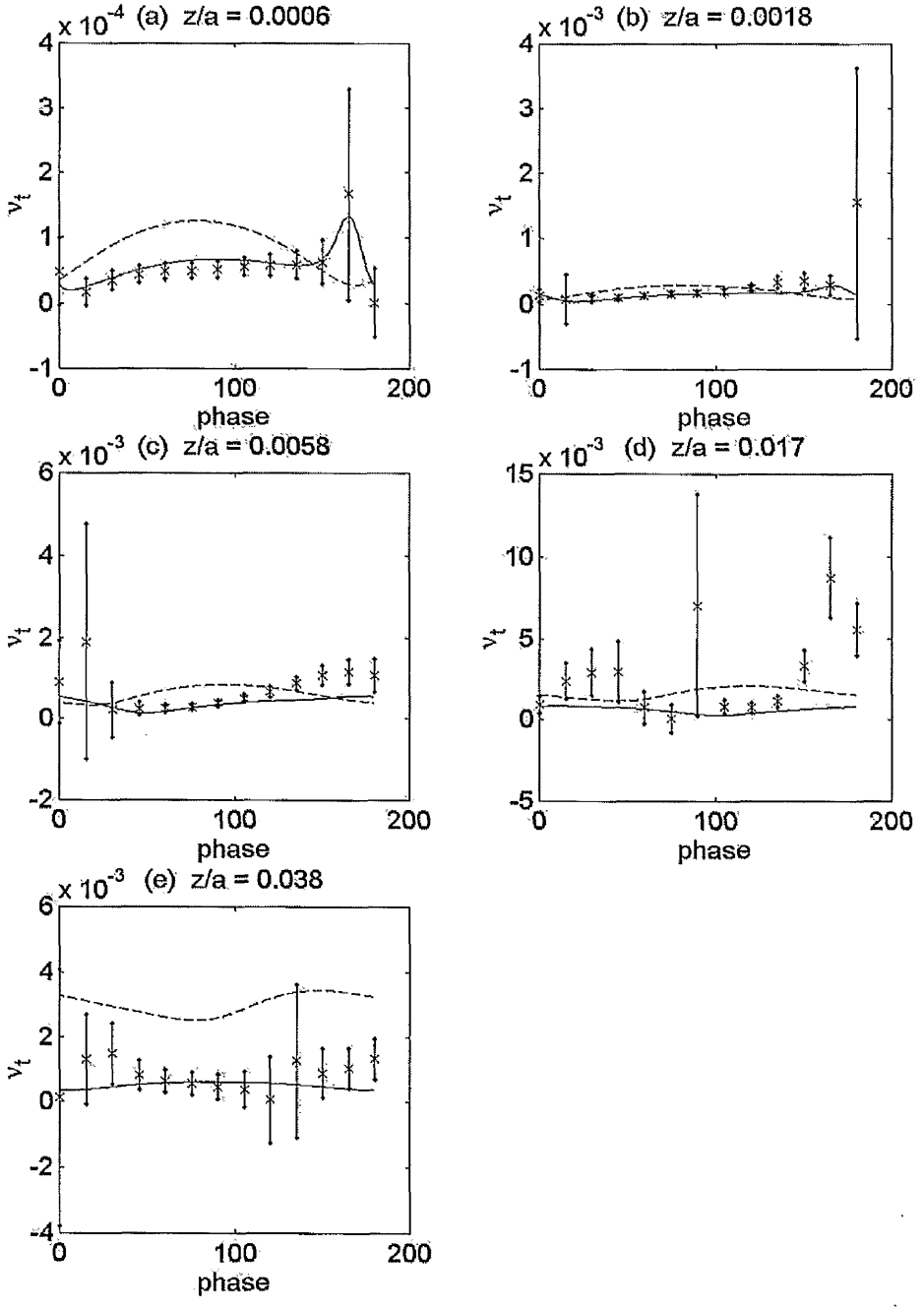

Figure (3): Turbulent eddy viscosity as a function of time at five distances from the bed, • experimental data from JSF [2], – . – . polynomial fit, —— k-ϵ model, - - - - k-l model; the vertical lines give a measure of uncertainty in the data.